Technische Universität München
TUM School of Engineering and Design

Clusters of Thermoacoustic Modes in Annular and Can-Annular Combustors

Guillaume Jean Jacques Fournier

Vollständiger Abdruck der von der TUM School of Engineering and Design der Technischen Universität München zur Erlangung eines

DOKTORS DER INGENIEURWISSENSCHAFTEN (DR.-ING.)

genehmigten Dissertation.

Vorsitz:
    Prof. Dr. Carlo L. Bottasso
Prüfer der Dissertation:
    Prof. Wolfgang Polifke, Ph.D.
    Prof. Dr. Nicolas Noiray

Die Dissertation wurde am 09.11.2023 bei der Technischen Universität München eingereicht und durch die TUM School of Engineering and Design am 08.02.2024 angenommen.

To my beloved Delphine and our wonderful children

"I think the world is too wonderful to have just happened."

— Arthur Schawlow

"Für den gläubigen Menschen steht Gott am Anfang, für den Wissenschaftler am Ende aller seiner Überlegungen"

— Max Planck

"Un peu de science éloigne de Dieu, mais beaucoup y ramène."

— Louis Pasteur

"As the depth of our insight into the wonderful works of God increases, the stronger are our feelings of awe and veneration in contemplating them and in endeavoring to approach their Author."

— Lord Kelvin

"What is man, that You make so much of him? and that You set Your heart upon him?"

— The Bible, Job 7:17

Abstract

This thesis aims at expanding the understanding of the thermoacoustic behavior of gas turbines. In particular, emphasis is given to the peculiar phenomenon of *mode clustering* in the spectra of annular and can-annular combustors, i.e. the appearance of sets of closely spaced eigenmodes. This thesis focuses on low-order network models, which represent complex systems as an ensemble of interconnected acoustic elements, to capture the essential underlying physics and provide valuable insight.

Thermoacoustic modes arise from two competing flow-flame-acoustic feedback loops, one involving the acoustics of the system, the other intrinsic to the flame and its immediate surrounding, leading to two types of eigenmodes, namely *acoustic* and *ITA*. Finding the later remains an arduous numerical task, thus motivating the use of TFD's in-house code *taX*, which solves for a linear eigenvalue problem to efficiently compute all eigenmodes. The capabilities of the toolbox have been enhanced, with, among others, a generalized flame element in state-space framework to account for arbitrary flame response.

If guaranteeing the completeness of the spectrum is of primary relevance, unambiguously identifying the nature of eigenmodes is equally crucial: acoustic and ITA modes exhibit different behaviors, in particular with respect to parameter change, which has direct consequences on mitigation strategies of unstable modes. A simple categorization criterion, based on the phase difference between the acoustic velocity states upstream and downstream the flame, is proposed. The novelty of this approach lies in the fact that the nature of a mode can be determined without requiring a tedious parameter sweep.

The discrete rotational symmetry of (can-)annular combustors allows to invoke Bloch theory to reduce the study to a single unit-cell, while preserving the dynamics of the complete system using quasi-periodic Bloch boundary conditions. If annular chambers can be modeled as ducts interconnected to a T-junction, leading to a thin annulus representation where plane waves propagate, can-annular combustors, in contrast, require to take into account the inertia of volume of fluid in the cross-talk area by means of a characteristic length. Both models can be derived analytically and the effects of the annular chamber or the acoustic cross-talk between cans are lumped into an effective outlet reflection coefficient that depends on the azimuthal order.

For low frequencies, and neglecting mean flow effects, this purely reactive acoustic coupling is approximated by an equivalent duct terminated by an open end, effectively simplifying the complex system into an elementary Rijke tube configuration. The resulting model allows to explain numerous observations. The equivalent downstream length changing with Bloch-wave number gives rise to clusters of both ITA and acoustic modes of various azimuthal order. Combined with phasor analysis, it also explains the structure of the spectra, where, in general, modes of higher azimuthal order are closest within a cluster and ITA modes are more damped. Additionally, acoustic and ITA eigenmodes are shown to follow specific trajectories in the complex plane, which are strongly influenced by the presence of exceptional points, highlighting that their interaction with the latter is essential to predict stability.

Kurzfassung

Ziel dieser Arbeit ist es, das Verständnis für das thermoakustische Verhalten von Gasturbinen zu erweitern. Der Schwerpunkt liegt dabei auf dem besonderen Phänomen des *Mode Clustering* in den Spektren von Ring- und Rohr-Ringbrennkammern, d. h. dem Auftreten von Gruppen eng beieinander liegender Eigenmoden. Diese Arbeit konzentriert sich auf Netzwerkmodelle niedriger Ordnung, die komplexe Systeme als ein Ensemble miteinander verbundener akustischer Elemente darstellen, um die wesentlichen zugrunde liegenden physikalischen Zusammenhänge zu erfassen und wertvolle Erkenntnisse zu gewinnen.

Thermoakustische Moden ergeben sich aus zwei konkurrierenden Rückkopplungsschleifen zwischen Strömung, Flamme und Akustik, von denen die eine die Akustik des Systems und die andere die Flamme und ihre unmittelbare Umgebung einbezieht, was zu zwei Arten von Eigenmoden führt, nämlich *akustische* und *ITA*. Letztere zu finden, ist nach wie vor eine mühsame numerische Aufgabe, was den Einsatz des TFD-eigenen Codes *taX* motiviert, der ein lineares Eigenwertproblem löst, um alle Eigenmoden effizient zu berechnen. Die Möglichkeiten der Toolbox wurden erweitert, u.a. durch ein verallgemeinertes Flammenelement im Zustandsraum, um beliebige Antworten der Flamme zu berücksichtigen.

Wenn die Gewährleistung der Vollständigkeit des Spektrums von primärer Bedeutung ist, ist die eindeutige Identifizierung der Art der Eigenmoden ebenso entscheidend: Akustische und ITA-Moden zeigen ein unterschiedliches Verhalten, insbesondere in Bezug auf Parameteränderungen, was direkte Auswirkungen auf die Strategien zur Eindämmung instabiler Moden hat. Es wird ein einfaches Kriterium zur Kategorisierung vorgeschlagen, das auf der Phasendifferenz zwischen den akustischen Geschwindigkeitszuständen stromaufwärts und stromabwärts der Flamme basiert. Die Innovation dieses Ansatzes liegt darin, dass die Art einer Mode bestimmt werden kann, ohne dass ein langwieriger Parameterstudie erforderlich ist.

Die diskrete Rotationssymmetrie von (Rohr-)Ringbrennkammern erlaubt es, die Bloch-Theorie heranzuziehen, um die Untersuchung auf eine einzige Einheitszelle zu reduzieren, wobei die Dynamik des Gesamtsystems durch quasi-periodische Bloch-Randbedingungen erhalten bleibt. Während Ringkammern als Kanäle modelliert werden können, die mit einer T-Verzweigung verbunden sind, was zu einer dünnen Ringdarstellung führt, in der sich ebene Wellen ausbreiten, muss bei Rohr-Ringbrennern die Trägheit des Fluidvolumens im Überschneidungsbereich durch eine charakteristische Länge berücksichtigt werden. Beide Modelle können analytisch hergeleitet werden und die Auswirkungen der Ringkammer bzw. der akustischen Wechselwirkung zwischen den Rohren werden in einem effektiven Auslassreflexionskoeffizienten zusammengefasst, der von der azimutalen Ordnung abhängt.

Für niedrige Frequenzen und unter Vernachlässigung der Effekte der mittleren Strömung wird diese rein reaktive akustische Kopplung durch einen äquivalenten Kanal mit offenem Ende approximiert, wodurch das komplexe System zu einer elementaren Rijke-Rohrkonfiguration vereinfacht wird. Mit dem daraus resultierenden Modell lassen sich zahlreiche Beobachtungen erklären. Die äquivalente stromabwärts gerichtete Länge, die sich mit der Bloch-Wellenzahl ändert, führt zu Clustern sowohl von ITA- als auch von akustischen Moden verschiedener azimutaler Ordnung. In Verbindung mit der Phasor-Analyse erklärt es auch die Struktur der Spektren, bei denen im Allgemeinen die Moden höherer azimutaler Ordnung innerhalb eines Clusters am nächsten liegen und die ITA-Moden stärker gedämpft sind. Darüber hinaus wird gezeigt, dass akustische und ITA-Eigenmoden bestimmten Bahnen in der komplexen Ebene folgen, die stark durch das Vorhandensein von *Exceptional Points* beeinflusst werden, was unterstreicht, dass ihre Interaktion mit letzteren für die Vorhersage der Stabilität wesentlich ist.

Vorwort

This is, by far, the part of a thesis I have always preferred to read because it perfectly emphasizes that a doctoral project is not “just” the achievement of an individual, but first and foremost a team effort involving many players, examplifying the verse “*in the multitude of counsellors there is safety*” (Proverbs 11:14).

During three and half years in the Space Division of Safran Aircraft Engines (which later became ArianeGroup), I discovered the world of rocket engine development. I have been fortunate to learn a lot from brilliant colleagues. Among others, many thanks to Martin Seive, David Testa, Fabien Juillet, Loic Penin, Sebastien Boufflert for the exciting discussions and your passion. David Tonon, with whom I shared an office, impressed me with his scientific rigor and was a source of inspiration. In the pursuit of scientific excellent, convinced that the latter is key for designing complex technological products, I decided to dedicate time and energy for a doctoral project. Many thanks to my car-sharing buddies, Julien Bruet, Guillaume Redoules, Aurélien Souto-Lebel, Arnaud Fontaine and Eric Véron, who supported me with this crazy career choice of going back to school.

And this is how, on a cold day of October 2018, I arrived in Munich to join TFD’s group at TUM. Wolfgang, I have learnt so much from you, but, for the sake of brevity, I can only write a short summary here. Thank you for trusting me with this project, for giving me a lot of freedom to explore my own ideas, while having always your door open for discussion. You pushed me to always do better. The high standards you set for yourself are a source of inspiration for the whole group. Many times, with well-chosen questions, you helped me clarify my own thoughts (“what’s the tweet of your paper?”) and your firm stance on the “assertion-evidence” format leads to high-quality presentations; this is one of my favourite things I learnt from you. A good summary was written by former colleague Shuai Guo: “you taught me how to go from a dependent idea implementer to an independent idea generator.”

This work would not have been possible without the tremendous help of Camilo F. Silva, who always showed great interest in my research. Your understanding of physics and your intuition have been an invaluable guidance to move forward and pinpoint the region of interest in my work, which translates in the many papers we wrote together. Max Meindl, with whom I shared my office, has been a great mentor and friend. Thank you for the countless hours spent answering my dumb and hopefully not too dumb questions, sharing your tips and tricks (I have become a great advocate of TikZ figures), cheering me up when I was lost. I could not have made it without you! Matthias Haeringer taught me everything about Bloch theory and azimuthal modes during whiteboard sessions in his office. I am forever grateful for your help. Thank you, Felicitas ~~Schaefer~~ Engelhardt, for your help finding the treacherous Exceptional Points, as well as for the nine-months *Elternzeit* you took that allowed me to have a contract extension. Many thanks to Felix Schily for your help mastering taX, but also all the non work-related stuff (phone calls *auf Deutsch* on my behalf, explanations of the intricacies of the German administration with Winterreifen, Zulassungsstelle, etc.).

Of course, a department cannot run smoothly without a high-quality “Sekretariat”. Many thanks to Helga Bassett for day-to-day handling, for your patience for explaining again and again how yellow vacations cards work or reminding me the correct address where to send my *Kostenrückerstattung*, which, despite 4 years at the chair, I couldn’t remember. Sigrid Schulz-Reichwald was of great help to manage the finances of the project.

I will keep great memories of the TD/TFD chair and all those whose paths I’ve crossed. Thank you for making these years unforgettable. Special mentions to my french speaking group (Anh Khoa Doan, Abdulla Ghani and Grégoire Varillon), my ITN fellows with whom I had great fun to travel all accross Europe before COVID struck (Sagar Kulkarni, Naman Purwar and Alireza Javareshkian), my TurboExpo 2022 travel buddies for an unforgettable week in Rotterdam (Gerrit Heilmann, Jonathan McClure, Jan-Andre Rosenkranz, Moritz Merk), and those I was happy to see again at TurboExpo 2023 in Boston (Jan Kaufmann, Manuel Vogel, Thomas Steinbacher, Martin March, Saskia Flebbe), Julian Renner, who, after four years, still cannot say my first name properly, Simon Tartsch and his daily joyful mood and energy to make the chair a better place, Shuai Guo and his strange fascination for corgi dogs, Thomas Hofmeister, the paper-writting machine, Christophe Wieland, Michael McCartney, Edoardo Scoletta, Marcin Rywik, Simon van Buren, ein WTP-Affe, and the new guys, whom I haven’t had time to get to know very well but who are really nice, Marcel Desor, Axel Zimmermann, Marian Hiestermann and Philipp Brokof. Philip Bonnaire, I was very happy to share my office with you for the last part of my time at the chair. I did my best to mentor you and give you as much as I had received from Max. I enjoyed every day with you, our discussion about any topics, and your kindness (I do not forget your help emptying the flat when we moved back to France!). My desk is now in the good hands of Alex Eder, and I trust he will put it to good use. Many thanks to Jens Hümmer and his help to organize memorable Einstandsfeier (and hopefully my Doktorsfeier soon) and Thomas Schleussner for repairing all my broken stuff, his good advices, and his constant effort for having me speak German to improve my *deutsche Sprachkenntnisse*.

Being part of a European project allowed me to regularly meet my fellow ESRs; special mention to Thomas Indlekofer, Yi Hao Kwah, Roberto Ciardiello, Francesco Gant, Karl Töpperwien, Abel Faure-Beaulieu, Ermanno Lo Schiavo, Preethi Rajendram Soundararajan and Sylvain Humbert. Many thanks to James Dawson for running flawlessly this project. I was delighted to meet and get to know incredible researchers from all over Europe who also showed interest in my research: Thierry Poinsot, Laurent Gicquel, Ronan Vicquelin, Matthew Juniper, Oliver Paschereit, Jonas Moeck, Alessandro Orchini, Stéphane Richard, Nicolas Noiray, Bruno Schuermans, Marco Zedda. I want to also thank Aimee Morgans and Tim Lieuwen for giving incredible lectures on thermoacoustic during the Cambridge Summer School in 2018.

ITN also rhyms with secondment. The two weeks I spent in Baden, hosted by Ansaldo Energia, were amazing. Thank you, Mirko Bothien, for making it possible and allowing me to explore ideas that were not planned in the original proposal. Despite COVID, which forced us to move towards a virtual format, this collaboration was very fruitful. Many thanks to the Thermoacoustics team for the warm welcome. In particular, I want to acknowledge the supervision and mentoring of Giulio Ghirardo who is a talented and inspiring researcher. Your advices and guidance helped me turn my vague initial ideas into a concrete journal paper.

I had the incredible opportunity to actively contribute to two workshops, one dedicated to Flame Dynamics, the other to Low-Order Modeling, for the ANNULIGhT and Polka ITN respectively. Thank you, Wolfgang, for trusting me with that mission and for allowing me to prepare and conduct tutorial sessions on your behalf. It truly was an enlightening experience. Another memorable milestone the organization of SoTiC 2021, the most important conference exclusively dedicated to thermoacoustics and combustion dynamics. If COVID forced us to change the in-person venue for a virtual format instead, the event was nevertheless a great success, with 170 participants from 12 countries. Thomas Sattelmayer, it was really great to work with you!

Moving abroad is also the opportunity to forge new friendships. We were very happy to meet the Pündterplatz 6 (now Unterschleißheim) Geschwister and tie bonds over the years. In particular, we are forever in debt to Christian and Manuela Kuhn, who opened their house and had me stay for two months before I could overcome the nightmare of finding a flat in the region of Munich! I keep great memories of all the moments we shared. Special mention to Katharina Lutterer, Rojeh & Alissa Bassal and Paul & Kathi Reinders, our closest neighbours that we always enjoyed meeting. Bayern is truly a wonderful region. These almost four years and associated memories will be forever remembered. We are thankful to the parents, in-laws, brothers and sisters, cousins and friends who came visit regularly.

Many thanks to my manager Stephan Zurbach, and my new colleagues at Safran Tech for their encouragments (and sometimes jokes) for finishing writing the diss: Nicholas Treleaven, my thermoacoustician fellow, Stefano Puggelli, my H_2 boss, Jean-Baptiste May-Carle, the impostor, Said Taileb, the one who does “fast propagating combustion”, Samer Maalouf and Ephraim Toubiana, our ~~foosball~~ thermal management experts and Quentin Holka, my ECL-TUM fellow. It is good to no longer be the only non-doctor in the team!

I am grateful to Prof. Carlo L. Bottasso for chairing the examination and Prof. Nicolas Noiray for reviewing my work. Nicolas, thank you for your interest in my research, for your constructive feedback and kind comments. It was a pleasure to discuss science with you and I hope that we will have the opportunity to work together in the future.

I am forever in debt to my parents who supported me during my entire studies. I cannot imagine how many hours, starting from primary school, you spent helping and accompanying me on this journey. As we say in the family, “*Merci pour tout !*”. And Papa, if I did not follow your path in medicine, nonetheless will there be another generation with a Dr. Fournier.

The last months have been rough, to say the least: moving back to France, starting a new job, welcoming our 3rd wonder, finishing taX coding and tutorials and writing the diss on weekends, paternity leave or any available minute of free time. I am grateful to my children, for whom I was often absent, for their patience. Now that this chapter comes to an end, we will make up for lost time.

Last but not least, my amazing wife, Delphine. Every day, you make my life wonderful and I learn to love you more. I would need three additional pages to list everything you bring to my life. Simply summarized, thank you for your love, your precious advices, your unconditional support. I am truly blessed and thankful to have you by my side. Thank you for trusting me with this crazy adventure. I loved these years in Freising, where our first children were born, and I am excited to live with you whatever future comes ahead. At the beginning of my doctoral project, when I was lost, discouraged and wanted to give up, you supported me and helped me to keep going. You are the reason this project came to an end and you deserve this title as much as I do, *Frau Doktor Fournier*.

This project has received funding from the European Union’s Horizon 2020 research and innovation programme under Grant Agreement No 765998 *Annular Instabilities and Transient Phenomena in Gas Turbine Combustors* (ANNULIGhT).

Funded by
the European Union

Contents

List of Figures

Nomenclature

Latin Letters

$\mathcal{A}$	Cross-sectional area
c	Speed of sound
$f,\ g$	Characteristic wave amplitudes
$\mathcal{F}$	Flame transfer function
F	Flame frequency response
H	Can width
L	Length
L^*	Aspect ratio of a can
L_g	Gap size
L_g^*	Coupling strength, $L_g^* = L_g / H$
$\mathcal{L}$	Equivalent length
m	Azimuthal order
n	Flame interaction index
N	Degree of discrete rotational symmetry
p	Pressure
$\dot{q}$	Heat release rate
r	Specific gas constant
R	Reflection coefficient
$\mathcal{R}$	Equivalent reflection coefficient
s	Laplace variable, $s = \sigma + i\omega$
s	Entropy
t	Time
T	Temperature
$\boldsymbol{u}$	Velocity vector
$\boldsymbol{x}$	Position vector
x	Axial coordinate

Greek Letters

α	Acoustic damping coefficient
γ	Heat capacity ratio
θ	Angular position in cylindrical coordinates
Θ	Normalized temperature ratio, $\Theta = (T_d - T_u)/T_u$
ν	Frequency
ξ	Ratio of specific impedances, $\xi = \bar{\rho}_u c_u / \bar{\rho}_d c_d$
ρ	Density
σ	Growth rate
ς	Background noise intensity
τ	Time delay
φ	Velocity potential
Φ	Categorization criterion
ψ	Acoustic mode shape
Ψ	Arbitrary function that satisfies Bloch decomposition
ω	Angular frequency, $\omega = 2\pi\nu$

Superscripts

$\bar{\square}$	Time-averaged quantity
$\square'$	Fluctuating quantity
$\dot{\square}$	First order time derivative
$\ddot{\square}$	Second order time derivative
$\square^*$	Normalized quantity

Subscripts

$\square_{char}$	Characteristic
$\square_d$	Downstream
$\square_F$	Flame
$\square_i$	Inlet
$\square_m$	Azimuthal-order-dependent quantity
$\square_o$	Outlet
$\square_u$	Upstream

Dimensionless Numbers

He	Helmholtz number
St	Strouhal number

Abbreviations

CFD	Computational Fluid Dynamics
FFR	Flame Frequency Response
FTF	Flame Transfer Function
ITA	Intrinsic Thermoacoustic
LEE	Linearized Euler Equations
LES	Large-Eddy Simulation
LEVP	Linear Eigenvalue Problem
LNSE	Linearized Navier-Stokes Equations
LOM	Low-Order Model
LRF	Linearized Reactive Flow
LTI	Linear Time Invariant
NLEVP	Non-Linear Eigenvalue Problem
UIR	Unit Impulse Response
TFD	Thermo-Fluid Dynamics Group
XP	Exceptional Point

1 Introduction

“*We choose to go to the moon in this decade and do the other things, not because they are easy, but because they are hard, because that goal will serve to organize and measure the best of our energies and skills, because that challenge is one that we are willing to accept, one we are unwilling to postpone, and one which we intend to win.*” [5].

When Kennedy gave, at Rice University, the famous speech that launched the race to the moon, little did he knew that this sentence would perfectly summarize the chaotic developement of liquid rocket engines, in particular the F-1 engine powering Saturn V. Crippled by combustion instabilities, the latter required years of effort and approximately two thousand full-scale tests to reach stability, for an estimated cost over a billion dollars [6]. While this remains probably the best-known example, thermoacoustics is encountered in other applications, for instance in ramjets and afterburners [7] or in gas turbines, in particular when operated in lean-premixed conditions [8, 9]. This type of self-excited instabilities result from the coupling between the heat release fluctuations of the flame and the acoustics of the system, which may result in a positive feedback loop inducing growing pressure oscillations. They must be avoided at all cost; not only do they degrade the operability, performance and emissions, but the repeated exposure to high pressure levels over time promote mechanical fatigue and may lead to catastrophic failure of the combustor [2].

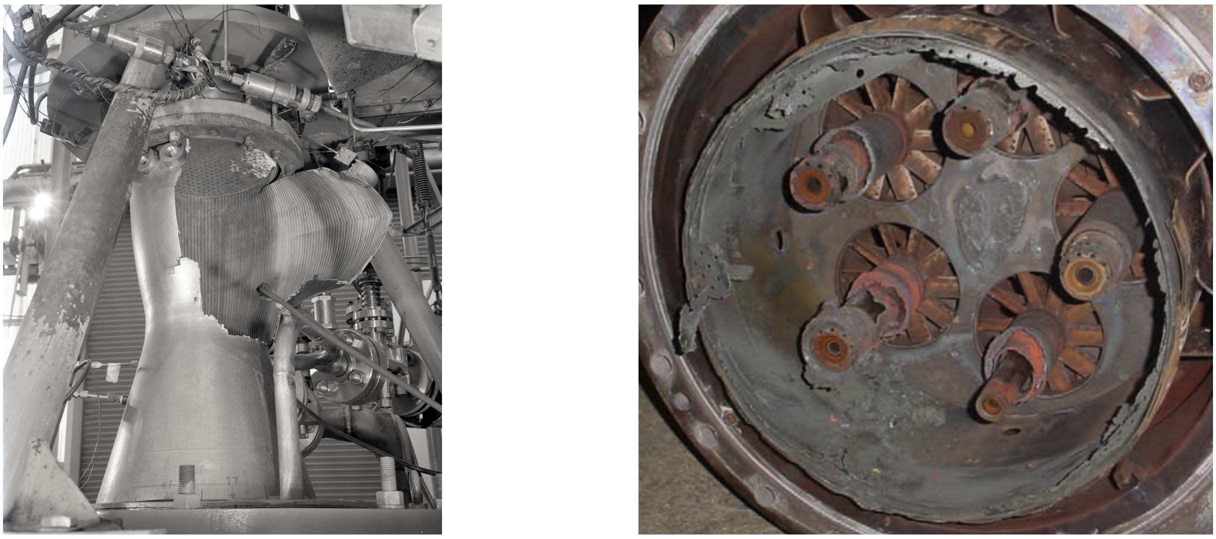

(a) **(b)**

Figure 1.1: (a) Engine failure in the *Rocket Engine Test Facility* test stand. Photo reproduced from [1]. (b) Gas turbine combustor damaged by combustion instabilities. Courtesy of Prof. Tim Lieuwen [2].

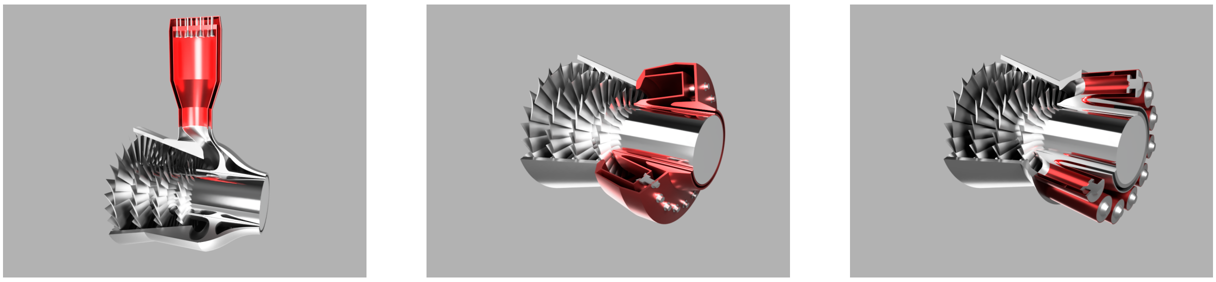

(a) Silo combustor **(b)** Annular combustor **(c)** Can-annular combustor

Figure 1.2: Evolution of gas turbines architectures. Courtesy of Dr. Abel Faure-Beaulieu [3].

To meet the need of improved performances, gas turbines architectures have greatly evolved over the last decades. Older machines often made use of *silo* combustors because of their simple design and construction, which allowed for easy accessibility. These were the times of long diffusion flames, thus explaining the significant dimensions of the combustor. Unfortunately, the price to pay was an increased number of large surfaces to cool, which proved to be both difficult and expensive. The complex air path from the compressor, flowing up along the silo to until the U-turn at the combustor entrance, also caused important pressure losses, i.e. a reduced efficiency. Despite a massive transition piece, a uniform distribution of the hot gases around the circumference was hardly possible resulting in problematic turbine inlet temperature profiles, only partially reduced by twin-silos configurations [10]. Their excessive weight restricted their use exclusively to land-based applications. In comparison, *annular* combustors are extremely compact by design and exhibit exceptional power density, making them perfect candidates for aero-engines. The lesser cooling surfaces, the better turbine-stage feeding and the overall efficiency were sufficient advantages to also motivate their use in land-based gas turbines [11, 12]. However, the recent years have seen this industry transition towards a new type of architecture, which consist of an ensemble of identical cans placed in an annular arrangement, hence the name *can-annular* combustors. The latter can be found in the H-class gas turbines of the major players, e.g. Ansaldo GT36 [13], Siemens SGT6 [14] or GE 9HA [15]. Besides the eased integration and sealing constraints, the improved accessibility and more practical maintenance, an important advantage of cans is the rig-to-engine transfer; although not perfectly reliable, inferring the behavior of the full engine from high-pressure single can testing will always be better than annular designs. A drawback of this architecture is, however, the need of either cross-fire tubes or one ignitor and flame supervision per can.

One of the challenges of the coming decades will be to meet the ever growing demand for energy while reducing the environmental impact of combustion systems [16]. For the aeronautical industry, the need to further reduce fuel consumption and NO_x emissions may require to move away from RQL (Rich-Quench-Lean) systems and consider other injection technologies such as Lean Direct Injection (LDI) or Lean Premixed Prevaporized (LPP) [17]. In the energy sector, gas turbines are foreseen to play a major role in stabilizing the electrical grid by counterbalacing the unsteadiness in supply of renewable sources or by storing the excess with “power-to-gas” solutions [18]. With the rise of new architectures as well as alternative fuels (hydrogen, SAF, etc.), thermoacoustic combustion instabilities are expected to remain a “hot topic” in the years to come. Despite being known since the 19^{th} century [19], they continue to be an industrial headache. The approach of NASA for Apollo, with enormous outlay of energy and resources, being no longer feasible for modern programs, a variety of numerical tools and methods have emerged to better understand, predict and mitigate instabilities [20]. If *Large-Eddy Simulations* have long been restricted to simple academic cases, the increased computational power allows nowadays to investigate complex industrial configurations [21, 22]. This high-fidelity approach, by solving the full set of nonlinear governing equations, requires the least modeling assumption, and thus provides the most accurate results and inherently captures nonlinear flame-flow interaction and nonlinear saturation of the flame response, i.e. naturally account for the formation of limit cycle oscillations. However, the costs remain excessive for such tool to be employed in design phases, which limits its use rather to a posteriori verifications of experimental observations. Consequently, as stated by Magri et al. [23], "*linear stability has remained a powerful mathematical tool to gain understanding of fluid behavior by tracking infinitesimal perturbations or observing responses to forcing*". Linearization of the Navier-Stokes equations, species transport equations and reaction mechanism for the source terms yields the *Linearized Reactive Flow* (LRF) approach [4, 24]. This monolithic formulation predicts thermoacoustic eigenmodes with increased accuracy compared to hybrid modeling strategies that employ stronger simplifications, e.g. *Linearized Navier-Stokes Equations* [25, 26], *Linearized Euler Equations* [27] (omitting viscous effects) or *Helmholtz Equation* [28] (neglecting mean flow). Finally, *low-order network models* represent complex systems as an ensemble of interconnected elementary acoustic elements. While simplistic in appearance, this approach, pioneered by Merk [29], is crucial to improve the fundamental understanding [8, 30–36].

The recent years have shown that many observations are still not perfectly understood. Among others, the spectra of annular and can-annular combustors have been shown to exhibit *clusters* of modes of various nature, i.e. sets of closely spaced eigenfrequencies [37, 38]. The focus of the work summarized in this publication-based thesis is to provide insight on the origin of these phenomena, employing low-order modeling techniques to explain the underlying physics. In particular, it is highlighted that acoustic models of annular chambers and cross-talk area of can-annular combustors can be derived analytically and used to enforce effective boundary conditions, allowing for convenient analogy with simple Rijke tube thermoacoustic models. This publication-based manuscript, whose purpose is to provide the context around and connections between the papers of this thesis, is organized as follows: in Chapter 2, a brief overview of low-order modeling is recalled. Eigenmodes of various nature can be categorized with a simple criterion, as discussed in Chapter 3. Then, analytical derivations of acoustic models for annular and can-annular configurations are summarized in Chapter 4, and used in Chapter 5 to explain clusters as well as the peculiar behavior of eigenmodes in the spectra. Finally, in Chapter 6, a detailed discussion put the papers that constitute this thesis into perspective with the existing literature. The reader's attention is drawn to the fact that Chapters 2-5 not only present the state of the art, but also contain concise descriptions of the original contributions of this thesis.

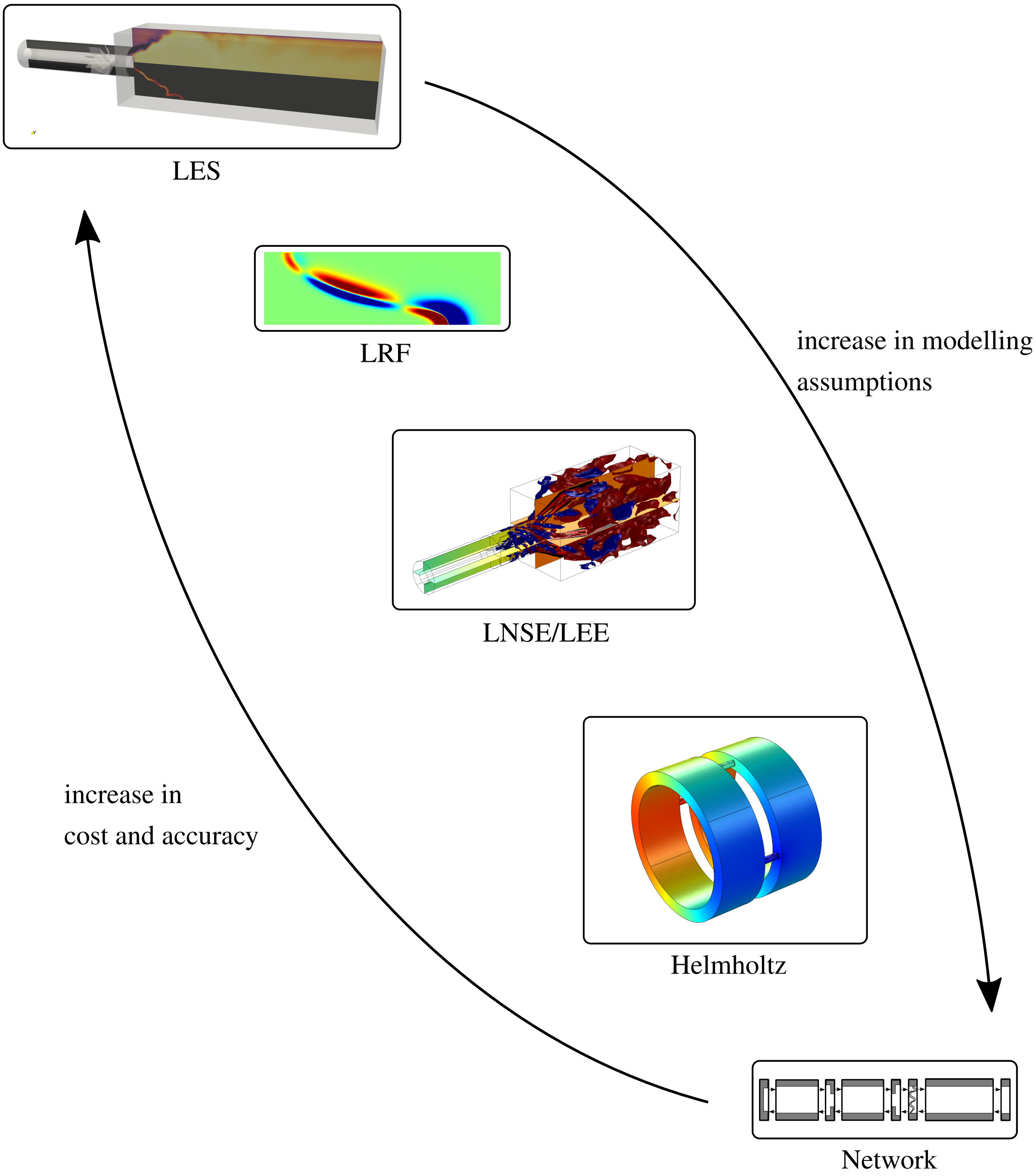

Figure 1.3: A variety of methods are available to investigate thermoacoustic combustion instabilities. Computational cost is reduced with increasing number of modeling assumption, at the expense of accuracy. Pictures are courtesy of Dr. Max Meindl [4] and Alexander J. Eder.

2 Fundamentals of Network Modeling

Network modeling relies on a *divide et impera* approach that enables to represent a complete thermoacoustic system as an ensemble of elementary interconnected acoustic elements. The modeling assumptions allow to reduce the complexity of the problem while preserving the essential physics. This chapter introduces the governing equations and gives an overview of commonly used acoustic elements.

2.1 Governing Equations

The motion of viscous Newtonian fluids is described with a set of three conservation equations. A detailed derivation can be found in the literature [39–41].

The *continuity equation* states the conservation of mass:

$$\frac{D\rho}{Dt} + \rho\nabla\cdot\boldsymbol{u} = 0 \tag{2.1}$$

where $\frac{D}{Dt} = \frac{\partial}{\partial t} + \boldsymbol{u}\cdot\nabla$ denotes the material derivative, ρ the density, t the time and $\boldsymbol{u}$ the velocity.

The *Navier-Stokes equation* arise from Newton's second law which states the principle of momentum conservation. Assuming absence of body forces and neglecting viscosity yields the *Euler equation*:

$$\rho\frac{D\boldsymbol{u}}{Dt} + \nabla p = 0 \tag{2.2}$$

The *energy equation* can be written in terms of internal energy or total enthalpy. In the absence of body forces, and neglecting viscous effects and heat conduction, it reduces to an isentropic condition:

$$\frac{D\mathrm{s}}{Dt} = 0 \tag{2.3}$$

Closure is provided with the assumption of *ideal gas* behavior. The equation of state relates pressure, density and temperature:

$$p = \rho r T \tag{2.4}$$

In acoustics, disturbances of the flow variables are small compared to their mean value, which allows for linearization of the governing equations. Using Reynolds decomposition, the quantities of interest consist of a steady-state mean value, denoted by a $\overline{\square}$, and a superimposed fluctuation, denoted by a $\square'$.

$$p(\boldsymbol{x},t) = \overline{p}(\boldsymbol{x}) + p'(\boldsymbol{x},t); \quad \boldsymbol{u}(\boldsymbol{x},t) = \overline{\boldsymbol{u}}(\boldsymbol{x}) + \boldsymbol{u}'(\boldsymbol{x},t); \quad \rho(\boldsymbol{x},t) = \overline{\rho}(\boldsymbol{x}) + \rho'(\boldsymbol{x},t) \tag{2.5}$$

2.2 Duct Acoustics

Considering only the fluctuating parts of the mass conservation equation Eq. (2.1) and Euler equation Eq. (2.2), assuming zero mean flow, and neglecting higher order terms yields:

$$\frac{\partial \rho'}{\partial t} + \bar{\rho}\nabla \cdot \boldsymbol{u}' = 0 \tag{2.6}$$

$$\bar{\rho}\frac{\partial \boldsymbol{u}'}{\partial t} + \nabla p' = 0 \tag{2.7}$$

From the state equation for an ideal gas in homentropic flow (i.e. constant and uniform entropy), it follows that pressure is a function of density only. A first order approximation is:

$$p' = c^2 \rho' \tag{2.8}$$

where $c = \sqrt{\gamma r \overline{T}}$ is the speed of sound and γ the ratio of specific heat capacities.

Inserting Eq. (2.8) into Eq. (2.6), taking the time derivative and subtracting the divergence of Eq. (2.7) yields the *wave equation* for pressure disturbances:

$$\frac{\partial^2 p'}{\partial t^2} - c^2 \nabla^2 p' = 0 \tag{2.9}$$

Assuming that only one-dimensional plane acoustic waves propagate, Eq. (2.9) can be factorized:

$$\left(\frac{\partial}{\partial t} + c\frac{\partial}{\partial x}\right)\left(\frac{\partial}{\partial t} - c\frac{\partial}{\partial x}\right) p' = 0 \tag{2.10}$$

The resulting formulation reveals two independent propagation equations. Consequently, the general solution of the wave equation is a superposition of two waves, traveling in the upstream and downstream direction respectively. The corresponding characteristic wave amplitudes are defined as follows:

$$f \equiv \frac{1}{2}\left(\frac{p'}{\bar{\rho}c} + u'\right), \quad g \equiv \frac{1}{2}\left(\frac{p'}{\bar{\rho}c} - u'\right) \tag{2.11}$$

Assuming harmonic time dependence, the acoustic scattering matrix of a simple duct of length L reads:

$$\begin{bmatrix} f_d \\ g_u \end{bmatrix} = \begin{bmatrix} e^{-s\tau} & 0 \\ 0 & e^{-s\tau} \end{bmatrix} \begin{bmatrix} f_u \\ g_d \end{bmatrix} \tag{2.12}$$

The term $e^{-s\tau}$ represents the phase change resulting from the acoustic propagation of the waves, $\tau = L/c$ being the time it takes to travel along the length L of the duct at speed c. The Laplace variable is defined as $s = \sigma + i\omega$, with σ the growth rate and $\omega = 2\pi\nu$ the angular frequency.

Equation (2.12) is non-linear in frequency s. Padé approximation allows to transform the exponential term in a rational polynomial in s, but suffers from several limitations [42]. Alternatively, a spatial discretization with finite difference leads to a set of linear time-invariant (LTI) ordinary differential equations (ODE) that can be written in state-space formalism:

$$\begin{cases} \dfrac{\mathrm{d}\mathbf{x}(t)}{\mathrm{d}t} = \mathbf{A}\mathbf{x}(t) + \mathbf{B}\begin{bmatrix} f_u \\ g_d \end{bmatrix} \\ \begin{bmatrix} f_d \\ g_u \end{bmatrix} = \mathbf{C}\mathbf{x}(t) \end{cases} \tag{2.13}$$

where **x** is state vector, the matrix **A** describes the dynamics of the system, **B** relates the time derivative of state to the input, **C** maps the state on the outputs and **D**, the feedthrough matrix, is null in this case. These matrices have constant coefficients that are independent of frequency s.

Such state-space formalism allows for an elegant and simple, yet accurate, representation of the considered system. For simplicity, mean flow effects are not considered in this thesis but can easily be accounted for [42]. Similarly, the presented framework holds for ducts with temperature gradients and varying cross-sectional area [43, 44].

2.3 Acoustically Compact Elements

Several elements may have an axial spatial extension much shorter than the wavelengths of interest, and, as such, can be considered acoustically compact. Nonetheless, the jump conditions may have a non-negligible impact on the overall system, thus the physics must properly be captured. Considering an element with a varying cross-sectional area, e.g. a contraction, an abrupt area expansion, coupling relations between the upstream and downstream locations are derived using the *unsteady Bernoulli equation*:

$$0 = \frac{\partial}{\partial x}\left(\frac{\partial \varphi}{\partial t} + \frac{u^2}{2} + \frac{\gamma}{\gamma - 1}\frac{p}{\rho}\right) \tag{2.14}$$

where φ is the velocity potential.

Integrated along a streamline of meanflow between the upstream x_u and downstream x_d coordinates, the first term Eq. (2.14) writes:

$$\int_{x_u}^{x_d} \frac{\partial}{\partial x}\left(\frac{\partial \varphi}{\partial t}\right) dx = \int_{x_u}^{x_d} \frac{\partial}{\partial t}\left(\frac{\partial \varphi}{\partial x}\right) dx = \frac{\partial}{\partial t}\int_{x_u}^{x_d} u(x)\, dx \approx \frac{\partial}{\partial t} u_u \int_{x_u}^{x_d} \frac{\mathcal{A}_u}{\mathcal{A}(x)} dx \tag{2.15}$$

where the approximation $\mathcal{A}(x)\, u(x) \approx \mathcal{A}_u u_u$ results from the acoustically compact assumption, as the flow through the element is effectively incompressible. Defining the characteristic length

$$L_{char} = \int_{x_u}^{x_d} \frac{\mathcal{A}_u}{\mathcal{A}(x)} dx \tag{2.16}$$

and assuming harmonic time dependence, Eq. (2.15) reduces to:

$$\int_{x_u}^{x_d} \frac{\partial}{\partial x}\left(\frac{\partial \varphi}{\partial t}\right) dx = s L_{char} u_u \tag{2.17}$$

Physically, the characteristic length accounts for the inertia of the volume of fluid between the two reference positions u and d, i.e. a change in pressure difference $p'_d - p'_u$ will lead to a *gradual* change in velocity u'_u leading to phase difference between the two terms.

The integral in space of the remaining two terms of Eq. (2.14) is simply evaluated at location x_u and x_d. Linearization with Reynolds decomposition, assuming zero mean flow and neglecting higher order terms yields:

$$s L_{char} u'_u + \frac{p'_d - p'_u}{\bar{\rho} c} = 0 \tag{2.18}$$

Similarly, by neglecting mean flow effects, mass conservation integrated over the control volume reduces to conservation of volumetric flow rate:

$$u'_d = \frac{\mathcal{A}_u}{\mathcal{A}_d} u'_u \tag{2.19}$$

Writing Eq. (2.18) and Eq. (2.19) in terms of characteristic wave amplitudes f and g leads to:

$$\begin{bmatrix} f_d \\ g_u \end{bmatrix} = \begin{bmatrix} \dfrac{2\mathcal{A}_u/\mathcal{A}_d}{1+\mathcal{A}_u/\mathcal{A}_d+sL_{char}} & 1-\dfrac{2\mathcal{A}_u/\mathcal{A}_d}{1+\mathcal{A}_u/\mathcal{A}_d+sL_{char}} \\ 1-\dfrac{2}{1+\mathcal{A}_u/\mathcal{A}_d+sL_{char}} & \dfrac{2}{1+\mathcal{A}_u/\mathcal{A}_d+sL_{char}} \end{bmatrix} \begin{bmatrix} f_u \\ g_d \end{bmatrix} \tag{2.20}$$

Equation 2.20 is simply the state-space representation of the considered element, where the state equation is null and the system is feedthrough-only, i.e. the outputs are directly related to the inputs. Derivation to account for mean flow effects and acoustic losses can be found in the literature [45].

2.4 Flame and Unsteady Heat-Release Modeling

2.4.1 Rankine-Hugoniot Equations

In the typical frequency range of interest, the length of a flame is much smaller than the relevant acoustic wavelengths. As a result, similarly to Sec. 2.3, the flame can reasonably be assumed acoustically compact. The conservation equations for mass, momentum and energy are linearized to relate fluctuations of heat release $\dot{q}'$, acoustic velocities u' and pressures p' upstream and downstream the flame. Introducing two dimensionless parameters, $\xi = \bar{\rho}_u c_u / \bar{\rho}_d c_d$ the ratio of specific impedances and $\Theta = (T_d - T_u)/T_u$ the normalized temperature ratio, and neglecting the higher order Mach number terms for simplicity, the derivation yields the *acoustic Rankine-Hugoniot jump conditions* [46–48]:

$$\begin{cases} \dfrac{p'_d}{\bar{\rho}_d c_d} = \xi \dfrac{p'_u}{\bar{\rho}_u c_u} \\ u'_d = u'_u + \Theta \bar{u}_u \dfrac{\dot{q}'}{\bar{\dot{q}}} \end{cases} \tag{2.21}$$

The first equation simply states that pressure is continuous through the flame. On the contrary, its gradient, i.e. acoustic velocity, is not: the flame acts as a source of volume and creates a discontinuity in acoustic velocity, as shown by the source term $\dot{q}'$ in the second equation. The latter is unknown and must be modeled to provide closure for the equation.

2.4.2 Flame Transfer Function

To account for the flow-flame coupling, the unsteady heat release $\dot{q}'$ is governed by an external model, like a *flame transfer function* (FTF). The latter can be obtained from experiments [49, 50], semi-analytical models [51, 52] or LES simulations with either monofrequency

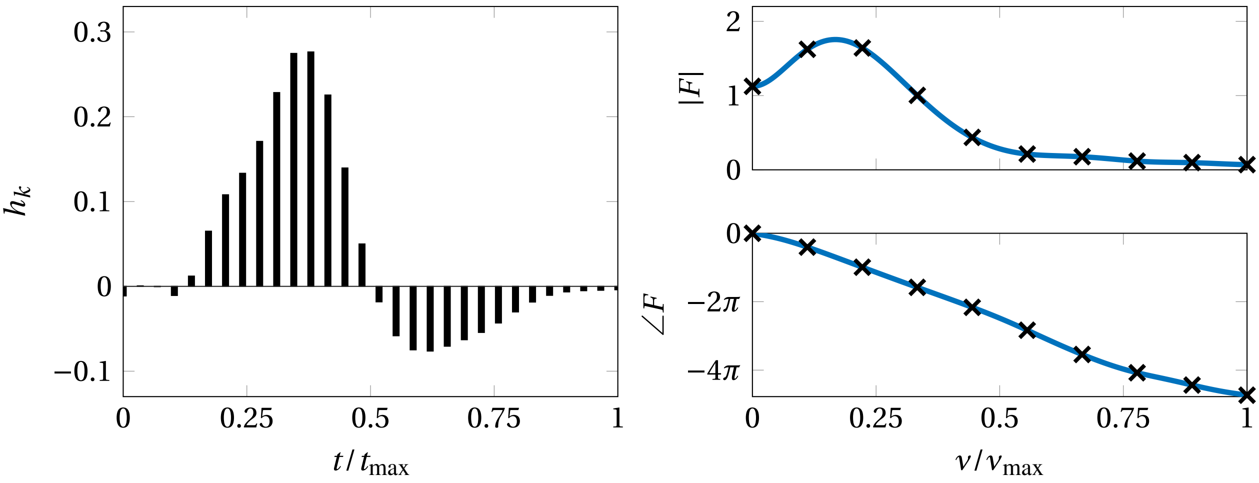

(a) **(b)**

Figure 2.1: (a) *Unit impulse response* (UIR) of a flame obtained with LES. Such time domain representation is completely equivalent to the FTF $\mathcal{F}(s)$ in the frequency domain. (b) Bode diagram of the *flame frequency response* (FFR) F (i.e. absolute value and phase of the FTF $\mathcal{F}(s)$ evaluated for zero growth rate) as a function of dimensionless frequency. The proposed continuous state-space representation shows excellent agreement with the discrete data obtained from LES.

excitation [53–55] or broadband forcing and system identification [56, 57]. The FTF $\mathcal{F}(s)$ is a linear model relating unsteady heat release fluctuations to acoustic velocity fluctuations at a reference position, e.g. just upstream the flame. The relation is normalized by the mean values and writes:

$$\frac{\dot{q}'}{\bar{\dot{q}}} = \mathcal{F}(s)\,\frac{u'_u}{\bar{u}_u} \tag{2.22}$$

A first approach was proposed by Crocco with the well-known $n-\tau$ model [58]:

$$\mathcal{F}(s) = n e^{-s\tau_F} \tag{2.23}$$

Although simple, such model captures the essential aspects of a generic flame. The latter responds to perturbations with a certain strength n. However, the response is not instantaneous but rather takes place with a time delay τ_F, expressed by the exponential term. This model continues to be widely used in the context of low-order networks because it often enables to derive analytical solutions and gain better insight.

To overcome the limitations of the $n-\tau$ model and obtain a quantitatively accurate description of a flame response, a natural generalization is to model the latter as *distributed time delays* (DTD) [59], as exemplified in Fig. 2.1. The *unit impulse response* (UIR), obtained either through LES or experiments, fully characterizes a LTI system. This time-domain point of view is completely equivalent to the FTF representation in the frequency domain:

$$\mathcal{F}(s) = \sum_{k=0}^{N} h_k e^{-s\Delta t k} \tag{2.24}$$

Such discrete FTF can be transformed into a continuous state-space representation with constant-coefficient matrices. It is well-known from control theory that a time delay can be expressed using an advection equation [60]. Since a DTD model is nothing but a collection of individual time delays, in a similar manner as the approach introduced in Sec. 2.2, a pseudo-space is discretized using finite difference to solve for an advection equation, which leads to the state-space representation:

$$\begin{cases} \dfrac{\mathrm{d}\mathbf{x}}{\mathrm{d}t} = \mathbf{A}\mathbf{x} + \mathbf{B}\dfrac{u'_u}{\overline{u}_u} \\ \dfrac{\dot{q}'}{\bar{\dot{q}}} = \begin{bmatrix} h_1 \dots h_N \end{bmatrix} \mathbf{x} + h_0 \dfrac{u'_u}{\overline{u}_u} \end{cases} \tag{2.25}$$

The **C** and **D** matrices of the output equation directly contain the coefficients h_k of the UIR. As highlighted in Fig. 2.1, such continuous model shows excellent agreement with the discrete reference, both in terms of gain and phase of the flame frequency response and exhibit the features typically observed in premixed swirling flames, i.e. low-pass behavior with excess gain in the low frequencies. Detailed derivation and analysis can be found in PAPER-FTF [61].

2.5 Boundary Conditions

Boundary conditions are essential to provide closure for the problem as they describe the acoustic behavior at the limit of the considered system. They usually constitutes a special case of the acoustically compact elements. They can be expressed in terms of impedance, relating u' and p', or in terms of reflection coefficients, relating the CWA f and g. The second approach often proves to be more convenient for network models as it allows to better understand the causality. The boundary conditions, written in terms of reflection coefficients, are

$$\begin{cases} f_i = R_i g_i \\ g_o = R_o f_o \end{cases} \tag{2.26}$$

for an inlet and an outlet respectively. Equation (2.26) can directly be interpreted as the state-space representation of a boundary. The reflected wave is entirely driven by the incoming wave through the feedthrough matrix. In the absence of mean flow, the boundaries can be fully reflective (e.g. an open end $R = -1$, a closed end $R = 1$), exhibit some losses ($R \neq \pm 1$) or be more sophisticated with a frequency-dependent response. When accounting for mean flow, boundaries must be treated with care and specific coupling relations must be derived to avoid introducing non-physical spurious acoustic energy that would invalidate any stability analysis [62].

2.6 A Fundamental Example: The Rijke Tube

Because of its simplicity, the Rijke tube [63] is a fundamental example as it encompasses the essential feature of a thermoacoustic system, namely a coupling between the acoustics and the delayed response of an unsteady heat source.

The system, shown in Fig. 2.2, consists of tube that contains either an electric heater or flame. Upstream and downstream of the heat source, only plane waves propagate and their motion is described by Eq. (2.12). The change in temperature across the unsteady heat source leads

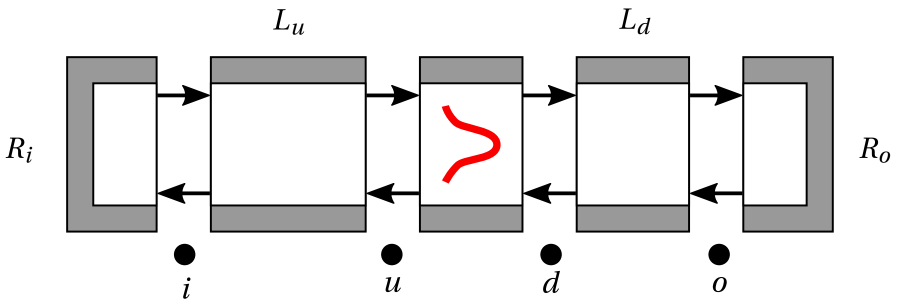

Figure 2.2: Schematic of a generic Rijke tube of length L_u upstream the flame, L_d downstream the flame. The acoustic boundaries are defined by the reflection coefficients R_i and R_o at the inlet and outlet respectively.

to different propagation velocities in the cold and hot regions. The jump conditions are given by the Rankine-Hugoniot equations Eq. (2.21) and the delayed response of the heat source to perturbations is described with a transfer function Eq. (2.22). The problem is closed with boundary conditions, such as Eq. (2.26), which describe the acoustic behavior at both ends of the tube.

Combined, the governing equations can be cast in the matrix form:

$$\begin{bmatrix} -1 & R_i & 0 & 0 & 0 & 0 & 0 & 0 \\ e^{-s\tau_u} & 0 & -1 & 0 & 0 & 0 & 0 & 0 \\ 0 & 1 & 0 & -e^{-s\tau_u} & 0 & 0 & 0 & 0 \\ 0 & 0 & -1-\Theta\mathcal{F}(s)-\xi & 1+\Theta\mathcal{F}(s)-\xi & 2 & 0 & 0 & 0 \\ 0 & 0 & 1+\Theta\mathcal{F}(s)-\xi & -1-\Theta\mathcal{F}(s)-\xi & 0 & 2 & 0 & 0 \\ 0 & 0 & 0 & 0 & e^{-s\tau_d} & 0 & -1 & 0 \\ 0 & 0 & 0 & 0 & 0 & -1 & 0 & e^{-s\tau_d} \\ 0 & 0 & 0 & 0 & 0 & 0 & -R_o & 1 \end{bmatrix} \begin{bmatrix} f_i \\ g_i \\ f_u \\ g_u \\ f_d \\ g_d \\ f_o \\ g_o \end{bmatrix} = \begin{bmatrix} 0 \\ 0 \\ 0 \\ 0 \\ 0 \\ 0 \\ 0 \\ 0 \end{bmatrix} \qquad (2.27)$$

Mathematically, this system of eight equations with eight unknowns admits non trivial solutions if the determinant of the matrix is null. Solving for the determinant leads to the dispersion relation:

$$\mathcal{D}(s) = (\xi + 1 + \Theta\mathcal{F}(s))\left(1 - R_i R_o e^{-2s(\tau_u+\tau_d)}\right) + (\xi - 1 - \Theta\mathcal{F}(s))\left(R_i e^{-2s\tau_u} - R_o e^{-2s\tau_d}\right) = 0 \qquad (2.28)$$

Equation (2.28) is non-linear in frequency s because of both the exponential terms due to acoustic propagation and the flame response $\mathcal{F}(s)$. It generally cannot be solved analytically, and solving numerically remains challenging. Instead, the state-space framework, presented along the previous sections, allows to transform Eq. (2.28) into a linear eigenvalue problem (LEVP), which facilitates the use of direct solvers. Such approach is adopted in the open-source MATLAB package *taX*[1], developed by TFD Group, to build and solve low-order thermoacoustic network models. Part of this doctoral project was dedicated to improving this toolbox. Among others, new features have been implemented and validated, the library has been enriched with new

---

[1] https://gitlab.lrz.de/tfd/tax

elements, the graphical user interface was reworked from scratch for a more user-friendly experience, etc. Furthermore, a significant effort has been devoted to documenting, disseminating and training users. A series of eight videos, totaling two hours of content, has been recorded and is available on TFD's YouTube channel. A broad range of topics is covered (e.g. installation, debugging and good practices, set-up of models, data analysis, parameter studies, development of new elements) in order to guide new users.

The solutions of the dispersion relation Eq. (2.28) are the eigenvalues. Associated with their corresponding eigenvectors, they constitutes the thermoacoustic modes of the system. The imaginary part of an eigenvalue is the frequency of oscillation of the mode, whereas the real part is its growth rate and reflects the fact that a mode can be stable (negative growth rate), marginally stable ($\sigma = 0$) or unstable (positive growth rate). For an aeronautical or land-based gas turbine to operate safely, it is critical to ensure the combustor stability. A profound understanding of the spectrum and of the eigenmodes nature is necessary. This is developed in the following chapters.

3 Categorization of Thermoacoustic Modes

This chapter gives an overview of two types of thermoacoustic instabilities that can be encountered. While both may lead to self-excited pressure oscillations, the underlying physics fundamentally differs. The two mechanisms are presented and a categorization criterion is given. The latter enables to understand the nature of an eigenmode, and, consequently, choose an appropriate risk mitigation strategy.

3.1 The Classical Understanding

Whether the interaction between combustion and the acoustics of a combustor gives rise to an instability depends in an essential manner on the relative phases, in particular on the phase between fluctuations of pressure and unsteady heat release at the flame. This has been known since Lord Rayleigh [19], who has proposed a criterion: "*For an instability to occur, heat must be added at the moment of greatest compression.*" Mathematically, the Rayleigh criterion may be formulated as follows:

$$\int_V \int_T p'(\boldsymbol{x},t)\dot{q}'(\boldsymbol{x},t)\,dt\,dV > 0 \tag{3.1}$$

If the pressure and heat release fluctuations are in phase, the integral over a period of oscillation is positive and the net energy of the acoustic field is increased [64, 65]. While true, this criterion is only a necessary but not sufficient condition, as it only considers the driving of the system. However, for an instability to develop, the driving component must overcome the losses and damping mechanisms, which exist in every combustor. Zinn and Lieuwen [66] summarized this statement as:

$$\underbrace{\int_V \int_T p'(\boldsymbol{x},t)\dot{q}'(\boldsymbol{x},t)\,dt\,dV}_{\text{Driving}} > \underbrace{\int_V \int_T \sum L_i(\boldsymbol{x},t)\,dt\,dV}_{\text{Damping}} \tag{3.2}$$

Many sources of damping are present in gas turbine engines, e.g. losses at the inlets and outlets of the combustor [67], losses due to bias flow liners [68, 69], perforated plates and Helmholtz resonators [70, 71], among others. If large enough, the combustor remains stable, regardless of the Rayleigh criterion.

The frequencies of thermoacoustic instabilities are often close to the natural eigenfrequencies of the combustor, i.e. the acoustic eigenfrequencies without unsteady heat release. Such observation can be explained with the following derivation. Similarly to Sec. 2.2, linearization and combination of the mass and momentum conservation equations with a volumetric heat source term yields the *inhomogeneous wave equation* [72]:

$$\frac{1}{c^2}\frac{\partial^2 p'}{\partial t^2} - \bar{\rho}\nabla\cdot\left(\frac{\nabla p'}{\bar{\rho}}\right) = \frac{\gamma-1}{c^2}\frac{\partial \dot{q}'}{\partial t} \tag{3.3}$$

A common strategy to solve Eq. (3.3) is through a Galerkin series expansion of the pressure and velocity fields [73–75]:

$$\begin{cases} p'(\boldsymbol{x},t) = \sum_{i=0}^{\infty} \dot{\eta}_i(t)\psi_i(\boldsymbol{x}) \\ u'(\boldsymbol{x},t) = -\sum_{i=0}^{\infty} \eta_i(t)\frac{\nabla\psi_i(\boldsymbol{x})}{\bar{\rho}} \end{cases} \tag{3.4}$$

where the functions $\eta_i(t)$ are unknown time-dependent coordinates and $\{\psi_i(\boldsymbol{x})\}_{i=0}^{\infty}$ is an arbitrarily-chosen set of admissible space functions that satisfies the spatial boundary conditions, commonly the eigenmodes of the homogeneous problem. Inserting Eq. (3.4) into Eq. (3.3) and making use of the orthogonality of the functions $\psi_i(\boldsymbol{x})$ leads to the second order stochastic nonlinear differential equation:

$$\ddot{\eta}_i(t) + \omega_i^2\eta_i(t) = Q[\eta_i,\dot{\eta}_i] - \alpha\dot{\eta}_i(t) + \varsigma\zeta(t) \tag{3.5}$$

which describes the temporal evolution of the considered eigenmode. In the absence of sources and sinks, the mode is marginally stable and the oscillations occur at the natural frequency ω_i. The presence of the flame introduces two forcing terms. The deterministic nonlinear operator $Q[\eta,\dot{\eta}]$ models the flame response to acoustic pressure and velocity perturbations [76, 77]. Combustion background noise, which results from non-coherent heat release fluctuations [78] (e.g. turbulence, indirect noise from entropy waves [79], etc.), can be approximated by a white Gaussian noise $\varsigma\zeta$. Acoustic sinks appear in the form of a damping term $-\alpha\dot{\eta}$. In summary, thermoacoustic modes can simply be interpreted as natural acoustic eigenmodes perturbed by the combustion [75], hence the similarity in the oscillation frequencies [40, 80]. The stability depends on an acoustic energy balance between the driving of the flame and the losses of the system.

3.2 The ITA Feedback Loop, a New Paradigm

Despite its solid theoretical foundation [72–75, 81] and the vast amount of experimental validations [82–86], the framework introduced in the previous section fails to explain numerous observations. For instance, Dowling and Stow [87] derived, in the frequency domain, a model based on the one-dimensional linearized Euler equations in order to assess the stability of lean premixed prevaporized gas turbine combustors. The authors reported a *“new set of modes associated with flame model”* but could not further elaborate. Similarly, the anomalous peaks in the acoustic flame response [88] and the so-called instability potentiality [89], which, unlike the Rayleigh criterion, is independent of the acoustic characteristics of the system, were, at that time, unexplained.

Eckstein et al. [90] experimentally investigated a spray combustor mounted with a swirl airblast atomizer, typical of aero-engines, and reported an instability at 120 Hz, far from any natural

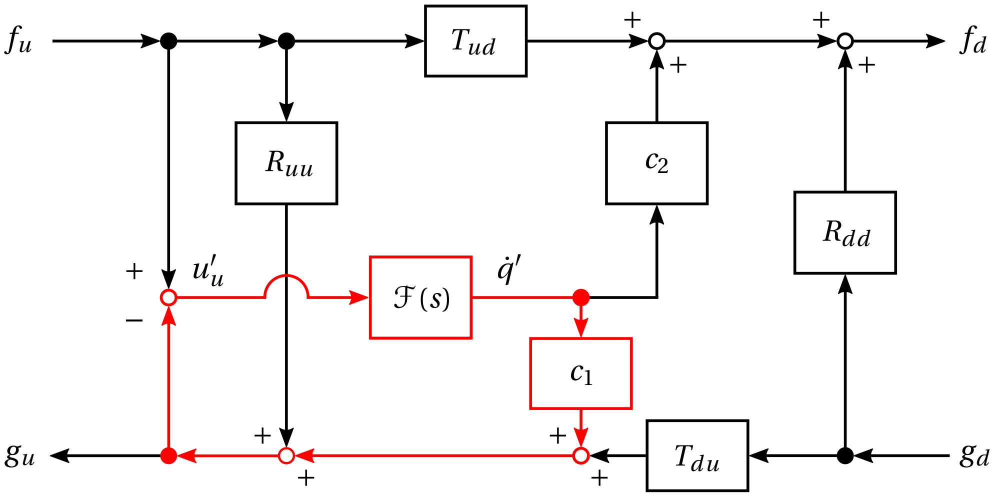

Figure 3.1: Schematic of the ITA feedback loop. At the flame, due to the temperature discontinuity, the incoming waves f_u and g_d are partially transmitted and reflected. The flame, which contributes to the overall acoustics as a monopole source of sound, is driven by the upstream velocity, thus closing a feedback loop (highlighted in red) intrinsic the flame and its immediate surroundings.

acoustic frequency of the system. The low frequency indicating a possible entropic mode, the downstream nozzle was removed to avoid any indirect noise perturbations. Surprisingly, not only had the instability not disappeared, but the amplitude of oscillation was larger. The instability was interpreted as a *"bulk mode"* [91]. Similarly, the model of Weyermann [92] could only retrieve the acoustic mode at 400 Hz but not the strong peak at 100 Hz observed in the corresponding experiment of a confined swirl-stabilized burner, without extensively tuning the time-delay between the reference location and the flame. Tay-Wo-Chong et al. [56] identified the flame transfer function of a resembling configuration using a Large Eddy Simulation and performed linear stability analysis with a network approach. Of the three identified eigenmodes, only two could be associated to the acoustics of the system, namely the Helmholtz mode of the plenum and the quarter-wave mode of the chamber, the remaining one being *"produced by flame dynamics"*, without further elaboration.

The established understanding of thermoacoustics was significantly challenged with the analytical and experimental work of Hoeijmakers et al. [93, 94], where instabilities of a laminar Bunsen-type flame placed in an anechoic environment were observed. This situation is paradoxical: acoustic waves can only leave the system without being reflected, the feedback loop being cut, no acoustic resonance can be triggered, and yet, an instability manifests itself. Bomberg et al. [48] formally identified the so-called *intrinsic thermoacoustic (ITA) feedback loop*, which does not involve any reflection of acoustic waves at the boundaries, as depicted in Fig. 3.1. The ITA feedback mechanism may be briefly summarized as follows: the flame responds to upstream velocity perturbations with fluctuations of heat release. The latter act as a monopole source of sound [95], and, consequently, generate acoustic waves traveling in both upstream and downstream direction. In turn, the waves traveling in the upstream direction perturb the acoustic velocity at the reference position, before even reaching the boundaries of the system, thus closing the feedback loop. In a sense, this flow-flame-acoustic interaction is *intrinsic* to the

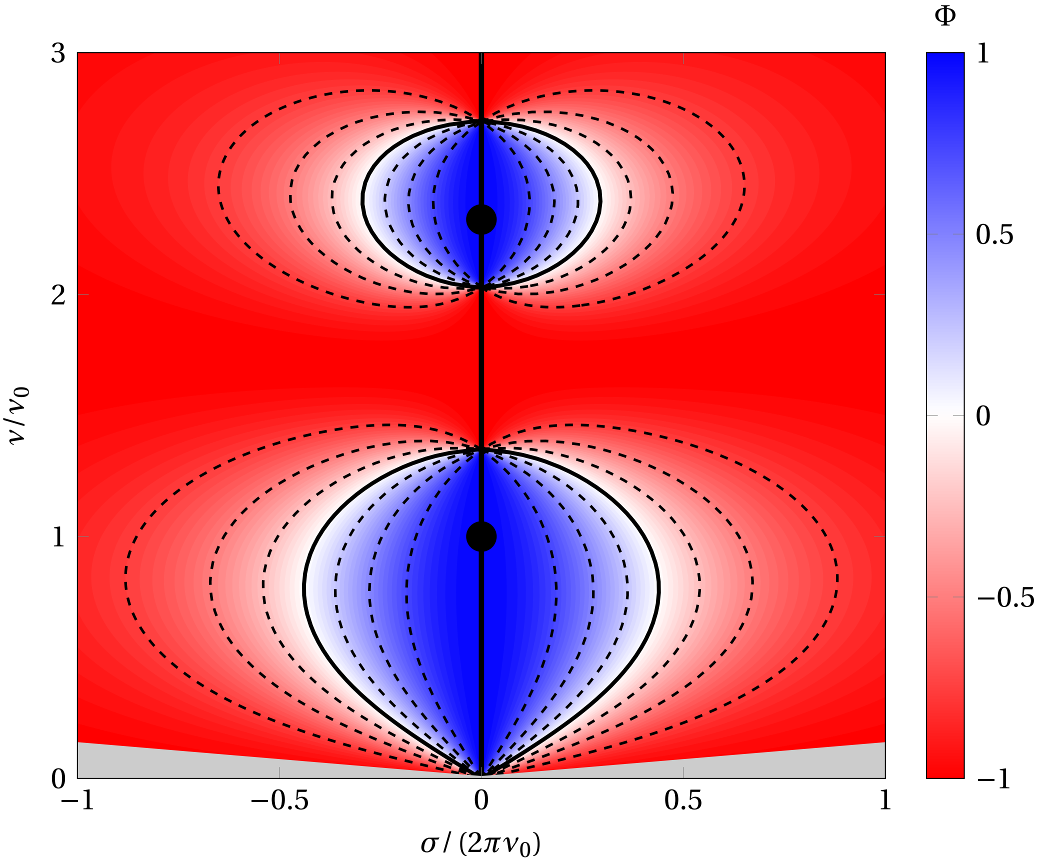

Figure 3.2: Contour map of the Φ criterion around the first two passive acoustic modes of an exemplary axial combustor. Close the passive acoustic modes, the thermoacoustic modes are rather classified as of acoustic nature. Conversely, away from the passive solutions, i.e. in the extremely damped and extremely unstable regions, thermoacoustic modes should be regarded as ITA.

flame and its immediate surroundings, hence the name.

The ITA feedback loop shed a new light on the hitherto unexplained phenomena described previously and provided a physical explanation [35] to the observations of Hoeijmakers [96], which were later confirmed by several high-fidelity compressible CFD simulations [97, 98]. Emmert et al. [36] demonstrated that the ITA feedback gives rise to a new set of eigenmodes also for reflecting boundaries, and identified such an “ITA mode” as the dominant unstable eigenmode in a premixed swirl-stabilized combustion test-rig. This new paradigm completely changed the understanding of thermoacoustic instabilities and, in the last decade, led to numerous studies, recently summarized by Silva [99].

3.3 A Categorization Criterion

Beyond curiosity and interest for the scientific community, the understanding of both mechanisms, and, consequently, of the nature of an eigenmode, is of great practical engineering relevance. For instance, Emmert et al. [36] highlighted that increasing the losses at the boundaries can further destabilize such an ITA mode. This counter-intuitive result demonstrates that the classical methods used to stabilize a combustor (e.g. increasing losses, using Helmholtz dampers, acoustic liners [100], etc.) may not necessarily produce the expected outcome.

Assuming harmonic time dependence, any variable of interest may be conveniently represented in terms of a *phasor*, i.e. a complex-valued vector. This concept allows for graphical representation in terms of an *Argand diagram*, where a phasor is simply an arrow in the complex plane whose length and orientation reflect the amplitude and phase of oscillation respectively. Depending on their nature, eigenmodes exhibit very different phasor diagrams. For instance, for a pure ITA mode (i.e. an ITA mode in a fully anechoic environment), the velocity phasors u'_u and u'_d, immediately upstream and downstream the flame respectively, are almost perfectly out of phase. Surprisingly, in a combustor with fully reflective boundaries, thermoacoustic modes that are highly damped or highly unstable share similar features: the velocity phasors at the flame exhibit a phase difference of π, and the heat release and pressure phasors are either almost perfectly aligned (maximum acoustic energy generation) or anti-aligned (maximum acoustic energy annihilation) for a unstable and stable mode respectively. As a result, such modes should be regarded as of *ITA type*. On the other hand, thermoacoustic modes that exhibit pressure and heat release phasors in quadrature and velocity phasors in phase are very similar to the passive acoustic eigenmodes of the system and, as such, should be classified as *acoustic*.

Except for the limit cases described above, in general, the velocity phasors of a given thermoacoustic mode are only partially (anti-)aligned. Consequently, a categorization criterion Φ, based on the normalized scalar product of the velocity phasors, is proposed:

$$\Phi = \frac{u'_u}{|u'_u|} \cdot \frac{u'_d}{|u'_d|} \tag{3.6}$$

By construction, Φ is bounded, $\Phi \in [-1, 1]$. An eigenmode can be considered more of acoustic type $\Phi > 0$ or of ITA type $\Phi < 0$. Not only does this simple criterion allow to determine the nature of any thermoacoustic mode, but it also enables to identify regions in the complex planes were acoustic and ITA modes can exist, as depicted by Fig. 3.2. The latter is not universal, as the size and position of the contours change with the flame location, but general trends can be infered. Modes of acoustic nature can only exist "relatively" close to the stability margin and the passive solution. On the other hand, modes highly damped or unstable are of ITA type. Depending on the flame location in the system of interest, ITA modes can also be found close to the neutral line. Further examples and discussions are given in PAPER-CATEGORIZATION [101].

Physically, the proposed criterion relates to the motion of the medium. In absence of a flame, the medium between two velocity nodes in a standing wave oscillates back and forth, i.e. *swings*. Conversely, for a pure ITA mode in an anechoic environment, the velocity phasors are anti-aligned, which describes an inwards-outwards oscillation, *breathing*. Consequently, for a given eigenmode, the oscillations of the medium in the vicinity of the flame is a superposition of a swinging and breathing motion. For a mode categorized acoustic, the swinging motion dominates, and vice versa for an ITA mode.

4 Acoustic Modeling of Annular and Can-Annular Combustors

Complex three-dimensional geometries, such as annular and can-annular combustors, can be modeled with low-order networks using one-dimensional elements. With Bloch theory, this 1,5D formulation can be simplified into an equivalent longitudinal burner with a complex-valued boundary condition that preserves the azimuthal dynamics of the complete system. Although the two combustor architectures share similarities, they require distinct modeling.

4.1 Bloch Theory for Discrete Rotational Symmetries

Typical modern combustors feature a discrete rotational symmetry. They consist of an ensemble of N identical sectors (denoted *unit-cell*) placed equidistantly in an annular arrangement. For an annular combustor, the unit-cell is composed typically of one burner and the respective sectors of the upstream plenum and combustion chamber. For a can-annular combustor, the unit-cell comprises one can and the respective sector of the plenum and annular gap in front of the high-pressure turbine inlet.

In general, the eigenvalues of problems with discrete spatial symmetries can be represented in the form of Bloch waves. This mathematical representation arises from quantum mechanics, following the work of Floquet [102] and Bloch [103], who investigated the resolution of the Schrödinger equation for crystal lattice exhibiting translational symmetry. The thermoacoustic eigenvalue problem shares similarities and the framework can easily be transposed [104], the only difference lies in the rotational symmetry, which will change the set of admissible Bloch wave numbers (denoted m in the following). Thus, the pressure eigenmode in the frequency domain may be written as

$$\hat{p}_m(\boldsymbol{x}) = \Psi_m(\boldsymbol{x})\, e^{im\theta}, \quad m = \begin{cases} -\dfrac{N}{2}+1, \ldots, -1, 0, 1, \ldots, \dfrac{N}{2} & \text{for } N \text{ even} \\ -\dfrac{N-1}{2}, \ldots, -1, 0, 1, \ldots, \dfrac{N-1}{2} & \text{for } N \text{ odd} \end{cases} \tag{4.1}$$

where $\boldsymbol{x} = (r, \theta, x)$ is the position vector in cylindrical coordinates. Ψ_m is a function that is identical in all unit-cell and periodic in θ with a period $2\pi/N$. It is not limited to a specific functional form but can be any function that satisfies the decomposition. m is the Bloch wave number and its absolute value $|m|$ represents the azimuthal order of the considered eigenmode.

Depending on the value m takes, the modes can be classified into three groups. For $m = 0$, the pressure is identical in every unit-cell, with no phase difference in the azimuthal direction θ and the eigenmodes are regarded as *axial*, sometimes also referred as *push-push*. When $m = N/2$,

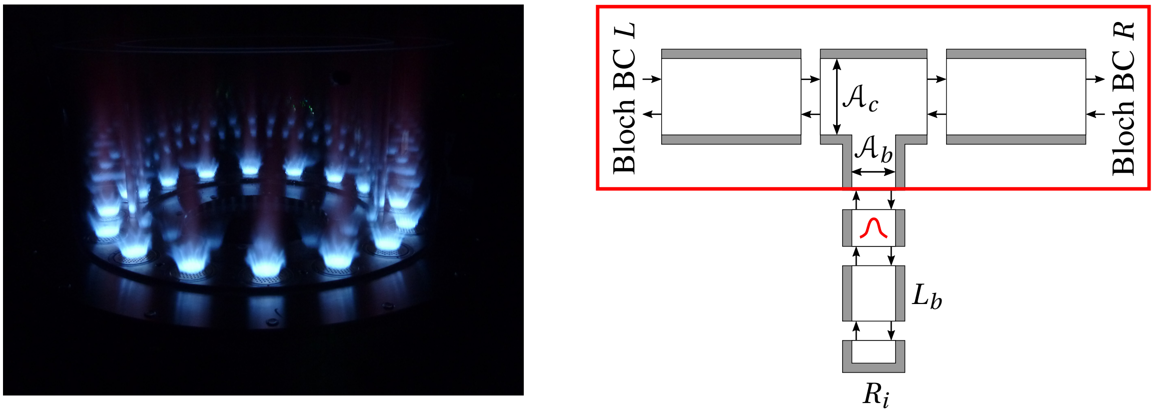

(a) **(b)**

Figure 4.1: (a) Annular Combustion Chamber MICCA, Laboratoire EM2C, CNRS/CentraleSupélec, Université Paris-Saclay. Courtesy of Dr. Daniel Durox. The MICCA combustor is a typical lab-scale annular chamber with a discrete rotational symmetry $N = 16$. (b) Exemplary network model of one unit-cell of a generic annular chamber.

the pressure field exhibit a pattern adjacent unit-cells with alternating sign, hence the name *push-pull* mode. For all other values of m, the modes are azimuthal. Additionally, if the unit-cell exhibit reflectionnal symmetry along a plane at constant θ, i.e. absence of mean flow in the azimuthal direction, the latter share the same frequency and differ only by their spinning direction, thus forming a degenerate pair of eigenmodes.

Because of Bloch-periodicity, a solution obtained on the unit-cell can be extrapolated to the entire domain to obtain the eigenmode of the full configuration. By imposing pseudo-periodic Bloch boundaries, and considering all positive Bloch-wave numbers m, the study of a single unit-cell becomes sufficient as the dynamics of the full system is preserved. This framework allows not only to drastically reduce the computational effort, but also to simplify the modeling approach in an elegant and efficient manner, as discussed in the following sections.

4.2 Annular Combustion Chambers

Figure 4.1 shows a network model of a generic annular combustor. As highlighted in the previous section, it is sufficient to consider a single unit-cell, in this case a burner tube and the corresponding sector of the annular chamber. For the sake of brevity, the plenum is considered decoupled [105, 106], but the model can be extended in a straight-forward manner to account for the upstream acoustics.

The network comprises of an ensemble of elementary elements, as described in Chapter 2. The chamber is modeled as a thin annulus using ducts. The latter are interconnected with the burner tube with a T-junction element. Assuming acoustically compact elements, the flame is placed at the outlet of the burner, just upstream the area change induced by the junction.

At the T-junction, momentum conservation leads to acoustic pressure continuity, while mass conservation equation implies the conservation of volumetric flow rate:

$$\sum_i \mathcal{A}_i u_i' = 0 \tag{4.2}$$

In the ducts, plane waves propagate, as described by Eq. 2.12. Finally, both sides of the unit-cell are mutually connected with pseudo-periodic Bloch boundaries, which can be written in terms of CWA as:

$$\begin{bmatrix} f_R \\ g_R \end{bmatrix} = \begin{bmatrix} e^{i\frac{2\pi m}{N}} & 0 \\ 0 & e^{i\frac{2\pi m}{N}} \end{bmatrix} \begin{bmatrix} f_L \\ g_L \end{bmatrix} \tag{4.3}$$

Combining these equations allows to lump all the effects of the annular chamber and the T-junction (identified by the red rectangle in Fig. 4.1) into an equivalent reflection coefficient "seen" by the burner tube. Thus, the initial unit-cell system is transformed into a completely equivalent longitudinal system where the outlet reflection coefficient $\mathcal{R}_m$ embeds the dynamics of the chamber and writes:

$$\mathcal{R}_m = 1 - \frac{4\cos(\mathrm{He}) - 4\cos\left(\dfrac{2\pi m}{N}\right)}{2\cos(\mathrm{He}) - 2\cos\left(\dfrac{2\pi m}{N}\right) + i\dfrac{\mathcal{A}_b}{\mathcal{A}_c}\sin(\mathrm{He})} \tag{4.4}$$

with the Helmholtz number He defined with the length L of the angular sector between two burners $\mathrm{He} = kL$. The detailed derivation is found in PAPER-ITA [107].

This equivalent reflection coefficient $\mathcal{R}_m$ is complex-valued, with an explicit dependence on frequency He, on the azimuthal order m and on the area ratio between the burner tube and the section of the chamber in the azimuthal direction. Figure 4.2 shows the evolution of the phase of $\mathcal{R}_m$ as a function of frequency for an exemplary generic annular chamber with ten burners. In the zero frequency limit, the chamber behaves as an open end for all eigenmodes except the axial mode, for which the chamber acts as hard wall. This observation is explained mathematically by the fact that the Galerkin series of an axial mode exhibits a Helmholtz mode at frequency $\mathrm{He} = 0$. The phase of the other modes is close to either π or $-\pi$, but changes abruptly from one value to the other with a periodic pattern, crossing the abscissa exactly at the frequencies of the passive acoustic modes of the annulus. This further illustrates that the dynamics of the full chamber is indeed well captured by the equivalent reflection coefficient $\mathcal{R}_m$.

4.3 Acoustic Coupling Between Cans

At first glance, a can-annular combustor could be interpreted as a special case of an annular combustor, where a can is simply a burner tube of large dimension and the gap in front of the turbine a thin annulus. However, Helmholtz simulations [38, 108] show that the plane wave assumption is not valid in the gap where strong 2D effects are present. Consequently, the model derived in the previous section does not apply and specific acoustic modeling of can-annular combustors is required.

While the conservation of mass described by Eq. 4.2 holds, the width of the can, and the resulting 2D effects, invalidate the assumption of acoustic pressure continuity in the T-junction.

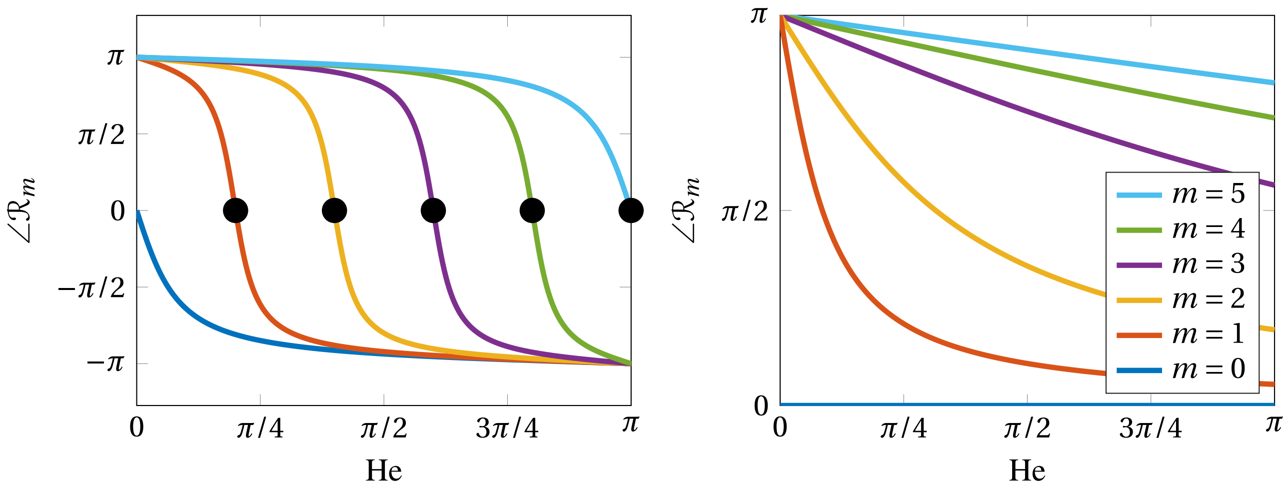

(a) **(b)**

Figure 4.2: (a) Evolution of the phase of the equivalent reflection coefficient $\mathcal{R}_m$ as a function of frequency for an annular configuration. Colors indicate the azimuthal order and circles the passive acoustic modes of the chamber. (b) Same results for the can-annular architecture.

Instead, each half of the can is treated as an acoustically compact converging nozzle. Similarly to Sec. 2.3, using unsteady Bernoulli equation, the pressure gradient is related to the acoustic velocity through a characteristic length $L_{char,\,m}$. The latter accounts for the inertia of the volume of fluid, which cannot be neglected in this configuration. Once again, the problem is closed using Bloch boundaries and relating both sides of the cross-talk area with Eq. 4.3. Combining the equations, the cross-talk area downstream of the can is replaced by an effective reflection coefficient $\mathcal{R}_m$ that writes:

$$\mathcal{R}_m = 1 - \frac{4\sin^2\left(\frac{\pi m}{N}\right)}{i\mathrm{He}\dfrac{L^*_{char,\,m}}{L^* L^*_g} + 2\sin^2\left(\dfrac{\pi m}{N}\right)} \tag{4.5}$$

where the Helmholtz number $\mathrm{He} = kL$ is defined with the length of the can L, $L^* = L/H$ is the ratio between the length and the width of the can, i.e. the aspect ratio, $L^*_g = L_g/H$ the ratio between the size of the gap and the width of the can, which can be seen as the coupling strength between neighboring cans. $L^*_{char,\,m} = L_{char,\,m}/H$ is the normalized characteristic length. The latter is an integral of the cross-section of the acoustic flow along the stream-path (and not of the geometric cross-section), thus the explicit dependence on the azimuthal mode order m.

Figure 4.2 show the phase response of the equivalent reflection coefficient $\mathcal{R}_m$ as a function of frequency, for all azimuthal orders m of a generic can-annular combustor of discrete rotational symmetrey $N = 10$. Besides the trivial behavior of the axial mode, for which the acoustic coupling has no effect, all azimuthal modes have the same low-frequency limit, an open end. The phase diminished with increasing frequencies and converges towards a limit $\angle\mathcal{R}_m = 0$. The slope is governed by the coupling strength L^*_g, whose effect is the same way for all the azimuthal orders, but also by the characteristic length $L^*_{char,\,m}$, which impact the eigenmodes differently, thus explaining why low azimuthal orders go faster towards zero. A more detailed derivation and discussion is found in PAPER-CAN [108].

In summary, both annular and can-annular configurations can be modeled with a network approach. The complexity of the full network can be reduced by utilizing Bloch boundaries, which enables to limit the study to a single unit-cell. Finally, the coupling effects (with the chamber and with the neighboring cans respectively) can be lumped into a reflection coefficient $\mathcal{R}_m$, effectively transforming the problem into a simpler yet completely equivalent longitudinal configuration.

5 Clusters of Thermoacoustic Modes

This chapter builds upon the acoustic models introduced in the previous chapter to provide insight on the origin of clusters of ITA and acoustic modes encountered in (can-)annular configurations. The ITA clusters are mainly driven by pure flame dynamics, whereas cavity clusters are primarily related to the geometry of the system. Both co-exist in can-annular combustors and the spectrum structure is influenced by the presence of exceptional points.

5.1 Origin of Clusters of ITA and Acoustic Modes

The term *cluster* refers to a large number of closely spaced eigenmodes. This phenomenom is a typical "signature" of ring-like weakly coupled oscillators [109]. In can-annular combustors, combustion and flame dynamics are not necessary for clusters to appear. The latter can be found in the simplest configuration, an ensemble of identical cans (the components) weakly coupled with a cross-talk area, as depicted in Fig. 5.1. Close to resonance, the dynamics of one component system can be modeled as an oscillator, as shown in Eq. 3.5. In the absence of source and loss terms, the resonance frequency is simply the natural frequency of the can. Clusters emerge from the eigenvalues of the uncoupled component systems (i.e. the isolated cans) when coupling is introduced as a perturbation. Invoking Bloch-wave mode structure due to symmetry, clusters containing exactly N eigenvalues[1] are present around the natural frequencies (fundamental mode and harmonics) of the cans.

The acoustic modeling approach developed in the previous chapter provides additional insight to this qualitative description of the origin of clusters. As shown in Fig. 4.2, for low frequencies, the phase of the reflection coefficient $\mathcal{R}_m$ scales linearly with respect to frequency, which indicates a constant time delay[2]. Consequently, $\mathcal{R}_m$ can be replaced by a duct of effective length $\mathcal{L}_m$ terminated by an open end $R_o = -1$. The length $\mathcal{L}_m$ can be derived analytically and writes:

$$\mathcal{L}_m = \frac{L_{char,\,m}}{2L_g^* \sin^2\left(\dfrac{\pi m}{N}\right)} \tag{5.1}$$

It exhibits an explicit dependence on the azimuthal order m (both through the $L_{char,\,m}$ and sine-squared terms) and the coupling strength L_g^*. The resulting low-order model is simply a longitudinal configuration of a resonating duct of total length $L + \mathcal{L}_m$, as depicted in Fig. 5.1. The higher the azimuthal order m, the shorter the equivalent duct $\mathcal{L}_m$, because both the terms $L_{char,\,m}$ and $1/\sin^2\left(\frac{\pi m}{N}\right)$ decrease with increasing values of m. As an example, Fig. 5.2 shows the first cluster of an ensemble of ten weakly coupled cans. The axial eigenmode remains unaffected by the coupling condition and correspond to the half-wave mode $\mathrm{He} = 0 + j\pi,\ j \in \mathbb{N}$, i.e.

---

[1] counting multiplicity

[2] for all azimuthal order except the axial mode $m = 0$

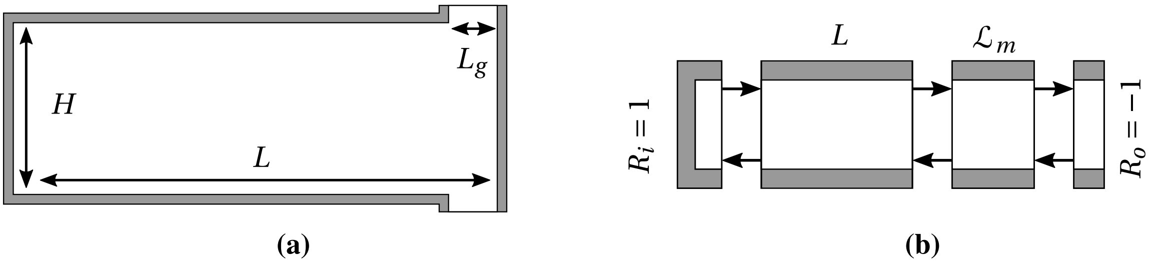

Figure 5.1: (a) Unit-cell of an ensemble of closed cans, acoustically coupled exclusively through the small gaps of size L_g. (b) Low-order model of the system. The effects of the coupling are lumped into the equivalent length $\mathcal{L}_m$.

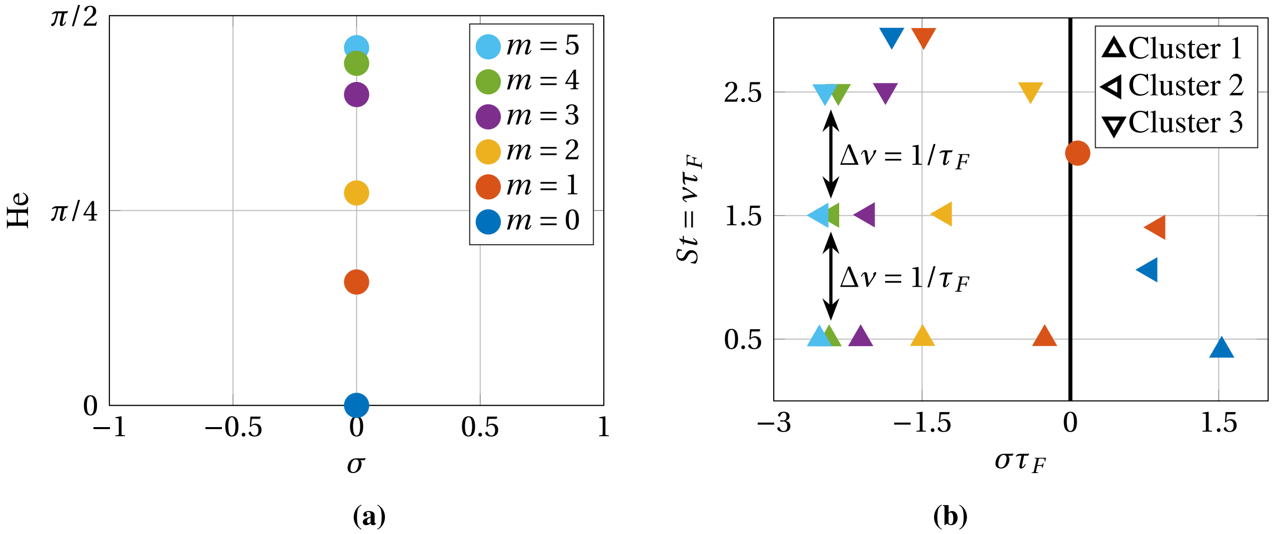

Figure 5.2: (a) Spectrum of a system of ten passive cans acoustically coupled through a small gap. The marginally stable eigenmodes form a cluster near the quarter-wave solution. Modes of higher azimuthal order m are closest within the cluster. (b) Spectrum of an annular combustor. Besides the first azimuthal acoustic mode, the system exhibit several clusters of ITA modes which align around the pure ITA frequencies. Modes with higher azimuthal order are more damped. Clusters are equidistant with a frequency spacing $\Delta\nu = 1/\tau_F$.

the eigenfrequency of the uncoupled component system. For all other azimuthal orders, the effective length $\mathcal{L}_m$ terminated by an open end makes the eigenmodes deviate from the uncoupled subsystem's solution. The low azimuthal modes exhibit the lowest frequencies. For increasing azimuthal order m, the equivalent duct becomes shorter, resulting in higher eigenfrequencies. In the limit case where $\mathcal{L}_m$ becomes almost negligible, the modes of the cluster converge towards the same solution, the quarter-wave mode $\mathrm{He} = \pi/2$ in this example. This is physically explained by the fact that the phase shift induced by the gap becomes negligible compared to the overall phase shift due to the propagation in the can itself, hence the outlet boundary condition becomes independent of the azimuthal order and all the eigenmodes converge to the same degenerate solution. Similarly, because $\mathcal{L}_m$ is non-linear in m and decreases faster for higher values of m, eigenmodes with higher azimuthal order are also closest within a cluster. This simple modeling approach not only explains the origin of acoustic cluster, but also sheds a new light by explaining the structure of the spectrum.

By many aspects, ITA clusters in annular combustors share similarities with the previous example. However, as ITA modes are mainly driven by flame dynamics, ITA clusters cannot exist in a passive system. As highlighted in Fig. 4.2, the phase of the reflection coefficient $\mathcal{R}_m$ modeling an annular chamber also scales linearly with frequency. In a comparable approach, $\mathcal{R}_m$ can, in turn, be modeled as a duct of length $\mathcal{L}_m$ terminated by an open end, effectively transforming the unit-cell of an annular system into a simple Rijke tube, such as depicted in Fig. 2.2. This simple Rijke tube modeling approach allows to transpose results from longitudinal burners to annular geometries. Figure 5.2 gives an example of a spectrum of a typical lab-scale annular combustor with ten injectors. For simplicity but without loss of generality, the flame response is described with a simple $n-\tau_F$ model. While the clusters of can-annular combustors spread across a wide frequency range, the ITA modes in annular geometries show instead extremely similar frequencies and differ mainly by their growth/damping rate. The eigenmodes align along the *pure ITA frequency*, which is the frequency an eigenmode would exhibit if the flame was placed in an anechoic environment. This peculiar behavior is explained by previous research on Rijke configurations. Numerous studies [110–113] showed that, even in the context of fully reflecting boundaries, for a given flame response, if the passive acoustic mode is sufficiently far away and does not *interplay* [114], the thermoacoustic ITA mode remains close to its pure ITA frequency. In the complex plane, the ITA trajectory when varying the flame strength is a straight line, i.e. the growth rate is changing but the frequency remains approximately constant. Since an annular combustor is nothing but a collection of small Rijke tubes, for all azimuthal order m, ITA modes remain centered along the pure ITA frequency, thus explaining the observed clusters. This result is, however, only valid for low frequencies. For higher frequencies, the Rijke tube hypothesis is invalidated, the interplay with the modes of acoustic origin becomes non negligible, both effects leading to a change in the ITA frequency. The higher the azimuthal order, the longer the Rijke tube approach holds, which explains why ITA modes of low azimuthal order m are first to drift away from their respective clusters of harmonics, as exemplified in Fig 5.2. Similarly, the constant frequency spacing $\Delta\nu = 1/\tau_F$ between clusters is explained by the analytical expression derived by Emmert et al. [35] for longitudinal burners. Finally, ITA modes of higher azimuthal order are in general more damped, which can be explained with phasors analysis. A more detailed discussion can be found in PAPER-ITA [107].

In conclusion, in spite of its simplicity, a low-order analytical approach captures the essential physics and, thus, proves to be sufficient to explain both the origin of clusters and the structure of the spectrum in annular and can-annular configurations.

5.2 Interplay of Clusters and Exceptional Points

While annular configurations can only contain ITA clusters, can-annular combustors, on the other hand, exhibit clusters of both ITA and acoustic nature. Furthermore, the substantial dimensions of such gas turbines leads to low frequency acoustic modes, whose time scales are of the same order of magnitude as combustion dynamics, i.e. ITA and acoustic modes are located within the same frequency range. This remarkable feature results in specific behaviors.

Figure 5.3 shows the spectra of two identical can-annular configurations that differ only by

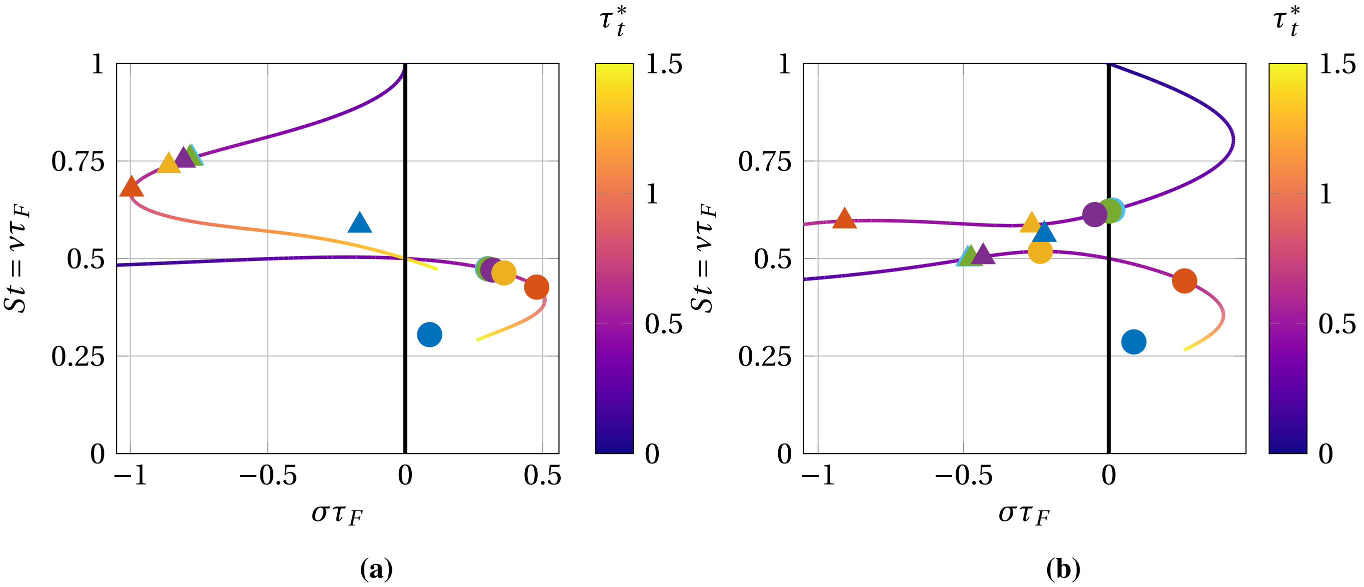

(a) **(b)**

Figure 5.3: Spectrum of a generic can-annular combustor. The configurations (a) and (b) differ only by the flame location inside the combustor. Eigenmodes follow specific trajectories imposed by the upstream condition. In the first configuration, the ITA and acoustic clusters are well separated. In the second case, the clusters are entangled and the trajectories are impacted by the presence of an exceptional point. Thermoacoustic modes can switch nature.

the flame location inside the cans. Using the low-order model approach described in the previous sections, the full system is approximated by a Rijke tube with an effective downstream length $\mathcal{L}_m$ changing with the azimuthal order. For a Rijke tube, when varying the length downstream of the flame, the eigenmodes follow specific trajectories in the complex plane that are imposed by the upstream parameters. Consequently, for a given can-annular combustor, because the upstream conditions and the flame response remain constant for all azimuthal orders[3], the eigenmodes necessarily lie on these trajectories. Their exact position is governed by the downstream parameters, namely the can length and the cross-talk region, the latter directly affecting the effective length $\mathcal{L}_m$. In the first example, the acoustic and ITA modes do not interplay, i.e. the acoustic and ITA clusters are well separated and easily identifiable. On the other hand, for a slightly different flame location, the spectrum widely changes and the clusters are entangled. Furthermore, the trajectories show a strong veering, indicating the presence of an exceptional point in the vicinity of the parameter space. Exceptional points (XPs), which are found in various disciplines, appear when at least two eigenvalues and their respective eigenfunctions coalesce. At these branch-point singularities, the eigenvalue sensitivity with respect to changes in parameters becomes infinite. In thermoacoustics, XPs are primarily attributed to the interplay between modes of ITA and acoustic nature [111, 115]. Mode veering is a manifestation of avoided crossing of eigenvalues [111, 112, 114, 116], resulting in the characteristic trajectories observed in Fig. 5.3. Additionally, a trajectory cannot be attributed to a specific type of thermoacoustic mode or dominant feedback loop, because eigenmodes switch nature when traveling along it.

This understanding of the structure of the spectrum and of eigenvalue sensitivity to parameter

---

[3] except the special case of the axial mode $m = 0$ which behaves differently

change is of practical interest when designing stable combustors. The design of injectors is usually achieved at an early program stage and focused on meeting performance criteria such as fuel consumption and pollutant emissions. As a result, the flame response becomes a known but fixed input for thermoacoustic stability analysis. However, other design parameters can be used as degree of freedom to shape the spectrum in order to guarantee stability. The upstream conditions, such as the flame position, impose the trajectories in the complex plane on which the eigenvalues necessarily lie, while the downstream parameters govern the exact location of the eigenmodes on these trajectories. However, it is highlighted that the downstream parameters affect the eigenvalues in different ways. For instance, a change in can length results in a change in acoustic characteristic time identical for all azimuthal orders, i.e. the entire cluster is equally translated along the trajectory. Conversely, the geometry of the cross-talk area induces a different response for each mode due to the explicit dependence of $\mathcal{L}_m$ to the azimuthal order m. A more detailed discussion is presented in PAPER-INTERPLAY [117].

6 Contextualization and Discussion of Publications

This chapter puts the papers that comprise this thesis into perspective with the existing literature.

6.1 The Challenges Associated to ITA Modes

6.1.1 Towards a Complete Spectrum

The presence of ITA modes in the spectrum has several implications. The first consequence is the need of appropriate methods to ensure finding all the eigenmodes in a frequency range of interest. Indeed, if finding classical *acoustic* modes is already difficult, the task proves to be even more arduous for ITA modes [118, 119], which partly explains why the latter were overlooked for a long time and discovered only in the last decade.

As shown in Chapter 2, even the simplest thermoacoustic system requires to solve for a non-linear eigenvalue problem (NLEVP). The non-linearity in the eigenvalue s comes from the delayed response of the flame but also appears when the boundaries of the system (combustor liner, turbine stage, etc.) exhibit frequency-dependent impedances. The NLEVP does not specifically arise with a network modeling approach, but is also encountered when solving for the Helmholtz equation [28], LEE (Linearized Euler Equations) [27], LNSE (Linearized Navier-Stokes Equations) [25, 26] or LRF (Linearized Reactive Flow) equations [24]. NLEVP are extremely difficult to solve [120–122] and three main strategies have been used in the thermoacoustic community.

Iterative methods have first been introduced by Nicoud et al. [28] with a fixed-point algorithm. The flame operator, quadratic in frequency s except for the contribution of the flame, is seen as a perturbation of the homogeneous acoustic problem, which motivates the use of the passive acoustic solutions as starting point for this iterative strategy. However, Nicoud's algorithm suffers from several shortcomings. When the user-defined initial guess is too distant[1] from the targeted mode, the algorithm may either never converge or find another eigenvalue. Because of the lack of general methodology to determine the most appropriate starting points, because of the a priori unknown number of eigenvalues, and because ITA modes are associated with extremely small basin of attraction [118], the latter are usually not found with Nicoud's approach and the spectrum obtained is incomplete. Mensah et al. [119] investigated Picard iteration [123], another kind of fixed-point method, and demonstrated that ITA modes can be repellors, which

---

[1] not necessarily in terms of frequency but, rather, whether the initial guess lies within the basin of attraction of the mode or not

implies that some eigenmodes can never be identified by fixed-point methods, regardless of the initial guess. Conversely, Newton-like methods are always guaranteed to converge to all eigenvalues. Among iterative algorithms, the adjoint-based Householder's method [124] should be preferred because of the reasonable computational cost and the increased size of basins of attraction of ITA modes [119].

The *contour integration method*, which relies on Beyn's algorithm [125], constitutes an alternative approach to solve the NLEVP. The method has proven to be capable of finding ITA modes in the spectrum [118], even when they come in significant number in a small region, e.g. the ITA clusters of the MICCA combustor [37]. While it removes the convergence issues of the iterative approach, the contour integration method comes with other drawbacks [126]. In particular, several additional user-defined parameters are required (i.e. a contour has to be prescribed, a number of sampling points has to be specified and a singular value decomposition tolerance needs to be defined) and are shown to affect the solution. Furthermore, the completeness of the spectrum and the precision of the eigenvalues are affected by the presence of other eigenvalues outside, but in the vicinity of the contour.

The last strategy is to transform the NLEVP into a *linear eigenvalue problem* (LEVP), significantly easier to solve, and for which efficient and robust methods are available [127, 128]. Merk et al. [126] demonstrated that the NLEVP can first be approximated by a REVP (Rational Eigenvalue Problem), still non-linear in s, but with the favorable property that it can be recast into a LEVP of higher dimension. While this last step is unnecessary for the LEE, LNSE and LRF, the reformulation can become expensive for the Helmholtz problem as it results in a doubling of the degrees of freedom (DoF). Thermoacoustic state-space models, such as *taX* [42, 129] introduced in Chapter 2, are commonly employed [26, 130, 131] and rely on this LEVP approach. Regardless of the problem and the modeling strategy, the flame response must be approximated by a linear model. While the flame dynamics obtained from experiments or LES is discrete[2], a time-continuous model is advantageous, allowing, for example, for efficient implementation of time-domain impedance boundary conditions when coupled with a variable time-step CFD simulation [132, 133]. To obtain such continuous flame models, common strategies are (i) Tustin or Padé approximation of the exponential terms [130, 131] or (ii) rational function fitting [24, 26, 126, 134]. The Tustin transform, which is the first-order Padé approximation, is based on the Taylor series expansion of the exponential term. Hence accuracy can only be expected for low frequencies, given that the sampling time of the discrete model is small. Higher-order Padé approximation, employed in [130, 131], improves the accuracy, but the resulting transfer function tends to become unstable with increased Padé orders [42], which effectively limits the application to low frequencies [135]. The second strategy is rational fitting of the discrete FFR, commonly achieved with the *Vector Fitting* algorithm [136]. The obtained reduced model generally provides satisfying results over the frequency range of interest with a limited number of DoF, as well as a limited number of spurious modes [126]. However, the algorithm requires a user-defined maximum allowable number of poles (i.e. the order of the function transfer), which influences the outcome of the fitting procedure: with too few poles, the key features of the FFR are not captured, while too many leads to overfitting, typically resulting in high peaks [134]. An a posteriori verification is thus necessary. PAPER-FTF [61] provides a third alternative, where the UIR is treated as a collection of individual time delays

---

[2] the FFR from experiments or monofrequency excited LES occur only at a few discrecte forcing frequencies, the UIR from system identification consist of a truncated series of discrete impulses.

that are approximated by discretizing an advection propagation equation in pseudo-space. As such, it is a generalization of the method of Emmert [42] for a single $n-\tau$ model. The number of DoF of the reduced model tends to be larger by one order of magnitude than the rational fitting approach, but remains reasonable for modern computing. The strength of the method lies in its stability, which is guaranteed by the use of a third-order upwind finite difference scheme, i.e. the spurious modes introduced by the approximation are always on the stable left half-plane, far away from the stability margin, and do not affect the predictions of a linear stability analysis. Consequently, this approach is beneficial for parametric studies that requires repeated evaluation of continuous models of flame dynamics or "on-the-fly" flame model identification.

6.1.2 Who's Who: How to Categorize Eigenmodes?

If finding the entirety of the spectrum is crucial, understanding the nature of the eigenmodes proves to be equally important. The most striking illustration of this necessity is the counter-intuitive behavior of mode destabilization with increased damping at the boundaries [36, 137]. Xu et al. [100] provided further experimental evidence, with an acoustic liner promoting instabilities associated to an ITA mode.

Two limiting cases suffer no ambiguity:

- In absence of a flame[3], the eigenmodes of the system can only be of *acoustic* nature.
- When a flame is placed in an anechoic environment, the acoustic feedback loop is cut and only the ITA feedback loop remains. The eigenmodes of the system are necessarily of ITA nature, and are commonly referred to as "*pure ITA modes*" in the literature [36, 110]. Their respective eigenfrequencies can be determined analytically [35].

Outside of these trivial limiting cases, both the ITA and acoustic feedback loops coexist and give rise to thermoacoustic modes whose nature is not trivially identifiable. A variety of categorization methods have been proposed over the years. By rearranging the equations in a collection of block matrices, Emmert et al. [36] interpreted the thermoacoustic system as two subsystems (the ITA and acoustic matrices on the diagonal) coupled by a parameter μ encountered on the off-diagonal blocks. This artificial parameter is used to modulate the coupling between the acoustic and ITA feedback loops. When set to $\mu = 0$, the feedback loops are fully decoupled and the eigenmodes separate into two distinct set of modes, *pure ITA modes* and *pure acoustic modes*. Therefore, Emmert suggested to label thermoacoustic modes as *ITA* or *acoustic* based on the "pure" eigenvalues they would converge to when gradually reducing the coupling μ from 1 to 0. The drawback of this approach is its sensitivity to the acoustic state of the system. For instance, in the vicinity of an exceptional point, a small variation in the acoustic state induces sudden change in the convergence limit [138], which highlights that this criterion lacks robustness.

Because the μ criterion does not offer physical interpretation, Hoesseini et al. [110] proposed to classify eigenmodes by varying physical parameters, namely the inlet and outlet reflection coefficients. They proposed an alternative criterion based on asymptotic behavior when reducing the reflection coefficients at boundaries. In the limit of zero reflection, a thermoacoustic mode can

---

[3] or if the flame is inactive and only acts as a temperature discontinuity

either become pure ITA or disappear, as the acoustic loop is cut. Consequently, thermoacoustic modes are labeled as ITA or acoustic based on their asymptotic limit when gradually reducing reflection at the boundaries. Similarly, Mukherjee and Shrira [113] demonstrated that, in the limit of small interaction index of the flame $n \to 0$ (i.e. the flame becomes inactive and only induces a temperature discontinuity in the system), two sets of modes are present in the spectrum, the classical acoustic modes and a set of highly damped modes with frequencies close the pure ITA modes. Consequently, they suggested to label eigenmodes based on their respective convergence limit when reducing n. This categorization criterion was used by Buschmann et al. [37] when explaining the spectrum of the MICCA combustor. However, if the use with an $n-\tau$ model is straight forward, the application to a more general DTD flame model [59] can be more challenging, unlike for the μ and reflection criteria.

The major drawback of all these methods is the need of a parameter sweep, which can be difficult to execute or even impractical due to excessive numerical or experimental costs. Furthermore, Orchini et al. [114] highlighted inconsistencies between the methods, where a thermoacoustic mode was labeled as ITA with the reflection criterion of [110] and as of acoustic nature with the n criterion of [37, 113]. Alternatively, categorization was achieved by assessing the proximity of pure ITA or pure acoustic modes [107, 116, 137]. Other studies made use of key characteristics of pure ITA modes, e.g. independence of the eigenfrequency from combustor length [100, 139], "convective scaling" of the eigenfrequency [140], etc. However, such approaches also suffer from limitations. For instance, for moderately large gains, the modes categorized as ITA and acoustic become indistinguishable, and the acoustic mode approaching the ITA "stops behaving like an acoustic mode anymore" [141]. Orchini et al. [114] gave further proof that, at an exceptional point, acoustic and ITA modes coalesce and share the same mode shape.

On the other hand, PAPER-CATEGORIZATION [101], which generalizes the approach of Yong et al. [142], proposed a categorization method that does not rely on a parameter sweep but exclusively on acoustic velocity phasors across the flame. More specifically, the Φ criterion, which indicates the phase relation between the acoustic velocities upstream and downstream the flame by means of a dot product, indicates which feedback loop is more "dominant". The strength of the method lies in the fact that the simple knowledge of two acoustic phasors is sufficient to determine the nature of any eigenmode. Additionally, it allows to build contour maps and exhibit regions where ITA and acoustic mode can be found. The criterion is not disconnected from physical interpretation, as it directly represent the oscillation of the medium, as discussed in Chapter 3. While not yet applied on experimental results, it is believed to be a more robust approach than the (extended) π-criterion [97, 99, 140], still widely used [143] but valid only for anechoic configurations or at the stability margin.

6.2 ITA Clusters in Annular Geometries

The interest on combustion instabilities in annular combustors rose when Siemens started reporting on their experiences [144, 145]. The early work was primarily focused on methods to mitigate the undesired instabilities. In particular, emphasis was put on active control [146, 147], which comprises an external subsystem that continuously "on-the-fly" perturbs the system to suppress oscillations. This method is nowadays often disregarded due to its complexity, cost and risk of failure[4], and a more pragmatic approach is adapted, where instabilities, rather than being directly controlled, are designed out (whenever possible), or dampened with passive Helmholtz resonators [148].

A remarkable feature of annular combustors is the unsteady nature of azimuthal instabilities. In contrast to longitudinal combustors, the annulus gives rise to azimuthal waves that can travel around in the clockwise or counter-clockwise directions, leading to do *spinning* modes, *standing* modes or a combination of both, i.e. *mixed* modes. These modes were found to transition spontaneously or periodically between different states, even for constant operating conditions, hence the naming *modal dynamics*. The behavior, observed in industrial gas turbines [145], was confirmed with LES [22]. To facilitate the study of this phenomena, and to overcome the limited industrial experimental data, several downscaled academic combustors were built, for instance in Cambridge [149, 150], and later operated at elevated pressure at NTNU [151], at the EM2C laboratory of CentraleSupélec with the MICCA combustor and its variety of injectors [152–154], at IIT Madras [155], or TU Berlin with a rig without combustion but electroacoustic feedback [156, 157], to name a few. Azimuthal acoustic modes are influenced by the background noise which leads to statistically preferred states [150], pushing the modes away from the spinning states [3, 81, 158]. Furthermore, they are strongly influenced by symmetry breaking, either with the use of different burners [159, 160], fuel staging [130, 161], or the presence of mean flow in the azimuthal direction [34, 157, 162–164]. These azimuthal acoustic eigenmodes usually correspond to the lowest eigenfrequencies and are the most prone to instability due to (i) lower losses in this frequency range and (ii) because the flame is acoustically compact and provide more efficiently acoustic energy to the cavity [3]. On the other hand, longitudinal modes occur at higher frequencies, commonly above the 3rd or 4th azimuthal modes. When the axial length of the chamber is sufficient, such a mode can, however, be excited simultaneously with an azimuthal mode of the same frequency leading to the so-called *slanted* state [165, 166]. While transverse excitation may lead to non-negligible effects [149, 150, 167], the review of O'Connor et al. [168] concludes that, in most cases, the dominant heat release oscillations are caused by indirect axial flow disturbances[5], thus justifying the common assumption to disregard the effects of transverse velocity on the heat release rate in the linear regime [33, 169–173].

Several modeling approaches have been used to study annular combustor. The simplest low-order models assume that only plane waves propagate in the azimuthal direction and all other types of waves are disregarded [87, 160, 173–176]. PAPER-ITA [107] introduces a model resembling the ATACAMAC approach of Parmentier et al. [160] and Bauerheim et al. [175], where the flame is placed inside the burner tube and the annulus is modeled with simple ducts. However, the tedious matrix operations to close and solve the problem are avoided by using Bloch boundaries, allowing for a simpler and easier-to-interpret model. However, all these models suffer from the same limitation: a choked outlet is assumed, i.e. combustors open to the atmosphere, such as MICCA, cannot be modeled in this manner. Indeed, because of the pressure node condition, purely azimuthal modes cannot exist and the combustor necessarily exhibit mixed modes[6]. A more elaborated quasi-2D model, based on ideas of Jakob J. Keller,

---

[4] in particular in the aero-engines industry with stringent certification procedures

[5] fluctuations of axial velocity through the burners, which are induced by the pressure field associated with transverse acoustic mode

[6] not in the sense of a superposition of a spinning and a standing modes, but rather in the sense that the eigen-

was introduced by Polifke et al. [33] and takes into account an axial and azimuthal wave number, as well as entropy effects, allowing to study the interference between acoustic and entropy waves. The model was used in subsequent studies, for instance, by Evesque and Polifke [169] to investigate the effect of broken symmetry, or by Kopitz et al. [170] for stability analysis of an annular chamber with validation against experiments. Recently, Yang et al. [177] revisited the model and demonstrated that experimental observations, such as the slanted modes of MICCA [165], can be captured. However, these models cannot be cast in a state-space approach, thus a non-linear eigenvalue problem must be solved with its associated challenges, as already discussed in the previous sections. Furthermore, with the increasing computing power, this 2D approach has become less attractive compared to directly solve for the Helmholtz equation [28, 37, 104, 118, 126], which does not require assumption on the modal shape, but relies on a discretization of the actual geometry, thus providing more accurate results. CFD simulations by means of LES [22] have also been employed. They require the least modeling assumptions, thus providing the most accurate results. However, because this is a time-domain approach, only the most unstable mode can be captured and not a complete spectrum. Nonetheless, such tool is extremely valuable, for instance to extract an FTF, a crucial input of any of the hybrid/reduced-order simulations mentioned previously. With the ever increasing computing capabilities, there is no doubt that LES will continue to play a major role in the years to come.

Compared to acoustic modes, ITA modes in annular combustors have received little attention, which is most likely explained by their late discovery. They were first identified by Buschmann et al. [118] who leveraged contour integration to obtain a more complete picture of the spectrum of the MICCA combustor. Solving for the Helmholtz equation, they demonstrated that ITA modes form clusters, i.e. groups of eigenmodes close in frequency. In a subsequent study, Buschmann et al. [37] highlighted that a 2D annulus model is sufficient to observe clusters of eigenmodes. This strongly suggests that ITA modes were present in the studies of Evesque [169] and Yang [177] but not captured because of the numerical challenge of finding these modes, as discussed in the previous sections. Additionally, Buschmann [37] provided more insight on the spectrum of MICCA obtained with 3D Helmholtz computations. In particular, the clusters align around the pure ITA frequencies. An interpretation was given with the fact that the modes are evanescent in the axial direction. In consequence, the flames do not “see” the outlet boundary and are placed in an effective anechoic environment, thus explaining the observed pure ITA frequencies. Modes of high azimuthal order are strongly cut-off, while low azimuthal modes are weakly cut-off and are first to deviate from the clusters. While this argument may be valid for the MICCA combustor, whose chamber exhibits a significant axial extent, it may not solely explain the presence of ITA clusters around the pure ITA frequency. Indeed, Orchini et al. [114] investigated the ATACAMAC configuration of [175] with the same 3D Helmholtz solver as in [37, 118], namely the Julia package *WavesAndEigenvalues*. Although the chamber is short in the axial direction, the three eigenmodes constituting the cluster were found extremely close to the analytical pure ITA frequency. Similarly, the low-order model of PAPER-ITA [107], which does not taken into account the axial extent and the evanescent nature of cut-off modes but solely azimuthal modes, captured the ITA clusters. The equivalent Rijke tube modeling, discussed in Chapter 5, was sufficient to explain clusters, and a phasor analysis provided additional insight, explaining why modes of high azimuthal order are usually more damped and low azimuthal order modes are first to deviate from the cluster. While not mentioned in the spectrum of ATA-

---

mode has both a longitudinal and azimuthal component

CAMAC by Bauerheim [175], ITA modes were most likely present but overlooked. Indeed, the strongly coupled and weakly coupled trajectories observed in [175] have been later confirmed by Orchini [114] and explained by the presence of two exceptional points, one where the two acoustic plenum and chamber modes coalesce, and the other due to the interaction between the first azimuthal chamber mode and first azimuthal ITA mode. To this day, ITA modes were never observed and formally identified as such in an annular combustor experiment. Literature suggests that they tend to usually be damped. However, even when stable, they should not be ignored: their presence alone, and the associated exceptional points, is sufficient to strongly influence the acoustic modes and the overall spectrum structure.

6.3 Clusters of Modes in Can-Annular Configurations

In contrast to annular chambers, which have been extensively investigated over the last decades, can-annular combustors have received less attention. They were first studied numerically by Bethke et al. [178] and Kaufmann et al. [179] by means of a finite-element analysis of the 3D Linearized Euler Equations. In particular, they showed that the full system exhibits eigenmodes that were not present in the isolated single can subsystem, because the mode shapes involve multiple cans. Their origin was associated to the cross-talk area in front of the turbine stage. These observations were later confirmed by the experimental results and modal analysis of Panek et al. [180]. In a following numerical study, Farisco et al. [181] performed LES of a simplified 2D configuration, for various gap geometries, and concluded that the can-to-can communication cannot be neglected. Ghirardo et al. [38] gave experimental and numerical (2D Helmholtz simulations) evidence that the weak coupling between cans gives rise to modes of various azimuthal orders and were first to report *clusters* of eigenmodes in can-annular configurations.

Consequently, many studies tackled the problem at a more fundamental level to provide valuable insight. Von Saldern et al. [182] proposed a low-order model, where only plane waves would propagate inside the cans, but with a coupling boundary conditions derived from mass conservation and Rayleigh conductivity K_R [183]. For simplicity, they chose a constant, geometrically-based Rayleigh conductivity, related to the diameter of the cans, which allows for an exact analytical derivation. The effects of the gap were lumped into an effective outlet reflection coefficient. The generic can-annular combustor considered in their study revealed the presence of numerous clusters. The impact of the acoustic coupling strength on the stability of modes in a cluster revealed a non-monotonic behavior, with either a stabilizing or destabilizing effect. The same model, later used for time domain simulations, revealed a strong interaction between modes, which can cause long transition times and allows modes that are not the most unstable in the linear regime to become dominant when considering nonlinear effects [184]. In parallel, the model proposed in PAPER-ITA for annular combustor was suggested to be a plausible approach for can-annular configurations. In PAPER-TUNING, it was employed to mimic the full-engine thermoacoustic behavior in single-can test-rigs by tuning the outlet acoustic properties. The proposed strategy was numerically applied to a full-scale Siemens gas turbine test-rig. As a result, a detailed comparison of both models from [182] and PAPER-ITA was proposed in PAPER-CAN, with, for the first time, validation against numerical simulations using a Helmholtz solver. While equivalent in the low frequency limit (the Rayleigh model being retrieved as a Taylor expansion of the model of PAPER-ITA), only the Rayleigh approach could properly capture the physics and provide qualitatively accurate results over a wide frequency range. However, because of the azimuthal-order-independent Rayleigh conductivity, quantitatively accurate results, compared to Helmholtz, could not be achieved: the eigenfrequencies were always underestimated. Consequently, an extension was proposed based on a characteristic length. The latter was derived to show an explicit dependence on azimuthal order, an essential feature to lump the 2D effects of the gap into a single parameter in an accurate manner. Using dimensionless numbers, scaling laws were given to generalize the results to configurations of arbitrary dimensions. Yoon [185] adopted an approach similar to the models of PAPER-ITA and ATACAMAC, modeling the gap as a thin annulus, however accounting for mean flow effects in the cans. The eigenfrequencies were always under-predicted, and, within a cluster, the higher the azimuthal order, the larger the error. This confirmed the findings of PAPER-CAN, which concluded that a model based purely on geometrical parameters could not be sufficient. The inclusion of mean-flow effects on the acoustic wave propagation did not drastically change the results.

The model of PAPER-CAN was later applied in PAPER-INTERPLAY to investigate the behavior of ITA and acoustic clusters in can-annular combustors, as recalled in Chapter 5. One finding of the study was the peculiar behavior of modes following specific trajectories in the complex plane imposed by the upstream conditions. However, von Saldern et al. [186] showed that this result breaks down when accounting for mean flow. They proposed a non-compact impedance model that includes density fluctuations, mean flow and dissipative effects in the cross-talk area. In contrast to the purely reactance coupling of PAPER-CAN and PAPER-INTERPLAY, their impedance exhibit a resistive contribution that is proportional to the grazing flow Mach number. The latter is Bloch number dependant, which implies that modes of various azimuthal order experience different damping levels. Exploiting this model, von Saldern et al. demonstrated that eigenmodes can be attenuated in an efficient manner using liners at the interface between adjacent cans for a well-chosen porosity. Pedergnana and Noiray [187] derived a coupled oscillator model where mean flow effects on the internal acoustics of the cans are disregarded but taken into account for the aeroacoustic coupling between cans. The unimodal projection of the Helmholtz equation in frequency domain was combined with Howe's derivation of the Rayleigh conductivity of uniform, two-sided grazing turbulent flow over a rectangular aperture of finite thickness [188]. The centerpiece of the model is the turbulent wake forming between neighbouring cans which is bounded by two vortex sheets. The displacement of the latter is induced by the oscillating pressure load across the aperture. Using a Bloch wave ansatz, the set of ODE was reduced to a single dispersion relation, which allowed for simple linear stability analysis and parameter study. The authors gave evidence of scenarii where the aeroacoustic coupling is dissipative, stabilizing a nominally unstable system, but also where the amplifying coupling is a able to destabilize a nominally stable system. Modes of higher Bloch number exhibit larger phase difference between neighbouring cans, leading to stronger apparent acoustic pressure gradients, thus a stronger response of the acoustic-hydrodynamic interaction. Orchini [189] extended the approach of [186] and proposed a general effective impedance model that embeds (i) the effects of the finite extension of the aperture on the acoustics, (ii) arbirtrary outlet acoustic properties expressed in terms of a prescribed impedance and (iii) the dynamics of the shear layer expressed in terms of a Rayleigh conductivity. The general expression was considered in a few limit cases of interest, such as an acoustically closed end, a compact aperture or an isolated duct, and results proved to be consistent with previous studies [182, 186]. In a follow-up study [190], the model was employed to numerically investigated the lab-scale setup of NTNU of eight interconnected cans [191]. A Rayleigh conductivity of an aperture with bias flow was chosen [188]. The dynamics of the V-shaped flame was modeled via a kinematic G-equation. In the frequency range considered, six clusters were present, two of thermoacoustic origin[7] and four resulting from the aeroacoustic coupling. The latter are easily identifiable because they do not exihibit axial modes $m = 0$. Indeed, no dynamic of the shear layer in the aperture occur if the cans oscillate in phase. The sensitivity of the clusters to parameter change was investigated. When gradually decreasing the flame response, the ITA cluster moves towards highly damped regions, whereas the acoustic cluster converges towards the passive acoustic solutions, both observations being in line with the existing litterature, as mentioned in the previous sections. The other clusters, which are dominated by shear layer dynamics, are, in general, almost independent of flame response. However, it was demonstrated that, when close to the passive acoustic solution, a cluster of aeroacoustic origin can exhibit a strong sensitivity to the flame strength, with mode veering. While not formally identified, the trajectories suggested the presence of an acoustic-aeroacoustic exceptional point. Conversely, acoustic clusters were shown to be insensitive to the aeroacoustic coupling, while the response of the ITA cluster is non trivial. Finally, by changing the outlet boundary, they highlighted that a cluster of aeroacoustic origin can become the most unstable, thus justifying that the effect of shear layer dynamics should not be neglected. Recently, Humbert and Orchini [192] were the first to propose an experimental setup dedicated to the systematic characterization of the acoustic response of a can-annular configuration as a function of the size of the annulus connecting the cans. The experimental results were compared to Helmholtz computations and a low-order model. The novelty of the latter lies in the fact that the acoustic field inside the cans is not described exclusively with plane waves, but also includes the first transverse (T1) mode, which influences the can-annulus coupling condition. The resulting dispersion relation exhibits, among others, Bessel functions of the first kind that show an explicit dependence on the azimuthal order and the discrete rotational symmetry. This LOM shows excellent agreement, compared to both Helmholtz and experimental data, over a wide range of annular gap-to-can volume ratios. Interestingly, when the T1 contribution is omitted, which is a reasonable approximation for low frequencies, it is retrieved that a model based purely on geometrical parameters tends to underpredict the eigenfrequencies. Finally, Brind [193] investigated in more details the effect of the downstream turbine stages. The model of Orchini [189] was combined with time-marching CFD to predict transfer functions between incident and reflected waves in a can-annular combustor terminated by a four-stage turbine. The study highlighted that resistive effects must be incorporated in the low-order model to accurately recover CFD results. The exploration of the coupled combustor-turbine design space showed that an optimal gap size can be determined to minimize the reflected energy. This approach is, however, limited by the necessity to calibrate resistive effects in the LOM using CFD simulations.

---

[7] one ITA cluster and one acoustic cluster

7 Outlook

The presence of clusters of eigenvalues in the spectrum of annular and can-annular combustors described in this thesis has profound consequences. A foundation is set for future research to build on.

From a practical engineering perspective, the challenge of designing stable combustion systems remains. In contrast to longitudinal combustors, where only a handful of eigenmodes may be unstable, (can-)annular architectures potentially exhibit numerous problematic modes if one or many clusters are found close to the stability margin. Several strategies can be considered.

- The geometry of the plenum and/or the combustor can be optimized in order to stabilize all eigenmodes. However, if done by trial and error, this iterative process can quickly become tedious and expensive. To ease the operation, Aguilar and Juniper [194] proposed an adjoint-augmented optimization routine, which proved to be capable of stabilizing all thermoacoustic modes of an annular combustor with minimum geometric change. Similarly, Falco and Juniper [195] applied an adjoint-based shape optimization to a 2D Helmholtz solver to accurately, albeit at low computational cost, determine the shape that most stabilizes a turbulent swirl combustor. While this approach has been applied only to longitudinal combustors so far, an extension to a can-annular combustor unit-cell with Bloch boundaries is appealing and should be investigated in the future.
- If the previous method assumes a given flame response and relies on the tuning of the acoustics to stabilize the system, an opposite approach can be considered. Indeed, if integration constraints are such that the geometry of plenum and chamber cannot be changed, a second course of action is to modify the injector design to obtain the desired flame response. In this spirit, the DeTAS procedure of Bade et al. [196] aimed at selecting the most stable burner geometry for a given combustor by relating geometrical parameters to combustion dynamics features. The ability to relate the shape of the FTF to geometrical parameters (such as swirl number, lengths, etc.) and operating conditions would open the door to innovative design perspectives for combustion systems. Although still a dream today, the recent progress in data assimilation, for instance combining experimental results with reduced-order model using Bayesian inference to accurately learn the parameters of the model to make the latter predictive [197, 198], are very encouraging.
- Recently, Casel and Ghani [199] proposed a novel approach where not only the acoustic and ITA modes were accounted for in the design process, but also the exceptional points (XPs). In particular, the locations of XPs in the spectra are explicitely computed and the impact of parameter change on their position was assessed. They highlighted that the strategy of choosing parameters such that the XP is highly damped led to a fully stabilized spectrum. In the context of can-annular combustors, where, as shown in this thesis, the presence of XPs influences the trajectories in the complex plane on which the eigenmodes

lie, an XPs placement strategy constitutes an interesting approach that should be further investigated.

In the future, all these aforementioned methods could be used in a *robust design* approach as in [200], where risk analysis is used in tandem with global optimization algorithms to find design parameters that are robust against various sources of uncertainty, leading to an efficient risk mitigation. However, the method should be adapted in a way that, instead of considering only one or two modes as done by Guo et al. [200], the entirety of the cluster of fundamentals modes, and eventually clusters of harmonics, are taken into account. For the stubborn eigenmodes that could not be stabilized by design, the use of dampers becomes necessary. Adjoint methods can be employed, for instance, to determine optimal Helmholtz resonator placement, even with a low-order network approach [201]. If liners and Helmholtz dampers have proven to be effective against acoustic modes, future studies should focus on determining optimal damping strategies for modes of ITA and aeroacoustic origin.

From a phenomenological perspective, the appearance of clusters is only one of the many fascinating manifestations of ring-like coupled oscillators. Indeed, such clustered eigenstructure makes the system highly sensitive to small perturbations [202], which has implications for both the linear and non-linear dynamics. The effects of symmetry breaking have been fairly well investigated for acoustic modes in annular combustors [34, 130, 157, 159–164]. Asymmetry causes a degenerate pair of eigenvalues to split into two distinct eigenmodes. The same phenomenon is to be expected from ITA and acoustic clusters, which comprise many degenerate eigenmodes. However, an additional remarkable linear phenomenon of weakly coupled oscillators is mode localization [109]. If asymmetry does not drastically change the eigenfrequency, the modeshape is significantly modified: in contrast to the purely symmetric case, where the modeshape spans across multiple cans, the mode is *localized*, i.e. only a few cans show activity, while the majority of cans remain quiet. This phenomenon, observed in experiments [203, 204] and briefly covered in the numerical study [38], has major engineering implications and requires to rethink the distribution of pressure sensors across cans, as well as the interpretation of online monitoring data, to efficiently define safety triggers and avoid catastrophic failures. Further efforts should be made to study mode localization at a fundamental level. In the non-linear regime, the presence of closely spaced eigenfrequencies may give rise to synchronization [205], i.e. finite amplitude oscillations that are a mixture of linear modes with different eigenfrequencies. Mutual synchronization has been famously examplified by Huygens' clocks [206], but also studied in the context of thermoacoustics, with laminar [207, 208] or turbulent [209, 210] coupled combustors. Depending on the coupling and the system parameters, a variety of complex dynamics may emerge [211, 212], such as quasiperiodicity, chaos, frequency/phase locking or chimeras, a hybrid pattern named from the Greek mythology by Abrams and Strogatz [213] to emphasize the simultaneous coexistence of regions of synchrony and asynchrony. Modeling and analysis methods could be further developed and applied to (can-)annular combustors.

8 Summary of Papers

This chapter summarizes the core findings of individual publications. The latter are not sorted stricly chronologically, but rather in a way that highlights the progress made on the topic of clusters of thermoacoustic modes. Additionally, for each paper, the respective contribution of the authors is stated.

8.1 Linear time-continuous state-space realization of flame transfer functions by means of a propagation equation

Label: PAPER-FTF [61]

Original Abstract: Low-order network models, commonly used to assess the thermo-acoustic stability of combustors, can be cast in a linear, time-continuous state-space representation. A standard linear eigenvalue problem for the system modes results, which can be solved in a robust and efficient manner. To represent the linear dynamics of any time-invariant flame in the state-space framework, this study presents an approximation of the distributed-time-delayed flame response to acoustic velocity perturbations based on a spatially discretized propagation equation (PE). We derive the rational flame transfer function of a first-order-upwind-PE state-space model and discuss its relation to the Tustin approximation of transfer functions. For an exemplary discrete finite impulse response of a flame, a third-order-upwind-PE state-space model is shown to match the discrete flame frequency response with an accuracy comparable to that of a rational approximation found by non-linear optimization. The numerical dissipation introduced by discretization of the PE ensures negligible gain above the Nyquist frequency of the underlying discrete flame impulse response. Finally, we apply the PE state-space flame model to a generic Rijke tube and show that the predicted thermoacoustic modes agree well with results obtained from a classical non-linearly optimized rational approximation of the frequency response function of the flame.

Relevance for the thesis: This paper introduces a method to represent any flame model in a continuous state-space framework, enabling to solve for a linear eigenvalue problem, and thus guaranteeing the completeness of the spectrum.

CRediT author statement: P. Brokof: Conceptualization, Methodology, Software, Validation, Formal analysis, Data curation, Writing - original draft, Writing - review & editing, Visualization. **G. J. J. Fournier:** Conceptualization, Methodology, Software, Validation, Formal analysis, Data curation, Writing - review & editing. **W. Polifke:** Conceptualization, Writing - review & editing, Supervision, Funding acquisition.

Status: Published in *INTERNOISE and NOISE-CON Congress and Conference Proceedings*.

Review process: Scopus listed.

Reference: P. Brokof, G. J. J. Fournier, and W. Polifke. “Linear time-continuous state-space realization of flame transfer functions by means of a propagation equation”. In *INTERNOISE and NOISE-CON Congress and Conference Proceedings*, pages 3490–3501, Glasgow, Scotland, 2023. Institute of Noise Control Engineering. DOI: 10.3397/IN_2022_0496. Reproduced on p.75ff.

8.2 Categorization of thermoacoustic modes in an ideal resonator with phasor diagrams

Label: PAPER-CATEGORIZATION [101]

Original Abstract: A recent study (*Yong, Silva, and Polifke, Combust. Flame 228* (*2021*)) proposed the use of phasor diagrams to categorize marginally stable modes in an ideal resonator with a compact, velocity-sensitive flame. Modes with velocity phasors that reverse direction across the flame were categorized as ITA modes. The present study extends this concept to growing and decaying modes. In other words, with the method proposed, it is possible to distinguish whether a given thermoacoustic mode – regardless of its stability – should be categorized as acoustic or ITA. The method proposed does not rely on any parametric sweep, but on the angle relating the velocity phasors across the flame. This method of categorization reveals distinct regions in the complex plane where acoustic and ITA eigenfrequencies are localized. Additionally, we analyze the medium oscillation at the flame location to construct a physically intuitive understanding of the proposed categorization method.

Relevance for the thesis: This paper provides a simple and elegant criterion to identify the nature of a thermoacoustic eigenmode.

CRediT author statement: K. J. Yong: Conceptualization, Methodology, Software, Validation, Formal analysis, Data curation, Writing - original draft, Writing - review & editing, Visualization. **C. F. Silva:** Conceptualization, Writing - review & editing, Supervision. **G. J. J. Fournier:** Conceptualization, Writing - review & editing. **W. Polifke:** Conceptualization, Writing - review & editing, Supervision, Funding acquisition.

Status: Published in *Combustion and Flame*.

Review process: Peer-reviewed, Scopus listed.

Reference: K. J. Yong, C. F. Silva, G. J. J. Fournier, and W. Polifke. “Categorization of thermoacoustic modes in an ideal resonator with phasor diagrams”. *Combustion and Flame*, 249:112605, March 2023. ISSN 00102180. DOI: 10.1016/j.combustflame.2022.112605. Reproduced on p.87ff.

8.3 Low-Order Modeling to Investigate Clusters of Intrinsic Thermoacoustic Modes in Annular Combustors

Label: PAPER-ITA [107]

Original Abstract: The intrinsic thermoacoustic (ITA) feedbackloop constitutes a coupling between flow, flame and acoustics that does not involve the natural acoustic modes of the system. One recent study showed that ITA modes in annular combustors come in significant number and with the peculiar behavior of clusters, i.e. several modes with close frequencies. In the present work an analytical model of a typical annular combustor is derived via Riemann invariants and Bloch theory. The resulting formulation describes the full annular system as a longitudinal combustor with an outlet reflection coefficient that depends on frequency and the azimuthal mode order. The model explains the underlying mechanism of the clustering phenomena and the structure of the clusters associated with ITA modes of different azimuthal orders. In addition, a phasor analysis is proposed, which enclose the conditions for which the 1D model remains valid when describing the thermoacoustic behavior of an annular combustor.

Relevance for the thesis: This paper provides an analytical model that allows to explain the origin of ITA clusters in annular combustors, as well as the spectrum structure.

CRediT author statement: G. J. J. Fournier: Conceptualization, Methodology, Software, Validation, Formal analysis, Data curation, Writing - original draft, Writing - review & editing, Visualization. **M. Haeringer:** Methodology, Writing - review & editing. **C. F. Silva:** Conceptualization, Writing - review & editing, Supervision. **W. Polifke:** Conceptualization, Writing - review & editing, Supervision, Funding acquisition.

Status: Published in *Journal of Engineering for Gas Turbines and Power*.

Review process: Peer-reviewed, Scopus listed.

Reference: G. J. J. Fournier, M. Haeringer, C. F. Silva, and W. Polifke. “Low-Order Modeling to Investigate Clusters of Intrinsic Thermoacoustic Modes in Annular Combustors”. *Journal of Engineering for Gas Turbines and Power*, 143(4):041025, April 2021. ISSN 0742-4795,1528-8919. DOI: 10.1115/1.4049356. Reproduced on p.100ff.

Comment: A first version of this publication was presented and published in the proceedings of the *ASME Turbo Expo 2020: Turbomachinery Technical Conference and Exposition* [214].

8.4 A Strategy to Tune Acoustic Terminations of Single-Can Test-Rigs to Mimic Thermoacoustic Behavior of a Full Engine

Label: PAPER-TUNING [215]

Original Abstract: Thermoacoustic properties of can-annular combustors are commonly investigated by means of single-can test-rigs. To obtain representative results, it is crucial to mimic can-can coupling present in the full engine. However, current approaches either lack a solid theoretical foundation or are not practicable for high-pressure rigs. In the present study we employ Bloch-wave theory to derive reflection coefficients that correctly represent can-can coupling. We propose a strategy to impose such reflection coefficients at the acoustic terminations of a single-can test-rig by installing passive acoustic elements, namely straight ducts or Helmholtz resonators. In an iterative process, these elements are adapted to match the reflection coefficients for the dominant frequencies of the full engine. The strategy is demonstrated with a network model of a generic can-annular combustor and a 3D model of a realistic can-annular combustor configuration. For the latter we show that can-can coupling via the compressor exit plenum is negligible for frequencies sufficiently far away from plenum eigenfrequencies. Without utilizing previous knowledge of relevant frequencies or flame dynamics, the test-rig models are adapted within a few iterations and match the full engine with good accuracy. Using Helmholtz resonators for test-rig adaption turns out to be more viable than using straight ducts.

Relevance for the thesis: This paper utilizes the model introduced in PAPER-ITA to describe the can-can acoustic coupling. The latter reveals to be imperfectly suited for this type application.

CRediT author statement: M. Haeringer: Conceptualization, Methodology, Software, Validation, Formal analysis, Data curation, Writing - original draft, Writing - review & editing, Visualization. **G. J. J. Fournier:** Methodology, Writing - review & editing. **M. Meindl:** Software, Writing - review & editing. **W. Polifke:** Conceptualization, Formal analysis, Writing - original draft, Writing - review & editing, Supervision, Funding acquisition.

Status: Published in *Journal of Engineering for Gas Turbines and Power*.

Review process: Peer-reviewed, Scopus listed.

Reference: M. Haeringer, G. J. J. Fournier, M. Meindl, and W. Polifke. “A Strategy to Tune Acoustic Terminations of Single-Can Test-Rigs to Mimic Thermoacoustic Behavior of a Full Engine”. *Journal of Engineering for Gas Turbines and Power*, 143(7):710029, July 2021. ISSN 0742-4795, 1528-8919. DOI: 10.1115/1.4048642. Reproduced on p.110ff.

Comment: A first version of this publication was presented and published in the proceedings of the *ASME Turbo Expo 2020: Turbomachinery Technical Conference and Exposition* [216].

8.5 Low-Order Modeling of Can-Annular Combustors

Label: PAPER-CAN [108]

Original Abstract: Heavy-duty land-based gas turbines are often designed with can-annular combustors, which consist of a set of identical cans, acoustically connected on the upstream side via the compressor plenum, and, downstream, with a small annular gap located at the transition with the first turbine stage. The modeling of this cross-talk area is crucial to predict the thermo-acoustic modes of the system. Thanks to the discrete rotational symmetry, Bloch wave theory can be exploited to reduce the system to a longitudinal combustor with a complex-valued equivalent outlet reflection coefficient, which models the annular gap. The present study reviews existing low-order models based purely on geometrical parameters and compares them to 2D Helmholtz simulations. We demonstrate that the modeling of the gap as a thin annulus is not suited for can-annular combustors and that the Rayleigh conductivity model only gives qualitative agreement. We then propose an extension for the equivalent reflection coefficient that accounts not only for geometrical but also flow parameters, by means of a characteristic length. The proposed model is in excellent agreement with 2D simulations and is able to correctly capture the eigenfrequencies of the system. We then perform a Design of Experiments study that allows us to explore various configurations and build correlations for the characteristic length. Finally, we discuss the validity limits of the proposed low-order modeling approach.

Relevance for the thesis: This paper compares the models of PAPER-ITA and the literature to FEM computations of a can-annular combustor. A new model that better describes the acoustic coupling between cans is proposed.

CRediT author statement: G. J. J. Fournier: Conceptualization, Methodology, Software, Validation, Formal analysis, Data curation, Writing - original draft, Writing - review & editing, Visualization. **M. Meindl:** Software, Writing - review & editing. **C. F. Silva:** Conceptualization, Writing - review & editing, Supervision. **G. Ghirardo:** Conceptualization, Writing - review & editing, Supervision. **M. R. Bothien:** Conceptualization, Writing - review & editing, Supervision, Funding acquisition. **W. Polifke:** Conceptualization, Writing - review & editing, Supervision, Funding acquisition.

Status: Published in *Journal of Engineering for Gas Turbines and Power*.

Review process: Peer-reviewed, Scopus listed.

Reference: G. J. J. Fournier, M. Meindl, C. F. Silva, G. Ghirardo, M. R. Bothien, and W. Polifke. “Low-Order Modeling of Can-Annular Combustors”. *Journal of Engineering for Gas Turbines and Power*, 143(12):121004, December 2021. ISSN 0742-4795, 1528-8919. DOI: 10.1115/1.4051954. Reproduced on p.121ff.

Comment: A first version of this publication was presented and published in the proceedings of the *ASME Turbo Expo 2021: Turbomachinery Technical Conference and Exposition* [217].

8.6 Interplay of Clusters of Acoustic and Intrinsic Thermoacoustic Modes in Can-Annular Combustors

Label: PAPER-INTERPLAY [117]

Original Abstract: Thermoacoustic systems can exhibit self-excited instabilities of two nature, namely cavity modes or intrinsic thermoacoustic (ITA) modes. In heavy-duty land-based gas turbines with can-annular combustors, the cross-talk between cans causes the cavity modes of various azimuthal order to create clusters, i.e. ensembles of modes with close frequencies. Similarly, in systems exhibiting rotational symmetry, ITA modes also have the peculiar behavior of forming clusters. In the present study, we investigate how such clusters interplay when they are located in the same frequency range. We first consider a simple Rijke tube configuration and derive a general analytical low-order network model using only dimensionless numbers. We investigate the trajectories of the eigenmodes when changing the downstream length and the flame position. In particular, we show that ITA and acoustic modes can switch nature and their trajectories are strongly influenced by the presence of exceptional points. We then study a generic can-annular combustor. We show that such configuration can be approximated by an equivalent Rijke tube. We demonstrate that, in the absence of mean flow, the eigenvalues of the system necessarily lie on specific trajectories imposed by the upstream conditions.

Relevance for the thesis: This paper makes use of the model of PAPER-CAN to investigate the behavior of ITA and acoustic clusters in a can-annular combustor. It is highlighted how eigenmodes follow specific trajectories, can switch nature and are influenced by the presence of exceptional points.

CRediT author statement: G. J. J. Fournier: Conceptualization, Methodology, Software, Validation, Formal analysis, Data curation, Writing - original draft, Writing - review & editing, Visualization. **F. Schaefer:** Software, Writing - review & editing. **M. Haeringer:** Conceptualization, Methodology, Writing - review & editing. **C. F. Silva:** Conceptualization, Writing - review & editing, Supervision. **W. Polifke:** Conceptualization, Writing - review & editing, Supervision, Funding acquisition.

Status: Published in *Journal of Engineering for Gas Turbines and Power*.

Review process: Peer-reviewed, Scopus listed.

Reference: G. J. J. Fournier, F. Schaefer, M. Haeringer, C. F. Silva, and W. Polifke. “Interplay of Clusters of Acoustic and Intrinsic Thermoacoustic Modes in Can-Annular Combustors”. *Journal of Engineering for Gas Turbines and Power*, 144(12):121015, December 2022. ISSN 0742-4795, 1528-8919. DOI: 10.1115/1.4055381. Reproduced on p.131ff.

Comment: A first version of this publication was presented and published in the proceedings of the *ASME Turbo Expo 2022: Turbomachinery Technical Conference and Exposition* [218].

Bibliography

[1] "Conducting a Test". https://www1.grc.nasa.gov/historic-facilities/rocket-engine-test-facility/conducting-a-test/. Cited on pp. xv and 1.

[2] T. Lieuwen and V. Yang, editors. *Combustion Instabilities in Gas Turbine Engines: Operational Experience, Fundamental Mechanisms and Modeling*, volume 210 of *Progress in Astronautics and Aeronautics*. American Institute of Aeronautics and Astronautics, Reston, VA, USA, 2005. ISBN 978-1-56347-669-3. Cited on pp. xv and 1.

[3] A. Faure-Beaulieu. *Modelling of Azimuthal Thermoacoustic and Aeroacoustic Instabilities in Axisymmetric Geometries*. PhD thesis, ETH Zurich, Zurich, Switzerland, May 2022. Cited on pp. xv, 2, and 35.

[4] M. Meindl. *Linearized Modeling of Thermoacoustic Systems Utilizing a Discontinuous Galerkin Finite Element Method*. PhD thesis, TU München, 2022. Cited on pp. xv, 3, and 4.

[5] J. W. Jordan. "Kennedy's Romantic Moon and Its Rhetorical Legacy for Space Exploration". *Rhetoric & Public Affairs*, 6(2):209–231, 2003. ISSN 1534-5238. DOI: 10.1353/rap.2003.0047. Cited on p. 1.

[6] J. C. Oefelein and V. Yang. "Comprehensive Review of Liquid-Propellant Combustion Instabilities in F-1 Engines". *Journal of Propulsion and Power*, 9(5):657–677, 1993. ISSN 0748-4658. DOI: 10.2514/3.23674. Cited on p. 1.

[7] B. Zinn and Y. Neumeier. "An overview of active control of combustion instabilities". In *35th Aerospace Sciences Meeting and Exhibit*, Reno, NV ,USA, January 1997. American Institute of Aeronautics and Astronautics. DOI: 10.2514/6.1997-461. Cited on p. 1.

[8] J. J. Keller. "Thermoacoustic Oscillations in Combustion Chambers of Gas Turbines". *AIAA Journal*, 33(12):2280–2287, 1995. ISSN 0001-1452, 1533-385X. DOI: 10.2514/3.12980. Cited on pp. 1 and 3.

[9] T. Lieuwen and K. McManus. "Combustion Dynamics in Lean-Premixed Prevaporized (LPP) Gas Turbines". *Journal of Propulsion and Power*, 19(5):721–721, September 2003. ISSN 0748-4658, 1533-3876. DOI: 10.2514/2.6171. Cited on p. 1.

[10] M. P. Boyce. *Gas Turbine Engineering Handbook*. Butterworth-Heinemann, 4th edition, 2011. ISBN 978-0-12-383842-1. Cited on p. 2.

[11] B. Becker, T. Schulenberg, and H. Termuehlen. “The “3A-Series” Gas Turbines With HBR® Combustors”. In *Volume 4: Heat Transfer; Electric Power; Industrial and Cogeneration*, page V004T10A024, Houston, TX, USA, June 1995. American Society of Mechanical Engineers. ISBN 978-0-7918-7881-1. DOI: 10.1115/95-GT-458. Cited on p. 2.

[12] S. Zahirovic and K. Knapp. “Ansaldo GT26 Sequential Combustor Performance in Long-Term Commercial Operation”. In *Volume 4B: Combustion, Fuels and Emissions*, page V04BT04A008, Charlotte, NC, USA, June 2017. American Society of Mechanical Engineers. ISBN 978-0-7918-5085-5. DOI: 10.1115/GT2017-64289. Cited on p. 2.

[13] D. A. Pennell, M. R. Bothien, A. Ciani, V. Granet, G. Singla, S. Thorpe, A. Wickstroem, K. Oumejjoud, and M. Yaquinto. “An Introduction to the Ansaldo GT36 Constant Pressure Sequential Combustor”. In *Volume 4B: Combustion, Fuels and Emissions*, page V04BT04A043, Charlotte, NC, USA, June 2017. American Society of Mechanical Engineers. ISBN 978-0-7918-5085-5. DOI: 10.1115/GT2017-64790. Cited on p. 2.

[14] V. Herda, W. Gallagher, and G. McQuiggan. “The Development and Operational Experience With the Latest Siemens SGT6-5000F Gas Turbine at the Great River Energy Elk River Peaking Plant”. In *Volume 1: Aircraft Engine; Ceramics; Coal, Biomass and Alternative Fuels; Education; Electric Power; Manufacturing Materials and Metallurgy*, pages 739–747, Glasgow, UK, October 2010. ASMEDC. ISBN 978-0-7918-4396-3. DOI: 10.1115/GT2010-22091. Cited on p. 2.

[15] C. Vandervort, D. Leach, D. Walker, and J. Sasser. “Commercialization and Fleet Experience of the 7/9HA Gas Turbine Combined Cycle”. In *Volume 3: Coal, Biomass, Hydrogen, and Alternative Fuels; Cycle Innovations; Electric Power; Industrial and Cogeneration; Organic Rankine Cycle Power Systems*, page V003T08A006, Phoenix, Arizona, USA, June 2019. American Society of Mechanical Engineers. ISBN 978-0-7918-5860-8. DOI: 10.1115/GT2019-91594. Cited on p. 2.

[16] G. A. Jones and K. J. Warner. “The 21st century population-energy-climate nexus”. *Energy Policy*, 93:206–212, June 2016. ISSN 03014215. DOI: 10.1016/j.enpol.2016.02.044. Cited on p. 2.

[17] Y. Liu, X. Sun, V. Sethi, D. Nalianda, Y.-G. Li, and L. Wang. “Review of modern low emissions combustion technologies for aero gas turbine engines”. *Progress in Aerospace Sciences*, 94:12–45, October 2017. ISSN 03760421. DOI: 10.1016/j.paerosci.2017.08.001. Cited on p. 2.

[18] M. Götz, J. Lefebvre, F. Mörs, A. McDaniel Koch, F. Graf, S. Bajohr, R. Reimert, and T. Kolb. “Renewable Power-to-Gas: A technological and economic review”. *Renewable Energy*, 85:1371–1390, January 2016. ISSN 09601481. DOI: 10.1016/j.renene.2015.07.066. Cited on p. 2.

[19] J. W. S. Rayleigh. “The Explanation of Certain Acoustical Phenomena”. *Nature*, 18: 319–321, 1878. DOI: 10.1038/018319a0. Cited on pp. 2 and 13.

[20] M. Bauerheim, F. Nicoud, and T. Poinsot. “Progress in Analytical Methods to Predict and Control Azimuthal Combustion Instability Modes in Annular Chambers”. *Physics of Fluids*, 28(2):021303, February 2016. ISSN 1070-6631, 1089-7666. DOI: 10.1063/1.4940039. Cited on p. 3.

[21] G. Staffelbach, L. Y. M. Gicquel, G. Boudier, and T. Poinsot. “Large Eddy Simulation of self excited azimuthal modes in annular combustors”. *Proceedings of the Combustion Institute*, 32(2):2909–2916, 2009. ISSN 1540-7489. DOI: 10.1016/j.proci.2008.05.033. Cited on p. 3.

[22] P. Wolf, G. Staffelbach, L. Y. M. Gicquel, J.-D. Müller, and T. Poinsot. “Acoustic and Large Eddy Simulation studies of azimuthal modes in annular combustion chambers”. *Combustion and Flame*, 159(11):3398–3413, November 2012. ISSN 0010-2180. DOI: 10.1016/j.combustflame.2012.06.016. Cited on pp. 3, 35, and 36.

[23] L. Magri, P. J. Schmid, and J. P. Moeck. “Linear flow analysis inspired by mathematical methods from quantum mechanics”. *Annual Review of Fluid Mechanics*, 55(1):541–574, January 2023. ISSN 0066-4189, 1545-4479. DOI: 10.1146/annurev-fluid-031022-044209. Cited on p. 3.

[24] A. Avdonin, M. Meindl, and W. Polifke. “Thermoacoustic analysis of a laminar premixed flame using a linearized reacting flow solver”. *Proceedings of the Combustion Institute*, 37(4):5307–5314, 2019. ISSN 15407489. DOI: 10.1016/j.proci.2018.06.142. Cited on pp. 3, 31, and 32.

[25] J. Gikadi, T. Sattelmayer, and A. Peschiulli. “Effects of the mean flow field on the thermoacoustic stability of aero-engine combustion chambers”. In *Volume 2: Combustion, Fuels and Emissions, Parts A and B*, pages 1203–1211, Copenhagen, Denmark, June 2012. American Society of Mechanical Engineers. ISBN 978-0-7918-4468-7. DOI: 10.1115/GT2012-69612. Cited on pp. 3 and 31.

[26] M. Meindl, A. Albayrak, and W. Polifke. “A state-space formulation of a discontinuous Galerkin method for thermoacoustic stability analysis”. *Journal of Sound and Vibration*, 481:115431, September 2020. ISSN 0022460X. DOI: 10.1016/j.jsv.2020.115431. Cited on pp. 3, 31, and 32.

[27] T. Hofmeister, T. Hummel, F. Berger, N. Klarmann, and T. Sattelmayer. “Elimination of Numerical Damping in the Stability Analysis of Noncompact Thermoacoustic Systems With Linearized Euler Equations”. *Journal of Engineering for Gas Turbines and Power*, 143(3):031013, March 2021. ISSN 0742-4795, 1528-8919. DOI: 10.1115/1.4049651. Cited on pp. 3 and 31.

[28] F. Nicoud, L. Benoit, C. Sensiau, and T. Poinsot. “Acoustic Modes in Combustors with Complex Impedances and Multidimensional Active Flames”. *AIAA Journal*, 45(2):426–441, 2007. ISSN 0001-1452, 1533-385X. DOI: 10.2514/1.24933. Cited on pp. 3, 31, and 36.

[29] H. J. Merk. “Analysis of heat-driven oscillations of gas flows. I. General considerations.”. *Applied Scientific Research, Section A*, 6(4):317–336, July 1957. ISSN 0365-7132. DOI: 10.1007/BF03184653. Cited on p. 3.

[30] M. A. Heckl. “Active Control of the Noise from a Rijke Tube”. *Journal of Sound and Vibration*, 124(1):117–133, July 1988. ISSN 0022460X. DOI: 10.1016/S0022-460X(88)81408-1. Cited on p. 3.

[31] U. Krüger, J. Hüren, S. Hoffmann, W. Krebs, and D. Bohn. “Prediction of Thermoacoustic Instabilities With Focus on the Dynamic Flame Behavior for the 3A-Series Gas Turbine of Siemens KWU”. In *ASME 1999 International Gas Turbine and Aeroengine Congress and Exhibition*, volume Volume 2: Coal, Biomass and Alternative Fuels; Combustion and Fuels; Oil and Gas Applications; Cycle Innovations, page V002T02A016, Indianapolis, Indiana, USA, June 1999. American Society of Mechanical Engineers. DOI: 10.1115/99-GT-111. Cited on p. 3.

[32] B. B. H. Schuermans, W. Polifke, and C. O. Paschereit. “Modeling Transfer Matrices of Premixed Flames and Comparison With Experimental Results”. In *Volume 2: Coal, Biomass and Alternative Fuels; Combustion and Fuels; Oil and Gas Applications; Cycle Innovations*, volume Volume 2: Coal, Biomass and Alternative Fuels; Combustion and Fuels; Oil and Gas Applications; Cycle Innovations, page V002T02A024, Indianapolis, Indiana, USA, June 1999. American Society of Mechanical Engineers. ISBN 978-0-7918-7859-0. DOI: 10.1115/99-GT-132. Cited on p. 3.

[33] W. Polifke, C. O. Paschereit, and K. Döbbeling. “Constructive and Destructive Interference of Acoustic and Entropy Waves in a Premixed Combustor with a Choked Exit”. *International Journal of Acoustics and Vibration*, 6(3):135–146, 2001. DOI: 10.20855/IJAV.2001.6.382. Cited on pp. 3, 35, and 36.

[34] M. Bauerheim, M. Cazalens, and T. Poinsot. “A theoretical study of mean azimuthal flow and asymmetry effects on thermo-acoustic modes in annular combustors”. *Proceedings of the Combustion Institute*, 35(3):3219–3227, 2015. ISSN 1540-7489. DOI: 10.1016/j.proci.2014.05.053. Cited on pp. 3, 35, and 42.

[35] T. Emmert, S. Bomberg, and W. Polifke. “Intrinsic Thermoacoustic Instability of Premixed Flames”. *Combustion and Flame*, 162(1):75–85, January 2015. ISSN 00102180. DOI: 10.1016/j.combustflame.2014.06.008. Cited on pp. 3, 16, 27, and 33.

[36] T. Emmert, S. Bomberg, S. Jaensch, and W. Polifke. “Acoustic and intrinsic thermoacoustic modes of a premixed combustor”. *Proceedings of the Combustion Institute*, 36(3):3835–3842, 2017. ISSN 15407489. DOI: 10.1016/j.proci.2016.08.002. Cited on pp. 3, 16, 17, and 33.

[37] P. E. Buschmann, G. A. Mensah, and J. P. Moeck. “Intrinsic thermoacoustic modes in an annular combustion chamber”. *Combustion and Flame*, 214:251–262, April 2020. ISSN 00102180. DOI: 10.1016/j.combustflame.2019.11.006. Cited on pp. 3, 32, 34, and 36.

[38] G. Ghirardo, C. Di Giovine, J. P. Moeck, and M. R. Bothien. “Thermoacoustics of Can-Annular Combustors”. *Journal of Engineering for Gas Turbines and Power*, 141(1):011007, January 2019. ISSN 0742-4795, 1528-8919. DOI: 10.1115/1.4040743. Cited on pp. 3, 21, 37, and 42.

[39] G. K. Batchelor. *An Introduction to Fluid Dynamics*. Cambridge Mathematical Library. Cambridge Univ. Press, Cambridge, 14. print edition, 2010. ISBN 978-0-521-66396-0. Cited on p. 5.

[40] T. C. Lieuwen. *Unsteady Combustor Physics*. Cambridge University Press, New York, N.Y., USA, 2012. ISBN 978-1-107-01599-9. Cited on pp. 5 and 14.

[41] M. Rieutord. *Fluid Dynamics: An Introduction*. Graduate Texts in Physics. Springer International Publishing : Imprint: Springer, Cham, 1st ed. 2015 edition, 2015. ISBN 978-3-319-09351-2. DOI: 10.1007/978-3-319-09351-2. Cited on p. 5.

[42] T. Emmert. *State Space Modeling of Thermoacoustic Systems with Application to Intrinsic Feedback*. PhD thesis, TU München, München, Germany, 2016. Cited on pp. 6, 7, 32, and 33.

[43] F. Schaefer and W. Polifke. "Low-order network modeling of a duct with non-uniform cross-section and arbitrary mean temperature gradient in the presence of mean flow". In *AIAA Propulsion and Energy 2019 Forum*, Indianapolis, IN, USA, August 2019. American Institute of Aeronautics and Astronautics. ISBN 978-1-62410-590-6. DOI: 10.2514/6.2019-4376. Cited on p. 7.

[44] F. Engelhardt. *Adjoint-Based Analysis of Low-Order Thermoacoustic Networks*. PhD thesis, TU München, Munich, Germany, 2023. Cited on p. 7.

[45] W. Polifke. "Combustion Instabilities". In J. Anthoine and A. Hirschberg, editors, *Advances in Aeroacoustics and Applications*, VKI LS 2004-05. Von Karman Institute, Rhode-St-Genèse, BE, 2004. ISBN 2-930389-54-0. Cited on p. 8.

[46] B.-T. Chu. "On the generation of pressure waves at a plane flame front". *Symposium (International) on Combustion*, 4(1):603–612, January 1953. ISSN 00820784. DOI: 10.1016/S0082-0784(53)80081-0. Cited on p. 8.

[47] J. Kopitz and W. Polifke. "CFD-based application of the Nyquist criterion to thermoacoustic instabilities". *Journal of Computational Physics*, 227(14):6754–6778, July 2008. ISSN 00219991. DOI: 10.1016/j.jcp.2008.03.022. Cited on p. 8.

[48] S. Bomberg, T. Emmert, and W. Polifke. "Thermal Versus Acoustic Response of Velocity Sensitive Premixed Flames". *Proceedings of the Combustion Institute*, 35(3):3185–3192, 2015. ISSN 15407489. DOI: 10.1016/j.proci.2014.07.032. Cited on pp. 8 and 15.

[49] S. Ducruix, D. Durox, and S. Candel. "Theoretical and experimental determinations of the transfer function of a laminar premixed flame". *Proceedings of the Combustion Institute*, 28(1):765–773, January 2000. ISSN 1540-7489. DOI: 10.1016/S0082-0784(00)80279-9. Cited on p. 8.

[50] T. Schuller, D. Durox, and S. Candel. "A Unified Model for the Prediction of Laminar Flame Transfer Functions: Comparisons Between Conical and V-Flame Dynamics". *Combustion and Flame*, 134(1-2):21–34, July 2003. ISSN 00102180. DOI: 10.1016/S0010-2180(03)00042-7. Cited on p. 8.

[51] C. Hirsch, D. Fanaca, P. Reddy, W. Polifke, and T. Sattelmayer. “Influence of the Swirler Design on the Flame Transfer Function of Premixed Flames”. In *Volume 2: Turbo Expo 2005*, pages 151–160, Reno, NV, USA, January 2005. ASMEDC. ISBN 978-0-7918-4725-1 978-0-7918-3754-2. DOI: 10.1115/GT2005-68195. Cited on p. 8.

[52] A. Huber and W. Polifke. “Dynamics of Practical Premix Flames, Part II: Identification and Interpretation of CFD Data”. *International Journal of Spray and Combustion Dynamics*, 1(2):229–249, June 2009. ISSN 1756-8277, 1756-8285. DOI: 10.1260/175682709788707440. Cited on p. 8.

[53] A. Kaufmann, F. Nicoud, and T. Poinsot. “Flow Forcing Techniques for Numerical Simulation of Combustion Instabilities”. *Combustion and Flame*, 131(4):371–385, December 2002. ISSN 0010-2180. DOI: 10.1016/S0010-2180(02)00419-4. Cited on p. 9.

[54] A. Giauque, L. Selle, L. Gicquel, T. Poinsot, H. Buechner, P. Kaufmann, and W. Krebs. “System Identification of a Large-Scale Swirled Partially Premixed Combustor Using LES and Measurements”. *Journal of Turbulence*, 6:1–21, January 2005. DOI: 10.1080/14685240512331391985. Cited on p. 9.

[55] A. Giauque. *Fonctions de Transfert de Flamme et Energies Des Perturbations Dans Les Ecoulements Reactifs*. PhD thesis, L’Institut National Polytechnique de Toulouse, Toulouse, France, 2007. Cited on p. 9.

[56] L. Tay-Wo-Chong, S. Bomberg, A. Ulhaq, T. Komarek, and W. Polifke. “Comparative Validation Study on Identification of Premixed Flame Transfer Function”. *Journal of Engineering for Gas Turbines and Power*, 134(2):021502, February 2012. ISSN 0742-4795, 1528-8919. DOI: 10.1115/1.4004183. Cited on pp. 9 and 15.

[57] M. Merk, C. F. Silva, W. Polifke, R. Gaudron, M. Gatti, C. Mirat, and T. Schuller. “Direct Assessment of the Acoustic Scattering Matrix of a Turbulent Swirl Combustor by Combining System Identification, Large Eddy Simulation and Analytical Approaches”. *Journal of Engineering for Gas Turbines and Power*, 141(2):021035, February 2019. ISSN 0742-4795, 1528-8919. DOI: 10.1115/1.4040731. Cited on p. 9.

[58] L. Crocco. “Aspects of Combustion Stability in Liquid Propellant Rocket Motors Part1: Fundamentals. Low frequency instability with monopropellants”. *Journal of the American Rocket Society*, 21(6):163–178, November 1951. ISSN 1936-9964. DOI: 10.2514/8.4393. Cited on p. 9.

[59] W. Polifke. “Modeling and analysis of premixed flame dynamics by means of distributed time delays”. *Progress in Energy and Combustion Science*, 79:100845, July 2020. ISSN 03601285. DOI: 10.1016/j.pecs.2020.100845. Cited on pp. 9 and 34.

[60] R. F. Curtain and H. J. Zwart. *An Introduction to Infinite-Dimensional Linear Systems Theory*. Number 21 in Texts in Applied Mathematics. Springer-Verlag, New York, 1995. ISBN 978-0-387-94475-3. Cited on p. 10.

[61] P. Brokof, G. J. J. Fournier, and W. Polifke. “Linear time-continuous state-space realization of flame transfer functions by means of a propagation equation”. In *INTER-NOISE and NOISE-CON Congress and Conference Proceedings*, pages 3490–3501,

Glasgow, Scotland, February 2023. Institute of Noise Control Engineering. DOI: 10.3397/IN_2022_0496. Cited on pp. 10, 32, and 44.

[62] W. Polifke. “Six Lectures on Thermoacoustic Combustion Instability”. In *21st CISM-IUTAM Int’l Summer School on Measurement, Analysis and Passive Control of Thermoacoustic Oscillations*, Udine, Italy, 2015. DOI: 10.5281/zenodo.7932641. Cited on p. 10.

[63] P. L. Rijke. “Notiz über eine neue Art, die in einer an beiden Enden offenen Röhre enthaltene Luft in Schwingungen zu versetzen”. *Annalen der Physik*, 183(6):339–343, April 1859. ISSN 00033804, 15213889. DOI: 10.1002/andp.18591830616. Cited on p. 10.

[64] B.-T. Chu. “On the energy transfer to small disturbances in fluid flow (Part 1)”. *Acta Mechanica*, 1(3):215–234, September 1965. ISSN 0001-5970, 1619-6937. DOI: 10.1007/BF01387235. Cited on p. 13.

[65] F. Nicoud and T. Poinsot. “Thermoacoustic instabilities: Should the Rayleigh criterion be extended to include entropy changes?”. *Combustion and Flame*, 142(1-2):153–159, July 2005. ISSN 00102180. DOI: 10.1016/j.combustflame.2005.02.013. Cited on p. 13.

[66] B. T. Zinn and T. C. Lieuwen. “Combustion Instabilities: Basic Concepts”. In *Combustion Instabilities In Gas Turbine Engines: Operational Experience, Fundamental Mechanisms, and Modeling*, volume 210 of *Progress in Astronautics and Aeronautics*, pages 3–26. American Institute of Aeronautics and Astronautics, 2005. ISBN 3-642-13871-3. DOI: 10.2514/5.9781600866807.0003.0026. Cited on p. 13.

[67] B. Zinn. “Longitudinal mode acoustic losses in short nozzles”. *Journal of Sound and Vibration*, 22(1):93–105, May 1972. ISSN 0022460X. DOI: 10.1016/0022-460X(72)90847-4. Cited on p. 13.

[68] I. J. Hughes and A. P. Dowling. “The absorption of sound by perforated linings”. *Journal of Fluid Mechanics*, 218:299–335, September 1990. ISSN 0022-1120, 1469-7645. DOI: 10.1017/S002211209000101X. Cited on p. 13.

[69] C. Lahiri and F. Bake. “A review of bias flow liners for acoustic damping in gas turbine combustors”. *Journal of Sound and Vibration*, 400:564–605, July 2017. ISSN 0022-460X. DOI: 10.1016/j.jsv.2017.04.005. Cited on p. 13.

[70] V. Bellucci, P. Flohr, C. O. Paschereit, and F. Magni. “On the Use of Helmholtz Resonators for Damping Acoustic Pulsations in Industrial Gas Turbines”. *Journal of Engineering for Gas Turbines and Power*, 126(2):271–275, April 2004. ISSN 0742-4795, 1528-8919. DOI: 10.1115/1.1473152. Cited on p. 13.

[71] I. D. J. Dupere and A. P. Dowling. “The Absorption of Sound near Abrupt Axisymmetric Area Expansions”. *Journal of Sound and Vibration*, 239(4):709–730, 2001. ISSN 0022460X. DOI: 10.1006/jsvi.2000.3224. Cited on p. 13.

[72] G. Ghirardo, F. Boudy, and M. R. Bothien. “Amplitude statistics prediction in thermoacoustics”. *Journal of Fluid Mechanics*, 844:216–246, June 2018. ISSN 0022-1120, 1469-7645. DOI: 10.1017/jfm.2018.173. Cited on p. 14.

[73] P. M. Morse and H. Feshbach. *Methods of Theoretical Physics, Part I*. McGraw-Hill Book Company, 1953. ISBN 978-0-07-043316-8. Cited on p. 14.

[74] P. M. Morse and H. Feshbach. *Methods of Theoretical Physics, Part II*. McGraw-Hill Book Company, 1953. ISBN 978-0-07-043317-5. Cited on p. 14.

[75] F. E. C. Culick. "Combustion instabilities in liquid-fuelled propulsion systems - an overview". In *Combustion Instabilities in Liquid-Fuelled Propulsion Systems*, volume 450, Neuilly-Sur-Seine, France, 1988. AGARD / NATO. Cited on p. 14.

[76] T. Lieuwen. "Modeling Premixed Combustion - Acoustic Wave Interactions: A Review". *Journal of Propulsion Power*, 19(5):765–781, September 2003. ISSN 0748-4658, 1533-3876. DOI: 10.2514/2.6193. Cited on p. 14.

[77] S. Candel, D. Durox, T. Schuller, J. F. Bourgouin, and J. P. Moeck. "Dynamics of Swirling Flames". *Annual Review of Fluid Mechanics*, 46(1):147–173, 2014. ISSN 0066-4189, 1545-4479. DOI: 10.1146/annurev-fluid-010313-141300. Cited on p. 14.

[78] A. P. Dowling and Y. Mahmoudi. "Combustion Noise". *Proceedings of the Combustion Institute*, 35(1):65–100, 2015. ISSN 15407489. DOI: 10.1016/j.proci.2014.08.016. Cited on p. 14.

[79] A. S. Morgans and I. Duran. "Entropy Noise: A Review of Theory, Progress and Challenges". *International Journal of Spray and Combustion Dynamics*, 8(4):285–298, December 2016. ISSN 1756-8277, 1756-8285. DOI: 10.1177/1756827716651791. Cited on p. 14.

[80] G. Ghirardo, M. P. Juniper, and M. R. Bothien. "The effect of the flame phase on thermoacoustic instabilities". *Combustion and Flame*, 187:165–184, January 2018. ISSN 00102180. DOI: 10.1016/j.combustflame.2017.09.007. Cited on p. 14.

[81] F. Gant. *Thermoacoustics of Advanced Reheat Combustion Systems*. PhD thesis, ETH Zurich, Zürich, Switzerland, 2021. Cited on pp. 14 and 35.

[82] I. C. Waugh and M. P. Juniper. "Triggering in a thermoacoustic system with stochastic noise". *International Journal of Spray and Combustion Dynamics*, 3(3):225–242, September 2011. ISSN 1756-8277, 1756-8285. DOI: 10.1260/1756-8277.3.3.225. Cited on p. 14.

[83] N. Noiray and B. Schuermans. "Deterministic quantities characterizing noise driven Hopf bifurcations in gas turbine combustors". *International Journal of Non-Linear Mechanics*, 50:152–163, April 2013. ISSN 00207462. DOI: 10.1016/j.ijnonlinmec.2012.11.008. Cited on p. 14.

[84] P. Subramanian, R. I. Sujith, and P. Wahi. "Subcritical bifurcation and bistability in thermoacoustic systems". *Journal of Fluid Mechanics*, 715:210–238, January 2013. ISSN 0022-1120, 1469-7645. DOI: 10.1017/jfm.2012.514. Cited on p. 14.

[85] V. S. Acharya, M. R. Bothien, and T. C. Lieuwen. "Non-linear dynamics of thermoacoustic eigen-mode interactions". *Combustion and Flame*, 194:309–321, August 2018. ISSN 00102180. DOI: 10.1016/j.combustflame.2018.04.021. Cited on p. 14.

[86] M. Lee, Y. Guan, V. Gupta, and L. K. B. Li. “Input-output system identification of a thermoacoustic oscillator near a Hopf bifurcation using only fixed-point data”. *Physical Review E*, 101(1):013102, January 2020. ISSN 2470-0045, 2470-0053. DOI: 10.1103/PhysRevE.101.013102. Cited on p. 14.

[87] A. P. Dowling and S. R. Stow. “Acoustic Analysis of Gas Turbine Combustors”. *Journal of Propulsion and Power*, 19(5):751–764, September 2003. ISSN 0748-4658. DOI: 10.2514/2.6192. Cited on pp. 14 and 35.

[88] A. Gentemann and W. Polifke. “Scattering and generation of acoustic energy by a premix swirl burner”. In *Volume 2: Turbo Expo 2007*, pages 125–133, Montreal, Canada, January 2007. ASMEDC. ISBN 978-0-7918-4791-6. DOI: 10.1115/GT2007-27238. Cited on p. 14.

[89] W. Polifke. “Thermo-Acoustic Instability Potentiality of a Premix Burner”. In *European Combustion Meeting, ECM2011*, Cardiff, UK, June 2011. British Section of the Combustion Institute. Cited on p. 14.

[90] J. Eckstein, E. Freitag, C. Hirsch, and T. Sattelmayer. “Experimental Study on the Role of Entropy Waves in Low-Frequency Oscillations in a RQL Combustor”. *Journal of Engineering for Gas Turbines and Power*, 128(2):264–270, April 2006. ISSN 0742-4795, 1528-8919. DOI: 10.1115/1.2132379. Cited on p. 14.

[91] J. Eckstein and T. Sattelmayer. “Low-order modeling of low-frequency combustion instabilities in aeroengines”. *Journal of Propulsion and Power*, 22(2):425–432, 2006. Cited on p. 15.

[92] F. Weyermann. *Numerische Berechnung Der Emission Verbrennungsinduzierten Lärms Automobiler Zusatzheizungen*. PhD thesis, TU München, Munich, Germany, May 2010. Cited on p. 15.

[93] M. Hoeijmakers, I. Lopez Arteaga, V. Kornilov, H. Nijmeijer, and P. de Goey. “Experimental Investigation of Intrinsic Flame Stability”. In *European Combustion Meeting, ECM2013*, Lund, Sweden, June 2013. Scandinavian-Nordic Section of the Combustion Institute. Cited on p. 15.

[94] M. Hoeijmakers, V. Kornilov, I. Lopez Arteaga, P. de Goey, and H. Nijmeijer. “Intrinsic Instability of Flame-Acoustic Coupling”. *Combustion and Flame*, 161(11):2860–2867, November 2014. DOI: 10.1016/j.combustflame.2014.05.009. Cited on p. 15.

[95] W. C. Strahle. “On combustion generated noise”. *Journal of Fluid Mechanics*, 49(2):399–414, September 1971. ISSN 0022-1120, 1469-7645. DOI: 10.1017/S0022112071002167. Cited on p. 15.

[96] M. Hoeijmakers. *Flame-Acoustic Coupling in Combustion Instabilities*. PhD thesis, TU Eindhoven, Eindhoven, Netherlands, 2014. Cited on p. 16.

[97] C. F. Silva, T. Emmert, S. Jaensch, and W. Polifke. “Numerical Study on Intrinsic Thermoacoustic Instability of a Laminar Premixed Flame”. *Combustion and Flame*, 162(9):3370–3378, September 2015. ISSN 00102180. DOI: 10.1016/j.combustflame.2015.06.003. Cited on pp. 16 and 34.

[98] E. Courtine, L. Selle, and T. Poinsot. “DNS of Intrinsic Thermoacoustic Modes in Laminar Premixed Flames”. *Combustion and Flame*, 162(11):4331–4341, November 2015. ISSN 00102180. DOI: 10.1016/j.combustflame.2015.07.002. Cited on p. 16.

[99] C. F. Silva. “Intrinsic thermoacoustic instabilities”. *Progress in Energy and Combustion Science*, 95:101065, March 2023. ISSN 03601285. DOI: 10.1016/j.pecs.2022.101065. Cited on pp. 16 and 34.

[100] L. Xu, J. Zheng, G. Wang, Z. Feng, X. Tian, L. Li, and F. Qi. “Investigation on the intrinsic thermoacoustic instability of a lean-premixed swirl combustor with an acoustic liner”. *Proceedings of the Combustion Institute*, 38(4):6095–6103, 2021. ISSN 15407489. DOI: 10.1016/j.proci.2020.06.155. Cited on pp. 17, 33, and 34.

[101] K. J. Yong, C. F. Silva, G. J. J. Fournier, and W. Polifke. “Categorization of thermoacoustic modes in an ideal resonator with phasor diagrams”. *Combustion and Flame*, 249: 112605, March 2023. ISSN 00102180. DOI: 10.1016/j.combustflame.2022.112605. Cited on pp. 17, 34, and 45.

[102] G. Floquet. “Sur les équations différentielles linéaires à coefficients périodiques”. *Annales scientifiques de l’École Normale Supérieure*, 12:47–88, 1883. ISSN 0012-9593, 1873-2151. DOI: 10.24033/asens.220. Cited on p. 19.

[103] F. Bloch. “Über die Quantenmechanik der Elektronen in Kristallgittern”. *Zeitschrift für Physik*, 52(7-8):555–600, July 1929. ISSN 1434-6001, 1434-601X. DOI: 10.1007/BF01339455. Cited on p. 19.

[104] G. A. Mensah, G. Campa, and J. P. Moeck. “Efficient Computation of Thermoacoustic Modes in Industrial Annular Combustion Chambers Based on Bloch-Wave Theory”. *Journal of Engineering for Gas Turbines and Power*, 138(8):081502, August 2016. ISSN 0742-4795, 1528-8919. DOI: 10.1115/1.4032335. Cited on pp. 19 and 36.

[105] T. Schuller, D. Durox, P. Palies, and S. Candel. “Acoustic decoupling of longitudinal modes in generic combustion systems”. *Combustion and Flame*, 159(5):1921–1931, May 2012. ISSN 0010-2180. DOI: 10.1016/j.combustflame.2012.01.010. Cited on p. 20.

[106] T. Poinsot and D. Veynante. *Theoretical and Numerical Combustion*. CNRS, Paris, 3 edition, 2012. ISBN 978-2-7466-3990-4. Cited on p. 20.

[107] G. J. J. Fournier, M. Haeringer, C. F. Silva, and W. Polifke. “Low-Order Modeling to Investigate Clusters of Intrinsic Thermoacoustic Modes in Annular Combustors”. *Journal of Engineering for Gas Turbines and Power*, 143(4):041025, April 2021. ISSN 0742-4795, 1528-8919. DOI: 10.1115/1.4049356. Cited on pp. 21, 27, 34, 35, 36, and 46.

[108] G. J. J. Fournier, M. Meindl, C. F. Silva, G. Ghirardo, M. R. Bothien, and W. Polifke. “Low-Order Modeling of Can-Annular Combustors”. *Journal of Engineering for Gas Turbines and Power*, 143(12):121004, December 2021. ISSN 0742-4795, 1528-8919. DOI: 10.1115/1.4051954. Cited on pp. 21, 22, and 48.

[109] C. Pierre and P. D. Cha. “Strong mode localization in nearly periodic disordered structures”. *AIAA Journal*, 27(2):227–241, February 1989. ISSN 0001-1452, 1533-385X. DOI: 10.2514/3.10085. Cited on pp. 25 and 42.

[110] N. Hosseini, V. Kornilov, I. Lopez Arteaga, W. Polifke, O. Teerling, and L. de Goey. “Intrinsic thermoacoustic modes and their interplay with acoustic modes in a Rijke burner”. *International Journal of Spray and Combustion Dynamics*, 10(4):315–325, December 2018. ISSN 1756-8277, 1756-8285. DOI: 10.1177/1756827718782884. Cited on pp. 27, 33, and 34.

[111] C. Silva, K. J. Yong, and L. Magri. “Thermoacoustic Modes of Quasi-One-Dimensional Combustors in the Region of Marginal Stability”. *Journal of Engineering for Gas Turbines and Power*, 141(2):021022, February 2019. ISSN 0742-4795, 1528-8919. DOI: 10.1115/1.4041118. Cited on pp. 27 and 28.

[112] C. F. Silva and W. Polifke. “Non-dimensional groups for similarity analysis of thermoacoustic instabilities”. *Proceedings of the Combustion Institute*, 37(4):5289–5297, 2019. ISSN 15407489. DOI: 10.1016/j.proci.2018.06.144. Cited on pp. 27 and 28.

[113] N. K. Mukherjee and V. Shrira. “Intrinsic Flame Instabilities in Combustors: Analytic Description of a 1-D Resonator Model”. *Combustion and Flame*, 185:188–209, November 2017. ISSN 00102180. DOI: 10.1016/j.combustflame.2017.07.012. Cited on pp. 27 and 34.

[114] A. Orchini, C. F. Silva, G. A. Mensah, and J. P. Moeck. “Thermoacoustic modes of intrinsic and acoustic origin and their interplay with exceptional points”. *Combustion and Flame*, 211:83–95, January 2020. ISSN 00102180. DOI: 10.1016/j.combustflame.2019.09.018. Cited on pp. 27, 28, 34, 36, and 37.

[115] G. A. Mensah, L. Magri, C. F. Silva, P. E. Buschmann, and J. P. Moeck. “Exceptional points in the thermoacoustic spectrum”. *Journal of Sound and Vibration*, 433:124–128, October 2018. ISSN 0022-460X. DOI: 10.1016/j.jsv.2018.06.069. Cited on p. 28.

[116] F. M. Sogaro, P. J. Schmid, and A. S. Morgans. “Thermoacoustic interplay between intrinsic thermoacoustic and acoustic modes: Non-normality and high sensitivities”. *Journal of Fluid Mechanics*, 878:190–220, November 2019. ISSN 0022-1120, 1469-7645. DOI: 10.1017/jfm.2019.632. Cited on pp. 28 and 34.

[117] G. J. J. Fournier, F. Schaefer, M. Haeringer, C. F. Silva, and W. Polifke. “Interplay of Clusters of Acoustic and Intrinsic Thermoacoustic Modes in Can-Annular Combustors”. *Journal of Engineering for Gas Turbines and Power*, 144(12):121015, December 2022. ISSN 0742-4795, 1528-8919. DOI: 10.1115/1.4055381. Cited on pp. 29 and 49.

[118] P. E. Buschmann, G. A. Mensah, F. Nicoud, and J. P. Moeck. “Solution of Thermoacoustic Eigenvalue Problems With a Noniterative Method”. *Journal of Engineering for Gas Turbines and Power*, 142(3):031022, March 2020. ISSN 0742-4795. DOI: 10.1115/1.4045076. Cited on pp. 31, 32, and 36.

[119] G. A. Mensah, P. E. Buschmann, and A. Orchini. “Iterative solvers for the thermoacoustic nonlinear eigenvalue problem and their convergence properties”. *International Journal of Spray and Combustion Dynamics*, 14(1-2):30–41, 2022. ISSN 1756-8277, 1756-8285. DOI: 10.1177/17568277221084464. Cited on pp. 31 and 32.

[120] V. Mehrmann and H. Voss. “Nonlinear eigenvalue problems: A challenge for modern eigenvalue methods: Nonlinear eigenvalue problems: A challenge for modern eigenvalue methods”. *GAMM-Mitteilungen*, 27(2):121–152, December 2004. ISSN 09367195. DOI: 10.1002/gamm.201490007. Cited on p. 31.

[121] P. C. Effenberger. *Robust Solution Methods for Nonlinear Eigenvalue Problems*. PhD thesis, EPFL, Lausanne, Switzerland, 2013. Cited on p. 31.

[122] S. Güttel and F. Tisseur. “The nonlinear eigenvalue problem”. *Acta Numerica*, 26:1–94, May 2017. ISSN 0962-4929, 1474-0508. DOI: 10.1017/S0962492917000034. Cited on p. 31.

[123] P. G. Ciarlet. *Linear and Nonlinear Functional Analysis with Applications: With 401 Problems and 52 Figures*. Number 130 in Applied Mathematics. Society for Industrial and Applied Mathematics, Philadelphia, 2013. ISBN 978-1-61197-258-0. Cited on p. 31.

[124] A. S. Householder. *The Numerical Treatment of a Single Nonlinear Equation*. McGraw-Hill, London, 1970. ISBN 978-0-07-030465-9. Cited on p. 32.

[125] W.-J. Beyn. “An integral method for solving nonlinear eigenvalue problems”. *Linear Algebra and its Applications*, 436(10):3839–3863, May 2012. ISSN 00243795. DOI: 10.1016/j.laa.2011.03.030. Cited on p. 32.

[126] M. Merk, P. E. Buschmann, J. P. Moeck, and W. Polifke. “The Nonlinear Thermoacoustic Eigenvalue Problem and Its Rational Approximations: Assessment of Solution Strategies”. *Journal of Engineering for Gas Turbines and Power*, 145(2):021028, February 2023. ISSN 0742-4795, 1528-8919. DOI: 10.1115/1.4055583. Cited on pp. 32 and 36.

[127] R. Lehoucq, D. Sorensen, and C. Yang. *ARPACK Users’ Guide*. Software, Environments and Tools. Society for Industrial and Applied Mathematics, January 1998. ISBN 978-0-89871-407-4. Cited on p. 32.

[128] Y. Saad. *Numerical Methods for Large Eigenvalue Problems*. Number 66 in Classics in Applied Mathematics. Society for Industrial and Applied Mathematics, Philadelphia, rev. ed edition, 2011. ISBN 978-1-61197-072-2. Cited on p. 32.

[129] T. Emmert, M. Meindl, S. Jaensch, and W. Polifke. “Linear State Space Interconnect Modeling of Acoustic Systems”. *Acta Acustica united with Acustica*, 102(5):824–833, September 2016. ISSN 16101928. DOI: 10.3813/AAA.918997. Cited on p. 32.

[130] B. Schuermans, V. Bellucci, and C. O. Paschereit. “Thermoacoustic Modeling and Control of Multi-Burner Combustion Systems”. In *Volume 2: Turbo Expo 2003*, pages 509–519, Atlanta, GA, USA, 2003. ASMEDC. ISBN 978-0-7918-3685-9 978-0-7918-3671-2. DOI: 10.1115/GT2003-38688. Cited on pp. 32, 35, and 42.

[131] M. Bothien, J. P. Moeck, A. Lacarelle, and C. O. Paschereit. “Time Domain Modelling and Stability Analysis of Complex Thermoacoustic Systems”. *Proceedings of the Institution of Mechanical Engineers, Part A: Journal of Power and Energy*, 221(5):657–668, January 2007. ISSN 0957-6509, 2041-2967. DOI: 10.1243/09576509JPE384. Cited on p. 32.

[132] S. Jaensch, C. Sovardi, and W. Polifke. “On the Robust, Flexible and Consistent Implementation of Time Domain Impedance Boundary Conditions for Compressible Flow Simulations”. *Journal of Computational Physics*, 314:145–159, June 2016. ISSN 00219991. DOI: 10.1016/j.jcp.2016.03.010. Cited on p. 32.

[133] Q. Douasbin, C. Scalo, L. Selle, and T. Poinsot. “Delayed-time domain impedance boundary conditions (D-TDIBC)”. *Journal of Computational Physics*, 371:50–66, October 2018. ISSN 00219991. DOI: 10.1016/j.jcp.2018.05.003. Cited on p. 32.

[134] F. Schily, T. Komarek, and W. Polifke. “A criterion for thermo-acoustic stability based on the flux of acoustic energy”. *Combustion and Flame*, 227:238–254, May 2021. ISSN 00102180. DOI: 10.1016/j.combustflame.2021.01.014. Cited on p. 32.

[135] T. Emmert, S. Jaensch, C. Sovardi, and W. Polifke. “taX - a Flexible Tool for Low-Order Duct Acoustic Simulation in Time and Frequency Domain”. In *7th Forum Acusticum*, Krakow, September 2014. DEGA. Cited on p. 32.

[136] B. Gustavsen and A. Semlyen. “Rational approximation of frequency domain responses by vector fitting.”. *IEEE Transactions on Power Delivery*, 14(3):1052–1061, July 1999. ISSN 0885-8977. DOI: 10.1109/61.772353. Cited on p. 32.

[137] C. F. Silva, M. Merk, T. Komarek, and W. Polifke. “The Contribution of Intrinsic Thermoacoustic Feedback to Combustion Noise and Resonances of a Confined Turbulent Premixed Flame”. *Combustion and Flame*, 182:269–278, August 2017. ISSN 00102180. DOI: 10.1016/j.combustflame.2017.04.015. Cited on pp. 33 and 34.

[138] A. Ghani and W. Polifke. “An exceptional point switches stability of a thermoacoustic experiment”. *Journal of Fluid Mechanics*, 920:R3, August 2021. ISSN 0022-1120, 1469-7645. DOI: 10.1017/jfm.2021.480. Cited on p. 33.

[139] M. Murugesan, B. Singaravelu, A. K. Kushwaha, and S. Mariappan. “Onset of flame-intrinsic thermoacoustic instabilities in partially premixed turbulent combustors”. *International Journal of Spray and Combustion Dynamics*, 10(3):171–184, 2018. ISSN 1756-8277, 1756-8285. DOI: 10.1177/1756827718758511. Cited on p. 34.

[140] A. Albayrak, T. Steinbacher, T. Komarek, and W. Polifke. “Convective Scaling of Intrinsic Thermo-Acoustic Eigenfrequencies of a Premixed Swirl Combustor”. *Journal of Engineering for Gas Turbines and Power*, 140(4):041510, April 2018. ISSN 0742-4795, 1528-8919. DOI: 10.1115/1.4038083. Cited on p. 34.

[141] N. K. Mukherjee and V. Shrira. “Coupling of Acoustic and Intrinsic Modes in 1D Combustor Models”. *Combustion Science and Technology*, 193(6):889–910, 2021. ISSN 0010-2202, 1563-521X. DOI: 10.1080/00102202.2019.1678593. Cited on p. 34.

[142] K. J. Yong, C. F. Silva, and W. Polifke. “A categorization of marginally stable thermoacoustic modes based on phasor diagrams”. *Combustion and Flame*, 228:236–249, June 2021. ISSN 0010-2180. DOI: 10.1016/j.combustflame.2021.01.003. Cited on p. 34.

[143] A. Katoch, T. F. Guiberti, D. V. de Campos, and D. A. Lacoste. “Dual-fuel, dual-swirl burner for the mitigation of thermoacoustic instabilities in turbulent ammonia-hydrogen flames”. *Combustion and Flame*, 246:112392, December 2022. ISSN 00102180. DOI: 10.1016/j.combustflame.2022.112392. Cited on p. 34.

[144] W. Krebs, G. Walz, and S. Hoffmann. “Thermoacoustic Analysis of Annular Combustor”. In *5th AIAA/CEAS Aeroacoustics Conference and Exhibit*, Bellevue, WA, USA, May 1999. American Institute of Aeronautics and Astronautics. DOI: 10.2514/6.1999-1971. Cited on p. 34.

[145] W. Krebs, P. Flohr, B. Prade, and S. Hoffmann. “Thermoacoustic stability chart for high intensity gas turbine combustion systems”. *Combustion Science and Technology*, 174(7):99–128, July 2002. ISSN 0010-2202, 1563-521X. DOI: 10.1080/00102200208984089. Cited on pp. 34 and 35.

[146] K. R. McManus, T. Poinsot, and S. M. Candel. “A Review of Active Control of Combustion Instabilities”. *Progress in Energy and Combustion Science*, 19(1):1–29, 1993. ISSN 03601285. DOI: 10.1016/0360-1285(93)90020-F. Cited on p. 34.

[147] J. R. Seume, N. Vortmeyer, W. Krause, J. Hermann, C. Hantschk, P. Zangl, S. Gleis, D. Vortmeyer, and A. Orthmann. “Application of Active Combustion Instability Control to a Heavy Duty Gas Turbine”. *Journal of Engineering for Gas Turbines and Power*, 120(4):721–726, October 1998. ISSN 0742-4795, 1528-8919. DOI: 10.1115/1.2818459. Cited on p. 34.

[148] T. Poinsot. “Prediction and control of combustion instabilities in real engines”. *Proceedings of the Combustion Institute*, 36(1):1–28, 2017. ISSN 15407489. DOI: 10.1016/j.proci.2016.05.007. Cited on p. 35.

[149] N. A. Worth and J. R. Dawson. “Self-excited circumferential instabilities in a model annular gas turbine combustor: Global flame dynamics”. *Proceedings of the Combustion Institute*, 34(2):3127–3134, 2013. ISSN 15407489. DOI: 10.1016/j.proci.2012.05.061. Cited on p. 35.

[150] N. A. Worth and J. R. Dawson. “Modal dynamics of self-excited azimuthal instabilities in an annular combustion chamber”. *Combustion and Flame*, 160(11):2476–2489, November 2013. ISSN 00102180. DOI: 10.1016/j.combustflame.2013.04.031. Cited on p. 35.

[151] M. Mazur, Y. H. Kwah, T. Indlekofer, J. R. Dawson, and N. A. Worth. “Self-excited longitudinal and azimuthal modes in a pressurised annular combustor”. *Proceedings of the Combustion Institute*, 38(4):5997–6004, 2021. ISSN 15407489. DOI: 10.1016/j.proci.2020.05.033. Cited on p. 35.

[152] J.-F. Bourgouin, D. Durox, J. P. Moeck, T. Schuller, and S. Candel. "Self-Sustained Instabilities in an Annular Combustor Coupled by Azimuthal and Longitudinal Acoustic Modes". In *Volume 1B: Combustion, Fuels and Emissions*, page V01BT04A007, San Antonio, TX, USA, June 2013. American Society of Mechanical Engineers. ISBN 978-0-7918-5511-9. DOI: 10.1115/GT2013-95010. Cited on p. 35.

[153] K. Prieur, D. Durox, T. Schuller, and S. Candel. "Strong Azimuthal Combustion Instabilities in a Spray Annular Chamber With Intermittent Partial Blow-Off". *Journal of Engineering for Gas Turbines and Power*, 140(3):031503, March 2018. ISSN 0742-4795, 1528-8919. DOI: 10.1115/1.4037824. Cited on p. 35.

[154] G. Vignat, D. Durox, T. Schuller, and S. Candel. "Combustion Dynamics of Annular Systems". *Combustion Science and Technology*, 192(7):1358–1388, July 2020. ISSN 0010-2202, 1563-521X. DOI: 10.1080/00102202.2020.1734583. Cited on p. 35.

[155] A. Roy, S. Singh, A. Nair, S. Chaudhuri, and R. Sujith. "Flame dynamics during intermittency and secondary bifurcation to longitudinal thermoacoustic instability in a swirl-stabilized annular combustor". *Proceedings of the Combustion Institute*, 38(4):6221–6230, 2021. ISSN 15407489. DOI: 10.1016/j.proci.2020.08.053. Cited on p. 35.

[156] S. C. Humbert, F. Gensini, A. Andreini, C. O. Paschereit, and A. Orchini. "Nonlinear analysis of self-sustained oscillations in an annular combustor model with electroacoustic feedback". *Proceedings of the Combustion Institute*, 38(4):6085–6093, 2021. ISSN 15407489. DOI: 10.1016/j.proci.2020.06.154. Cited on p. 35.

[157] S. C. Humbert, J. P. Moeck, A. Orchini, and C. O. Paschereit. "Effect of an Azimuthal Mean Flow on the Structure and Stability of Thermoacoustic Modes in an Annular Combustor Model With Electroacoustic Feedback". *Journal of Engineering for Gas Turbines and Power*, 143(6):061026, June 2021. ISSN 0742-4795, 1528-8919. DOI: 10.1115/1.4048693. Cited on pp. 35 and 42.

[158] G. Ghirardo and F. Gant. "Averaging of thermoacoustic azimuthal instabilities". *Journal of Sound and Vibration*, 490:115732, January 2021. ISSN 0022460X. DOI: 10.1016/j.jsv.2020.115732. Cited on p. 35.

[159] A. Morgans and S. Stow. "Model-based control of combustion instabilities in annular combustors". *Combustion and Flame*, 150(4):380–399, September 2007. ISSN 00102180. DOI: 10.1016/j.combustflame.2007.06.002. Cited on pp. 35 and 42.

[160] J.-F. Parmentier, P. Salas, P. Wolf, G. Staffelbach, F. Nicoud, and T. Poinsot. "A simple analytical model to study and control azimuthal instabilities in annular combustion chambers". *Combustion and Flame*, 159(7):2374–2387, July 2012. ISSN 0010-2180. DOI: 10.1016/j.combustflame.2012.02.007. Cited on pp. 35 and 42.

[161] M. R. Bothien, N. Noiray, and B. Schuermans. "Analysis of Azimuthal Thermo-acoustic Modes in Annular Gas Turbine Combustion Chambers". *Journal of Engineering for Gas Turbines and Power*, 137(6):061505, June 2015. ISSN 0742-4795, 1528-8919. DOI: 10.1115/1.4028718. Cited on pp. 35 and 42.

[162] M. Bauerheim, P. Salas, F. Nicoud, and T. Poinsot. “Symmetry breaking of azimuthal thermo-acoustic modes in annular cavities: A theoretical study”. *Journal of Fluid Mechanics*, 760:431–465, December 2014. ISSN 1469-7645. DOI: 10.1017/jfm.2014.578. Cited on pp. 35 and 42.

[163] M. Bauerheim, A. Ndiaye, P. Constantine, S. Moreau, and F. Nicoud. “Symmetry breaking of azimuthal thermoacoustic modes: The UQ perspective”. *Journal of Fluid Mechanics*, 789:534–566, February 2016. ISSN 0022-1120, 1469-7645. DOI: 10.1017/jfm.2015.730. Cited on pp. 35 and 42.

[164] A. Faure-Beaulieu and N. Noiray. “Symmetry breaking of azimuthal waves: Slow-flow dynamics on the Bloch sphere”. *Physical Review Fluids*, 5(2):023201, February 2020. ISSN 2469-990X. DOI: 10.1103/PhysRevFluids.5.023201. Cited on pp. 35 and 42.

[165] J. F. Bourgouin, D. Durox, J. P. Moeck, T. Schuller, and S. Candel. “A new pattern of instability observed in an annular combustor: The slanted mode”. *Proceedings of the Combustion Institute*, 35(3):3237–3244, 2015. ISSN 1540-7489. DOI: 10.1016/j.proci.2014.06.029. Cited on pp. 35 and 36.

[166] J. P. Moeck, D. Durox, T. Schuller, and S. Candel. “Nonlinear thermoacoustic mode synchronization in annular combustors”. *Proceedings of the Combustion Institute*, 37(4): 5343–5350, 2019. ISSN 15407489. DOI: 10.1016/j.proci.2018.05.107. Cited on p. 35.

[167] N. Purwar, M. Haeringer, B. Schuermans, and W. Polifke. “Flame response to transverse velocity excitation leading to frequency doubling and modal coupling”. *Combustion and Flame*, 230:111412, August 2021. ISSN 00102180. DOI: 10.1016/j.combustflame.2021.111412. Cited on p. 35.

[168] J. O’Connor, V. Acharya, and T. Lieuwen. “Transverse combustion instabilities: Acoustic, fluid mechanic, and flame processes”. *Progress in Energy and Combustion Science*, 49:1–39, August 2015. ISSN 03601285. DOI: 10.1016/j.pecs.2015.01.001. Cited on p. 35.

[169] S. Evesque and W. Polifke. “Low-Order Acoustic Modelling for Annular Combustors: Validation and Inclusion of Modal Coupling”. In *ASME Turbo Expo 2002: Power for Land, Sea, and Air*, volume Volume 1: Turbo Expo 2002, pages 321–331, Amsterdam, The Netherlands, June 2002. ASMEDC. ISBN 978-0-7918-3606-4. DOI: 10.1115/GT2002-30064. Cited on pp. 35 and 36.

[170] J. Kopitz, A. Huber, T. Sattelmayer, and W. Polifke. “Thermoacoustic Stability Analysis of an Annular Combustion Chamber With Acoustic Low Order Modeling and Validation Against Experiment”. In *ASME Turbo Expo 2005: Power for Land, Sea, and Air*, pages 583–593, Reno, Nevada, USA, June 2005. ASMEDC. ISBN 978-0-7918-4725-1 978-0-7918-3754-2. DOI: 10.1115/GT2005-68797. Cited on pp. 35 and 36.

[171] V. Acharya, Shreekrishna, D.-H. Shin, and T. Lieuwen. “Swirl effects on harmonically excited, premixed flame kinematics”. *Combustion and Flame*, 159(3):1139–1150, March 2012. ISSN 0010-2180. DOI: 10.1016/j.combustflame.2011.09.015. Cited on p. 35.

[172] A. Saurabh, R. Steinert, J. P. Moeck, and C. O. Paschereit. “Swirl Flame Response to Traveling Acoustic Waves”. In *Volume 4B: Combustion, Fuels and Emissions*, page V04BT04A043, Düsseldorf, Germany, June 2014. American Society of Mechanical Engineers. ISBN 978-0-7918-4569-1. DOI: 10.1115/GT2014-26829. Cited on p. 35.

[173] G. Ghirardo, M. P. Juniper, and J. P. Moeck. “Weakly nonlinear analysis of thermoacoustic instabilities in annular combustors”. *Journal of Fluid Mechanics*, 805:52–87, October 2016. ISSN 0022-1120, 1469-7645. DOI: 10.1017/jfm.2016.494. Cited on p. 35.

[174] N. Noiray, M. Bothien, and B. Schuermans. “Investigation of azimuthal staging concepts in annular gas turbines”. *Combustion Theory and Modelling*, 15(5):585–606, October 2011. ISSN 1364-7830, 1741-3559. DOI: 10.1080/13647830.2011.552636. Cited on p. 35.

[175] M. Bauerheim, J.-F. Parmentier, P. Salas, F. Nicoud, and T. Poinsot. “An analytical model for azimuthal thermoacoustic modes in an annular chamber fed by an annular plenum”. *Combustion and Flame*, 161(5):1374–1389, May 2014. ISSN 0010-2180. DOI: 10.1016/j.combustflame.2013.11.014. Cited on pp. 35, 36, and 37.

[176] G. Ghirardo and M. P. Juniper. “Azimuthal instabilities in annular combustors: Standing and spinning modes”. *Proceedings of the Royal Society A: Mathematical, Physical and Engineering Science*, 469(2157):20130232, September 2013. ISSN 1364-5021, 1471-2946. DOI: 10.1098/rspa.2013.0232. Cited on p. 35.

[177] D. Yang, D. Laera, and A. S. Morgans. “A systematic study of nonlinear coupling of thermoacoustic modes in annular combustors”. *Journal of Sound and Vibration*, 456: 137–161, September 2019. ISSN 0022-460X. DOI: 10.1016/j.jsv.2019.04.025. Cited on p. 36.

[178] S. Bethke, W. Krebs, P. Flohr, and B. Prade. “Thermoacoustic Properties of Can Annular Combustors”. In *8th AIAA/CEAS Aeroacoustics Conference & Exhibit*, Breckenridge, CO, USA, June 2002. American Institute of Aeronautics and Astronautics. ISBN 978-1-62410-119-9. DOI: 10.2514/6.2002-2570. Cited on p. 37.

[179] P. Kaufmann, W. Krebs, R. Valdes, and U. Wever. “3D Thermoacoustic Properties of Single Can and Multi Can Combustor Configurations”. In *Volume 3: Combustion, Fuels and Emissions, Parts A and B*, pages 527–538, Berlin, Germany, January 2008. ASMEDC. ISBN 978-0-7918-4313-0 978-0-7918-3824-2. DOI: 10.1115/GT2008-50755. Cited on p. 37.

[180] L. Panek, F. Farisco, and M. Huth. “Thermo-Acoustic Characterization of Can-Can Interaction of a Can-Annular Combustion System Based on Unsteady CFD LES Simulation”. In *Proceedings of the 1st Global Power and Propulsion Forum*, pages GPPF–2017–81, Zurich, Switzerland, January 2017. GPPS. Cited on p. 37.

[181] F. Farisco, L. Panek, and J. B. Kok. “Thermo-acoustic cross-talk between cans in a can-annular combustor”. *International Journal of Spray and Combustion Dynamics*, 9(4):452–469, December 2017. ISSN 1756-8277, 1756-8285. DOI: 10.1177/1756827717716373. Cited on p. 37.

[182] J. von Saldern, A. Orchini, and J. Moeck. “Analysis of Thermoacoustic Modes in Can-Annular Combustors Using Effective Bloch-Type Boundary Conditions”. *Journal of Engineering for Gas Turbines and Power*, 143(7):071019, July 2021. ISSN 0742-4795, 1528-8919. DOI: 10.1115/1.4049162. Cited on pp. 37 and 38.

[183] M. S. Howe. *Acoustics of Fluid-Structure Interactions*. Cambridge University Press, 1 edition, August 1998. ISBN 978-0-521-63320-8 978-0-521-05428-7 978-0-511-66289-8. DOI: 10.1017/CBO9780511662898. Cited on p. 37.

[184] J. G. R. von Saldern, J. P. Moeck, and A. Orchini. “Nonlinear interaction between clustered unstable thermoacoustic modes in can-annular combustors”. *Proceedings of the Combustion Institute*, 38(4):6145–6153, 2021. ISSN 15407489. DOI: 10.1016/j.proci.2020.06.236. Cited on p. 37.

[185] M. Yoon. “Thermoacoustics and combustion instability analysis for multi-burner combustors”. *Journal of Sound and Vibration*, 492:115774, February 2021. ISSN 0022460X. DOI: 10.1016/j.jsv.2020.115774. Cited on p. 38.

[186] J. G. R. von Saldern, A. Orchini, and J. P. Moeck. “A Non-Compact Effective Impedance Model for Can-to-Can Acoustic Communication: Analysis and Optimization of Damping Mechanisms”. *Journal of Engineering for Gas Turbines and Power*, 143(12):121024, December 2021. ISSN 0742-4795, 1528-8919. DOI: 10.1115/1.4052077. Cited on p. 38.

[187] T. Pedergnana and N. Noiray. “Coupling-induced instability in a ring of thermoacoustic oscillators”. *Proceedings of the Royal Society A: Mathematical, Physical and Engineering Sciences*, 478(2259):20210851, March 2022. ISSN 1364-5021, 1471-2946. DOI: 10.1098/rspa.2021.0851. Cited on p. 38.

[188] M. Howe. “Influence of Wall Thickness on Rayleigh Conductivity and Flow-Induced Aperture Tones”. *Journal of Fluids and Structures*, 11(4):351–366, May 1997. ISSN 08899746. DOI: 10.1006/jfls.1997.0087. Cited on pp. 38 and 39.

[189] A. Orchini. “An effective impedance for modelling the aeroacoustic coupling of ducts connected via apertures”. *Journal of Sound and Vibration*, 520:116622, March 2022. ISSN 0022460X. DOI: 10.1016/j.jsv.2021.116622. Cited on pp. 38 and 39.

[190] A. Orchini, T. Pedergnana, P. E. Buschmann, J. P. Moeck, and N. Noiray. “Reduced-order modelling of thermoacoustic instabilities in can-annular combustors”. *Journal of Sound and Vibration*, 526:116808, May 2022. ISSN 0022460X. DOI: 10.1016/j.jsv.2022.116808. Cited on p. 38.

[191] P. E. Buschmann, N. A. Worth, and J. P. Moeck. “Experimental study of thermoacoustic modes in a can-annular model combustor”. In *SoTiC 2021 - Symposium on Thermoacoustics in Combustion: Industry Meets Academia (2021)*, Virtual, September 2021. Cited on p. 38.

[192] S. C. Humbert and A. Orchini. “Acoustics of can-annular combustors: Experimental characterisation and modelling of a lab-scale multi-can setup with adjustable geometry”.

Journal of Sound and Vibration, 564:117864, November 2023. ISSN 0022460X. DOI: 10.1016/j.jsv.2023.117864. Cited on p. 39.

[193] J. Brind. “Acoustic Boundary Conditions for Can-Annular Combustors”. *International Journal of Turbomachinery, Propulsion and Power*, 8(3):32, September 2023. ISSN 2504-186X. DOI: 10.3390/ijtpp8030032. Cited on p. 39.

[194] J. G. Aguilar and M. P. Juniper. “Adjoint Methods for Elimination of Thermoacoustic Oscillations in a Model Annular Combustor via Small Geometry Modifications”. In *Volume 4A: Combustion, Fuels, and Emissions*, page V04AT04A054, Oslo, Norway, June 2018. American Society of Mechanical Engineers. ISBN 978-0-7918-5105-0. DOI: 10.1115/GT2018-75692. Cited on p. 41.

[195] S. Falco and M. P. Juniper. “Shape Optimization of Thermoacoustic Systems Using a Two-Dimensional Adjoint Helmholtz Solver”. *Journal of Engineering for Gas Turbines and Power*, 143(7):071025, July 2021. ISSN 0742-4795, 1528-8919. DOI: 10.1115/1.4049305. Cited on p. 41.

[196] S. Bade, M. Wagner, C. Hirsch, T. Sattelmayer, and B. Schuermans. “Design for Thermo-Acoustic Stability: Modeling of Burner and Flame Dynamics”. *Journal of Engineering for Gas Turbines and Power*, 135(11):111502, November 2013. ISSN 0742-4795, 1528-8919. DOI: 10.1115/1.4025001. Cited on p. 41.

[197] F. Garita, H. Yu, and M. P. Juniper. “Assimilation of Experimental Data to Create a Quantitatively Accurate Reduced-Order Thermoacoustic Model”. *Journal of Engineering for Gas Turbines and Power*, 143(2):021008, February 2021. ISSN 0742-4795, 1528-8919. DOI: 10.1115/1.4048569. Cited on p. 41.

[198] M. P. Juniper and M. Yoko. “Generating a physics-based quantitatively-accurate model of an electrically-heated Rijke tube with Bayesian inference”. *Journal of Sound and Vibration*, 535:117096, September 2022. ISSN 0022460X. DOI: 10.1016/j.jsv.2022.117096. Cited on p. 41.

[199] M. Casel and A. Ghani. “Thermoacoustic System Design Utilizing Exceptional Points”. In *11th European Combustion Meeting*, Rouen, France, April 2023. Cited on p. 41.

[200] S. Guo, C. F. Silva, and W. Polifke. “Efficient Robust Design for Thermoacoustic Instability Analysis: A Gaussian Process Approach”. *Journal of Engineering for Gas Turbines and Power*, 142(3):031026, March 2020. ISSN 0742-4795, 1528-8919. DOI: 10.1115/1.4044197. Cited on p. 42.

[201] F. Schaefer, L. Magri, and W. Polifke. “A Hybrid Adjoint Network Model for Thermoacoustic Optimization”. *Journal of Engineering for Gas Turbines and Power*, 144(3):031017, March 2022. ISSN 0742-4795, 1528-8919. DOI: 10.1115/1.4051959. Cited on p. 42.

[202] M. Triantafyllou and G. Triantafyllou. “Frequency coalescence and mode localization phenomena: A geometric theory”. *Journal of Sound and Vibration*, 150(3):485–500, November 1991. ISSN 0022460X. DOI: 10.1016/0022-460X(91)90899-U. Cited on p. 42.

[203] K. Moon, C. Yoon, and K. T. Kim. “Influence of rotational asymmetry on thermoacoustic instabilities in a can-annular lean-premixed combustor”. *Combustion and Flame*, 223: 295–306, January 2021. ISSN 00102180. DOI: 10.1016/j.combustflame.2020.10.012. Cited on p. 42.

[204] P. E. Buschmann, N. A. Worth, and J. P. Moeck. “Thermoacoustic oscillations in a can-annular model combustor with asymmetries in the can-to-can coupling”. *Proceedings of the Combustion Institute*, 39(4):5707–5715, 2023. ISSN 15407489. DOI: 10.1016/j.proci.2022.07.060. Cited on p. 42.

[205] Y. Guan, K. Moon, K. T. Kim, and L. K. Li. “Synchronization and chimeras in a network of four ring-coupled thermoacoustic oscillators”. *Journal of Fluid Mechanics*, 938:A5, May 2022. ISSN 0022-1120, 1469-7645. DOI: 10.1017/jfm.2022.130. Cited on p. 42.

[206] J. Peña Ramirez, L. A. Olvera, H. Nijmeijer, and J. Alvarez. “The sympathy of two pendulum clocks: Beyond Huygens’ observations”. *Scientific Reports*, 6(1):23580, March 2016. ISSN 2045-2322. DOI: 10.1038/srep23580. Cited on p. 42.

[207] N. Thomas, S. Mondal, S. A. Pawar, and R. I. Sujith. “Effect of time-delay and dissipative coupling on amplitude death in coupled thermoacoustic oscillators”. *Chaos: An Interdisciplinary Journal of Nonlinear Science*, 28(3):033119, March 2018. ISSN 1054-1500, 1089-7682. DOI: 10.1063/1.5009999. Cited on p. 42.

[208] N. Thomas, S. Mondal, S. A. Pawar, and R. I. Sujith. “Effect of noise amplification during the transition to amplitude death in coupled thermoacoustic oscillators”. *Chaos: An Interdisciplinary Journal of Nonlinear Science*, 28(9):093116, September 2018. ISSN 1054-1500, 1089-7682. DOI: 10.1063/1.5040561. Cited on p. 42.

[209] H. Jegal, K. Moon, J. Gu, L. K. Li, and K. T. Kim. “Mutual synchronization of two lean-premixed gas turbine combustors: Phase locking and amplitude death”. *Combustion and Flame*, 206:424–437, August 2019. ISSN 00102180. DOI: 10.1016/j.combustflame.2019.05.017. Cited on p. 42.

[210] K. Moon, H. Jegal, J. Gu, and K. T. Kim. “Combustion-acoustic interactions through cross-talk area between adjacent model gas turbine combustors”. *Combustion and Flame*, 202:405–416, April 2019. ISSN 00102180. DOI: 10.1016/j.combustflame.2019.01.027. Cited on p. 42.

[211] M. P. Juniper and R. I. Sujith. “Sensitivity and Nonlinearity of Thermoacoustic Oscillations”. *Annual Review of Fluid Mechanics*, 50(1):661–689, January 2018. ISSN 0066-4189, 1545-4479. DOI: 10.1146/annurev-fluid-122316-045125. Cited on p. 42.

[212] R. I. Sujith and V. R. Unni. “Complex system approach to investigate and mitigate thermoacoustic Instability in turbulent combustors”. *Physics of Fluids*, 32(6):061401, June 2020. ISSN 1070-6631, 1089-7666. DOI: 10.1063/5.0003702. Cited on p. 42.

[213] D. M. Abrams and S. H. Strogatz. “Chimera States for Coupled Oscillators”. *Physical Review Letters*, 93(17):174102, October 2004. ISSN 0031-9007, 1079-7114. DOI: 10.1103/PhysRevLett.93.174102. Cited on p. 42.

[214] G. J. J. Fournier, M. Haeringer, C. F. Silva, and W. Polifke. “Low-Order Modeling to Investigate Clusters of ITA Modes in Annular Combustors”. In *ASME Turbo Expo 2020: Turbomachinery Technical Conference and Exposition*, volume Volume 4B: Combustion, Fuels, and Emissions, page V04BT04A031, Virtual, Online, September 2020. American Society of Mechanical Engineers. ISBN 978-0-7918-8413-3. DOI: 10.1115/GT2020-15985. Cited on p. 46.

[215] M. Haeringer, G. J. J. Fournier, M. Meindl, and W. Polifke. “A Strategy to Tune Acoustic Terminations of Single-Can Test-Rigs to Mimic Thermoacoustic Behavior of a Full Engine”. *Journal of Engineering for Gas Turbines and Power*, 143(7):710029, July 2021. ISSN 0742-4795, 1528-8919. DOI: 10.1115/1.4048642. Cited on p. 47.

[216] M. Haeringer, G. J. J. Fournier, M. Meindl, and W. Polifke. “A Strategy to Tune Acoustic Terminations of Single-Can Test-Rigs to Mimic Thermoacoustic Behavior of a Full Engine”. In *ASME Turbo Expo 2020: Turbomachinery Technical Conference and Exposition*, volume Volume 4B: Combustion, Fuels, and Emissions, page V04BT04A031, Virtual, Online, September 2020. American Society of Mechanical Engineers. ISBN 978-0-7918-8413-3. DOI: 10.1115/GT2020-16078. Cited on p. 47.

[217] G. J. J. Fournier, M. Meindl, C. F. Silva, G. Ghirardo, M. R. Bothien, and W. Polifke. “Low-Order Modeling of Can-Annular Combustors”. In *ASME Turbo Expo 2021: Turbomachinery Technical Conference and Exposition*, volume Volume 3A: Combustion, Fuels, and Emissions, page V03AT04A027, Virtual, Online, June 2021. American Society of Mechanical Engineers. ISBN 978-0-7918-8494-2. DOI: 10.1115/GT2021-58947. Cited on p. 48.

[218] G. J. J. Fournier, F. Schaefer, M. Haeringer, C. F. Silva, and W. Polifke. “Interplay of Clusters of Acoustic and Intrinsic Thermoacoustic Modes in Can-Annular Combustors”. In *ASME Turbo Expo 2022: Turbomachinery Technical Conference and Exposition*, volume Volume 3A: Combustion, Fuels, and Emissions, page V03AT04A026, Rotterdam, Netherlands, June 2022. American Society of Mechanical Engineers. ISBN 978-0-7918-8599-4. DOI: 10.1115/GT2022-80785. Cited on p. 49.

Appendices

Linear time-continuous state-space realization of flame transfer functions by means of a propagation equation

Philipp Brokof[1], Guillaume J. J. Fournier[2], Wolfgang Polifke[3]
Technical University of Munich,
TUM School of Engineering and Design,
Department of Engineering Physics and Computation
Boltzmannstr. 15, 85747 Garching, Germany

ABSTRACT

Low-order network models, commonly used to assess the thermo-acoustic stability of combustors, can be cast in a linear, time-continuous state-space representation. A standard linear eigenvalue problem for the system modes results, which can be solved in a robust and efficient manner. To represent the linear dynamics of any time-invariant flame in the state-space framework, this study presents an approximation of the distributed-time-delayed flame response to acoustic velocity perturbations based on a spatially discretized propagation equation (PE). We derive the rational flame transfer function of a first-order-upwind-PE state-space model and discuss its relation to the Tustin approximation of transfer functions. For an exemplary discrete finite impulse response of a flame, a third-order-upwind-PE state-space model is shown to match the discrete flame frequency response with an accuracy comparable to that of a rational approximation found by non-linear optimization. The numerical dissipation introduced by discretization of the PE ensures negligible gain above the Nyquist frequency of the underlying discrete flame impulse response. Finally, we apply the PE state-space flame model to a generic Rijke tube and show that the predicted thermo-acoustic modes agree well with results obtained from a classical non-linearly optimized rational approximation of the frequency response function of the flame.

1. INTRODUCTION

Thermo-acoustic instability problems involve length scales ranging from acoustic wave lengths in the order of the dimensions of the combustion device to flame thicknesses of a few millimeters [1]. To predict the stability of a combustor with reasonable computational effort, a common strategy is to divide the problem into sub-models with tailored complexity. Flame transfer functions (FTF) stemming from high-fidelity simulations can be incorporated into low-order acoustic networks [2]. Similarly, acoustic network models can be applied as boundary conditions in high-fidelity simulations to reduce the size of the computational domain [3].

---

[1] philipp.brokof@tum.de

[2] guillaume.fournier@tum.de

[3] polifke@tum.de

Thermo-acoustic low-order networks usually lead to a non-linear eigenvalue problem for the system dynamics, i.e. system modes and their corresponding frequencies and growth rates. This non-linear eigenvalue problem is mainly a result of the phase shift experienced by acoustic waves traveling through the geometry and the distributed-time-delayed reactions [4] of flames to acoustic velocity perturbations, both leading to terms where the (complex-valued) frequency occurs in the exponent of the exponential function. Furthermore, non-linearities can be introduced by non-trivial boundary conditions, represented by complex-valued reflection coefficients, and acoustic inertia in models of acoustically compact elements, e.g. for long holes in [5]. Solving this non-linear eigenvalue problem by iterative root-finding [6] is computationally expensive. More crucial, the choice of the initial conditions for the search algorithm [7] determines which modes are found, and there is no guarantee that one finds *all* roots of the system. Contour integral methods, which ensure that all eigenmodes within a contour in the complex-plane are found, offer a remedy [7]. However, these methods remain computationally expensive [8].

Schuermans et al. [9] introduced the state-space approach to acoustic modeling, based on a modal expansion technique and sub-model interconnection by the Redheffer Star Product. Emmert at al. [10], on the other hand, connect sub-models with a feed-through equation. State-space formulations for network elements are deduced from rational polynomials that represent the respective transfer functions or from a spatial discretization of a propagation equation. If the state-space models of all individual elements are linear, the resulting state-space model of the overall acoustic network is also linear and a linear eigenvalue problem results, which can be solved in a robust and efficient manner. This is an important advantage of state-space models over the standard formulation of network models [8, 11].

The crucial point is the formulation of linear state-space models for network elements with time-delays/phase shifts. For example, for a duct element, the characteristic amplitudes of acoustic waves entering and leaving the duct can be set as the inputs and outputs of the state-space model, respectively. Since the acoustic waves simply propagate through the duct, leading to a phase shift, a linearized description of the system dynamics can be obtained by discretizing the propagation equation (PE) in space [10].

The n-τ flame model shows great similarity to the aforementioned duct element if the time-delay is interpreted as the time that the input to the model (acoustic velocity perturbation) needs to propagate through a pseudo space until it affects the output of the model (heat release perturbation). The length of the pseudo space and the propagation speed of the perturbation are matched to the desired time-delay of the flame. In literature, states stemming from the discretization of the pseudo space are referred to as "lagged states" [12] or "history states" [13]. The PE was used to realize the n-τ model into state-space by Meindl et al. [11], and Mangesius and Polifke [13]. However, Schmid et al. [14] point out that the n-τ model should only be used if the absolute time lag of the flame is known and Subramanian et al. [12] advocate for distributed time-delay response functions to capture the rich complexity of flame dynamics.

More sophisticated descriptions of flame dynamics can be obtained by (1) harmonic forcing of the flame to identify the frequency response function (FRF) or (2) broad-band excitation and a correlation analysis to identify the impulse response of the flame. However, an analytic time-continuous description of frequency response function (FRF) or impulse response cannot be obtained from these system identification (SI) techniques. The FRF will only be available at discrete frequencies and the impulse response will consist of a truncated series of discrete impulses, also known as finite impulse response (FIR). However, we require a time-continuous state-space (CSS) model for stability analysis. The advantage of such a time-continuous model is the possibility of coupling with a variable time step computational fluid dynamics (CFD) simulation, allowing an efficient implementation of time domain impedance boundary conditions [3, 15]. Common strategies to obtain CSS models from discrete FRF data are (1) fitting a rational function [12, 16–18], or (2) first-order bilinear/Tustin and higher-order Padé approximation [9, 19] of exponential terms. For either method, the obtained rational function is subsequently transformed into a CSS model, e.g. in Jordan canonical form [20].

The contribution of the present study is to formulate a PE based CSS model for arbitrary FIRs. Furthermore, an analytic analysis of the model is given and its performance is compared to the rational-fitting strategy for an example FIR of a laminar premixed flame [21] obtained by SI [2]. In this study, the FIR is taken as input and details on its computation are out of the scope of the presentation.

This paper is organized as follows: Section 2 reviews common low-order representations of flames, i.e. FIR and FTF. Subsequently, Section 3 introduces the PE based CSS realization of flame transfer functions. In Section 4, the performance of the presented PE CSS model is compared with a CSS based on rational-fitting. Both CSS models are compared regarding the recovery of the discrete frequency response of the flame, and the influence of the CSS realization strategy on the eigenvalues of a generic Rijke tube is assessed. Finally, Section 5 concludes this study with a summary of the findings.

2. LOW-ORDER FLAME MODELS IN THERMO-ACOUSTICS

This section reviews the concepts of flame impulse response and flame transfer function. We point out the interrelation between frequency and time domain in both, the time-discrete and time-continuous case. A graphical overview of the different domains can be found in [4], Figure 2.

The discrete response series r_l of a causal linear system to any discrete signal series s_l can be obtained by convolution of the signal with the system's FIR $\mathbf{h} = (h_0, h_1, ..., h_N)$ of length N. For a velocity sensitive flame, the input signal consists of the normalized velocity perturbation $\overline{u'/\bar{u}}$ at a reference point and the response of interest is the normalized fluctuating heat release $\dot{Q}'/\overline{\dot{Q}}$ of the flame. For harmonic input signals $s_l = \hat{u}/\bar{u}e^{s\Delta t l}$, the discrete FTF $\mathcal{F}_d(s)$ that corresponds to the FIR $\mathbf{h}$ becomes

$$r_l = \sum_{k=0}^{N} h_k \frac{\hat{u}}{\bar{u}} e^{s\Delta t(l-k)} = \frac{\hat{u}}{\bar{u}} e^{s\Delta t l} \sum_{k=0}^{N} h_k e^{-s\Delta t k} \Rightarrow \mathcal{F}_d(s) = \frac{\hat{\dot{Q}}/\overline{\dot{Q}}}{\hat{u}/\bar{u}} = \sum_{k=0}^{N} h_k e^{-s\Delta t k}, \tag{1}$$

where $s = \sigma + i\omega$ is the Laplace variable and $\hat{(\cdot)}$ denotes the complex amplitude. From Eq. (1), it is evident that the FTF can be interpreted as the sum of the distributed-time-delayed responses of the flame to impulse forcing and is non-linear in s.

The discrete equivalent to the Laplace transform is the z-transform. By substituting $z = e^{s\Delta t}$ in Eq. (1), we find that the z-transform of the FIR equals the FTF. A rational approximation of $\mathcal{F}(s)$ can be found by setting

$$z = \frac{e^{s\frac{\Delta t}{2}}}{e^{-s\frac{\Delta t}{2}}} \approx \frac{1 + \frac{\Delta t}{2}s}{1 - \frac{\Delta t}{2}s}, \tag{2}$$

which is known as bilinear transform or Tustin transform [22]. The Tustin transform keeps the mapping properties of the exponential function between Laplace and z-space and, therefore, conserves stability properties of the time-discrete model when used to find a time-continuous description and vice versa. Equation (2) shows that the Tustin transform, which is the first-order Padé approximation [23], is based on the first-order Taylor series expansion $e^x \approx 1 + x$. Hence, accuracy can only be expected for sufficiently small frequencies or small time increments Δt. Rational approximations of the time-delay term for higher frequencies were achieved in [9, 19] using Padé approximations of higher orders.

3. CONTINUOUS STATE-SPACE REALIZATION BY PROPAGATION EQUATION

This sections presents a CSS realization based on a PE. We start with a minimal example and realize a FIR consisting of three impulses in a first-order-upwind-PE CSS model. Subsequently, the equivalent continuous flame transfer function is generalized for arbitrary FIRs. From this generalization, the stability and mapping properties from z-space to Laplace space of the first-order-upwind-PE CSS model are assessed.

3.1. Minimal Example

Let us assume a FIR consisting of three impulses, $\mathbf{h} = (h_0, h_1, h_2)$, as shown in Figure 1. The FIR is sampled with a constant time increment Δt. Let the pseudo space in Θ be discretized with $\Delta\Theta = \Delta t/2$. The flame responds instantaneously with h_0 to the velocity perturbation signal $u'/\bar{u}$, but the signal has to travel the distance $2\Delta\Theta = \Delta t$ with unity propagation speed through the pseudo space until the time-delay corresponding to h_1 has passed. Similarly, the signal has to travel twice the distance until the time-delay of h_2 has passed. Introducing history states $\mathbf{x} = (x_1, ..., x_4)^T$, which store the signal at different positions in pseudo space, the evolution of the state variables $\mathbf{x}$ is completely described by a PE. Rearranging the PE for the time derivative of x and discretizing the spatial derivative with a first-order upwind finite difference stencil yields

$$\frac{\partial x}{\partial t} = -\frac{\partial x}{\partial \theta} \approx -\left[\frac{x_i - x_{i-1}}{\Delta\theta}\right]. \tag{3}$$

Application of Eq. (3) to all states $\mathbf{x}$ gives

$$\begin{pmatrix} \dot{x}_1 \\ \dot{x}_2 \\ \dot{x}_3 \\ \dot{x}_4 \end{pmatrix} = \underbrace{\begin{pmatrix} -\frac{1}{\Delta\Theta} & 0 & 0 & 0 \\ \frac{1}{\Delta\Theta} & \frac{-1}{\Delta\Theta} & 0 & 0 \\ 0 & \frac{1}{\Delta\Theta} & \frac{-1}{\Delta\Theta} & 0 \\ 0 & 0 & \frac{1}{\Delta\Theta} & \frac{-1}{\Delta\Theta} \end{pmatrix}}_{\mathbf{A}} \begin{pmatrix} x_1 \\ x_2 \\ x_3 \\ x_4 \end{pmatrix} + \underbrace{\begin{pmatrix} \frac{1}{\Delta\Theta} \\ 0 \\ 0 \\ 0 \end{pmatrix}}_{\mathbf{B}} \frac{u'}{\bar{u}}, \tag{4}$$

where $\mathbf{A}$ is the system matrix and $\mathbf{B}$ is the input matrix. We can formulate the output equation for fluctuating heat release as

$$\frac{\hat{\dot{Q}}}{\bar{\dot{Q}}} = \underbrace{\begin{pmatrix} 0 & h_1 & 0 & h_2 \end{pmatrix}}_{\mathbf{C}} \begin{pmatrix} x_1 \\ x_2 \\ x_3 \\ x_4 \end{pmatrix} + \underbrace{h_0}_{\mathbf{D}} \frac{\hat{u}}{\bar{u}}, \tag{5}$$

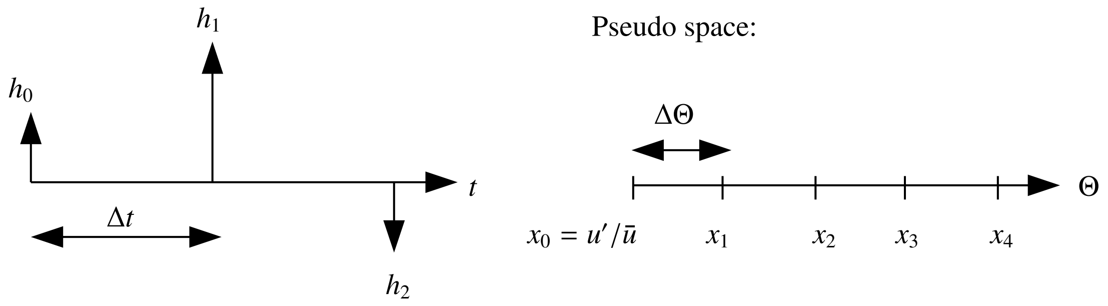

Figure 1: Minimal example: FIR consisting of three discrete impulses. Pseudo space is resolved with $\Delta\theta = \Delta t/2$.

where **C** and **D** are the output and feed-through matrix, respectively. Equations (4) and (5) form a continuous state-space model $(\mathbf{A}, \mathbf{B}, \mathbf{C}, \mathbf{D})$ with scalar input $\hat{u}/\bar{u}$ and scalar output $\hat{Q}/\overline{Q}$.

3.2. Analysis of the Resulting Flame Transfer Function

The system matrix **A** resulting from the first-order upwind discretization is triangular, allowing straightforward determination of its eigenvalues that characterize the dynamics of the CSS model. Note that the system matrix depends only on the discretization scheme and pseudo space resolution, and not on the impulse response **h**. Furthermore, the coefficients of the system matrix are constant and frequency independent.

Equations (4) and (5) can be Laplace transformed and rearranged to find the corresponding continuous flame transfer function

$$\mathcal{F}(s)_{\Delta\Theta=\frac{\Delta t}{m}} = \frac{\hat{Q}/\overline{Q}}{\hat{u}/\bar{u}} = \mathbf{C}(s\mathbf{I}-\mathbf{A})^{-1}\mathbf{B} + \mathbf{D} = \sum_{k=0}^{N} \frac{h_k}{\left[s\frac{\Delta t}{m}+1\right]^{km}}, \tag{6}$$

where the parameter m controls the resolution of the pseudo space and N is the length of the FIR. Equation (6) shows that the corresponding FTF is a rational function with only stable poles of multiplicity mk at $s = -m/\Delta t$. Furthermore, for higher resolution of the pseudo space, the poles move to a strongly damped region that is not of concern for the stability analysis of thermo-acoustic systems.

Comparison with Eq. (1) shows that Eq. (6) is obtained from the exact FTF by substituting

$$z = e^{s\Delta t} = e^{s\frac{\Delta t}{m}m} = (e^{s\frac{\Delta t}{m}})^m \approx \left[s\frac{\Delta t}{m}+1\right]^m \Rightarrow z(i\omega) = \left[1+\left(\frac{\omega\Delta t}{m}\right)^2\right]^{m/2} e^{i\operatorname{atan}(\frac{\omega\Delta t}{m})m}. \tag{7}$$

Thus, the first-order-upwind-PE CSS model is, as the Tustin transform, based on a first-order Taylor series expansion of the exponential function. However, compared to the Tustin transform, the exponent is scaled by $1/m$ resulting in better performance at higher frequencies. For a fine resolution of the pseudo space, Eq. (7) recovers the mapping properties of the z-transform. This is evident from the complex pointer representation of the mapping. For high values of m, $|z(i\omega)| \to 1$, so that the imaginary axis is mapped on the unit circle.

4. COMPARISON OF PE AND DATA-FITTING BASED CSS MODELS

In this section, the performance of the PE CSS model is compared with a rational fit based CSS, where the sixth-order rational fit was obtained with the MATLAB [24] *tfest* function, requiring a quality of 99 % and constraining the poles to be stable. For further information about the rational fit CSS model, the reader is referred to [12, 16–18]. We assess (1) the mean square error (MSE) of the continuous frequency response function to the original discrete model and (2) the influence of the CSS realization strategy on the eigenvalues of a generic Rijke tube. The FIR for flame modeling consists of $N = 44$ discrete impulses and was obtained by SI from the simulation of a Kornilov flame [21]. It is indicated in Figure 3 with blue dots.

4.1. Recovery of Discrete Flame Transfer Function

The difference between the FRF F_c of the CSS models and the original discrete FRF F_d is measured by the mean square error (MSE) in the complex plane over all N_d frequencies of the discrete model, i.e.

$$\mathrm{MSE} = \frac{1}{N_d}\sum_{k=1}^{N_d} \left|F_{d,k} - F_{c,k}\right|^2. \tag{8}$$

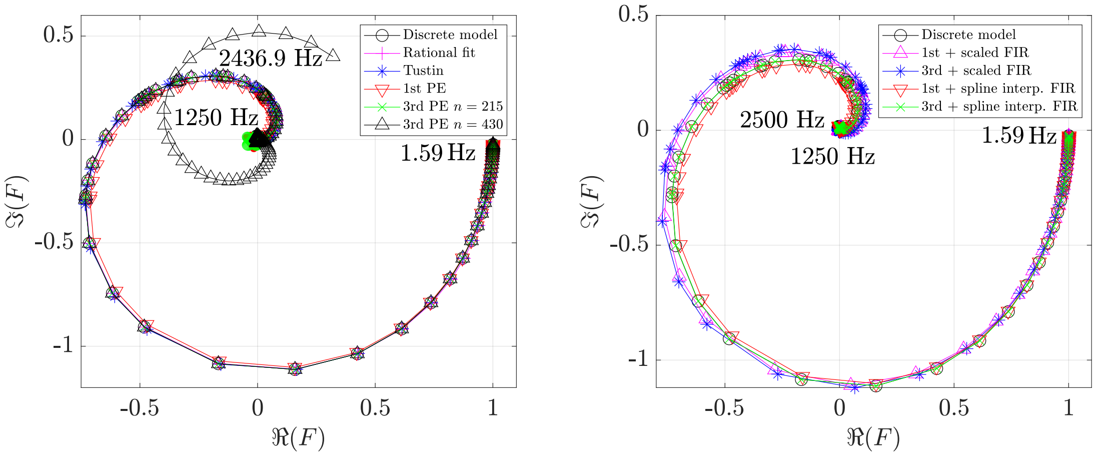

Figure 2: Left: Comparison between loci of discrete frequency response and continuous frequency responses from different CSS realizations. Right: Loci of frequency responses of PE CSS models based on resampled FIR.

The loci of the compared FRFs are shown in the left part of Figure 2. Note that the discrete model is only plotted up to its Nyquist frequency $f = 1/(2\Delta t) = 1250$Hz. The performance of the Tustin CSS model is good at low frequencies but severe deviations to the discrete model can be observed in phase for higher frequencies (the locations of markers on the parametric curve do not coincide with those of the discrete model). However, at high frequencies the gain of the FRF is low so that even big discrepancies in phase become unimportant. This is reflected by the low error of MSE = $7.16e^{-4}$. Per construction, the number of states of the Tustin model equals the number of time-delayed impulses in the FIR. The rational fit CSS model, with only six states, shows a small error of MSE = $1.34e^{-5}$, justifying its frequent use in literature. To achieve an error MSE = $1.09e^{-4}$, hence of the same order as for the Tustin CSS model, with the first-order-upwind-PE CSS model introduced in Section 3, the number of states increases drastically to 860. Remedy can be found by increasing the order of the upwind stencil for the PE discretization from first-order to third-order. The third-order-upwind-PE CSS model with 215 states shows an error of MSE = $1.51e^{-7}$, and a more accurate fit of the phase than the first-order-upwind-PE model. However, the system matrix of the third-order-upwind-PE CSS model is not triangular anymore, leading to a complex pole pattern of the corresponding rational FTF (in contrast to Eq. (6)).

Inspection of Figure 2 (left) reveals that the PE CSS models show spurious gain above the Nyquist frequency of the underlying discrete model. This is more significant for the third-order scheme and becomes even more significant if the number of states of the third-order model is increased from $n = 215$ to $n = 430$. In a frequency domain analysis, this spurious gain can be ignored since it occurs above the frequency range of interest, i.e. above the Nyquist frequency. However, in a time domain analysis that couples the CSS model to unsteady CFD [3, 15], this nonphysical behavior at higher frequencies would be present. The discrete model is only valid up to its Nyquist frequency of $f \approx 1250$ Hz. For higher frequencies, the z-transformed FRF is symmetric in magnitude and anti-symmetric in phase around this Nyquist frequency [4]. Hence, a continuous extrapolation based on the discrete model is expected to show symmetric high frequency peaks in gain. The spurious gain is damped only as a beneficial side effect of the numerical dissipation of the discretization scheme used in the PE CSS model.

To overcome this problem, we resample the FIR at every history state to increase the Nyquist frequency and push the (symmetric) spurious peak to higher frequencies where the numerical damping is stronger. In Figure 3 (left), additional sampling points are inserted and the FIR is step-wise rescaled to ensure a constant total impulse of the response. In Figure 3 (right), the original FIR was converted

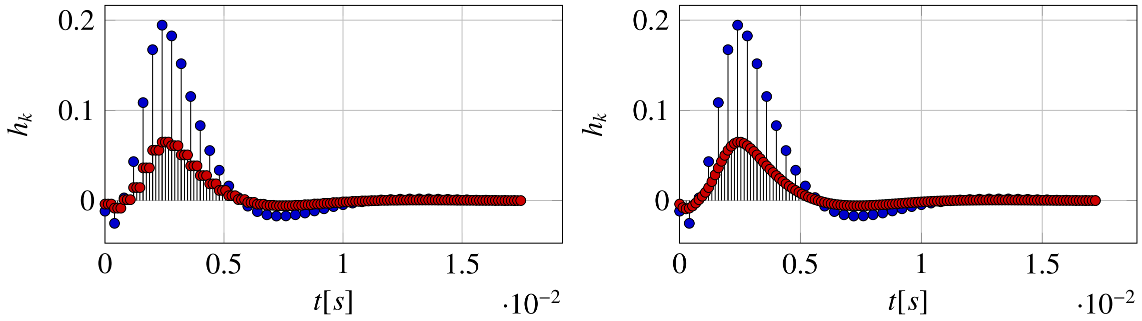

Figure 3: Comparison of different refinement strategies of the FIR: Scaling of the FIR (left) and scaling with spline interpolation (right).

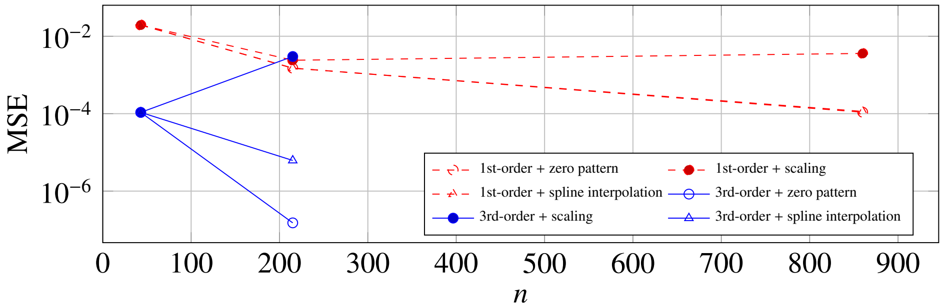

Figure 4: MSE to discrete model for increasing number of state variables n for resampled and original PE CSS models.

to a time series with a hold function, spline interpolated, and converted back to an impulse series under consideration of the finer sampling time.

Figure 2 (right) shows that for both resampling strategies the spurious gain observed before between 1250 Hz and 2500 Hz is suppressed. Inspection at frequencies up to twice of the new Nyquist limit showed no further peak in gain. The mere scaling strategy recovers the phase of the discrete model only at low frequencies. Figure 3 (left) shows that the scaling operation delays the overall impulse response. Since the phase of the FRF is closely related to the time-delay of the FIR, this effect becomes visible in the unmatched phase. In contrast, the phase accuracy of the spline-interpolated third-order-upwind-PE CSS is excellent. Figure 4 compares the MSEs of the resampled PE CSS models with the original PE CSS model, where the output matrix $\mathbf{C}$ was zero patterned, see Eq. (5). For the same number of states n, the error for the spline interpolation strategy is one order of magnitude higher than for the original zero patterning strategy in case of the third-order-upwind-PE CSS model. The phase accuracy of the merely scaled CSS model is poor and it is not guaranteed that the model's accuracy improves with increased number of states.

4.2. Influence of the CSS Realization on the Eigenvalues of a Rijke Tube

So far, the PE CSS model was only assessed for zero growth rate by limiting the analysis to the FRF. However, as pointed out by Schmid et al. [14], for linear stability analysis we have to solve the eigenvalue problem in the complex plane. The PE CSS model is a linear approximation of the time-delayed dynamics of the flame. Thus, the linear eigenvalue problem can only be expected to give similar eigenvalues as the original non-linear problem if this approximation is sufficiently good in the complex plane [8, 14].

Figure 5 shows magnitude and phase of the flame transfer functions $\mathcal{F}$ of the original distributed time-delay model according to Eq. (1), the third-order-upwind-PE CSS model with spline-interpolated

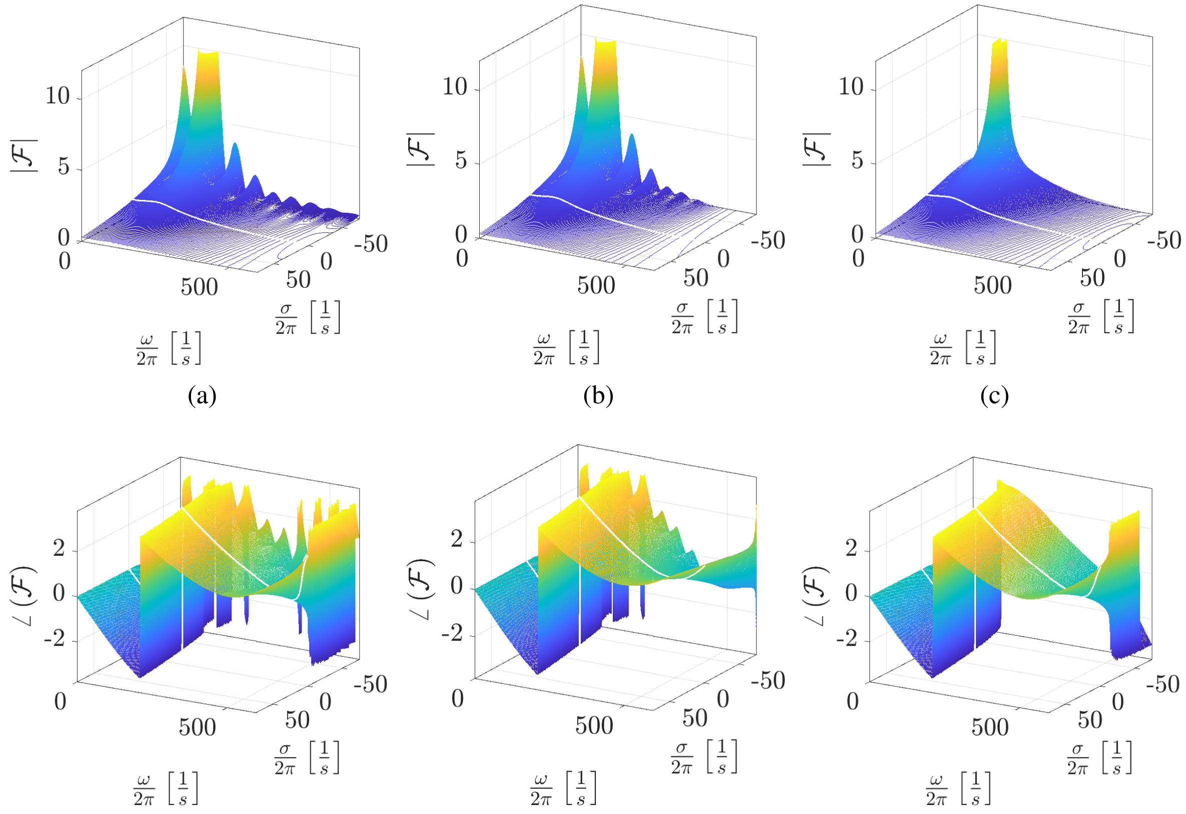

(a) (b) (c)

(d) (e) (f)

Figure 5: Magnitude and phase of the flame transfer functions $\mathcal{F}$ of the original distributed time-delay model according to Eq. (1) (a, d), 3rd-order-upwind-PE CSS model with spline-interpolated FIR (b, e) and 6th-order rational fit CSS model (c, f). The frequency response function (FRF) at zero growth rate is indicated by a white line.

FIR and the sixth-order rational fit CSS model. Although the fit of the FRF by the rational fit model was excellent, the FTF in the complex plane varies qualitatively from the FTF of the distributed time-delay model for normalized growth rates $\sigma/(2\pi) < -50$ 1/s. On the other hand, the FTF of the third-order-upwind-PE CSS is qualitatively more similar to the FTF of the distributed time-delay model.

To assess the linear approximation of the FTF obtained with the third-order-upwind-PE CSS model, we compute the eigenvalues of a one-dimensional Rijke tube with quiescent flow as shown in Figure 6 and compare them with the eigenvalues computed based on the rational fit CSS. Only planar one-dimensional acoustic waves are non-evanescent and the waves travelling between network elements are indicated with curved arrows in Figure 6. Both ends of the Rijke tube are open and modeled with reflection coefficients $R_u = R_d = -1$. The flame is placed between an upstream duct of length $L_u = 0.25$ m and a downstream duct of length L_d that is varied from 0.75 m to 2.0 m in a parameter study. The speed of sound in the upstream duct is $c = 341$ m/s. The flame dynamics are modeled by the FIR shown in Figure 3 and standard acoustic Rankine-Hugoniot jump conditions [25, 26] with a temperature jump $T_d/T_u = 4.96$ and constant isentropic exponent $\gamma = 1.4$. The complete CSS model of the Rijke tube was obtained with the open source software taX[4] [10].

Figure 7 (left) shows the pole map of the Rijke tube obtained with the third-order-upwind-PE CSS model with spline interpolated FIR. The length of the downstream duct varies from 0.75 m (black

---

[4] https://gitlab.lrz.de/tfd/tax

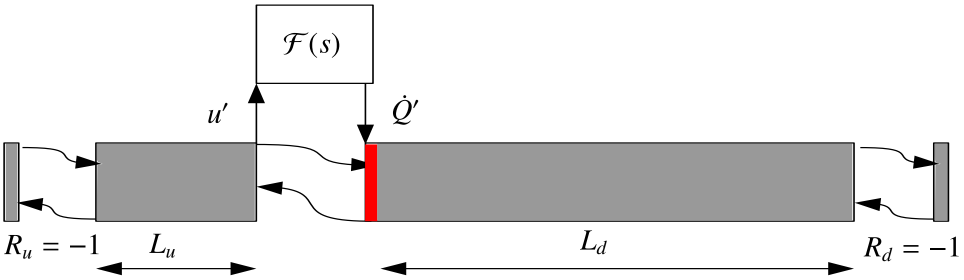

Figure 6: Low-order acoustic network model of a Rijke tube.

markers) to 2 m (gray markers). Also indicated are the poles and zeros of the flame model in red. The blue squares indicate the eigenvalues of the original non-linear problem with $L_d = 0.75$ m, i.e. exponential expressions for the phase shifts due to acoustic wave propagation in the ducts and the time-delayed behavior of the flame, as obtained with an iterative solver assuming the CSS eigenvalue spectra as initial condition. Figure 7 (right) shows the same information for a Rijke tube, where the flame was modeled with the rational fit CSS. In contrast to the rational fit based CSS model of the flame, the PE-based CSS model of the flame has no pole in the investigated region of the complex plane since upwind discretization of the PE guaranties stability and highly damped poles.

For normalized growth rates $\sigma/(2\pi) > -50$ 1/s, the predicted trajectories of the poles of the Rijke tube for both models agree well. According to Figure 5, this is the region of the complex plane where the FTFs of the third-oder-upwind-PE CSS and rational fit CSS agree well with the FTF of the original time-delayed flame model. In contrast, in the region -80 1/s $< \sigma/(2\pi) < -50$ 1/s, 0 Hz $< \omega/(2\pi) < 500$ Hz, where the FTFs of the third-order-upwind-PE CSS and rational fit CSS differ significantly, the PE-based Rijke tube model predicts three additional poles. These additional poles are located close to zeros of the FTF and two of them depend only weakly on the length of the downstream duct. Since these poles do not converge towards a solution of the non-linear Rijke tube model, they are most likely a consequence of the PE discretization and of spurious nature.

Looking at the modes close to the stability border $\sigma = 0$, it seems possible that a less accurate flame model can lead to wrongly predicted instability. It is emphasized that the CSS model must capture

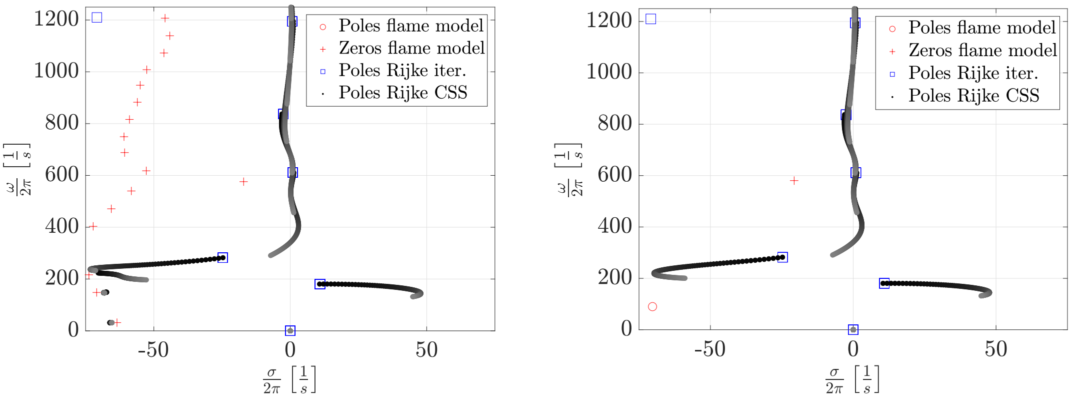

(a) Third-oder-upwind-PE CSS flame model.

(b) Sixth-order rational fit CSS flame model.

Figure 7: Poles of the Rijke tube are shown for a variation of the downstream duct length from $L_d = 0.75$ (black) to $L_d = 2.0$ (gray). Also shown in red are the poles and zeros of the applied flame model. Blue squares indicate poles confirmed by iterative solution of the non-linear model for $L_d = 0.75$.

the phase of the flame response sufficiently well, since thermo-acoustic instabilities are sensitive to the timing between acoustic pressure and heat release fluctuations (Rayleigh criterion) [27]. This underlines that a third-order discretization of the PE is preferable despite its more complicated pole pattern than a first-order PE CSS model.

5. SUMMARY, CONCLUSION AND OUTLOOK

A continuous state-space (CSS) realization of discrete flame impulse responses allows to formulate thermoacoustic stability analysis as a linear eigenvalue problem. The present paper closes the gap between state-space realizations of the simplistic n-τ flame model based on a propagation equation (PE) [11, 13] and more realistic flame models based on rational-fitting [12, 16–18].

The distributed-time-delayed response of flames to velocity perturbations was linearly approximated by discretizing a propagation equation (PE) in pseudo space. We showed that PE-based CSS models lead to rational flame transfer functions, too, and presented an explicit analytical expression for the flame transfer function of the first-order-upwind-PE CSS. Comparison of numerical results demonstrated very good performance of the rational-fitting approach, as it leads to state-spaces models that are two orders of magnitude smaller than PE-based realizations with comparable accuracy. On the downside, the rational fits must be constrained to poles in the negative real half-plane for stability reasons and an increase in the degrees of freedom of the rational function does not guarantee a better fit but can lead to over-fitting of the data. Hence, for parametric studies that require repeated evaluation of CSS models of flame dynamics, the upwind-PE approach is preferable, since it guarantees stability of the state-space model of the flame. Furthermore, the quality of the model is guaranteed to increase with state-space size. It is preferable to discretize the PE with a third-order upwind stencil in order to achieve an accuracy that is comparable to rational-fitting based CSS. For a generic Rijke tube, spurious modes where found close to the zeros of the PE CSS model of the flame. This phenomenon should be kept in mind when analyzing eigenvalue spectra obtained by PE-based CSS models and needs further investigation.

In addition to the PE and rational-fitting strategy, control theory knows many techniques to realize a state-space model from the discrete impulse response (Markov parameters) of a system. The central tool in these strategies is a singular value decomposition of the Hankel matrix [22]. In the present study, these techniques were not further investigated since they lead to a time-discrete state-space model. However, for acoustic networks based on time-discrete state-space models, these methods can prove useful and should be considered. For an application in the context of acoustics see Pelling and Sarradj [28]. A direct comparison with the PE CSS model presented here can be the scope of further work.

REFERENCES

[1] T. Lieuwen. Modeling Premixed Combustion - Acoustic Wave Interactions: A Review. *Journal of Propulsion Power*, 19(5):765–781, 2003.

[2] Wolfgang Polifke. Black-Box System Identification for Reduced Order Model Construction. *Annals of Nuclear Energy*, 67C:109–128, May 2014.

[3] S. Jaensch, C. Sovardi, and W. Polifke. On the Robust, Flexible and Consistent Implementation of Time Domain Impedance Boundary Conditions for Compressible Flow Simulations. *Journal of Computational Physics*, 314:145–159, June 2016.

[4] Wolfgang Polifke. Modeling and Analysis of Premixed Flame Dynamics by Means of Distributed Time Delays. *Prog. Energy Combust. Sci.*, 79:100845, 2020.

[5] Xiaodong Jing and Xiaofeng Sun. Experimental investigations of perforated liners with bias flow. *The Journal of the Acoustical Society of America*, 106(5):2436–2441, November 1999.

[6] F. Nicoud, L. Benoit, C. Sensiau, and T. Poinsot. Acoustic Modes in Combustors with Complex Impedances and Multidimensional Active Flames. *AIAA Journal*, 45(2):426–441, 2007.

[7] Philip E. Buschmann, Georg A. Mensah, Franck Nicoud, and Jonas P. Moeck. Solution of Thermoacoustic Eigenvalue Problems With a Noniterative Method. *Journal of Engineering for Gas Turbines and Power*, 142(3), March 2020.

[8] Moritz Merk, Philip E. Buschmann, Jonas P. Moeck, and Wolfgang Polifke. The nonlinear thermoacoustic eigenvalue problem and its rational approximations: assessment of solution strategies. In *Proceedings of the ASME Turbo Expo 2022*, Rotterdam, The Netherlands, 2022. ASME (accepted for publication).

[9] B. Schuermans, V. Bellucci, and C. O. Paschereit. Thermoacoustic Modeling and Control of Multi-Burner Combustion Systems. In *Proceedings of the ASME Turbo Expo 2003, collocated with the 2003 International Joint Power Generation Conference*, GT2003-38688, pages 509–519, Atlanta, GA, USA, 2003. ASME.

[10] Thomas Emmert, Max Meindl, Stefan Jaensch, and Wolfgang Polifke. Linear State Space Interconnect Modeling of Acoustic Systems. *Acta Acustica united with Acustica*, 102(5):824–833, 2016.

[11] Max Meindl, Thomas Emmert, and Wolfgang Polifke. Efficient calculation of thermoacoustic modes utilizing state-space models. In *23nd Int. Congress on Sound and Vibration (ICSV23)*, Athens, Greece, 2016.

[12] P. Subramanian, R. S. Blumenthal, R. Sujith, and W. Polifke. Distributed Time Lag Response Functions for the Modelling of Combustion Dynamics. *Combustion Theory and Modelling*, 19(2):223–237, February 2015.

[13] Herbert Mangesius and Wolfgang Polifke. A discrete-time, state-space approach for the investigation of non-normal effects in thermoacoustic systems. *Int. J. Spray Comb. Dynamics*, 3(4):331–350, 2011.

[14] Martin Schmid, Ralf Blumenthal, Moritz Schulze, Wolfgang Polifke, and Thomas Sattelmayer. Quantitative Stability Analysis Using Real Frequency Response Data. *Journal of Engineering for Gas Turbines and Power*, 135(12):121601, 2013.

[15] Q. Douasbin, C. Scalo, L. Selle, and T. Poinsot. Delayed-time domain impedance boundary conditions (D-TDIBC). *Journal of Computational Physics*, 371:50–66, 2018.

[16] Felix Schily, Thomas Komarek, and Wolfgang Polifke. A criterion for thermo-acoustic stability based on the flux of acoustic energy. *Combustion and Flame*, 227:238–254, May 2021.

[17] A. Avdonin, Max Meindl, and W. Polifke. Thermoacoustic analysis of a laminar premixed flame using a linearized reacting flow solver. *Proceedings of the Combustion Institute*, 37:5307–5314, 2019.

[18] Max Meindl, Alp Albayrak, and Wolfgang Polifke. A state-space formulation of a discontinuous Galerkin method for thermoacoustic stability analysis. *Journal of Sound and Vibration*, 481:115431, 2020.

[19] Mirko Bothien, Jonas Moeck, Arnaud Lacarelle, and Christian Oliver Paschereit. Time Domain Modelling and Stability Analysis of Complex Thermoacoustic Systems. *Proceedings of the Institution of Mechanical Engineers, Part A: Journal of Power and Energy*, 221(5):657–668, January 2007.

[20] James R. Leigh. *Control theory: a guided tour*. Number 72 in IET control engineering series. The Inst. of Engineering and Technology, London, 3. ed edition, 2012.

[21] V. N. Kornilov, R. Rook, J. H. M. ten Thije Boonkkamp, and L. P. H. de Goey. Experimental and Numerical Investigation of the Acoustic Response of Multi-Slit Bunsen Burners. *Combustion and Flame*, 156(10):1957 – 1970, October 2009.

[22] Athanasios C. Antoulas. *Approximation of Large-Scale Dynamical Systems*. Society for Industrial and Applied Mathematics, January 2005.

[23] H. Padé. Sur la représentation approchée d'une fonction par des fractions rationnelles. *Annales scientifiques de l'École normale supérieure*, 9:3–93, 1892.

[24] MATLAB, Version R2021b, Copyright 2009-2020 The MathWorks, Inc.

[25] Thomas Emmert, Sebastian Bomberg, and Wolfgang Polifke. Intrinsic Thermoacoustic Instability of Premixed Flames. *Combustion and Flame*, 162(1):75–85, 2015.

[26] Boa-Teh Chu. On the generation of pressure waves at a plane flame front. *Symposium (International) on Combustion*, 4(1):603–612, January 1953.

[27] John William Strutt Rayleigh. *The theory of sound. Vol. 2*. Dover classics of science and mathematics. Dover Publ, New York, repr. of 2. ed. rev. and enl., 1894 edition, 1969. OCLC: 830808857.

[28] Art J. R. Pelling and Ennes Sarradj. Efficient Forced Response Computations of Acoustical Systems with a State-Space Approach. *Acoustics*, 3(3):581–594, August 2021.

Combustion and Flame 249 (2023) 112605

Contents lists available at ScienceDirect

Combustion and Flame

journal homepage: www.elsevier.com/locate/combustflame

Categorization of thermoacoustic modes in an ideal resonator with phasor diagrams

Kah J. Yong*, Camilo F. Silva, Guillaume J.J. Fournier, Wolfgang Polifke

TUM School of Engineering and Design, Department of Engineering Physics and Computation, Technical University of Munich, Garching D-85747, Germany

ARTICLE INFO

Article history:
Received 1 August 2022
Revised 25 December 2022
Accepted 26 December 2022

Keywords:
Thermoacoustic stability
Intrinsic thermoacoustic (ITA) modes
Phasor analysis

ABSTRACT

A recent study (*Yong, Silva, and Polifke, Combust. Flame 228 (2021)*) proposed the use of phasor diagrams to categorize marginally stable modes in an ideal resonator with a compact, velocity-sensitive flame. Modes with velocity phasors that reverse direction across the flame were categorized as ITA modes. The present study extends this concept to growing and decaying modes. In other words, with the method proposed, it is possible to distinguish whether a given thermoacoustic mode – regardless of its stability – should be categorized as acoustic or ITA. The method proposed does not rely on any parametric sweep, but on the angle relating the velocity phasors across the flame. This method of categorization reveals distinct regions in the complex plane where acoustic and ITA eigenfrequencies are localized. Additionally, we analyze the medium oscillation at the flame location to construct a physically intuitive understanding of the proposed categorization method.

1. Introduction

Thermoacoustic combustion instabilities (TCI) have been the subject of investigation over the past several decades due to their detrimental effects on combustion systems. Recently, the increased demand for cleaner, more efficient and more flexible combustion technologies has driven the need for lean premixed combustors, which are deemed more susceptible to TCI [1–3]. The onset of TCI is attributed to a positive feedback coupling between a fluctuating flame and acoustic perturbations [1,4–6]. Acoustic waves are generated by the unsteady volumetric expansion in the reactive region. According to the established understanding, these acoustic waves propagate upstream or downstream until reaching the acoustic boundaries, where they are reflected back towards the flame. At the flame, the reflected waves may perturb the flow variables associated with the flame such as the equivalence ratio, the swirl number, and especially the velocity of the incoming premixture, which in turn perturb the heat release rate, thus closing the feedback loop. If the heat release rate fluctuations are in-phase with the pressure fluctuations (fully or partially), i.e., if heat is given to the medium at the moment of greatest condensation, energy is transferred from the flame to the acoustic field [7]. Provided that acoustic dissipation is low, self-excited oscillations may ensue. However, in the feedback loop mechanism described above, the flame may be insensitive to acoustic fluctuations, i.e., a passive flame that only induces a temperature discontinuity. In this case, the reflected acoustic waves result in a standing wave mode – '*pure* acoustic mode'. Such mode is either marginally stable or damped, if dissipation and losses are taken into account.

This description of flame-acoustic feedback was shown to be incomplete, as the 'intrinsic thermoacoustic (ITA) feedback loop' was discovered [8,9]. This ITA loop may be visualized in a signal flow chart as in Fig. 1 (red-dashed pathway). This feedback loop describes a more immediate route for the flame-acoustic perturbation to occur without involving the boundary reflections: the upstream velocity perturbation u'_u triggers a flame response $\dot{Q}'$, which in turn generates an acoustic wave g_u that travels upstream to perturb the upstream velocity, thereby closing the loop [8,9]. Thermoacoustic modes generated solely through this feedback loop are known as '*pure* ITA modes'. We may deduce from Fig. 1 that all modes observed in a system with non-vanishing boundary reflections and a fluctuating flame are the result of the interplay between both the acoustic and ITA feedback loops. Indeed, Emmert et al. [10] introduced the notion that a thermoacoustic mode in an echoic chamber can be predominantly associated either with the ITA loop – 'ITA modes' – or with the acoustic loop – 'acoustic modes', after demonstrating that the number of modes in a closed-open combustor exceeds the number of acoustic modes. The results of other numerical studies, which examined the changes in frequency and growth rate as the boundary reflection coefficients gradually increased from zero [8,11], are consistent with this assertion.

---

* Corresponding author.
E-mail address: yong@tfd.mw.tum.de (K.J. Yong).

https://doi.org/10.1016/j.combustflame.2022.112605

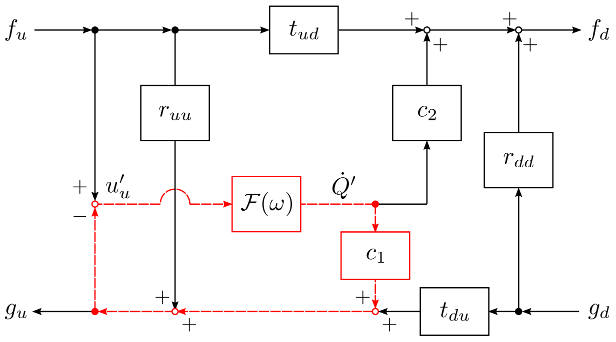

Fig. 1. The signal flow chart visualizes the scattering pathways of the characteristic wave amplitudes $f_{[\ ]}, g_{[\ ]}$ at the discontinuity due to the presence of a velocity sensitive flame. The indexes $[\ ]_u$ and $[\ ]_d$ indicate the location at the immediate upstream and downstream of the flame. $r_{uu}, t_{ud}, t_{du}, r_{dd}$ are scattering matrix elements that describes the acoustic wave scattering due to the an impedance change across the flame interface (see Emmert et al. [9] for the exact definitions). c_1, c_2 are the gain factors that correspond to the production of acoustic waves traveling upstream and downstream g_u, f_d due to the fluctuating heat release rate $\dot{Q}'$. The red-dashed lines highlight the ITA feedback mechanism: the upstream velocity perturbation u'_u triggers a flame response $\dot{Q}'$ described by the flame transfer function $\mathcal{F}(\omega)$. The flame response facilitates the production of an acoustic wave travelling upstream g_u, which in turn mediates u'_u, closing the feedback loop. (For interpretation of the references to color in this figure legend, the reader is referred to the web version of this article.)

The ability to distinguish ITA modes from acoustic modes becomes important, when one tries to understand if certain behavior observed either in simulations or in experiments are inherent to ITA modes. One of the most discussed behaviors, which was attributed to ITA modes in the studies [10,12], is mode destabilization upon boundary damping. This phenomenon was also confirmed in an experiment [13], where an acoustic liner at the end of the combustor suppressed instabilities associated with acoustic modes, but promoted those associated with ITA modes. Furthermore, eigenfrequencies of ITA modes are thought to be less sensitive to changes in combustor length than acoustic modes [12,14]. This conclusion was supported by the fact that the intrinsic feedback loop of the flame does not require acoustic waves traveling through the entire combustor (see above).

A variety of ad hoc methods were proposed to achieve the goal of mode categorization. Emmert et al. [10] introduced a coupling parameter μ to modulate the coupling between the acoustic and ITA feedback loops in a thermoacoustic system, i.e., the coupling between the fluctuating heat release rate $\dot{Q}'$ and the characteristic wave amplitudes f, g. As μ was gradually reduced from unity to 0, the existing eigenmodes either tracked to a ‘pure ITA mode’– modes found exclusively in an anechoic environment – or to a ‘pure acoustic mode’ – modes found in a system with a passive flame (flame that is insensitive to acoustic fluctuations). These modes were thus categorized as ITA and acoustic modes, respectively. In the same vein, other authors [15–18] performed the sweep of parameters such as the flame gain or the reflection coefficients. Alternatively, proximity to a pure ITA or pure acoustic mode is used to identify an ITA or acoustic mode [11,19–21]. Other studies, including [13,22], simply made use of the established characteristics of pure ITA modes, say, independence of eigenfrequency from combustor length or eigenfrequency correspondence with a characteristic time delay of the flame response, to identify ITA modes.

Aside from being impractical in situations where parametric variation is difficult or expensive, these methods suffer from multiple limitations. For instance, methods that rely on the closeness of a mode eigenfrequency to the corresponding frequency of pure acoustic or ITA modes, are only applicable to a limited number of modes. A parameter sweep often entails a stark variation of system parameters, which modifies the nature of the modes of interest. Indeed, Mukherjee et al. [23] observed that the pressure profile of the ITA modes and the acoustic modes categorized by the tracking of the flame gain become indistinguishable from each other for a moderately large gain. As an acoustic mode ‘approaches a nearby ITA mode, it stops behaving like an acoustic mode’. The concept of modes switching identities under parametric variation was asserted by Hosseini et al. [18], as a complex interplay between ITA and acoustic modes was demonstrated under variation of parameters such as time delay, reflection coefficients, or temperature ratio across the flame. This assertion was reinforced by the results in Silva et al. [16], Sogaro et al. [19]. The lack of a physically based categorization method has led to the claim that mode identities do not correlate with specific mode behaviors. As such, Mukherjee et al. [23] speak of ‘born acoustic’ or ‘born ITA’ modes, which are modes that tracked to pure acoustic or pure ITA modes at the limit of small gain and have no correlation to the established characteristics typical for a pure acoustic or pure ITA mode. Similarly, Orchini et al. [17] classified the eigenmodes into modes of ‘acoustic origin’ and ‘ITA origin’, while highlighting the shared mode shape features between them in the proximity of an exceptional point.

Yong et al. [24] proposed a method that does not involve a parameter sweep to categorize marginally stable modes in an ideal cavity. Phasors and phasor diagrams were used to represent the acoustic variables, i.e., the characteristic wave amplitudes and the fluctuations in pressure, velocity and heat release rate. The phasor diagram in an anechoic environment reveals that pure ITA modes exhibit velocity phasors that are perfectly out of phase across the flame, which implies a change in sign of the pressure gradient across the flame. Interestingly, the same phasor characteristic is applicable to marginally stable modes in an ideal resonator, providing that the respective flame is sufficiently strong in gain and acts in the opposite direction of the upstream velocity. Due to the analogous phasor characteristic to pure ITA modes, these marginally stable modes are subsequently categorized as ITA modes. This method of ITA mode categorization is coherent with the previous works that investigated pure ITA modes [8,9,15], which concluded that ITA modes may arise when the FTF phase is equal to an odd multiple of π – the ‘π-criterion’.

Unlike the previously proposed methods, the phasor based categorization proposed by Yong et al. is physically motivated, not limited to a specific flame model such as the $n-\tau$ model, applicable in a variety of combustor setups, and also readily implementable in experimental settings. However, that proposed criterion has its limitation as Yong et al. [24] only investigated the marginally stable modes in an ideal resonator. In this work, we extend the scope of the phasor analysis to growing or decaying thermoacoustic modes, which allows the generalization of the phasor criterion.

This paper is structured as follows: The next section introduces phasor diagrams for wave propagation and thermoacoustic coupling across a compact heat source for non-zero growth rates. The differences to the phasor diagram of a marginally stable mode are highlighted. In the process, the influence of the non-zero growth rates on the flame transfer function (FTF) in terms of magnitude and phase are discussed. The second section serves as a preparatory stage for the core findings in the following sections. Here, the categorization of marginally stable thermoacoustic modes that relies on the direction reversal of the velocity phasors across the flame is recapitulated. Then, two limiting cases – highly decaying and highly unstable modes – are analyzed using the previous criterion. The third section inspects the phasor diagrams of a large variety of moderately unstable and decaying modes. Based on their distribution in a stability map, modes with partially aligned or partially anti-aligned velocity phasors across the flame are categorized as acoustic or ITA, respectively. It is demonstrated that a continuous increase or decrease in growth rates necessarily leads to a continuous transition of marginally stable acoustic modes into ITA modes at infinite growth and decay rates. In the subsequent section, the relative orientation of the velocity phasors is quantified in terms of the scalar product and visualized in contour maps that reveal the regions of acoustic and ITA modes. In the contour maps, an alternating pattern of decreasing and increasing size of the acoustic regions along the real axis is observed. This pattern is shown to directly correspond to the flame position. To complete the section, the transitional magnitude and phase of the FTF are derived. Finally, a physical interpretation is given to the categorization criterion, where the velocity phasors at the flame are interpreted as the physical motion of the flame medium. Acoustic modes and ITA modes are described as modes that predominantly exhibit a back-and-forth versus an inwards-and-outwards oscillation at the flame, respectively. The paper ends with summary, conclusions and outlook.

Note that this work is a follow-up study of Yong et al. [24]. Thus, we highly recommend the readers to read the previous paper, to gain a better understanding on the construction of phasors and phasor diagrams, as well as the notations and keywords used.

2. Phasor diagrams of characteristic wave amplitudes for non-zero growth rates

In this section, we explore the spatial dependency of the characteristic wave amplitudes of modes with non-zero growth, and produce the corresponding phasor diagrams. The propagation of 1D plane waves may be expressed in terms of characteristic waves f and g

$$f(x,t) = \hat{f}(x)e^{i\omega t} = \hat{f}(x_{\text{ref}})e^{i\omega t - ikx},$$
$$g(x,t) = \hat{g}(x)e^{i\omega t} = \hat{g}(x_{\text{ref}})e^{i\omega t + ikx} \tag{1}$$

where

$$\hat{f}(x) = \hat{f}(x_{\text{ref}})e^{-ikx}, \quad \hat{g}(x) = \hat{g}(x_{\text{ref}})e^{ikx} \tag{2}$$

describes the characteristic wave amplitudes (CWA), which propagate at the mean speed of sound $\bar{c}$ in $\pm x$ direction, respectively; $k = \omega/\bar{c}$ is the wave number for a medium at rest; ω is the eigenfrequency; x_{ref} indicates a reference location. As shown in Yong et al. [24], for real-valued frequencies $\omega \in \mathbb{R}$, the CWAs in Eq. (2) describe a respective f and g phasors rotation in the clockwise and counterclockwise direction as x increases, with an angle of rotation $\varphi = kx$. Figure 2 illustrates the 2D phasor diagram at an arbitrary location x in a cavity with the reflection coefficient at x_{ref} being

$$R_{\text{ref}} = \frac{\hat{f}(x_{\text{ref}})}{\hat{g}(x_{\text{ref}})} = 1. \tag{3}$$

The phasors of the primitive acoustic variables, i.e., fluctuations of normalized pressure $p'^{*} = p'/(\overline{\rho c})$ and velocity u' are obtained by adding and subtracting f, g phasors, according to the relation

$$p^{*\prime} = \frac{p'}{\overline{\rho c}} = \hat{f} + \hat{g}; \quad u' = \hat{f} - \hat{g}, \tag{4}$$

where $\overline{\rho}$ and $\overline{\rho c}$ represent mean density and specific impedance, respectively. For brevity, the apostrophe [ ]′, which indicates a fluctuation, and the hat [ˆ], which indicates a Fourier transformed variable, are omitted in all following figures as well as texts and equations. The overline $\overline{[\ ]}$ remains to indicate a mean value. A series of 2D phasor diagrams at different locations may be combined to generate a 3D phasor plot to depict the complete phasor evolution along the length of the cavity $x \in [0, L]$, as shown in Fig. 3 in Yong et al. [24]. The readers are invited to verify that the constraints of ideal boundaries and real-valued ω always result in a mirror symmetrical rotation of f, g. As a consequence, p^{*} and u are always in quadrature throughout the resonator.

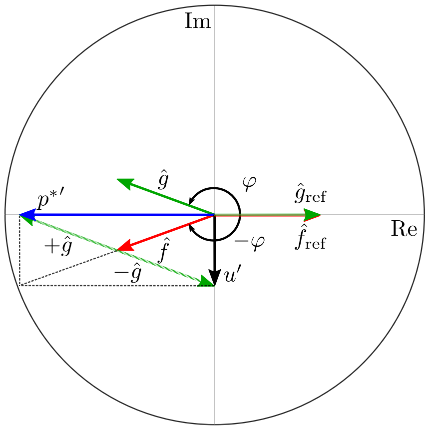

Fig. 2. A 2D phasor diagram depicting the evolution of the phasors of the CWAs $\hat{f}, \hat{g}$ in the $+x$ direction. The phase advance of the $\hat{f}, \hat{g}$ relative to the reference position $x = 0$ is given by $\varphi = kx$ in the clockwise- and counterclockwise directions, respectively, according to the factor $e^{\mp ikx}$ given in Eq. (2). It is important to note that the time harmonic factor $e^{i\omega t}$ is factored out in a phasors representation. The phasor of the primitive variables $p^{*\prime}, u'$ are obtained through addition and subtraction between the $\hat{f}, \hat{g}$ phasors, according to Eq. (4).

Fig. 3. Schematic representation of a simple quasi-1D cavity with a velocity-sensitive flame located at x_f. The locations of inlet, outlet, flame upstream and flame downstream are indicated by 'in', 'out', 'u', and 'd' respectively. These labels are used as indices for the variables throughout this paper to point to the given specific locations. The inlet at $x = 0$ and the outlet at $x = L$ are ideally closed ($u_{\text{in}} = 0$) and open ($p_{\text{out}} = 0$), respectively. The 'cold' and 'hot' sections are colored white and orange, with constant mean temperatures T_u and T_d, respectively.

In the case of net generation or loss of acoustic energy at the compact elements (flame, area change, damper, ...) or at the system terminations, ω may be complex valued,

$$\omega = \omega_r + i\omega_i = \omega_r - i\sigma, \tag{5}$$

where ω_r is the angular frequency and σ is the growth rate, with $\sigma > 0$ describing a growth of acoustic variables f, g as well as p, u in time. Recalling (2) and the dependence of wave number on frequency $k = \omega/\bar{c}$, it is evident that the f phasor amplitude decreases, while the g phasor amplitude increases with x, in the case of $\sigma > 0$. It appears counter-intuitive, but a growth in the time domain corresponds to a decay in space. This characteristic is visualized in Fig. 4. From the flame location x_f, f and g waves propagate upstream and downstream at constant amplitude, respectively. As time progresses, stronger characteristic waves are being produced at x_f due to the positive growth. As a result, the wave profiles appear to be decaying in the direction of wave propagation.

2.1. Flame-acoustic coupling

Growing or decaying thermoacoustic modes are the result of imbalanced acoustic gain and loss. In this work, we consider an active flame, i.e., a flame with unsteady heat release, the sole mechanism for the gain or loss of acoustic energy in an ideal closed-open resonator as depicted in Fig. 3. At low Mach numbers, a compact premixed flame introduces a discontinuity in the acoustic field in two ways: first, the increase in mean temperature across the flame

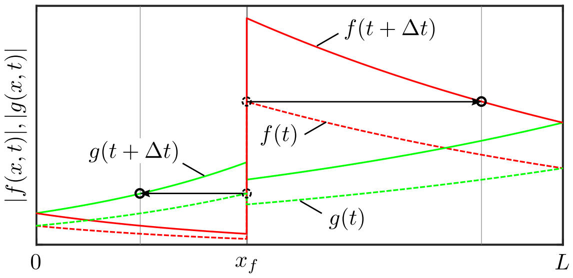

Fig. 4. The amplitude of the characteristic waves $|f|$ (red) and $|g|$ (green) as a function of x at different time delay Δt for a growing thermoacoustic mode $\sigma > 0$. Without essential loss of generality, the flame position is chosen to be the reference position, $x_{\text{ref}} = x_f$. The dashed and solid lines indicate the profiles at initial time and delayed time respectively. The arrows show the direction of wave propagation. In general, f and g grow with time due to energy production at the flame. As time progresses, they propagate without loss or growth across the ideal resonator, resulting in the decaying profile in the direction of propagation. (For interpretation of the references to color in this figure legend, the reader is referred to the web version of this article.)

changes the specific impedance, thus also the partial transmission and reflection of acoustic waves; second, the unsteady heat release rate modifies the relation of velocity perturbation (magnitude and phase) between locations just up- and downstream of the flame. These effects are summarized in the coupling relations for acoustic variables across the flame – the linearized 'Rankine-Hugoniot' (RH) relations [25–28]. For low Mach number flow ($\bar{u}_u \ll \bar{c}_u$), the RH relations reduce to

$$p_d^* = \xi p_u^*, \quad u_d = u_u + \underbrace{\theta \bar{u}_u \frac{\dot{Q}}{\bar{\dot{Q}}}}_{u_q}, \tag{6}$$

where the indices $[\ ]_u$ and $[\ ]_d$ indicate the flame upstream and downstream positions, $\xi = (\bar{\rho}_u \bar{c}_u)/(\bar{\rho}_d \bar{c}_d)$ is the ratio of specific impedance, $\theta = \bar{T}_d/\bar{T}_u - 1$ is the relative temperature increment, and u_q is the displacement rate contribution due to heat release rate fluctuation $\dot{Q}$.[1]As summarized in the Rayleigh index (RI) [4,6,7], acoustic energy will be produced by the flame, if the heat release rate fluctuations are (fully or partially) in-phase with the pressure perturbations,

$$\text{RI} \equiv \oint p\dot{Q}\ \mathrm{d}t > 0. \tag{7}$$

In an ideal resonator, where acoustic energy is not lost through the boundaries or flow entropies, a positive Rayleigh index at the flame corresponds directly to the onset of instabilities, which is represented by a positive growth rate $\sigma > 0$.

The heat release rate of a compact premixed flame is velocity sensitive [6,11,29,30]. As such, the dependency of the heat release rate fluctuation $\dot{Q}$ on the velocity perturbation on the flame upstream u_u may be characterized by a frequency dependent *flame transfer function* (FTF) $\mathcal{F}(\omega)$ as given in Eq. (8).

$$\frac{\dot{Q}(\omega)}{\bar{\dot{Q}}} = \mathcal{F}(\omega)\frac{u_u(\omega)}{\bar{u}_u} \tag{8}$$

In general, the FTF may be written as

$$\mathcal{F}(\omega) = |\mathcal{F}(\omega)| e^{i\phi_f(\omega)}. \tag{9}$$

where $|\mathcal{F}(\omega)|$ is the magnitude, and $\phi_f(\omega)$ is the phase of the FTF relative to the upstream velocity perturbation. For stability analysis, the FTF needs to be evaluated over all complex frequencies $\omega \in \mathbb{C}$. It should be distinguished from the *flame frequency response* (FFR) $F(\omega_r)$, which describes the flame response at real valued frequencies[2]

Table 1
Impulse response coefficients h_k for DTD model.

k	2	3	4	5	6	7	8	9
h_k	0.1	0.3	0.6	0.3	0.1	−0.1	−0.2	−0.1

$$F = \mathcal{F}(\omega_r). \tag{10}$$

This distinction is important, as for a given frequency ω_r and growth rate $\sigma \neq 0$, the magnitude of the FTF, does not equal the *gain* of the FFR. To illustrate the dependency of the FTF on σ, we consider, by way of example, the simple $n-\tau$ model [31]

$$\mathcal{F}(\omega) = ne^{-i\omega\tau} = ne^{-\sigma\tau}\ e^{-i\omega_r\tau}. \tag{11}$$

Comparing Eqs. (9) and (11) gives the FTF magnitude and phase

$$|\mathcal{F}(\omega)| = ne^{-\sigma\tau}, \quad \phi_f(\omega) = -\omega_r\tau, \tag{12}$$

where n represents the gain of the corresponding FFR. In this model, σ contributes purely to the FTF magnitude, while the oscillation frequency ω_r contributes to the phase. In a more realistic flame model that exhibits excess gain and a low-pass behavior, such as the distributed time delay (DTD) model [32]

$$\mathcal{F}(\omega) = \sum_{k=0}^{+\infty} h_k e^{-i\omega k\Delta t} = \sum_{k=0}^{+\infty} h_k e^{-\sigma k\Delta t}\ e^{-i\omega_r k\Delta t}, \tag{13}$$

with the impulse response coefficients h_k, and the sampling time step Δt, both the FTF magnitude and phase are influenced by the growth rate and frequency. However, due to the exponential scaling of $e^{-\sigma k\Delta t}$, one might expect that non-zero growth rates have a greater impact on the FTF magnitude than on the phase. From Eq. (13), it is not difficult to see that $\sigma \gg 0$ will result in a reduction of the corresponding weights of the impulse response h_k, i.e., $e^{-\sigma k\Delta t} \ll 1$, and thus an overall reduction of the FTF magnitude. As an example, the FTF magnitude and phase of a DTD modeled flame with eight coefficients h_k (c.f., Table 1) are depicted in Fig. 5. Essentially, we observe that an increase in growth rate generally results in the reduction of $|\mathcal{F}(\omega)|$ for a given flame, but has relatively small impact on $\phi_f(\omega)$.

In an experiment where only the FFR is available, the corresponding FTF could be generated from the FFR by extrusion, Taylor expansion, or filtering [32–36].

2.2. Dispersion relation of the thermoacoustic system

The interaction between flame and acoustics in a resonator may be summarized by the corresponding dispersion relation. For the setup illustrated in Fig. 3, the dispersion relation is given by

$$\xi \underbrace{\frac{\cos\varphi_u(\omega)}{\sin\varphi_u(\omega)}}_{-iZ_u(\omega)} - (1+\theta\mathcal{F}(\omega)) \underbrace{\frac{\sin\varphi_d(\omega)}{\cos\varphi_d(\omega)}}_{-iZ_d(\omega)} = 0 \tag{14}$$

with $\varphi_u(\omega) = \omega x_f/L$, $\varphi_d(\omega) = \omega(1 - x_f/L)$, and $Z_{[u,d]}(\omega) = p^*_{[u,d]}/u_{[u,d]}$ being the frequency dependent acoustic impedance of the flame upstream and downstream (see Yong et al. [24] for detailed derivations). On the one hand, this dispersion relation could be solved for the eigenfrequencies ω and thus the eigenmodes, if

---

[1] Without essential loss of generality, u_q is used interchangeably to represent $\dot{Q}$ in this work. These quantities are proportional and in-phase.

[2] Note that in the literature there is often no strict distinction between the FTF and the FFR. We find it helpful to distinguish between them here, as the FTF magnitude incorporates a non-zero growth rate (see above), which goes against the intuitive understanding of flame strength, i.e., FFR gain.

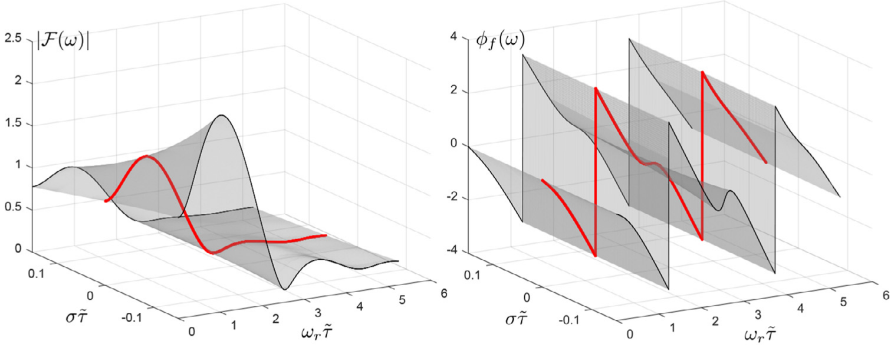

(a) (b)

Fig. 5. Surface plot of the (a) FTF magnitude $|\mathcal{F}(\omega)|$ and (b) phase $\phi_f(\omega)$ of a DTD model with h_k given in Table 1, $\tilde{\tau} = 10\Delta t$, with respect to the oscillation frequency ω_r and growth rate σ. The inscribed red curves along the real frequency axis mark the FFR. An increase in σ reduces the magnitude of the FTF, but has a minimal impact on its phase. (For interpretation of the references to color in this figure legend, the reader is referred to the web version of this article.)

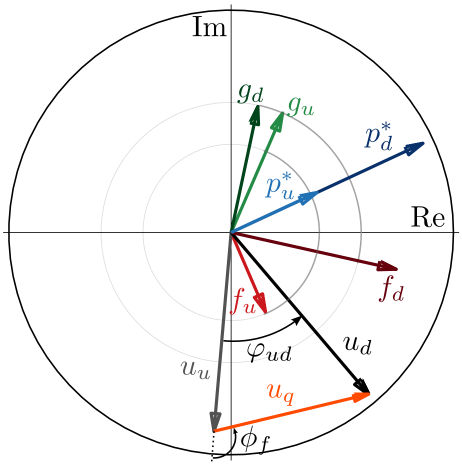

Fig. 6. 2D phasor diagram depicting the phasors of an unstable mode ($\sigma > 0$) at the upstream $[\ ]_u$ and the downstream $[\ ]_d$ of the flame at $x = x_f = 0.4L$, with the FTF gain and phase being $|\mathcal{F}| = 0.2$ and $\phi_f = 0.6\pi$, respectively. The concentric circles act as a guide to highlight the difference in magnitude between the f and g. The non-symmetrical f, g phasors result in a phase difference between u_u and u_d, $\varphi_{ud} \in (0, \pi)$.

the FTF is known. On the other hand, it could also be solved for the FTF, if the mode eigenfrequency ω is given,

$$\mathcal{F}(\omega) = \frac{1}{\theta}\left(\xi \frac{Z_u(\omega)}{Z_d(\omega)} - 1\right). \tag{15}$$

The phasor diagram in Fig. 6 depicts, by way of example, the phasors of acoustic variables immediately upstream and downstream of the flame for a growing mode $\sigma > 0$ (RI > 0) in the ideal closed-open resonator depicted in Fig. 3. In contrast to marginally stable modes analyzed in Yong et al. [24], the relative phase between the velocity phasors u_u, u_d is not restricted to $\varphi_{ud} = 0$ or $\varphi_{ud} = \pi$, but may have intermediate values $\varphi_{ud} \in [-\pi, \pi]$ determined by the growth rates. The phasor plot also highlights the asymmetrical f, g phasors (w.r.t. the real axis) and correspondingly the non-perpendicular p, u phasors (compare these features against the phasors arrangement for a case $\sigma = 0$ as in Yong et al. [24]). For illustrative purpose, the 3D phasor plot is given in Fig. 7.

3. Thermoacoustic modes with infinite growth or decay rates in an ideal resonator

In this section, we briefly recapitulate the ITA categorization of marginally stable modes as proposed in Yong et al. [24]. Subsequently, we investigate the phasors characteristics of extreme cases in the same ideal closed-open cavity, i.e., modes with extreme growth/decay rates $\sigma \to \pm\infty$. We will show that such modes may be categorized as ITA or acoustic modes using the existing criterion. These observations will set the basis for the general case in the next section.

3.1. Marginally stable modes

In our previous work [24], the marginally stable modes in an ideal resonator, i.e., modes with real-valued frequencies $\omega \in \mathbb{R}$, were analyzed in terms of the velocity phasors. It was demonstrated that due to the symmetric rotation of the f, g phasors (as discussed), the velocity phasors before and after the flame u_u, u_d must be either perfectly aligned or anti-aligned. The modes with perfectly aligned u_u, u_d are categorized as acoustic modes. In contrast, the modes with perfectly anti-aligned u_u, u_d are categorized as ITA modes due to their resemblance to pure ITA modes, i.e., thermoacoustic modes in an anechoic environment. On the frequency axis, acoustic modes continuously transition into ITA modes and vice versa under a continuous variation of the FTF magnitude (or FFR gain, see discussions above), c.f., in Yong et al. [24].

3.2. Extremely growing modes

At positive growth rates $\sigma > 0$, the amplitudes of the outgoing acoustic waves generated at the flame f_d, g_u are larger than the incoming waves g_d, f_u. Recall from the previous section that the resonator and the boundaries are regarded as ideal, which allows the acoustic waves generated by the flame to propagate without dissipation to and from the boundaries. Thus, the incoming waves, say, g_d in the downstream cavity, may be regarded as outgoing waves f_d generated at earlier times, which were reflected back at the downstream termination $x = L$, c.f., Fig. 4. Thus, we may formulate

$$g_d(t) = -f_d(t - 2\tau_d) \quad \Rightarrow \quad |g_d| = |f_d|\ e^{-2\sigma\tau_d} < |f_d| \tag{16}$$

where $\tau_d = (L - x_f)/c_d$. Correspondingly, in the upstream cavity

$$f_u(t) = g_u(t - 2\tau_u) \quad \Rightarrow \quad |f_u| = |g_u|\ e^{-2\sigma\tau_u} < |g_u| \tag{17}$$

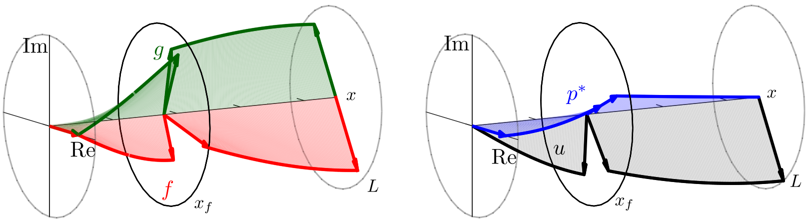

(a) (b)

Fig. 7. 3D phasor diagram of (a) f, g and (b) p^*, u for an unstable thermoacoustic mode $\sigma > 0$, with FTF gain $|\mathcal{F}| = 0.13$ and phase $\phi_f = 0.6\pi$, and $x_f = 0.4L$. Within the system boundaries, the f, g phasors are non-symmetric, due to an amplitude decay of f, while simultaneously an amplitude growth of g in the $+x$ direction. As a result, the p^*, u phasors are not in quadrature to each other.

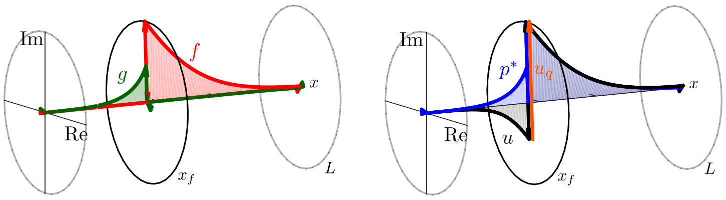

(a) (b)

Fig. 8. 3D Phasor diagrams of an ITA mode with $\sigma = 10^3$ and $x_f = 0.4L$, depicting the evolution of (a) f, g phasors and (b) p^*, u phasors in the $+x$ direction in an ideal closed-open cavity. The dominant outgoing CWAs f_d, g_u and negligible incoming CWAs f_u, g_d are visualized in (a). As evident in (b), the velocity phasor at the immediate flame downstream u_d is almost at π-radians phase difference with respect to the upstream velocity u_u. At the same time, the heat release phasors u_q is almost aligned with the pressure fluctuation p^* to generate a maximum acoustic energy. Note that the phasor diagrams of the pure ITA mode at the same frequency are completely identical. The animation showing the medium oscillation for this mode is provided as supplementary material^6 following the discussions in Section 5.2.

where $\tau_u = x_f/c_u$. In the limit of $\sigma \to +\infty$, the incoming waves f_u, g_d vanish, as would be the case in an anechoic environment. Recalling Eq. (4), the acoustic variables p^*, u immediately upstream and downstream of the flame must satisfy

$$\begin{array}{ll} p_d^* = f_d + g_d = f_d, & u_d = f_d - g_d = f_d \\ p_u^* = f_u + g_u = g_u, & u_u = f_u - g_u = -g_u \end{array} \quad \Leftrightarrow \quad \begin{array}{ll} p_d^* & = u_d \\ p_u^* & = -u_u \end{array} \tag{18}$$

Inserting Eq. (18) into the pressure coupling relation given in Eq. (6), we obtain

$$u_d = -\xi u_u. \tag{19}$$

As shown above, the infinite growth rate implies a flipping of velocity phasor across the flame. Generalizing the categorization established in our previous study, we conclude that extremely growing thermoacoustic modes should be regarded as ITA modes.

Substituting Eq. (19) into Eq. (6), we derive the FTF magnitude $|\mathcal{F}(\omega)|$ at the limit of $\sigma \to +\infty$.

$$\lim_{\sigma \to +\infty} \mathcal{F}(\omega) = -\frac{\xi + 1}{\theta} \in \mathbb{R}^-, \ \omega \in \mathbb{C} \tag{20}$$

$$\Rightarrow \quad |\mathcal{F}(\omega)| = \frac{\xi + 1}{\theta}, \quad \phi_f(\omega) = (2m+1)\pi \tag{21}$$

With this FTF, we can show that the unsteady heat release rate $\dot{Q}$, which is represented by u_q

$$u_q = u_u \theta \mathcal{F}(\omega) = -(1+\xi) u_u \tag{22}$$

is perfectly in-phase with the pressure fluctuation (c.f., Fig. 8), thus satisfying the Rayleigh criterion for a thermoacoustic instability

$$\begin{aligned} \mathrm{RI} &\equiv p_u^* \cdot u_q \\ &= (-u_u) \cdot (-(1+\xi) u_u) \\ &= (1+\xi)|u_u|^2 > 0. \end{aligned} \tag{23}$$

To achieve the high growth rates, the strength of the flame response, which is represented by the FFR gain must be infinitely large. Take the $n - \tau$ model for example, where the FFR gain is directly proportional to the growth factor $e^{\sigma\tau}$.

$$|\mathcal{F}(\omega)| = n e^{-\sigma\tau} = \frac{\xi + 1}{\theta} \quad \Leftrightarrow \quad n = \frac{\xi + 1}{\theta} e^{\sigma\tau} \tag{24}$$

Evidently, the growth of acoustic waves is not directly associated with the FTF magnitude, but with the gain of the FFR. If a flame with an extremely high gain responds in the opposite phase with respect to the upstream velocity perturbation, instability with extremely high growth rate will ensue (as expected).

3.3. *Extremely decaying modes*

Another limiting case is that of extremely decaying modes $\sigma \to -\infty$. In this case, we find a complete annihilation of acoustic energy at the flame, such that no acoustic waves are transmitted or produced. The amplitude of the outgoing acoustic waves becomes negligibly small $f_d, g_u \to 0$. In analogy to the previous subsection, one derives from (16), (17)

$$p_d^* = -u_d, \quad p_u^* = u_u; \tag{25}$$

and the coupling relation

$$u_d = -\xi u_u, \tag{26}$$

which is identical to that given in Eq. (19). A change in sign of the velocity fluctuations across the flame is expected, thus strongly decaying modes are as well ITA modes. We obtain the FTF magnitude and phase $|\mathcal{F}(\omega)| = (\xi + 1)/\theta$, $\phi_f = (2m+1)\pi$, which is identical to Eq. (21). Although the FTF is identical to that in the extremely unstable case, we are not dealing with the same flame as discussed. In fact, the FFR gain approaches 0 here, which is however scaled up by the high decay rate $\sigma \to -\infty$ (see (24)). Physically, this case describes an annihilation of the pressure buildup at the flame by the reduction in heat release rate fluctuation due to the diminishing flame gain.

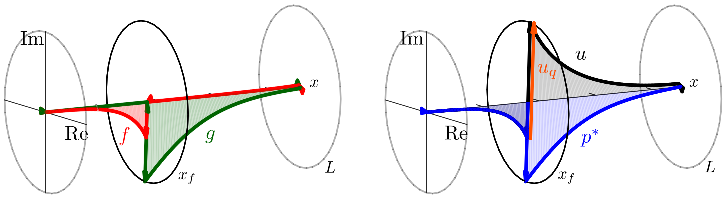

(a) (b)

Fig. 9. 3D Phasor diagrams of an ITA mode with large decay rate $\sigma = -10^3$ and $x_f = 0.4L$, depicting the evolution of (a) f, g phasors and (b) p^*, u phasors in the $+x$ direction in an ideally closed-open cavity. (a) visualizes the dominant incoming CWAs f_u, g_d and negligible outgoing CWAs f_d, g_u. As evident in (b), the velocity phasor at the immediate flame downstream u_d is almost at π-radians phase difference with respect to the upstream velocity u_u. At the same time, the heat release phasors u_q is almost fully anti-aligned with the pressure fluctuation p^* to cause maximum annihilation of acoustic energy. Note that u_u is hidden by p_u^* in (b).

Table 2
Setup parameters for the computation of thermoacoustic modes.

Parameter	Value
x_f/L	0.4
L	0.9 m
T_u	300 K
T_d	1500 K
θ	4
ξ	2.24

In Fig. 9, the 3D phasor plot for an extremely decaying mode is visualized. The localized amplitudes of the incoming waves f_u, g_d is immediately visible in the f, g plot. Beside that, the u_q phasor that is almost fully out-of-phase with p^* indicates that acoustic energy is annihilated by the thermoacoustic interactions at the flame

$$\begin{aligned} \mathrm{RI} &\equiv p_u^* \cdot u_q \\ &= (u_u) \cdot (-(1+\xi)u_u) \\ &= -(1+\xi)|u_u|^2 < 0. \end{aligned} \tag{27}$$

The conclusion that extremely decaying thermoacoustic modes are generally ITA is coherent with the findings in several studies, in particular [15,17]. It was shown that the characteristic equation in (14) may be simplified to that of a pure ITA mode [9], as the ratio of acoustic impedances $Z_u(\omega)/Z_d(\omega)$ approaches -1 at $\sigma \to -\infty$

$$1 + \xi + \theta\mathcal{F}(\omega) = 0. \tag{28}$$

4. Transition between acoustic and ITA modes with non-zero growth rates

In the previous section, we have seen that modes in the extreme case of $\sigma \to \pm\infty$ are generally ITA. Conversely, modes on the real frequency axis consist of alternating acoustic and ITA modes [24]. This leads to the obvious questions: what happens for intermediate values of growth rates and where are transitions from acoustic to ITA modes away from the real axis? More importantly, how to define ITA modes that are not marginally stable? The latter question is warranted, as the u_u and u_d phasors are not perfectly aligned or anti-aligned (see above). In that case, such modes are not readily categorizable with the criterion outlined in our previous work [24].

To identify, in a heuristic manner, a meaningful phasor characteristic for the purpose of mode categorization, a large variety of thermoacoustic modes are computed with random combinations of FTF magnitude $|\mathcal{F}(\omega)|$ and phase $\phi_f(\omega)$. The dispersion relation in (14) is solved for the corresponding complex eigenfrequencies. The relevant setup parameters are given in Table 2.

With the frequencies and FTFs known, the velocity phasors u_u, u_d are generated and the frequencies are plotted in a stability map, c.f., Fig. 10. Note that only a handful of these phasor plots are depicted in the figure (labeled with numbers) to limit clutter. The stability map reveals:

(i) groups of modes in the vicinity of pure acoustic modes $\omega_{p,i}$ – modes for the passive flame case – on the neutral curve with partially aligned velocity phasors u_u, u_d (represented by the blue triangles) ;
(ii) modes outside of the groups in (i), with partial anti-alignment of u_u, u_d (represented by the red circles).

Generalizing this observation, we categorize the former as acoustic modes and the latter as ITA modes. At the transition region between acoustic and ITA modes, u_u and u_d phasors are perpendicular to each other. For illustrative purpose, the full 2D phasor diagrams of an acoustic mode (“1” in Fig. 10) and an ITA mode (“6” in Fig. 10) are visualized in Fig. 11.

In an effort to closer investigate the mode transition from acoustic to ITA, we take an acoustic mode on the real axis and judiciously modify the FTF such that the growth rate decreases. This yields a set of thermoacoustic modes with the same oscillation frequency ω_r but different growth rates $\sigma \in (-\infty, 0]$. The corresponding FTFs (magnitude and phase) are computed using Eq. (15). The resulting phasor diagrams are displayed in Fig. 12. The locations in a stability map of each mode in Fig. 12(a)–(e) are labeled correspondingly in Fig. 10 along the dotted vertical line. As the growth rate decreases, u_q phasor rotates clockwise, such that the phase difference between itself and the pressure fluctuation $p_{[u,d]}$ grows – a direct consequence of a reduction of Rayleigh Index (as discussed). Consequently, u_d rotates in the same direction, which increases its phase deviation to u_u, $\varphi_{ud} > 0$. Figure 12(c) marks the transition of acoustic to ITA mode, where u_u, u_d – which are 90 degrees apart – switch from being partially aligned to partially anti-aligned. The rotation continues allowing u_u, u_d to reach full anti-alignment at high decay rates, at which the rotation stalls. This observation elucidates that the transition of the u_u, u_d phasors from aligned to anti-aligned is continuous in the complex plane. An analogous trend may be observed, if the growth rate is increased from 0 to $+\infty$ (not shown). In this case, instead of a clockwise rotation, u_q rotates counterclockwise to increase instability, which causes a similar change observed in Fig. 12. Note that the direction of rotation of u_q depends on the phase lag between the pressure and velocity phasors of the marginally acoustic mode. In this example given in Fig. 12(a), u lags p^*. Hence, a clockwise rotating u_q increases stability and vice versa.

5. Criterion for ITA modes with non-zero growth rates

In consideration of the above findings, we define a general criterion – Φ criterion – based on the scalar product between the

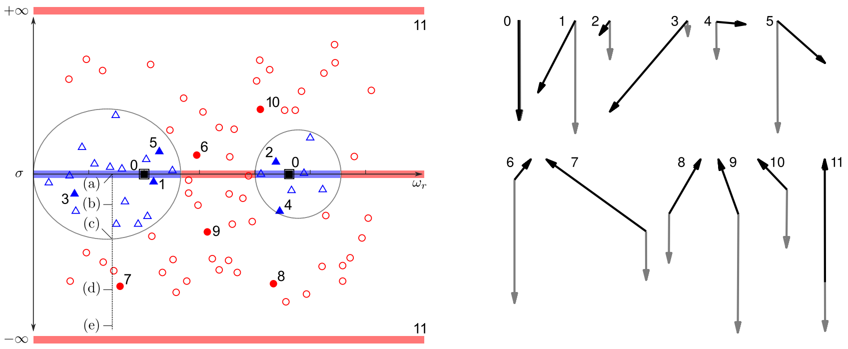

(a) (b)

Fig. 10. (a) A stability map depicting the distribution of modes with partially aligned u_u, u_d phasors (blue triangles) and those with partially anti-aligned u_u, u_d phasors (red circles). The black squares mark the pure acoustic modes $\omega_{p,i}$ ("0"). The red highlighted regions at $\sigma \to \pm\infty$ mark the known ITA modes in previous section, while the blue and red highlighted regions at $\sigma = 0$ are known respective acoustic and ITA modes in Yong et al. [24]. The phasor diagrams of modes at locations labeled (a)–(e) along the vertical dotted arrow are detailed in Fig. 12. The oval patches trace the approximate areas that separate the red circles from the blue triangles. (b) Five examples of velocity phasor plots among the blue triangles ("1–5") and the red circles ("6–10") are shown. For comparison purpose, the velocity phasor plot of the pure acoustic modes ("0"), and the ITA modes at $\sigma \to \pm\infty$ ("11") are included. The grey arrow represents u_u and the black arrow u_d. (For interpretation of the references to color in this figure legend, the reader is referred to the web version of this article.)

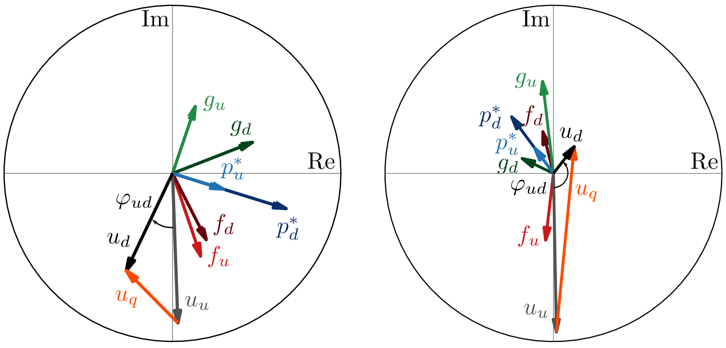

(a) (b)

Fig. 11. 2D Phasor diagrams depicting phasors at the immediate flame upstream $[\ ]_u$ and downstream $[\ ]_d$. (a) and (b) show the case where the velocity phasors u_u, u_d are partially aligned and partially anti-aligned, respectively (c.f., Fig. 10: "1" and "6"). The animations showing the medium oscillation for these modes are provided as supplementary materials[78] following the discussions in Section 5.2.

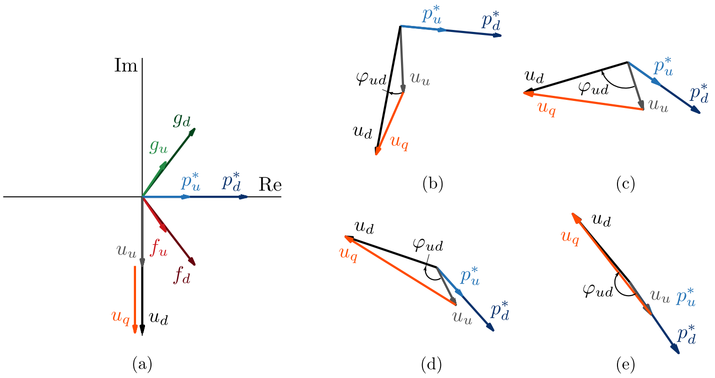

Fig. 12. The phasor diagrams for thermoacoustic modes with $\omega_r/\omega_{p,1} = 0.85$ and $\sigma/\omega_{p,1} \in [-2, 0]$. The FTF is computed using the dispersion relation in (15), which along with the complex frequency fully defines a mode. Besides (a), the phasor diagrams do not include the f, g phasors to reduce cluttering. (a) shows the full phasor diagram of a marginally stable acoustic mode (u_u, u_d in-phase, $p \perp u$). (b) shows a decaying acoustic mode ($\varphi_{ud} < \pi/2$). (c) shows a transitional mode ($\varphi_{ud} = \pi/2$). (d) shows a decaying ITA mode ($\varphi_{ud} > \pi/2$). (e) shows a highly decaying ITA mode, c.f., Section 3.3.

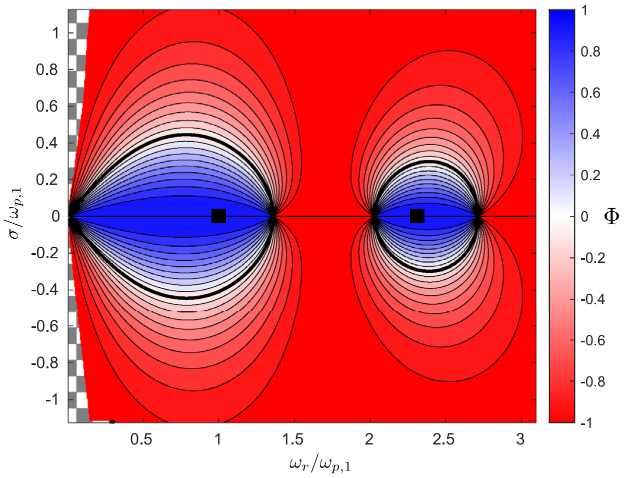

Fig. 13. Contour map of Φ within the range of $\omega_r/\omega_{p,1} \in (0, 3.1]$ and $\sigma/\omega_{p,1} \in [-1.2, 1.2]$ for $x_f = 0.4L$. The blue regions indicate acoustic modes ($\Phi > 0$) while the red region indicates ITA modes ($\Phi < 0$). The black squared markers on the neutral curve indicate the pure acoustic modes $\omega_{p,i}$. The black thickened lines tracing a semi circular path around $\omega_{p,i}$ indicate the transition of acoustic modes into ITA, and vice versa ($\Phi = 0$). The region with checkered background is where the dispersion relation could not be easily solved due to $\omega_r \to 0$. (For interpretation of the references to color in this figure legend, the reader is referred to the web version of this article.)

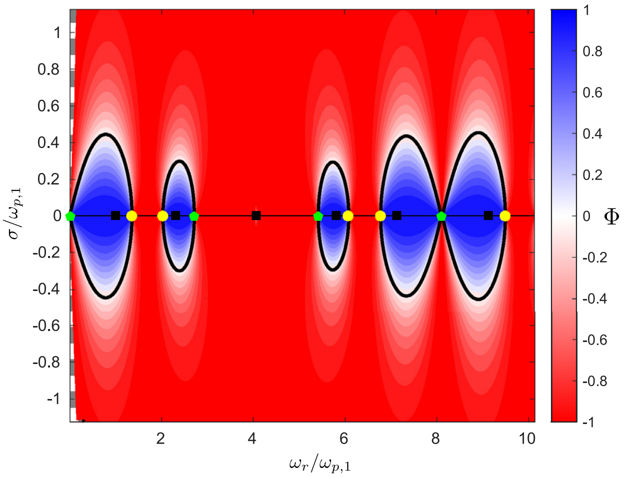

Fig. 14. Contour map of Φ for larger range of ω_r compared to Fig. 13. The black squares on the neutral curve indicate the pure acoustic modes $\omega_{p,i}$. The yellow circles indicate the acoustic-ITA transition of the marginally stable mode at which $\mathcal{F}(\omega) = -1/\theta$ and the green pentagons are poles of the dispersion relation given in Eq. (15) (c.f., Yong et al. [24]). Other features in this map are identical to Fig. 13. In this setup, ITA modes are most prevalent around $\omega_r/\omega_{p,1} = 4$ (there is a small acoustic region, which is not noticeable at this scale). Note that the size and shape of the sixth acoustic region in the frequency range $\omega_r/\omega_{p,1} \approx [8.15, 9.7]$ are comparable to that of the first, indicating a repetition of the previous pattern. (For interpretation of the references to color in this figure legend, the reader is referred to the web version of this article.)

velocity phasors u_u and u_d

$$\Phi \equiv \frac{u_u}{|u_u|} \cdot \frac{u_d}{|u_d|} = \tilde{u}_u \cdot \tilde{u}_d. \tag{29}$$

$0 < \Phi < 1$ and $-1 < \Phi < 0$ indicate acoustic modes and ITA modes, respectively. Φ is a continuous (differentiable) function in the complex plane, c.f., Appendix B. Thus, any continuous variation in system parameters will result in a continuous change in eigenvalues of the system, and subsequently a mode transition from acoustic to ITA or vice versa. This property of Φ is inline with the observations made by previous authors [18,19,23], where a parametric sweep may entail a mode switching, say, from acoustic to ITA and vice versa.[3]

Using the same computation method as that in Fig. 12, all thermoacoustic modes in the stability map within the range of $\omega_r/\omega_{p,1} \in (0, 3.1]$ and $\sigma/\omega_{p,1} \in [-1.2, 1.2]$ are evaluated. The Φ values are visualized in the contour map shown in Fig. 13. The blue regions encapsulated by the oval curves ($\Phi = 0$) represent the regions of acoustic modes, while the red region contains the ITA modes.

Note that the 'islands' of acoustic modes have different sizes around the various pure acoustic modes $\omega_{p,i}$. To get an insight on how the size of the islands changes as the frequency grows, the contour map is extended to include higher values of ω_r, c.f., Fig. 14. The size of the acoustic island decreases initially but grows again. In this setup, we observe that the shrinking and growing of the acoustic islands repeats after $\omega_r/\omega_{p,1} \approx 8.15$, which creates an alternating pattern in the complex plane. ITA modes are most prevalent at around $\omega_r/\omega_{p,1} \approx 4$ (there is a very small acoustic region, which is not noticeable at this scale). The size of each island is determined by the distance between the acoustic-ITA transitional point of marginally stable modes (yellow dots) and the pole of the dispersion relation (green pentagon) given in Eq. (15), i.e when $\mathcal{F}(\omega) \to \infty$ (refer to Yong et al. [24] for detailed discussions). The FTF at the transitional point on the real axis is given by $\mathcal{F} = -1/\theta$ and the dispersion relation may be simplified to

$$\cos(\omega_r \tau_u) \cos(\omega_r \tau_d) = 0 \tag{31}$$

which yields the transition frequencies

$$\omega_{r,\mathrm{tran}} = \frac{2m+1}{2} \frac{\pi}{\tau_{u/d}}. \tag{32}$$

At the poles, the dispersion relation is given by

$$\sin(\omega_r \tau_u) \sin(\omega_r \tau_d) = 0 \tag{33}$$

which yields the pole frequencies

$$\omega_{r,\mathrm{pol}} = \frac{m\pi}{\tau_{u/d}}. \tag{34}$$

The prevalence of acoustic modes in the vicinity of the real axis, which is determined by

$$\Delta\omega_r = |\omega_{r,\mathrm{pol}} - \omega_{r,\mathrm{tran}}|, \tag{35}$$

is thus a function of τ_u and τ_d, or rather the flame position x_f. This conclusion sheds a new light into the observation in Fournier et al. [37], where it was shown that the flame position inside a simple Rijke tube or a can-annular combustor could strongly influence the nature of the observed eigenmodes, and modes could easily switch nature between acoustic and ITA as the flame position varies.

The acoustic regions are at maximum size with $\tau_u = \tau_d$, resulting in every $\omega_{r,\mathrm{tran}}$ being exactly the average of two consecutive $\omega_{r,\mathrm{pol}}$. In this case, an ITA mode does not exist on the real axis, c.f., Fig. 15. Of course, the derivations that lead to this conclusion revolves around the dispersion relation given in Eq. (14), which

---

[3] In the phasor representation, the complex variables u_u and u_d are represented as ordinary vectors in a 2D space, allowing the scalar product operation. Mathematically, the scalar product of two phasors equals the real value of the inner product between the complex variables in the complex vector space

$$\Phi = \mathrm{Re} < \tilde{u}_u | \tilde{u}_d > = \mathrm{Re}(\tilde{u}_u^{\dagger} \tilde{u}_d) \tag{30}$$

where † indicates a complex conjugation.

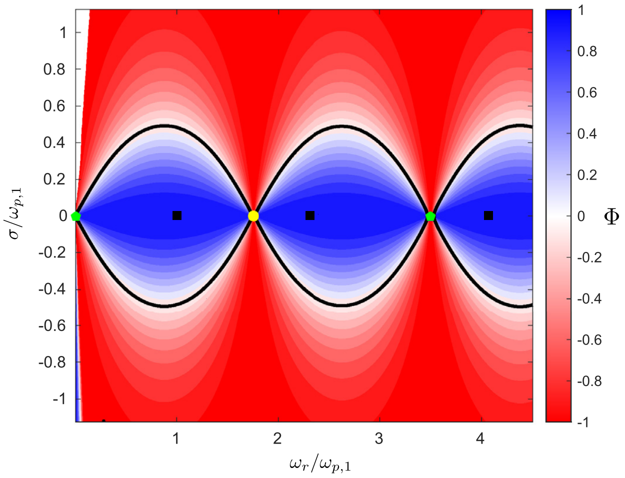

Fig. 15. Contour map of Φ for $x_f = 0.313L$, i.e., $\tau_u = \tau_d$. Other features in this map is identical to Fig. 13. In this case, ITA mode does not exist on the real axis.

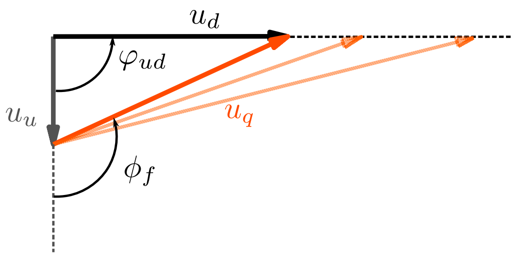

Fig. 16. Orientation of the velocity phasors across the flame of a mode at the acoustic-ITA transition. u_q must be out-of-phase with u_u, while the $|\mathcal{F}(\omega)|$ must so large, so that $u_d \perp u_u$.

is unique to an ideally closed-open resonator. More general conclusions on resonators with different boundary conditions are not developed in this study.

5.1. Transitional FTF magnitude and phase

At the transition, the velocity phasors u_u, u_d are perpendicular to each other (with the exception of the marginally stable transitional mode, where $u_d = 0$), which results in $\Phi = 0$. Substituting the Eq. (6) into Eq. (29), yields

$$u_u \cdot u_d = |u_u|^2 \big(1 + \theta |\mathcal{F}(\omega)| \cos(\phi_f)\big) = 0 \qquad (36)$$

The equation is satisfied only for $\cos(\phi_f) < 0$, which yields the necessary transitional FTF magnitude $|\mathcal{F}_T|$ and phase ϕ_f

$$|\mathcal{F}_T(\omega)| = -\frac{1}{\theta \cos(\phi_f)}, \quad \text{with } |\phi_f| \in \left(\frac{\pi}{2}, \frac{3\pi}{2}\right). \qquad (37)$$

In order for an acoustic mode to transition to ITA, the volumetric oscillation caused by the active flame must be strong enough to act against the upstream displacement rate, with the flame being out-of-phase with the upstream velocity. With an FTF magnitude larger than the transitional value

$$|\mathcal{F}(\omega)| > |\mathcal{F}_T(\omega)| \qquad (38)$$

we have an ITA mode at hand. Figure 16 shows schematically various combination of FTF gain and phase at the transition. In the limit case where $\phi_f \to \pi/2$ or $\phi_f \to 3\pi/2$, the $\mathcal{F}_T$ must be infinitely large (at the poles). A mode with $\phi_f < \pi/2$ or $\phi_f > 3\pi/2$ is always an acoustic mode.

Note that the transitional FTF magnitude and phase given in Eq. (37) are generally applicable, i.e., independent of the FTF models. For instance, we computed the FTFs (magnitude and phase) from Eq. (15) for the modes discussed in Fig. 13, without considering a specific FTF model, as shown in Fig. 17. Using the FTF phase $\phi_f(\omega)$ in Fig. 17(b), one may compute the transitional values $|\mathcal{F}_T(\omega)|$ and compare them against the $|\mathcal{F}(\omega)|$ in Fig. 17(a) to define the acoustic and ITA regions. Naturally, the results match those identified previously.

In practice, where a flame is described by a specific FTF model, the eigenmodes are only sparsely populated on the complex plane and therefore are a subset of the solutions presented here. As an example, the mode categorization in a test case with a flame described by a DTD model is demonstrated in Appendix A.

5.2. Velocity phasors as vectors of medium displacement rates

The change in sign of the pressure gradient was featured in Yong et al. [24] as a readily discernible characteristic of the proposed categorization method. In this work, we will instead use the velocities of the medium (gas) to develop an intuitive understanding to the question ‘what does it mean for a mode to be acoustic or ITA?’.

The real part of a velocity phasor represents the displacement rate of the medium

$$\dot{x}_j(x,t) = \mathrm{Re}\big(u_j(x,t)\big) = |u_j| e^{\sigma t} \cos(\omega_r t + \alpha_j), \quad j = u, d \qquad (39)$$

where $\alpha_j = \arg(u_j)$ is the relative phase between u_j phasor and the real axis. $\dot{x}_j > 0$ signifies a displacement in the $+x$ direction.

Without an active flame, the medium between two velocity nodes in a standing wave oscillates back and forth - *swings* – at a given resonant frequency. This is coherent with the aligned u_u, u_d phasors observed in pure acoustic modes.[4] In contrast, an active flame acts as a monopole source of volume. Thus, in an anechoic environment, u_u, u_d phasors are anti-aligned, which describes an inwards-outwards oscillation – *pulsation* – at the flame. However, as shown, u_u, u_d are in general partially aligned or anti-aligned, i.e., the medium at the vicinity of the flame oscillates in a superposed swinging and pulsating motion. For an acoustic mode, the swinging oscillation dominates, and vice versa for an ITA mode.

Exemplary animations visualizing the oscillation of a pure acoustic[5] and a pure ITA mode[6] (corresp. Fig. 8), as well as an acoustic[7] (corresp. Fig. 11(a)) and an ITA mode[8] (corresp. Fig. 11(b)) are uploaded as supplementary materials. The mathematical description of the medium oscillations, which could lead to the derivation of the Φ criterion (29) is detailed in Appendix D.

6. Summary, conclusion and outlook

In extension to the work of Yong et al. [24], this study used phasor diagrams to visualize the propagation of characteristic wave amplitudes of *growing* as well as *decaying* thermoacoustic modes in an ideal closed-open resonator, which contains a compact, velocity sensitive flame. The inspection of the phasor diagrams suggests that the velocity phasor may shift by an intermediate phase between $-\pi$ and π across the flame, as a result of the non-zero growth rate. At extremely high growth and decay rates, the velocity phasor changes direction across the flame, implying ITA modes

---

[4] The special case, in which the flame, i.e., the region of interest, is located exactly at the velocity node is not analyzed, as they are not meaningful for the discussions in this work. For pedagogical purposes, it is discussed in detail in Yong et al. [24] in the Appendix chapters.

[5] PureAcoustic.mp4.

[6] PureITA_Fig8.mp4.

[7] Acoustic_Fig11(a).mp4.

[8] ITA_Fig11(b).mp4.

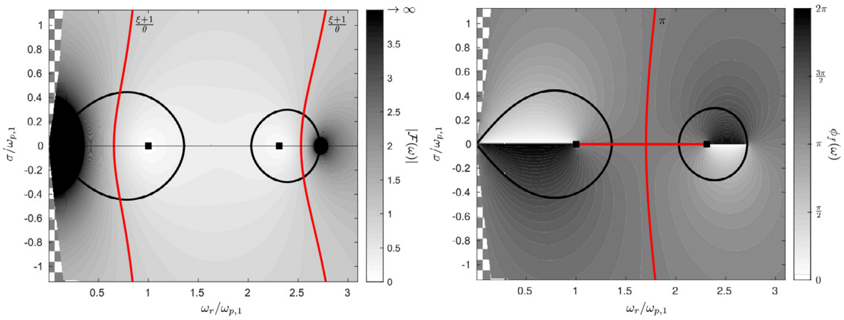

(a) $|\mathcal{F}(\omega)|$ (b) $\phi_f(\omega)$

Fig. 17. Contour maps of $\mathcal{F}(\omega)$ for $x_f = 0.4L$. The red line in (a) marks the value of $|\mathcal{F}(\omega)|$ that extends to $\sigma \to \pm\infty$, i.e., $|\mathcal{F}(\omega)| = \frac{\xi+1}{\theta}$, while in (b) marks the $\phi_f(\omega)$ value for marginally stable modes that also extends to $\pm\infty$, i.e., $\phi_f(\omega) = (2m+1)\pi$. The black thickened lines indicating the transition of acoustic modes into ITA and the black squared markers indicating the pure acoustic modes $\omega_{p,i}$ are included as references to Fig. 13. The region with checkered background is where the dispersion relation could not be easily solved due to $\omega_r \to 0$. (For interpretation of the references to color in this figure legend, the reader is referred to the web version of this article.)

according to the established criterion in Yong et al. [24]. The phasor diagrams of a variety of randomly selected modes were constructed and their corresponding locations in a stability map were determined. A clear pattern emerged: groups of modes around the pure acoustic modes have partially aligned flame upstream and downstream velocity phasors, while modes beyond these groups have partially anti-aligned velocity phasors. The first group of modes was subsequently categorized as acoustic modes, while the latter as ITA modes. It was demonstrated that the mode transition from acoustic to ITA and vice versa is a continuous process.

Representing the acoustic variables as phasors in the ordinary vector space allow the formulation of a generalized categorization criterion – Φ criterion – based on the dot product between the upstream and downstream velocity phasors, given in Eq. (29). A contour map depicting the distribution of acoustic and ITA modes was generated. Interestingly, the size of the acoustic region varies as the frequency increases, signifying that the prevalence of ITA modes, and correspondingly acoustic modes, in the proximity of the real frequency axis may vary for different combustor setups. Indeed, the size of the acoustic region is a function of flame position, as well as of reflective boundary conditions. As an extension to the Φ criterion, the transitional FTF magnitude was derived to enable a more practical mode categorization, where the corresponding FTF is compared against the transitional value.

Physically, the real value of a velocity phasor represents the displacement rate of the medium in a resonator. The perfectly anti-aligned velocity phasors across the flame, as typically seen in a pure ITA mode, indicate an unsteady volumetric oscillation – ‘pulsating’ – in the reactive region of the flame. A pair of perfectly aligned velocity phasors, on the other hand, represents the ordinary back and forth motion – ‘swinging’ – observed in a standing wave. In an echoic resonator with an active flame, the acoustic feedback is coupled with the ITA feedback mechanism. Thus, a superposition of both oscillation motions is expected. Note that the swinging and pulsating characteristics are equivalent to the transitional FTF magnitude, both of which can be derived from the Φ criterion. Thus, a mode may be categorized by analyzing either the FTF data or the velocity measurements on the flame upstream and downstream, depending on the circumstances and available diagnostic tools in an experiment.

In this work, we demonstrated that growing as well as decaying ITA modes could be reasonably categorized by means of phasors analysis. In addition to the known benefits of the phasor based categorization, such as straightforward implementation, physical relevance and low computational cost, the categorization of modes with partially aligned and anti-aligned velocity phasors across the flame widens its application.

In future works, more complex systems with non-ideal boundaries, internal losses or area changes, as well as can-annular geometries, shall be analyzed. In essence, we expect the Φ criterion to be valid in these cases. Besides, the unique characteristics of ITA modes categorized this way shall be explored. It is interesting to investigate, if the peculiar characteristics observed in Silva et al. [11,12], Xu et al. [13], Mukherjee and Shrira [15] could be explained with the phasor characteristics of ITA modes.

Declaration of Competing Interest

The authors declare that they have no known competing financial interests or personal relationships that could have appeared to influence the work reported in this paper.

Acknowledgments

Financial support has been provided by the German Research Foundation (Deutsche Forschungsgemeinschaft - DFG) for the Self-iXs project, DFG PO 710/21-1, in the framework of the International Collaborative Research Project Initiative ANR-DFG NLE 2018. Guillaume J. J. Fournier acknowledges the funding from the European Union’s Horizon 2020 research and innovation programme under Grant Agreement no. 765998 Annular Instabilities and Transient Phenomena in Gas Turbine Combustors (ANNULIGhT).

Supplementary material

Supplementary material associated with this article can be found, in the online version, at doi:10.1016/j.combustflame.2022.112605.

Appendix A. Test case with a DTD flame model

In this section, we will demonstrate the implementation of the proposed categorization criterion in a test case with an FTF modeled by the DTD model given in Eq. (13). The corresponding impulse response coefficients h_k are tabulated in Table A.3.

Table A.3
The impulse response coefficients h_k of the DTD model at the corresponding element k. The discrete time step in this model is $\Delta t = 2 \times 10^{-4}$s.

k	2	3	4	5	6	7	8	9
h_k	0.1	0.3	0.8	0.3	0.1	−0.2	−0.4	−0.2

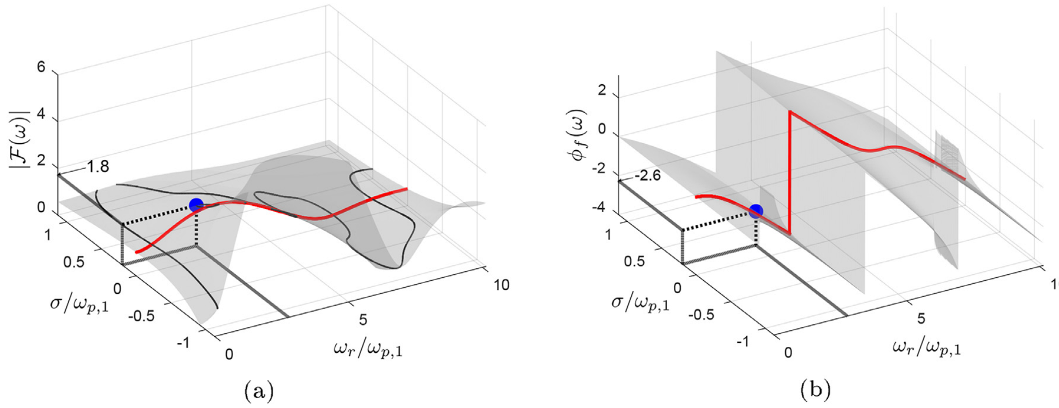

Fig. A.18. The surface plots of (a) FTF magnitude and (b) phase of a DTD flame model with excess gain and exhibit a low pass behaviour. The red curve depicts the FFR. The black curves on the surface in (a) mark the solutions that satisfy Eq. (A.1). The solutions for the phase are not shown in (b) to reduce clutter. The blue filled circle is the mode of interest with $\omega_r/\omega_{p,1} = 2.8$ and $\sigma/\omega_{p,1} = 0.2$.

The resultant FTF of the DTD model in terms of magnitude and phase are visualized in Fig. A.18. This FTF must simultaneously satisfy the dispersion relation given in Eq. (15), such that

$$|\mathcal{F}(\omega)|_{\mathrm{DTD}} = |\mathcal{F}(\omega)|_{\mathrm{sys}} \tag{A.1}$$

$$\phi_f(\omega)\Big|_{\mathrm{DTD}} = \phi_f(\omega)\Big|_{\mathrm{sys}} \tag{A.2}$$

where the index $[\ ]_{\mathrm{DTD}}$ indicates the FTF of the flame model, and $[\ ]_{\mathrm{sys}}$ indicates the FTF computed with the dispersion relation (15), the results of which are visualized in Fig. 17. The solutions that satisfy Eq. (A.1) are indicated by the black line in Fig. A.18(a). The solutions for Eq. (A.2) are not shown to reduce cluttering.

The solutions satisfying both the Eqs. (A.1)-(A.2) are the eigenvalues of the thermoacoustic system at hand, as visualized in Fig. A.19 (blue circles).

We investigate one of the unstable mode with $\omega_r/\omega_{p,1} = 2.8$ and $\sigma/\omega_{p,1} = 0.2$ (blue filled circle). Owing to the fact that the case at hand (ideal closed-open boundaries, $x_f = 0.4L$) is thus far discussed in detail, we could readily determine that this mode is indeed an ITA mode using Fig. 17 or rather Fig. 13. Nevertheless, it is crucial to realize that the proposed criterion that relates the angle of the velocity phasors across the flame should be valid for other general cases, where the flame position differs or the boundary conditions are non-ideal, say. In such cases, the convoluted process of solving the dispersion relation and producing the contour maps may be omitted. Instead, one could determine the 'ITA-ness' of the given mode by comparing the corresponding FTF magnitude to the transitional value (Eq. (37)). To demonstrate this using the example at hand, we read off Fig. A.18 to obtain $|\mathcal{F}(\omega)| = 1.8$ and $\phi_f(\omega) = -0.83\pi$. The FTF phase satisfies $\pi/2 < |\phi_f(\omega)| < 3\pi/2$ and yields a transitional FTF magnitude of $|\mathcal{F}_T(\omega)| = 0.29$. With $|\mathcal{F}(\omega)| > |\mathcal{F}_T(\omega)|$, we come to the same conclusion that the mode at hand is an ITA mode. The phasor diagram in Fig. A.20 also confirms this conclusion.

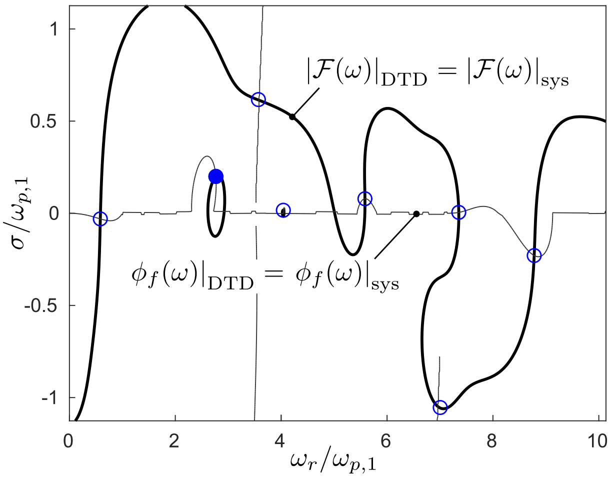

Fig. A.19. The thickened and thin curves satisfy Eq. (A.1) and (A.2) respectively. The intersection between them are all the eigenvalues to the thermoacoustic system (blue circles). The filled circle indicates the mode of interest with $\omega_r/\omega_{p,1} = 2.8$ and $\sigma/\omega_{p,1} = 0.2$.

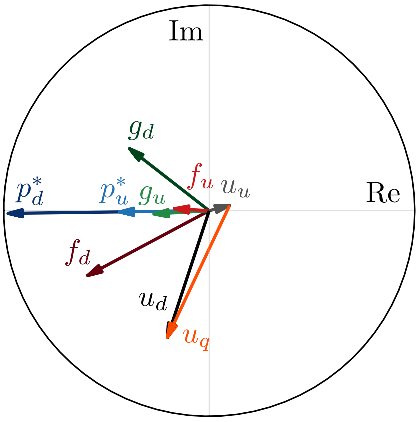

Fig. A.20. 2D phasor diagram of the mode with $\omega_r/\omega_{p,1} = 2.8$ and $\sigma/\omega_{p,1} = 0.2$. The partially out-of-phase u_u and u_d indicate an ITA mode.

References

[1] S. Candel, Combustion dynamics and control: progress and challenges, Proc. Combust. Inst. 29 (1) (2002) 1–28.

[2] T. Lieuwen, K. McManus, Combustion dynamics in lean-premixed prevaporized (LPP) gas turbines, J. Propul. Power 19 (5) (2003) 721, doi:10.2514/2.6171.

[3] T. Poinsot, Prediction and control of combustion instabilities in real engines, Proc. Combust. Inst. 36 (2017) 1–28, doi:10.1016/j.proci.2016.05.007.

[4] T. Poinsot, D. Veynante, Theoretical and Numerical Combustion, RT Edwards, Inc., 2005.

[5] A.P. Dowling, The calculation of thermoacoustic oscillation, J. Sound Vib. 180 (4) (1995) 557–581, doi:10.1006/jsvi.1995.0100.

[6] , Progress in Astronautics and Aeronautics, vol. 210, Combustion Instabilities in Gas Turbine Engines: Operational Experience, Fundamental Mechanisms and Modeling, American Institute of Aeronautics and Astronautics, Reston, VA, 2005.

[7] J.W.S. Rayleigh, The explanation of certain acoustical phenomena, Nature 18 (1878) 319–321, doi:10.1038/018319a0.

[8] M. Hoeijmakers, V. Kornilov, I. Lopez Arteaga, P. de Goey, H. Nijmeijer, Intrinsic instability of flame-acoustic coupling, Combust. Flame 161 (11) (2014) 2860–2867, doi:10.1016/j.combustflame.2014.05.009.

[9] T. Emmert, S. Bomberg, W. Polifke, Intrinsic thermoacoustic instability of premixed flames, Combust. Flame 162 (1) (2015) 75–85, doi:10.1016/j.combustflame.2014.06.008.

[10] T. Emmert, S. Bomberg, S. Jaensch, W. Polifke, Acoustic and intrinsic thermoacoustic modes of a premixed combustor, Proc. Combust. Inst. 36 (3) (2017) 3835–3842, doi:10.1016/j.proci.2016.08.002.

[11] C.F. Silva, T. Emmert, S. Jaensch, W. Polifke, Numerical study on intrinsic thermoacoustic instability of a laminar premixed flame, Combust. Flame 162 (9) (2015) 3370–3378, doi:10.1016/j.combustflame.2015.06.003.

[12] C.F. Silva, M. Merk, T. Komarek, W. Polifke, The contribution of intrinsic thermoacoustic feedback to combustion noise and resonances of a confined turbulent premixed flame, Combust. Flame 182 (2017) 269–278, doi:10.1016/j.combustflame.2017.04.015.

[13] L. Xu, J. Zheng, G. Wang, Z. Feng, X. Tian, L. Li, F. Qi, Investigation on the intrinsic thermoacoustic instability of a lean-premixed swirl combustor with an acoustic liner, Proc. Combust. Inst. 38 (4) (2021) 6095–6103, doi:10.1016/j.proci.2020.06.155.

[14] M. Murugesan, B. Singaravelu, A.K. Kushwaha, S. Mariappan, Onset of flame-intrinsic thermoacoustic instabilities in partially premixed turbulent combustors, Int. J. Spray Combust. Dyn. (2018), doi:10.1177/1756827718758511. 1756827718758511

[15] N.K. Mukherjee, V. Shrira, Intrinsic flame instabilities in combustors: analytic description of a 1-D resonator model, Combust. Flame 185 (2017) 188–209, doi:10.1016/j.combustflame.2017.07.012.

[16] C. Silva, K.J. Yong, L. Magri, Thermoacoustic modes of quasi-one-dimensional combustors in the region of marginal stability, J. Eng. Gas Turbines Power 141 (2) (2019) 021022, doi:10.1115/1.4041118.

[17] A. Orchini, C.F. Silva, G.A. Mensah, J.P. Moeck, Thermoacoustic modes of intrinsic and acoustic origin and their interplay with exceptional points, Combust. Flame 211 (2020) 83–95, doi:10.1016/j.combustflame.2019.09.018.

[18] N. Hosseini, V. Kornilov, I. Lopez Arteaga, W. Polifke, O. Teerling, L. de Goey, Intrinsic thermoacoustic modes and their interplay with acoustic modes in a Rijke burner, Int. J. Spray Combust. Dyn. 10 (4) (2018) 315–325, doi:10.1177/1756827718782884.

[19] F.M. Sogaro, P.J. Schmid, A.S. Morgans, Thermoacoustic interplay between intrinsic thermoacoustic and acoustic modes: non-normality and high sensitivities, J. Fluid Mech. 878 (2019) 190–220, doi:10.1017/jfm.2019.632.

[20] P.E. Buschmann, G.A. Mensah, J.P. Moeck, Intrinsic thermoacoustic modes in an annular combustion chamber, Combust. Flame 214 (2020) 251–262, doi:10.1016/j.combustflame.2019.11.006.

[21] G.J.J. Fournier, M. Haeringer, C.F. Silva, W. Polifke, Low-order modeling to investigate clusters of intrinsic thermoacoustic modes in annular combustors, J. Eng. Gas Turbines Power 143 (4) (2021) 041025, doi:10.1115/1.4049356.

[22] A. Albayrak, T. Steinbacher, T. Komarek, W. Polifke, Convective scaling of intrinsic thermo-acoustic eigenfrequencies of a premixed swirl combustor, J. Eng. Gas Turbines Power 140 (4) (2017) 041510, doi:10.1115/1.4038083.

[23] N.K. Mukherjee, V. Shrira, Coupling of acoustic and intrinsic modes in 1D combustor models, Combust. Sci. Technol. (2019) 1–22, doi:10.1080/00102202.2019.1678593.

[24] K.J. Yong, C.F. Silva, W. Polifke, A categorization of marginally stable thermoacoustic modes based on phasor diagrams, Combust. Flame 228 (2021) 236–249, doi:10.1016/j.combustflame.2021.01.003.

[25] W. Polifke, System modelling and stability analysis, in: J. Anthoine (Ed.), Basics of Aeroacoustics and Thermoacoustics, VKI LS 2007-09, Von Karman Institute, Rhode-St-Genèse, BE (2007), pp. 1–51.

[26] J. Kopitz, W. Polifke, CFD-based application of the nyquist criterion to thermoacoustic instabilities, J. Comput. Phys. 227 (2008) 6754–6778, doi:10.1016/j.jcp.2008.03.022.

[27] J.J. Keller, Thermoacoustic oscillations in combustion chambers of gas turbines, AIAA J. 33 (12) (1995) 2280–2287, doi:10.2514/3.12980.

[28] L. Strobio Chen, S. Bomberg, W. Polifke, Propagation and generation of acoustic and entropy waves across a moving flame front, Combust. Flame 166 (2016) 170–180, doi:10.1016/j.combustflame.2016.01.015.

[29] A. Fleifil, A.M. Annaswamy, Z.A. Ghoneim, A.F. Ghoniem, Response of a laminar premixed flame to flow oscillations: a kinematic model and thermoacoustic instability results, Combust. Flame 106 (1996) 487–510, doi:10.1016/0010-2180(96)00049-1.

[30] S. Ducruix, D. Durox, S. Candel, Theoretical and experimental determinations of the transfer function of a laminar premixed flame, Proc. Combust. Inst. 28 (1) (2000) 765–773, doi:10.1016/S0082-0784(00)80279-9.

[31] L. Crocco, Aspects of combustion stability in liquid propellant rocket motors part1: fundamentals. Low frequency instability with monopropellants, J. Am. Rocket Soc. 21 (6) (1951) 163–178, doi:10.2514/8.4393.

[32] W. Polifke, Modeling and analysis of premixed flame dynamics by means of distributed time delays, Prog. Energy Combust. Sci. 79 (2020) 100845, doi:10.1016/j.pecs.2020.100845.

[33] M. Schmid, R. Blumenthal, M. Schulze, W. Polifke, T. Sattelmayer, Quantitative stability analysis using real frequency response data, J. Eng. Gas Turbines Power 135 (12) (2013) 121601, doi:10.1115/1.4025299.

[34] L. Tay-Wo-Chong, S. Bomberg, A. Ulhaq, T. Komarek, W. Polifke, Comparative validation study on identification of premixed flame transfer function, J. Eng. Gas Turbines Power 134 (2) (2012) 021502–1–8, doi:10.1115/1.4004183.

[35] P. Subramanian, R.S. Blumenthal, R. Sujith, W. Polifke, Distributed time lag response functions for the modelling of combustion dynamics, Combust. Theor. Model 19 (2) (2015) 223–237, doi:10.1080/13647830.2014.1001438.

[36] P. Brokof, G.J.J. Fournier, W. Polifke, Linear time-continuous state-space realization of flame transfer functions by means of a propagation equation, Internoise 2022, Glasgow, Scotland, 2022.

[37] G.J.J. Fournier, F. Schaefer, M. Haeringer, C.F. Silva, W. Polifke, Interplay of clusters of acoustic and intrinsic thermoacoustic modes in can-annular combustors, Proceedings of ASME Turbo Expo 2022 Turbomachinery Technical Conference and Exposition, ASME, Rotterdam, NL (2022).

Guillaume J. J. Fournier[1]
Department of Mechanical Engineering,
Technical University of Munich,
Garching D-85747, Germany
e-mail: fournier@tfd.mw.tum.de

Matthias Haeringer
Department of Mechanical Engineering,
Technical University of Munich,
Garching D-85747, Germany
e-mail: haeringer@tfd.mw.tum.de

Camilo F. Silva
Department of Mechanical Engineering,
Technical University of Munich,
Garching D-85747, Germany
e-mail: silva@tfd.mw.tum.de

Wolfgang Polifke
Department of Mechanical Engineering,
Technical University of Munich,
Garching D-85747, Germany
e-mail: polifke@tum.de

Low-Order Modeling to Investigate Clusters of Intrinsic Thermoacoustic Modes in Annular Combustors

The intrinsic thermoacoustic (ITA) feedbackloop constitutes a coupling between flow, flame and acoustics that does not involve the natural acoustic modes of the system. One recent study showed that ITA modes in annular combustors come in significant number and with the peculiar behavior of clusters, i.e. several modes with close frequencies. In the present work, an analytical model of a typical annular combustor is derived via Riemann invariants and Bloch theory. The resulting formulation describes the full annular system as a longitudinal combustor with an outlet reflection coefficient that depends on frequency and the azimuthal mode order. The model explains the underlying mechanism of the clustering phenomena and the structure of the clusters associated with ITA modes of different azimuthal orders. In addition, a phasor analysis is proposed, which encloses the conditions for which the 1D model remains valid when describing the thermoacoustic behavior of an annular combustor. [DOI: 10.1115/1.4049356]

Introduction

To tackle environmental issues and reduce emissions, in particular NO_x pollutants, lean premixed combustion systems have been developed. However this combustion technology is more prone to thermoacoustic combustion instabilities [1,2]. This type of self-excited instability results from coupling between the unsteady heat release of the flame and acoustic waves, which may result in a positive feedback loop, thus inducing growing pressure fluctuations. Repeated exposure to high pressure levels over time will promote mechanical fatigue and may lead to catastrophic failure of the combustor [3]. From a safety perspective, it is crucial to identify the important flow-flame-acoustic interaction and feedback mechanisms in order to prevent this type of instability.

Bomberg et al. [4] identified the so-called intrinsic thermoacoustic (ITA) feedback loop, which does not involve reflection of acoustic waves at the combustor inlet or exit. Instead, the ITA feedback mechanism may be described as follows: velocity sensitive flames respond to a perturbation of upstream velocity with a change in the heat release rate, which in turn generates acoustic waves that travel in both up- and downstream directions. The wave traveling in the upstream direction will directly perturb the acoustic velocity, before even reaching the boundaries of the acoustic system. This mechanism of flow-flame-acoustic interaction is, in a sense, *intrinsic* to the flame and its immediate surrounding, hence its name.

Anomalous peaks in the acoustic flame response, i.e. the magnitude of coefficients of the flame scattering matrix [5], and in the so-called instability potentiality [6] were explained as resonances of the ITA feedback loop [4,7]. Furthermore, ITA feedback provided an explanation [7] of the physical nature of thermoacoustic instabilities of a flame in an anechoic environment, which were reported and analyzed by Hoeijmakers et al. [8,9] and subsequently confirmed by high-fidelity computational fluid dynamics simulations with nonreflecting boundary conditions [10,11]. Emmert et al. [12] then argued that ITA feedback gives rise to additional thermoacoustic modes that are not related to acoustic eigenmodes of the combustor and identified such an "ITA mode" as the dominant unstable eigenmode in a premix swirl combustion test rig. This constitutes a significant deviation from the established interpretation of thermoacoustic instabilities as acoustic eigenmodes of the combustor driven by unsteady heat release [13].

The concept of ITA feedback can explain in hindsight a number of hitherto inexplicable phenomena described in earlier studies. For example, the "new set of modes associated with flame model" described by Dowling and Stow [14] quite obviously should be considered as "modes of ITA origin" [15]. Similarly, there is strong evidence that the low frequency "bulk mode" discussed by Eckstein and Sattelmayer [16] results from ITA feedback [17]. Finally, "convective scaling" of thermoacoustic eigenfrequencies—i.e. the dependence of eigenmode frequency on the bulk flow velocity inside the burner, but not on the speed of sound in plenum or combustor—may be regarded as a consequence of ITA feedback [18].

Hosseini et al. [19] investigated the interplay between thermoacoustic modes of ITA and acoustic origin and showed that when the passive acoustic mode is far away from the ITA, the two do not interplay with each other. More recently, Sogaro et al. [20] investigated a pairwise interplay between acoustic and ITA modes and showed that modal sensitivities increase as the two modes approach each other. Silva et al. [21] and Orchini et al. [22] further investigated ITA and acoustic modes and their interplay with exceptional points. They demonstrated that away from the exceptional point and the acoustic mode, the ITA trajectories when varying the gain and time delay of the flame are straight lines, i.e. their growth rate changes but the frequency remains approximately constant.

Previous studies [7,9,15] showed analytically that eigenfrequencies of ITA modes in a one-dimensional Rijke tubes with anechoic boundary conditions have solution in the form

$$\omega = \frac{\pi(2j+1)}{\tau} - \frac{i}{\tau}\ln\left(\frac{n\theta}{1+\xi}\right), \quad j \in \mathbb{N} \tag{1}$$

where $\xi = \rho_u c_u / \rho_d c_d$ is the ratio of specific impedances upstream and downstream the flame, n and τ the gain and time delay associated with the flame response respectively and $\theta = (T_d - T_u)/T_u$ the normalized temperature ratio. In the rest of this paper, we will

---

[1] Corresponding author.

Manuscript received September 2, 2020; final manuscript received September 15, 2020; published online March 10, 2021. Editor: Jerzy T. Sawicki.

refer to Eq. (1), the frequency of the ITA mode in an anechoic environment, as the pure ITA frequency. Mukherjee and Shrira [15] showed that, for a Rijke tube with fully reflecting boundaries, in the limit of small n, the ITA mode is highly damped but its frequency remains close to a corresponding “pure ITA frequency”.

Buschmann et al. [23,24] and Orchini et al. [22] observed the existence of ITA modes in annular combustors. These modes come in significant number and have the peculiar behavior of appearing in clusters, i.e. several modes with different growth rate, but very close frequencies. So far, little has been done to explain their origin. Recall at this point Emmert et al. [12] who demonstrated that, in longitudinal combustors with partially reflecting boundaries, ITA modes should not be ignored and indeed can be the most unstable modes. Furthermore, the analysis suggested that established methods for passive control (dampers, etc.) have little influence on ITA modes, or worse, can lead to the opposite effect and trigger an instability. Therefore, it is crucial to understand the underlying physics behind ITA modes. The goal of the present study is to investigate ITA modes in annular chambers.

Various tools are available to study thermoacoustic instabilities: high-fidelity large eddy simulations [25,26], linearized reactive flow [27], linearized Navier–Stokes equations [28,29] give excellent results, but at considerable computational cost. Helmholtz solvers [30] are more affordable and able to accurately model complex 3D geometries, but computational cost remains non-negligible. On the other hand, low-order network models [31–35] applied for annular geometries have proven to give satisfactory agreement at extremely low computational cost. Bloch theory [36], which exploits the rotational symmetry of a system, has recently been applied in the thermoacoustic community [22,37–39]. This approach reduces a system with rotational symmetries to a single unit cell and facilitates its computation without loss in accuracy.

In the present study, we propose a low-order network model formulated with Bloch boundary conditions to investigate ITA modes in an annular combustor. The paper is structured as follows: we first describe the network model with Bloch boundary conditions that represents the combustor. We then derive an analytical expression of the equivalent reflection coefficient that models the chamber behavior and demonstrate that the system can be reduced to a simple longitudinal setup. This reduced model is applied to a typical lab-scale combustor to explain the origin of ITA clusters. It also enables us to explain the spectrum of the combustor and the damping of modes with higher azimuthal order. We then give explanations on the shift of certain modes and the offset from their respective clusters.

Network Model of an Annular Geometry With Bloch Boundary Conditions

Case and Flow Description. The combustor consists of N perfectly premixed burners connected to an annular combustion chamber. For the sake of simplicity, the plenum is not taken into account, because it can often be decoupled [40,41]. The area ratio between plenum and burners is assumed large enough such that the burners can be modeled by ducts terminating in a large vessel. For low Mach numbers, this leads to a reflection coefficient at the inlet of the burners of $R_{\text{in}} = -1$. At the exit of a gas turbine combustion chamber, a high pressure turbine stage is placed in order to extract energy from the fluid and transform it into mechanical work. Marble and Candel [42] showed that the acoustic response of the turbine inlet can be modeled with a fixed gain lower than 1 and a zero phase response. To simplify the study, we choose here a reflection of $R_{\text{out}} = 1$, and we expect little quantitative change when accounting for the losses [43]. In this study, we also neglect entropy waves, assuming they play a negligible role [44].

The model is based on a network approach. The burners and the combustion chamber are modeled by ducts where only 1D planar acoustic waves propagate. In the chamber, only purely azimuthal modes are considered. The axial length of the chamber is assumed to be small compared to the azimuthal length P_c; mixed modes will occur at higher frequencies and are not considered here. Transverse modes are also out of the scope of this study. The chamber is decomposed into N ducts of length L, where L is the distance between two burners. Similarly to Parmentier et al. [33], burners and chamber are connected with T-junctions, and the flames are placed inside the burners, just before the area change with the chamber. The flames and the T-junctions are assumed to be acoustically compact.

Flame and Unsteady Heat Release Model. The acoustic flame model is based on linearized Rankine Hugoniot jump equations across a compact heat source [7,45] with heat release fluctuations

$$\begin{cases} \dfrac{p'_d}{\bar{\rho}_d c_d} = \xi \dfrac{p'_u}{\bar{\rho}_u c_u} \\ u'_d = u'_u + \theta \dot{q}' \end{cases} \tag{2}$$

where $\xi = \bar{\rho}_u c_u / \bar{\rho}_d c_d$ is the ratio of specific impedances, $\theta = (T_d - T_u)/T_u$ the normalized temperature ratio, and $\dot{q}' = \dot{Q}'\bar{u}_u/\bar{\dot{Q}}$ the normalized global heat release fluctuations of the flame.

The model is closed by a flame transfer function (FTF) which relates upstream velocity fluctuations at the reference position with the normalized global heat release fluctuations of the flame. Crocco [46] introduced a simple model with only two parameters, a gain n and a time delay τ, which represent the delay between the acoustic perturbation and the actual response of the flame

$$\frac{\dot{q}'}{u'_u} = \mathscr{F}(\omega) = n e^{-i\omega\tau} \tag{3}$$

This model is simplistic but captures essential aspects of a generic flame response and is convenient to use in the context of analytical models. Especially, the pure ITA frequency can be analytically expressed as recalled in Eq. (1).

Bloch-Wave Theory. Bauerheim et al. [47] showed analytically that azimuthal modes are strongly influenced by symmetry breaking. Both geometrical or flow symmetry breaking cause the degenerate pairs of azimuthal modes to split into two distinct modes. In this study, the influence of symmetry breaking is not taken into account: the burners are identical, and the chamber does not exhibit any mean flow in the azimuthal direction. Because of the discrete rotational symmetry, according to Bloch theory [36,37], the acoustic pressure in the frequency domain can be written in the form

$$\hat{p}(\boldsymbol{x}) = \psi(\boldsymbol{x}) e^{im\theta}, \quad m = \begin{cases} -\dfrac{N}{2}+1, \ldots, \dfrac{N}{2} & N \text{ even} \\ -\dfrac{N-1}{2}, \ldots, \dfrac{N-1}{2} & N \text{ odd} \end{cases} \tag{4}$$

where θ is the azimuthal coordinate around the axis of discrete rotational symmetry, $\psi(\boldsymbol{x})$ is a function identical in all unit cell and periodic in θ with a period $2\pi/N$ and m is the Bloch wave number. In this application, the absolute value of the Bloch wave number $|m|$ is identical to the azimuthal mode order because, in time domain, the solution $p(\boldsymbol{x},t) = \hat{p}(\boldsymbol{x})e^{i\omega t} = \psi(\boldsymbol{x})e^{i(\omega t + m\theta)}$ is a traveling wave in the azimuthal coordinate θ [38].

Depending on the values of m, the modes can be classified into three categories: axial, spinning and “push-pull” modes. For $m = 0$, Eq. (4) shows that the pressure is identical in every unit cell with no phase difference in the azimuthal direction, i.e. an axial mode. Mode order $m = N/2$ only exists when the number of discrete rotational symmetry is even. In this case, the acoustic field of one burner is in antiphase with respect to the acoustic field of its two neighbors and, for this reason, is called "push-pull". Spinning modes in the (anti-)clockwise direction appear for Bloch wave numbers of $m = \pm 1, \ldots, \pm(N/2-1)$. Because the system exhibit reflectional symmetry (negligible mean flow in azimuthal direction), these modes are degenerate pairs that share the same eigenfrequency and differ only by their spinning direction.

From the study of one unit cell only, and for all possible values of m, one can assess the response of the complete system accounting for all azimuthal modes [37–39]. The complete system burners-chamber can be reduced to the study of only one unit cell as depicted in Fig. 1. The model is very similar to the one introduced by Parmentier et al. [33], but Bloch theory, by introducing a quasi-periodic boundary condition mutually connecting the left and right boundaries of the unit cell, allows to avoid tedious matrix products to find the dispersion relation.

Equivalent Longitudinal Burner

In order to better understand the underlying physics and further simplify the system, we derive a model, and the combustion chamber (identified by the box in Fig. 1) is replaced by its equivalent reflection coefficient. We show that, with Bloch theory, we can reduce a complex annular geometry to an equivalent longitudinal burner.

Modeling of the T-Junction and the Chamber. The T-junction is considered acoustically compact and its volume is null. The chamber does not exhibit any mean flow in the azimuthal direction; therefore, the mass conservation equation integrated over the control volume reduces to conservation of volumetric flow rate:

$$S_c u'_C = S_c u'_B + S_b u'_A \tag{5}$$

The momentum conservation equation applied to an inviscid 1D flow leads to pressure continuity in the junction:

$$p'_C = p'_B = p'_A \tag{6}$$

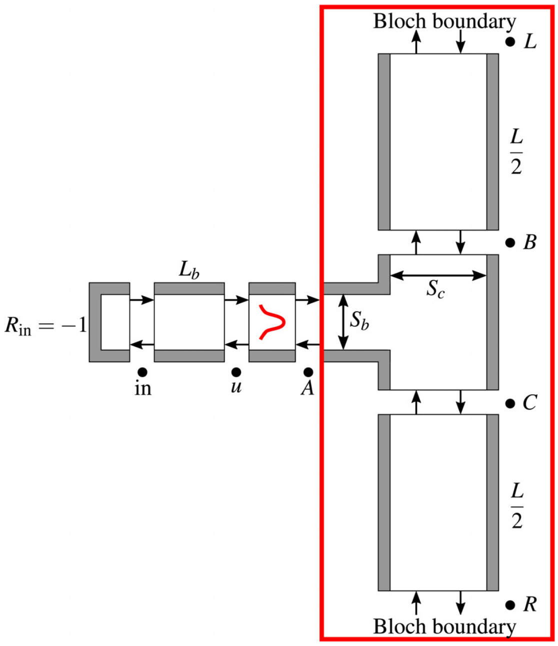

Fig. 1 Network model of one unit cell of an annular chamber exhibiting rotational and reflectional symmetry

To investigate ITA modes, it is often more convenient to use Riemann invariants. In this context, we recall the definition of characteristic waves amplitudes

$$f \equiv \frac{1}{2}\left(\frac{p'}{\bar{\rho}c} + u'\right), \quad g \equiv \frac{1}{2}\left(\frac{p'}{\bar{\rho}c} - u'\right) \tag{7}$$

Using Riemann invariants definition from Eq. (7), Eqs. (5) and (6) become

$$\begin{cases} f_C + g_C = f_B + g_B = f_A + g_A & (8a) \\ f_C - g_C = f_B - g_B + \alpha(f_A - g_A) & (8b) \end{cases}$$

where $\alpha = S_b/S_c$ is the area ratio between burner and chamber.

The objective is to replace the system T-junction and chamber by the equivalent reflection coefficient seen by the burner, i.e. to express g_A, the wave coming back from the chamber and traveling in the upstream direction, as a function of the incoming wave f_A. We define the reflection coefficient $\mathscr{R}_m$ as:

$$g_A = \mathscr{R}_m f_A \tag{9}$$

From the T-junction, plane waves propagate in the chamber to the locations L and R (left and right boundaries of the unit cell respectively, as shown in Fig. 1)

$$\begin{bmatrix} f_R \\ g_R \end{bmatrix} = \begin{bmatrix} e^{-ik\frac{L}{2}} & 0 \\ 0 & e^{ik\frac{L}{2}} \end{bmatrix} \begin{bmatrix} f_C \\ g_C \end{bmatrix}, \quad \begin{bmatrix} f_B \\ g_B \end{bmatrix} = \begin{bmatrix} e^{-ik\frac{L}{2}} & 0 \\ 0 & e^{ik\frac{L}{2}} \end{bmatrix} \begin{bmatrix} f_L \\ g_L \end{bmatrix} \tag{10}$$

Locations L and R are mutually connected with Bloch boundaries as in Haeringer and Polifke [39].

$$\begin{bmatrix} f_R \\ g_R \end{bmatrix} = \begin{bmatrix} e^{i\frac{2\pi m}{N}} & 0 \\ 0 & e^{i\frac{2\pi m}{N}} \end{bmatrix} \begin{bmatrix} f_L \\ g_L \end{bmatrix} \tag{11}$$

Combining Eqs. (9)–(11) leads to the homogeneous linear system of equations defined through the matrix

$$\underbrace{\begin{bmatrix} 1 - e^{i\left(\frac{2\pi m}{N} + kL\right)} & 1 - e^{i\left(\frac{2\pi m}{N} - kL\right)} \\ e^{i\left(\frac{2\pi m}{N} + kL\right)} - \alpha\frac{1-\mathscr{R}_m}{1+\mathscr{R}_m} - 1 & 1 - e^{i\left(\frac{2\pi m}{N} - kL\right)} - \alpha\frac{1-\mathscr{R}_m}{1+\mathscr{R}_m} \end{bmatrix}}_{\mathbf{M}(\omega,m)} \tag{12}$$

The linear system of equations for f_B and g_B reads

$$\mathbf{M}(\omega, m)\begin{bmatrix} f_B \\ g_B \end{bmatrix} = \begin{bmatrix} 0 \\ 0 \end{bmatrix} \tag{13}$$

The detailed derivation can be found in Appendix A. The system shows nontrivial solution if the determinant of $\mathbf{M}(\omega, m)$ is null, which gives a condition for the reflection coefficient:

$$\mathscr{R}_m(\omega) = \frac{-2\cos\left(\frac{2\pi m}{N}\right) + 2\cos(\mathrm{He}) - i\alpha\sin(\mathrm{He})}{2\cos\left(\frac{2\pi m}{N}\right) - 2\cos(\mathrm{He}) - i\alpha\sin(\mathrm{He})} \tag{14}$$

with the Helmholtz number being defined as $\mathrm{He} = \omega L/c$. Note that $\mathscr{R}_m(\omega)$ depends on the frequency and the mode order.

Interpretation of the Reflection Coefficient. The equivalent reflection coefficient $\mathscr{R}_m(\omega)$ depends not only on the frequency ω, as it is often the case for boundary conditions, but also on the azimuthal mode order m. Depending on the order of the mode present in the chamber, the burner tube is exposed to a different outlet acoustic boundary condition.

At zero growth rate, Eq. (14) shows that the gain of the reflection coefficient is trivially unity at all frequencies and for all mode orders. This result was to be expected because no loss mechanism was taken into account and no energy is added to the system. On the other hand, the phase is different for all the modes and changes with the frequency. Figure 2 presents the evolution of the phase as a function of the dimensionless frequency He for an annular combustor of 12 burners and with an area ratio of $\alpha = 1/15$. We observe that, in the zero frequency limit, the chamber behaves as a hard wall ($\mathscr{R}_0 = 1$) for the axial mode whereas it behaves as an open end ($\mathscr{R}_m = -1$) for all other azimuthal mode orders. Corresponding observations for a can-annular combustor were made by Ghirardo et al. [38] and were explained mathematically by the fact that the Galerkin series of an axial mode has a Helmholtz mode at frequency $\omega = 0$. We can also interpret it physically. The mode is of axial type, the acoustic field is uniform in the azimuthal direction, the T-junction is compact, so the boundary condition seen by the burner is exactly the same as the one at the inlet of the turbine ($R_{\text{out}} = 1$ in this case), thus explaining the phase going to 0 in the low frequency limit.

For the other modes, the phase is rather close to either π or $-\pi$ but changes abruptly from one to the other with a periodic pattern. Indeed, for each mode, at a given frequency, the reflection coefficient becomes $\mathscr{R}_m = 1$. From Eq. (14), we can show analytically that

$$\begin{aligned} \mathscr{R}_m(\omega) = 1 &\iff \cos(\text{He}) = \cos\left(\frac{2\pi m}{N}\right) \\ &\iff \text{He} = kL = 2\pi h \pm \frac{2\pi m}{N}, \quad h \in \mathbb{N} \\ &\iff \frac{kP_c}{2} = (Nh \pm m)\pi, \quad h \in \mathbb{N} \end{aligned} \tag{15}$$

where $P_c = NL$ is the total perimeter of the chamber. $\mathscr{R}_m = 1$ is the special case where the burner tube has a velocity node at its outlet, and therefore, the flame is not influencing at all the chamber. In that sense, the burner tube is decoupled, and the chamber is a simple annular duct whose eigenfrequency (or resonance frequency) is defined by Eq. (15). These frequencies correspond to the passive acoustic modes of the chamber. For a pure chamber mode, the burner outlet is equivalent to a hard wall.

The area jump between burners and chamber will also strongly influence the equivalent reflection coefficient. Figure 3 shows the evolution of the phase for the modes $m = 1$ and $m = N/2$ with α varying from 0.05 to 20. When α is large, the phase tends to be 0 for all frequencies, which means $\mathscr{R}_m = 1$. This is the limit case of a can-annular configuration: the burner tube is similar to a can exposed to a choked exit. In contrast, when α is small, $\mathscr{R}_m$ tends to be equal to -1, the burner tube ends in a large vessel (combustion chamber), which is a representation of an annular configuration. Ghirardo et al. [38] introduced the notion of equivalent reflection coefficient for a 2D can-annular configuration. In the present study, we derived a general 1D expression for the equivalent reflection coefficient seen by a duct terminating in an annular chamber. Although in this paper an annular combustor is considered, the model could easily be applied to a can-annular configuration. This 1D model is simple but gives good qualitative agreement compared to 2D and 3D computations [38,48]. Note that the derivation also holds for the plenum side; the impact of the plenum could be investigated in future work with the same model.

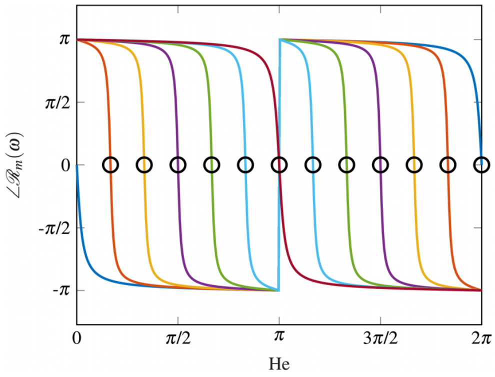

Fig. 2 Phase of the equivalent reflection coefficient $\mathscr{R}_m$ for an annular combustor with 12 burners for the azimuthal modes $m = 0$ [▬], $m = 1$ [▬], $m = 2$ [▬], $m = 3$ [▬], $m = 4$ [▬], $m = 5$ [▬], and $m = 6$ [▬]. Circles: passive acoustic modes of the combustion chamber.

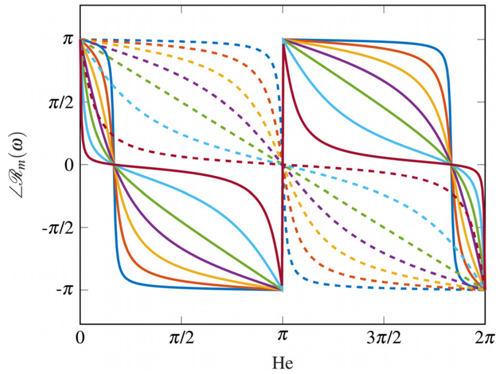

Fig. 3 Phase of the equivalent reflection coefficient for an annular combustor with 12 burners with area ratio between burner and chamber $\alpha = S_b/S_c = 1/20$ [▬], $\alpha = 1/5$ [▬], $\alpha = 1/2$ [▬], $\alpha = 1$ [▬], $\alpha = 2$ [▬], $\alpha = 5$ [▬], $\alpha = 20$ [▬]. Full lines: azimuthal mode $m = 1$. Dashed lines: azimuthal mode $m = 6$.

Reduction of the System to a Longitudinal Burner. In the Interpretation of the Reflection Coefficient section, we showed that the entire chamber can be modeled with an equivalent reflection coefficient $\mathscr{R}_m(\omega)$ that depends on frequency ω and azimuthal order m. The unit cell considered in Fig. 1 can therefore be further reduced into $N/2$ simpler subsystems, which consist only of longitudinal burners as depicted in Fig. 4. It is remarkable that a complex annular system can be analytically reduced to such a simple longitudinal configuration. Such burners have been already studied in the context of ITA modes.

Following the approach proposed by Silva et al. [10], the equations for such a configuration are written as:

$$\begin{bmatrix} -1 & R_{\text{in}} & 0 & 0 \\ T_{11} & T_{12} & -1 & 0 \\ T_{21} & T_{22} & 0 & -1 \\ 0 & 0 & \mathscr{R}_m(\omega) & -1 \end{bmatrix} \begin{bmatrix} f_{\text{in}} \\ g_{\text{in}} \\ f_d \\ g_d \end{bmatrix} = \begin{bmatrix} 0 \\ 0 \\ 0 \\ 0 \end{bmatrix} \tag{16}$$

where T_{ij} are the coefficients of the overall acoustic transfer matrix formed by the propagation of the waves inside the burner tubes and the flame

$$T = \frac{1}{2} \begin{bmatrix} \xi + 1 + \theta\mathscr{F}(\omega) & \xi - 1 - \theta\mathscr{F}(\omega) \\ \xi - 1 - \theta\mathscr{F}(\omega) & \xi + 1 + \theta\mathscr{F}(\omega) \end{bmatrix} \begin{bmatrix} e^{-i\omega L_b/c_c} & 0 \\ 0 & e^{i\omega L_b/c_c} \end{bmatrix} \tag{17}$$

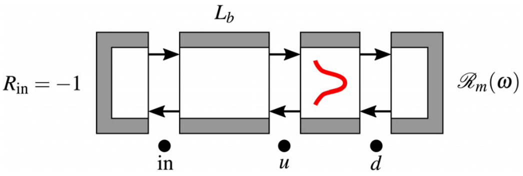

Fig. 4 Annular geometry reduced to a single longitudinal burner. The outlet reflection coefficient $\mathscr{R}_m(\omega)$ depends on frequency and mode order and models the behavior of the combustion chamber.

The determinant of the system matrix from Eq. (16) leads to the corresponding dispersion relation

$$T_{22} - \mathscr{R}_m(\omega)T_{12} - T_{21} + \mathscr{R}_m(\omega)T_{11} = 0 \tag{18}$$

Equation (18) is highly nonlinear and can generally not be solved analytically. To overcome the problem, the system is computed with taX. taX is an open-source MATLAB package developed by the Thermo-Fluid Dynamics group to build and solve low-order thermoacoustic network models [49,50]. With the use of finite differences in a state-space framework, taX reduces Eq. (18) to a generalized linear eigenvalue problem, which facilitates the use of direct solvers to compute the complete spectrum of eigenvalues and eigenmodes. This key feature proves to be crucial to find ITA modes in a simple manner. Mensah [51] and Buschmann et al. [23] have shown that if, instead, the nonlinear eigenvalue problem is solved by iterative methods, finding ITA modes remains difficult as they are associated with small basin of attraction.

On the Origin of Intrinsic Thermoacoustic Clusters

In this section, we apply our model to a lab-scale combustor, which has chamber cavity modes far away from the pure ITA fundamental frequency, and explain the origin of ITA clusters. We also explain why the damping of ITA modes increases with the azimuthal order.

Equivalent Rijke Tube. We apply our model to a realistic lab-scale combustor. Geometrical and thermodynamics parameters are given in Table 1. The time delay of the flame model is $\tau = 2\text{ms}$, so the pure ITA fundamental frequency is evaluated at $f_{\text{ITA}} = 250\text{Hz}$. The length between two burners L is rather small, the total length of the chamber is 0.6 m, which guarantees chamber cavity modes at much higher frequencies than the pure ITA frequency. Indeed the first azimuthal passive chamber mode is evaluated at $f = c_d/P_c = 1090\text{Hz}$. The combustor has 12 burners therefore ITA modes up to order 6 will arise.

Figure 5 presents the equivalent reflection coefficient in the frequency range of interest [0–400 Hz]. In Fig. 2, it corresponds to a Helmholtz number He between 0 and 0.25. In that frequency range, for mode order m between 1 and $N/2$, starting from π at zero frequency, the phase of each mode depends linearly on the frequency He. Therefore, for each m, the phase is modeled by the simple equation $\angle\mathscr{R}_m = \pi - a_m\text{He}$, where the slope of the line is the positive coefficient a_m. Because the gain of $\mathscr{R}_m$ is unity, the equivalent reflection coefficient writes:

$$\mathscr{R}_m(\omega) = -e^{-ia_m\text{He}} = -e^{-i2k\mathscr{L}_m}, \quad \mathscr{L}_m = \frac{a_m L}{2c_d} \tag{19}$$

From Eq. (19), we can directly see that the reflection coefficient $\mathscr{R}_m$ is equivalent to a duct of length $\mathscr{L}_m$ terminated by an open end. Therefore, the longitudinal burner introduced in Fig. 4 can be transformed into the completely equivalent, yet simpler, Rijke tube depicted in Fig. 6. The boundary conditions are fully reflecting and are independent of the frequency. The length of the equivalent duct $\mathscr{L}_m$ varies with the mode order m: the lower the azimuthal order, the longer the equivalent duct (the line is steeper for low azimuthal order in Fig. 5). Following the exact same reasoning for the axial mode, the system can also be reduced to a Rijke tube but with a closed end as outlet boundary condition. Indeed, in Fig. 2, we can see that the phase of the axial mode is zero in the low frequency limit.

Thermoacoustic modes of acoustic or ITA origin have already been studied for the Rijke configuration. Hosseini et al. [19] showed that, for fully reflecting boundary conditions, when the pure ITA mode is far away from the passive acoustic modes, the two do not interplay and the frequency associated with the thermoacoustic mode of ITA origin stays close to the pure ITA frequency. The same result can also be observed in the star shape introduced by Silva et al. [21] or in other recent studies by Orchini et al. [22] and Mukherjee and Shrira [15]. For a pure ITA frequency away enough from the passive acoustic mode, the trajectory in the complex plane of the thermoacoustic mode of ITA origin will be a straight line when varying n (Fig. 6 from Ref. [22]): the growth rate of the mode is changing with the interaction index, but the frequency remains approximately constant.

The annular geometry has been reduced to a simple Rijke tube configuration. For this reduced system, we need to compare the

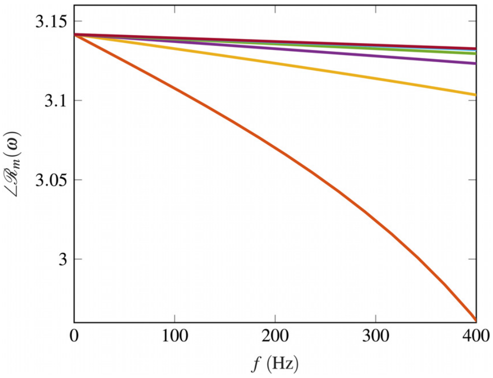

Fig. 5 Phase of the equivalent reflection coefficient $\mathscr{R}_m$ in the case where the chamber mode is far away from the ITA mode. Colors indicate the azimuthal order as defined in Fig. 2.

Table 1 Numerical parameters of the lab-scale combustor

N	12
α	1/15
L_b [m]	1.5×10^{-2}
L [m]	5×10^{-2}
c_u [ms^{-1}]	341
T_d/T_u [–]	4
n	1
τ [s]	2×10^{-3}

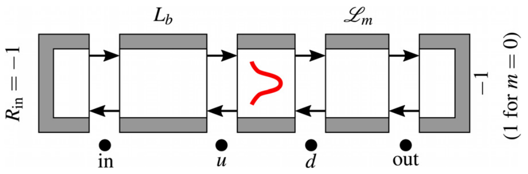

Fig. 6 Equivalent Rijke tube with fully reflecting boundary conditions. The equivalent length $\mathscr{L}_m$ varies with the azimuthal order and models the behavior of the chamber.

pure ITA frequency $f_{\mathrm{ITA}} = \frac{1}{2\tau}$ to the passive acoustic mode of the Rijke tube of total length $L_{\mathrm{tot}} = L_b + \mathscr{L}_m$. For lab-scale combustors, the burners are rather short, of the order of magnitude of a centimeter (1.5 cm in our application case). Following Eq. (19), because the speed of sound is usually high in the chamber, it is straight forward to prove analytically that, for all azimuthal order m, $\mathscr{L}_m$ is always at least one order of magnitude lower than L, the distance between two burners. For such combustors, the effective length $\mathscr{L}_m$ is small, of the order of magnitude of a centimeter for low azimuthal mode order, and much smaller for higher mode order. Therefore, the total length of the equivalent Rijke tube is of the order of magnitude of 1–10 cm, which leads to passive acoustic modes at high frequencies (above 1000 Hz). On the other hand, because the time delay of the flame response is usually between 1 and 2 ms, the pure ITA fundamental frequency $f_{\mathrm{ITA}} = \frac{1}{2\tau}$ will be below 500 Hz. The passive acoustic mode is far away from the pure ITA fundamental frequency. Therefore, for all azimuthal mode order m, thermoacoustic modes of acoustic and ITA origin do not interplay: ITA modes of various azimuthal order will remain close to the pure ITA frequency, and thus creating clusters of ITA modes. Note that this result may not directly apply for industrial configurations where the dimensions are much more significant and could lead to ITA-acoustic interplay. Similarly, this hypothesis is also not valid for clusters of ITA harmonics which are located at higher frequencies. In both cases, clusters are still present but may not contain all azimuthal mode order: some modes may shift and be offset from their respective clusters. This will be developed in the Intrinsic Thermoacoustic Modes Drifting Away From Their Cluster section.

Figure 7 presents the spectrum of our application case. The equivalent Rijke tube reduced model (squares) shows excellent agreement with the full system predictions (crosses) computed by taX. Some discrepancy is observed for the axial mode and is discussed in the Intrinsic Thermoacoustic Modes Drifting Away From Their Cluster section. Thermoacoustic modes of acoustic origin are completely out of the frequency range of interest and do not interplay with thermoacoustic modes of ITA origin. The latter, as expected, lie around the pure ITA frequency, at 250 Hz. Their growth rate changes with the mode order: modes with higher azimuthal order are more damped, as it was also observed by Buschmann et al. [23,24]. We explain this phenomena in the On the Damping of Intrinsic Thermoacoustic Modes section.

On the Damping of Intrinsic Thermoacoustic Modes. In this section, we want to investigate how the damping of an ITA mode is affected by the azimuthal order. As a first case, we consider a Rijke tube, as depicted in Fig. 6, where the effective length $\mathscr{L}_m$ is about the same length as the burner L_b. The flame is located approximately in the middle of the Rijke tube, away from the boundaries. This first case models a low azimuthal order ITA mode. This one-dimensional thermoacoustic system is studied here by means of a phasor analysis. The spatial evolution of Riemann invariants f and g along the system is modeled with phasors rotating in the complex plane. Such analysis was previously applied in the context of ITA modes [17,18] and has proven to be convenient to study linear stability.

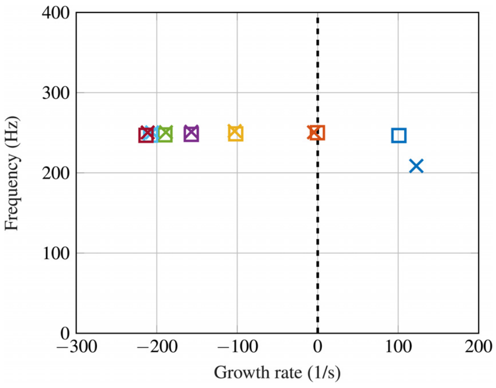

Fig. 7 Thermoacoustic spectrum where ITA modes show various azimuthal order. Crosses: full system. Squares: equivalent Rijke tube model. Colors indicate the azimuthal order as defined in Fig. 2.

For simplicity, we consider a mode at the stability limit (zero growth rate) in order to impose a fixed length to each phasor. A phasor diagram associated with the acoustic waves f and g is displayed in Fig. 8. For convenience, it is assumed that the phasor f_{in} is aligned with the real axis of the complex plane. The reflecting condition at the inlet implies that $g_{\mathrm{in}} = -f_{\mathrm{in}}$. The acoustic wave f will travel from the inlet to the flame along the duct of length L_b. The wave at the location u, upstream of the flame, is related to the inlet by $f_u = f_{in} e^{-i\omega L_b / c_u}$. On the phasors plot, this leads to a rotation of an angle $\varphi_u = \omega L_b / c_u$. Conversely, the g phasor will rotate with the same angle φ_u but in the opposite direction. Sum and subtraction of the phasors yield the acoustic phasors p' and u' respectively.

The same analysis is performed from the downstream boundary. The top of Fig. 9 presents the phasors plot rotating from the outlet to the location just downstream the flame. For the sake of simplicity in the diagrams, we assume that $\bar{\rho}_u c_u = \bar{\rho}_d c_d = 1$. Such a simplification allows to define $p' = f + g$ and $u' = f - g$. Note that taking into account the temperature jump across the flame would lead to the same conclusion. The direction of f_{out} and g_{out} are known because the outlet boundary condition needs to be satisfied, but their length is not known a priori. From the outlet, f and g rotate by an angle $\varphi_d = \omega \mathscr{L}_m / c_d$. Note that their sense of rotation is opposed with respect to the ones of f_u and g_u because waves propagate now from the downstream side. The direction of the phasors f_d and g_d downstream the flame is therefore known. Jump conditions across the flame need to be fulfilled. Knowing the direction and the magnitude of p'_u, and knowing the directions of f_d and g_d, it is possible to geometrically construct the lengths of the latter. Using Eqs. (7) and (2), determining the heat release $\dot{q}'$ is straight forward.

We now consider a second case where the upstream part of the flame is identical, but the effective length $\mathscr{L}_m$ downstream the flame is shorter, about half of the length of the first case. The flame is now located closer to the outlet boundary. This second case is representative of a higher azimuthal order ITA mode. Because the upstream part is unchanged, the upstream phasor plot is identical to Fig. 8. On the other hand, the downstream phasor plot differs. Because $\mathscr{L}_m$ is smaller, the phasors will rotate from the outlet with a smaller angle φ_d, as shown in the bottom of Fig. 9. Because the pressure continuity at the flame still needs to be fulfilled, the length of f_d and g_d should be adapted accordingly. As a result, the phasors f_d and g_d are longer than in the first case, which leads to a longer phasor of velocity u'_d. The latter implies that Eq. (2) is satisfied for larger values of $\dot{q}'$.

Summarizing, we have shown that $\dot{q}'$ for the second case is larger than $\dot{q}'$ for the first case in the region of marginal stability.

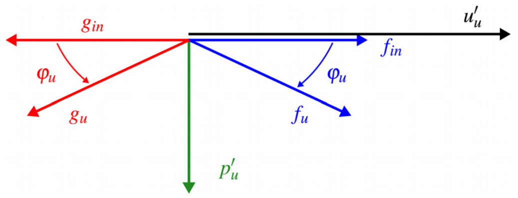

Fig. 8 Phasors diagram of acoustic waves f and g at the inlet and at the location u, just upstream of the flame. Sum and subtraction of these phasors yield the acoustic phasors p' and u'.

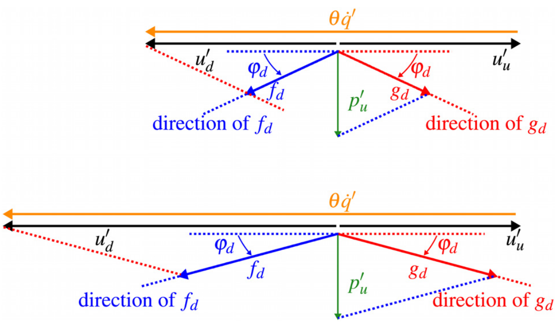

Fig. 9 Phasors diagram of acoustic waves *f* and *g* at the outlet and at the location *d*, just downstream of the flame. Top: ITA mode with a low azimuthal order. Bottom: ITA mode with a higher azimuthal order.

Accordingly, we conclude that the second system requires more energy than the first one to remain neutrally stable, and, therefore, its critical interaction index n_c is higher. Said differently, if we inject the same amount of energy $\dot{q}'$ in both systems (i.e. if both systems have the same interaction index n), the second one will exhibit higher damping. The proposed phasor analysis sheds a light on the spectrum shown in Fig. 7: the effective length $\mathscr{L}_m$ decreases with the mode order m, therefore higher azimuthal order ITA modes are more damped.

Intrinsic Thermoacoustic Modes Drifting Away From Their Cluster

In Fig. 7, we observed that the axial mode is slightly offset from the cluster: its frequency is around 222.7 Hz, compared to the 250 Hz of the pure ITA frequency. The reduced Rijke tube model is not able to capture this drift. In this section, we investigate the cause of ITA modes shifting away from their cluster. We will demonstrate that this phenomena takes place when the π-criterion [8] is broken. Two causes are identified.

The first cause is the gain or losses introduced by acoustic boundaries. The gain of the equivalent reflection coefficient as defined in Eq. (14) is not always unity for complex-valued frequencies. Figure 10 shows the evolution of the gain of $\mathscr{R}_0$ with respect to frequency and growth rate around the pure ITA frequency. The gain drifts from unity by up to 20%. Hence, away from zero growth rate, the boundary is not anymore fully reflecting but introduces some losses/amplification. For azimuthal order, as shown in Fig. 11 for $m=1$, the gain of $\mathscr{R}_m$ is unity and uniform away from the passive acoustic chamber mode $f=\frac{mc_d}{P_c}$. But, in the region close to the passive chamber mode, at nonzero growth rate, the gain of $\mathscr{R}_m$ exhibits important variations, also transforming the fully reflecting boundaries into boundaries with losses/gain.

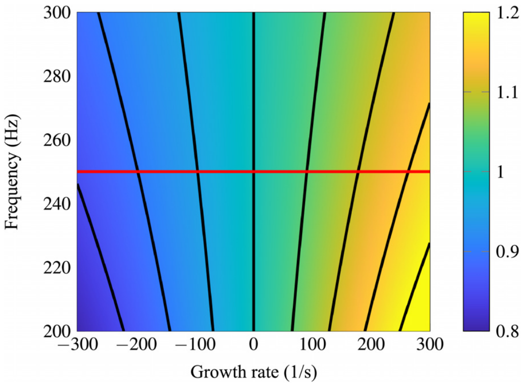

Fig. 10 Gain of the equivalent reflection coefficient $\mathscr{R}_0$ as a function of frequency and growth rate. Red line: pure ITA frequency. Black lines: isolines varying from 0.85 to 1.2 with an increment of 0.05. Away from the real axis, the gain differs from unity; the boundary is not fully reflecting but introduces damping/amplification.

The second cause is the range of validity of the model where the phase $\mathscr{R}_m$ is considered linear with respect to frequency. Indeed, this model is valid for low frequencies and up to a certain extent. For higher frequencies, the phase of the equivalent reflection coefficient $\mathscr{R}_m$ stops evolving linearly with He, and is rather similar to Fig. 2. The approximation of the system by a Rijke tube is not valid anymore. Nevertheless, the system can still be modeled by a longitudinal combustor with an outlet boundary that depends on the frequency as in Fig. 4.

The two aforementioned effects lead to ITA modes drifting away from their pure ITA frequency. When the boundaries are fully reflecting, p' and u'_d are orthogonal, as illustrated on the left side of Fig. 12. The velocities u'_u and u'_d are aligned with the real axis but have opposite directions. The phase difference between u'_u and u'_d is $\varphi=\pi$. It is possible to estimate the frequency of the ITA mode $f=\varphi/2\pi\tau=1/2\tau$. We here retrieve the classic π-criterion to identify ITA modes [8]. However, when the outlet boundary is not fully reflecting, p' and u'_d are not orthogonal. The phase between the velocities u'_u and u'_d changes and therefore, the π-criterion is broken, as depicted on the right side of Fig. 12. The frequency of the ITA mode is different from the pure ITA frequency, i.e. the mode is offset from its cluster.

It is interesting to notice from Fig. 2 that the phase of $\mathscr{R}_m$ is linearly dependent on frequency over a wider frequency range for modes with a higher azimuthal order. The higher the mode order, the larger the region of validity of the Rijke tube model with fully reflecting boundaries. This means that, for ITA harmonics, modes with low azimuthal order are the first to deviate from the cluster. Figure 13 presents the spectrum of an annular chamber with ITA fundamental modes and first harmonics. Note that, because the full system can be reduced to a longitudinal burner, the analytical expression of the frequency spacing between ITA modes $\Delta f = 1/\tau$ derived by Emmert et al. [7] applies here. Therefore, this explains the constant frequency spacing between clusters. In the first cluster, all the modes are around the pure ITA frequency, besides the axial mode, as explained earlier. In the second cluster, the first azimuthal mode is also offset from its cluster. Indeed, at

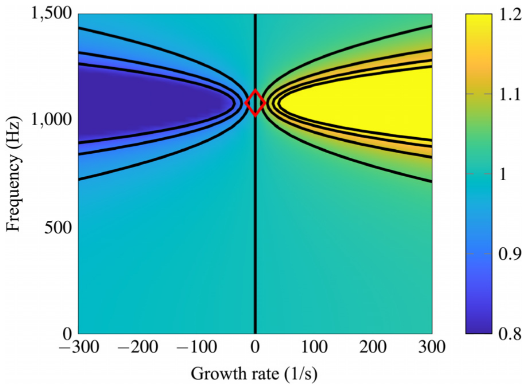

Fig. 11 Gain of the equivalent reflection coefficient $\mathscr{R}_1$ as a function of frequency and growth rate. Diamond: passive acoustic mode of the chamber. Black lines: isolines varying from 0.85 to 1.2 with an increment of 0.05. In the region of the passive acoustic chamber mode, the gain differs from unity; the boundary is not fully reflecting but introduces damping/amplification. Results are similar for other mode orders. Note that the frequency range of interest is different from Fig. 10.

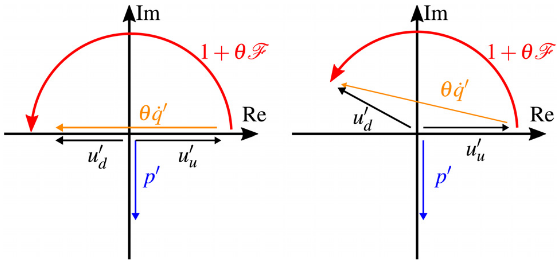

Fig. 12 Phasors diagram in the case of fully reflecting boundaries (left) and non-fully reflecting boundaries (right). For the second case, the π-criterion for ITA modes is not fulfilled. The mode will shift away from the pure ITA frequency.

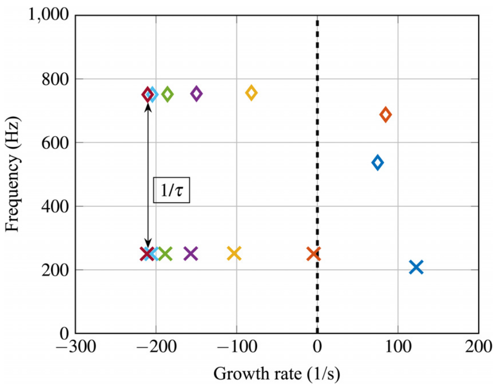

Fig. 13 Thermoacoustic spectrum of an annular chamber. In the first cluster, only the axial mode is offset. In the second one, both axial and first azimuthal order are offset from their cluster. Crosses: first ITA cluster. Diamonds: second ITA cluster. Colors indicate the azimuthal order as defined in Fig. 2.

such frequency, the Rijke tube approximation is not valid, the outlet boundary of the equivalent longitudinal burner is not fully reflecting and the π-criterion is not fulfilled: the ITA mode cannot be around the pure ITA frequency of the first harmonic. The same observations can be made by considering higher harmonics: the second azimuthal order mode will deviate, then the third and so on.

Conclusion

In this paper, we proposed a new approach that combines network models and Bloch theory to describe ITA modes in an annular chamber. Bloch boundary conditions are convenient to use because they enable us to limit the study to a single unit cell and reconstruct the results for the full system without loss of accuracy. We analytically derived a reflection coefficient that models the chamber and how the latter affects the acoustic in the burner. With the use of Bloch theory and Riemann invariants, an annular configuration, where axial and radial dimensions are negligible compared to the azimuthal direction, can be reduced to a simple equivalent longitudinal combustor. The equivalent reflection coefficient depends on the frequency and the azimuthal order of the mode present in the chamber. The area ratio between burners and chamber also widely influences the coupling between the latter and consequently the acoustic response of the burners. The model was derived without loss of generality and is suitable to describe various cases, from annular geometries to can-annular configurations where the burners dimensions are much more significant and the chamber consists only of a small cross-talk area.

The suggested model was applied to a lab-scale combustor. For such configurations, when the acoustic mode of the chamber is far away from the pure ITA frequency, we showed that the longitudinal burner can be reduced to an even simpler model, a Rijke tube with fully reflecting boundaries. The length of the Rijke tube and the flame position in it depends on the azimuthal mode considered. But, because the acoustic mode of the Rijke tube and the ITA frequency are away from each other, thermoacoustic modes of acoustic and ITA origin do not interplay with each other. Therefore, for every azimuthal order, each ITA mode has a frequency close to the pure ITA frequency: this explains the origin of ITA clusters.

The reduced Rijke tube model also allowed us to explain the structure of the spectrum. The flame position in the Rijke tube varies with the azimuthal order, the higher the order, the closer the flame is to the outlet boundary. With the use of a phasors analysis for ITA modes, we showed that, for a flame close to the outlet, the system requires more energy to stay at the stability limit than for a case where the flame is far from the outlet. Said differently, for a given heat release rate, the closer the flame to the outlet, the more damped the mode. This result explains the spectrum structure where ITA modes of higher order are always more damped.

Finally, we investigated the phenomenon of ITA modes drifting away from their clusters. When the outlet boundary is not fully reflecting, pressure and velocity are not orthogonal and the π-criterion is broken. The frequency of the ITA mode is different from its pure ITA frequency, i.e. the mode is offset from its cluster. We demonstrated that low azimuthal order modes deviates first. The impact of the plenum and a possible interplay between thermoacoustic modes of ITA and acoustic origin can be investigated in future work.

Acknowledgment

This project has received funding from the European Union's Horizon 2020 research and innovation programme under Grant Agreement No 765998 *Annular Instabilities and Transient Phenomena in Gas Turbine Combustors* (ANNULIGhT). The authors gratefully acknowledge the Research Association for Combustion Engines (Forschungsvereinigung Verbrennungskraftmaschinen e.V. FVV, project number 6012700) for the financial support to Matthias Haeringer. The authors would also like to thank Max Meindl and Felix Schily for valuable discussions.

Funding Data

- Forschungsvereinigung Verbrennungskraftmaschinen (Grant No. 6012700; Funder ID: 10.13039/501100003162).
- Horizon 2020 (Grant No. 765998; Funder ID: 10.13039/501100007601).

Nomenclature

α = cross section ratio between burner tube and chamber
c_d = speed of sound downstream the flame
c_u = speed of sound upstream the flame
f, g = Riemann invariants
FTF = flame transfer function
He = Helmholtz number
L = length between two burners
$\mathscr{L}_m$ = effective length
L_b = length of the burner tubes
m = Bloch wave number
n = interaction index of the FTF
N = number of burners
p' = acoustic pressure
P_c = total length of the combustion chamber
$\dot{q}'$ = normalized global heat release fluctuations

$\mathscr{R}_m$ = equivalent reflection coefficient
S_b = cross section area of the burner tube
S_c = cross section area of the combustion chamber
u' = acoustic velocity
θ = normalized temperature ratio
ξ = ratio of specific impedances
τ = time delay of the FTF
ω = complex frequency

Appendix A: Derivation of T-Junction Model

The derivation does not show any major difficulties but requires some mathematical precautions. Equation (8) has six unknowns for only three equations. The unknown g_A can be easily eliminated by inserting Eq. (9) in Eq. (8)

$$\begin{cases} f_C + g_C = f_B + g_B & \text{(A1)} \\ f_C - g_C = f_B - g_B + \alpha f_A (1 - \mathscr{R}_m) & \text{(A2)} \end{cases}$$

Combining Eqs. (10) and (11) allows us to directly connect locations B and C of the T-junction

$$\begin{bmatrix} f_C \\ g_C \end{bmatrix} = \begin{bmatrix} e^{i\left(\frac{2\pi m}{N}+kL\right)} & 0 \\ 0 & e^{i\left(\frac{2\pi m}{N}-kL\right)} \end{bmatrix} \begin{bmatrix} f_B \\ g_B \end{bmatrix} \tag{A3}$$

With Eq. (A3), Eqs. (A1) and (A2) simply become

$$\begin{cases} e^{i\left(\frac{2\pi m}{N}+kL\right)} f_B + e^{i\left(\frac{2\pi m}{N}-kL\right)} g_B = f_B + g_B & \text{(A4)} \\ e^{i\left(\frac{2\pi m}{N}+kL\right)} f_B - e^{i\left(\frac{2\pi m}{N}-kL\right)} g_B = f_B - g_B + \alpha f_A (1 - \mathscr{R}_m) & \text{(A5)} \end{cases}$$

which is a system of two equations for three unknowns. But the unknown f_A can be expressed as a function of f_B and g_B using Eq. (8*a*)

$$f_A = \frac{f_B + g_B}{1 + \mathscr{R}_m} \tag{A6}$$

This requires the reflection not to be $\mathscr{R}_m = -1$, but this is a meaningful hypothesis for this configuration. Indeed if the reflection coefficient is $\mathscr{R}_m = -1$, Eq. (8*a*) leads to

$$\begin{cases} f_B = -g_B & \text{(A7)} \\ f_C = -g_C & \text{(A8)} \end{cases}$$

Inserting Eqs. (A3) and (A8) into Eq. (A7) writes

$$f_C e^{i\frac{2\pi m}{N}} \left(e^{ikL} - e^{-ikL}\right) = 0 \tag{A9}$$

Equation (A9) is satisfied for one of the following conditions:

- $f_C = 0$. This implies that $f_A = g_A = f_B = g_B = g_C = f_C = 0$, which is the trivial case where no acoustics is present in the system.
- $\left(e^{ikL} - e^{-ikL}\right) = 0$. The frequency is then imposed by the condition

$$kL = \mathrm{He} = h\pi, \quad h \in \mathbb{N} \tag{A10}$$

The equivalent reflection coefficient $\mathscr{R}_m$ can be equal to –1 only if Eq. (A10) is satisfied. Because of the periodicity of the complex exponential, we can limit the study to only 2 cases: $\mathrm{He} = 0$ and $\mathrm{He} = \pi$.

We consider the first case where $\mathrm{He} = 0$. Equation (A4) simply becomes

$$\left(e^{i\frac{2\pi m}{N}} - 1\right)(f_B + g_B) = 0 \tag{A11}$$

Equation (A11) is satisfied for the following conditions:

- $m = 0$. Inserting this condition into Eq. (A5) leads to the only non trivial solution $\mathscr{R}_0(\mathrm{He} = 0) = 1$.
- if $m \neq 0$, we have the condition $f_B + g_B = 0 = f_A + g_A$ which directly reads to $\mathscr{R}_m(\mathrm{He} = 0) = -1$.

We now consider the second case where $\mathrm{He} = \pi$. Equation (A4) becomes

$$\left(e^{i\frac{2\pi m}{N}} + 1\right)(f_B + g_B) = 0 \tag{A12}$$

Equation (A12) is satisfied for the following conditions:

- $m = N/2$. Inserting this condition into Eq. (A5) leads to the only non trivial solution $\mathscr{R}_{N/2}(\mathrm{He} = \pi) = 1$.
- if $m \neq N/2$, we have the condition $f_B + g_B = 0 = f_A + g_A$ which directly reads to $\mathscr{R}_m(\mathrm{He} = \pi) = -1$.

The equivalent reflection coefficient $\mathscr{R}_m$ takes the value –1 only at frequency $\mathrm{He} = 0$ for all azimuthal orders, except the axial mode, and at frequency $\mathrm{He} = \pi$ for all azimuthal orders, except the push-pull mode. Otherwise, for every other frequency, $\mathscr{R}_m \neq -1$. Inserting Eq. (A6) in Eq. (A5) allows us to eliminate the unknown f_A and have a final system of two equations with two unknowns whose final form is Eq. (13).

References

[1] Lieuwen, T., and McManus, K., 2003, "Introduction: Combustion Dynamics in Lean-Premixed Prevaporized (LPP) Gas Turbines," J. Propul. Power, **19**(5), pp. 721–721.
[2] Poinsot, T., 2017, "Prediction and Control of Combustion Instabilities in Real Engines," Proc. Combust. Inst., **36**(1), pp. 1–28.
[3] Lieuwen, T., and Yang, V., eds., 2005, Combustion Instabilities in Gas Turbine Engines: Operational Experience, Fundamental Mechanisms and Modeling, Progress in Astronautics and Aeronautics. American Institute of Aeronautics and Astronautics, Reston, VA, No. v. 210.
[4] Bomberg, S., Emmert, T., and Polifke, W., 2015, "Thermal Versus Acoustic Response of Velocity Sensitive Premixed Flames," Proc. Combust. Inst., **35**(3), pp. 3185–3192.
[5] Gentemann, A., and Polifke, W., 2007, "Scattering and Generation of Acoustic Energy by a Premix Swirl Burner," ASME Paper No. GT2007-27238.
[6] Polifke, W., 2011, "Thermo-Acoustic Instability Potentiality of a Premix Burner," European Combustion Meeting, ECM2011, British Section of the Combustion Institute, Cardiff, UK, June 27–July 1.
[7] Emmert, T., Bomberg, S., and Polifke, W., 2015, "Intrinsic Thermoacoustic Instability of Premixed Flames," Combust. Flame, **162**(1), pp. 75–85.
[8] Hoeijmakers, M., Lopez Arteaga, I., Kornilov, V., Nijmeijer, H., and de Goey, P., 2013, "Experimental Investigation of Intrinsic Flame Stability," European Combustion Meeting, ECM2013, Scandinavian-Nordic Section of the Combustion Institute, Lund, Sweden, June 25–28.
[9] Hoeijmakers, M., Kornilov, V., Lopez Arteaga, I., de Goey, P., and Nijmeijer, H., 2014, "Intrinsic Instability of Flame-Acoustic Coupling," Combust. Flame, **161**(11), pp. 2860–2867.
[10] Silva, C. F., Emmert, T., Jaensch, S., and Polifke, W., 2015, "Numerical Study on Intrinsic Thermoacoustic Instability of a Laminar Premixed Flame," Combust. Flame, **162**(9), pp. 3370–3378.
[11] Courtine, E., Selle, L., and Poinsot, T., 2015, "DNS of Intrinsic Thermoacoustic Modes in Laminar Premixed Flames," Combust. Flame, **162**(11), pp. 4331–4341.
[12] Emmert, T., Bomberg, S., Jaensch, S., and Polifke, W., 2017, "Acoustic and Intrinsic Thermoacoustic Modes of a Premixed Combustor," Proc. Combust. Inst., **36**(3), pp. 3835–3842.
[13] Lieuwen, T. C., 2012, *Unsteady Combustor Physics*, Cambridge University Press, New York.
[14] Dowling, A. P., and Stow, S. R., 2003, "Acoustic Analysis of Gas Turbine Combustors," J. Propul. Power, **19**(5), pp. 751–764.
[15] Mukherjee, N., and Shrira, V., 2017, "Intrinsic Flame Instabilities in Combustors: Analytic Description of a 1-D Resonator Model," Combust. Flame, **185**, pp. 188–209.
[16] Eckstein, J., and Sattelmayer, T., 2006, "Low-Order Modeling of Low-Frequency Combustion Instabilities in Aeroengines," J. Propul. Power, **22**(2), pp. 425–432.
[17] Ghani, A., Steinbacher, T., Albayrak, A., and Polifke, W., 2019, "Intrinsic Thermoacoustic Feedback Loop in Turbulent Spray Flames," Combust. Flame, **205**(7), pp. 22–32.
[18] Albayrak, A., Steinbacher, T., Komarek, T., and Polifke, W., 2018, "Convective Scaling of Intrinsic Thermo-Acoustic Eigenfrequencies of a Premixed Swirl Combustor," ASME J. Eng. Gas Turbines Power, **140**(4), p. 041510.

[19] Hosseini, N., Kornilov, V., Lopez Arteaga, I., Polifke, W., Teerling, O., and de Goey, L., 2018, "Intrinsic Thermoacoustic Modes and Their Interplay With Acoustic Modes in a Rijke Burner," Int. J. Spray Combust. Dyn., **10**(4), pp. 315–325.

[20] Sogaro, F. M., Schmid, P. J., and Morgans, A. S., 2019, "Thermoacoustic Interplay Between Intrinsic Thermoacoustic and Acoustic Modes: Non-Normality and High Sensitivities," J. Fluid Mech., **878**, pp. 190–220.

[21] Silva, C., Yong, K. J., and Magri, L., 2019, "Thermoacoustic Modes of Quasi-One-Dimensional Combustors in the Region of Marginal Stability," ASME J. Eng. Gas Turbines Power, **141**(2), p. 021022.

[22] Orchini, A., Silva, C. F., Mensah, G. A., and Moeck, J. P., 2020, "Thermoacoustic Modes of Intrinsic and Acoustic Origin and Their Interplay With Exceptional Points," Combust. Flame, **211**, pp. 83–95.

[23] Buschmann, P. E., Mensah, G. A., Nicoud, F., and Moeck, J. P., 2019, "Solution of Thermoacoustic Eigenvalue Problems With a Non-Iterative Method," ASME Paper No. GT2019-90834.

[24] Buschmann, P. E., Mensah, G. A., and Moeck, J. P., 2020, "Intrinsic Thermoacoustic Modes in an Annular Combustion Chamber," Combust. Flame, **214**, pp. 251–262.

[25] Staffelbach, G., Gicquel, L. Y. M., Boudier, G., and Poinsot, T., 2009, "Large Eddy Simulation of Self Excited Azimuthal Modes in Annular Combustors," Proc. Combust. Inst., **32**(2), pp. 2909–2916.

[26] Wolf, P., Staffelbach, G., Gicquel, L. Y. M., Müller, J.-D., and Poinsot, T., 2012, "Acoustic and Large Eddy Simulation Studies of Azimuthal Modes in Annular Combustion Chambers," Combust. Flame, **159**(11), pp. 3398–3413.

[27] Avdonin, A., Meindl, M., and Polifke, W., 2019, "Thermoacoustic Analysis of a Laminar Premixed Flame Using a Linearized Reacting Flow Solver," Proc. Combust. Inst., **37**(4), pp. 5307–5314.

[28] Gikadi, J., 2013, "Prediction of Acoustic Modes in Combustors Using Linearized Navier-Stokes Equations in Frequency Space," Ph.D. thesis, Technische Universität München, Garching, Germany.

[29] Schulze, M., Hummel, T., Klarmann, N., Berger, F. M., Schuermans, B., and Sattelmayer, T., 2017, "Linearized Euler Equations for the Prediction of Linear High-Frequency Stability in Gas Turbine Combustors," ASME J. Eng. Gas Turbines Power, **139**(3), p. 031510.

[30] Nicoud, F., Benoit, L., Sensiau, C., and Poinsot, T., 2007, "Acoustic Modes in Combustors With Complex Impedances and Multidimensional Active Flames," AIAA J., **45**(2), pp. 426–441.

[31] Krüger, U., Hüren, J., Hoffmann, S., Krebs, W., and Bohn, D., 1999, "Prediction of Thermoacoustic Instabilities With Focus on the Dynamic Flame Behavior for the 3A-Series Gas Turbine of Siemens KWU," ASME Paper No. 99-GT-111.

[32] Evesque, S., and Polifke, W., 2002, "Low-Order Acoustic Modelling for Annular Combustors: Validation and Inclusion of Modal Coupling," ASME Paper No. GT-2002-30064.

[33] Parmentier, J.-F., Salas, P., Wolf, P., Staffelbach, G., Nicoud, F., and Poinsot, T., 2012, "A Simple Analytical Model to Study and Control Azimuthal Instabilities in Annular Combustion Chambers," Combust. Flame, **159**(7), pp. 2374–2387.

[34] Bauerheim, M., Parmentier, J.-F., Salas, P., Nicoud, F., and Poinsot, T., 2014, "An Analytical Model for Azimuthal Thermoacoustic Modes in an Annular Chamber Fed by an Annular Plenum," Combust. Flame, **161**(5), pp. 1374–1389.

[35] Yang, D., Laera, D., and Morgans, A. S., 2019, "A Systematic Study of Nonlinear Coupling of Thermoacoustic Modes in Annular Combustors," J. Sound Vib., **456**, pp. 137–161.

[36] Bloch, F., 1929, "Über Die Quantenmechanik Der Elektronen in Kristallgittern," Z. Für Phys., **52**(7–8), pp. 555–600.

[37] Mensah, G. A., Campa, G., and Moeck, J. P., 2016, "Efficient Computation of Thermoacoustic Modes in Industrial Annular Combustion Chambers Based on Bloch-Wave Theory," ASME J. Eng. Gas Turbines Power, **138**(8), p. 081502.

[38] Ghirardo, G., Di Giovine, C., Moeck, J. P., and Bothien, M. R., 2019, "Thermoacoustics of Can-Annular Combustors," ASME J. Eng. Gas Turbines Power, **141**(1), p. 011007.

[39] Haeringer, M., and Polifke, W., 2019, "Time Domain Bloch Boundary Conditions for Efficient Simulation of Thermoacoustic Limit-Cycles in (Can-)Annular Combustors," ASME J. Eng. Gas Turbines Power, **141**(12), p. 121005.

[40] Poinsot, T., and Veynante, D., 2012, *Theoretical and Numerical Combustion*, 3rd ed., CNRS, Paris.

[41] Schuller, T., Durox, D., Palies, P., and Candel, S., 2012, "Acoustic Decoupling of Longitudinal Modes in Generic Combustion Systems," Combust. Flame, **159**(5), pp. 1921–1931.

[42] Marble, F. E., and Candel, S. M., 1977, "Acoustic Disturbance From Gas Non-Uniformities Convected Through a Nozzle," J. Sound Vib., **55**(2), pp. 225–243.

[43] Bauerheim, M., Duran, I., Livebardon, T., Wang, G., Moreau, S., and Poinsot, T., 2016, "Transmission and Reflection of Acoustic and Entropy Waves Through a Stator–Rotor Stage," J. Sound Vib., **374**, pp. 260–278.

[44] Morgans, A. S., and Duran, I., 2016, "Entropy Noise: A Review of Theory, Progress and Challenges," Int. J. Spray Combust. Dyn., **8**(4), pp. 285–298.

[45] Chu, B.-T., 1953, "On the Generation of Pressure Waves at a Plane Flame Front," Symp. (Int.) Combust., **4**(1), pp. 603–612.

[46] Crocco, L., 1951, "Aspects of Combustion Stability in Liquid Propellant Rocket Motors Part1: Fundamentals. Low Frequency Instability With Monopropellants," J. Am. Rocket Soc., **21**(6), pp. 163–178.

[47] Bauerheim, M., Cazalens, M., and Poinsot, T., 2015, "A Theoretical Study of Mean Azimuthal Flow and Asymmetry Effects on Thermo-Acoustic Modes in Annular Combustors," Proc. Combust. Inst., **35**(3), pp. 3219–3227.

[48] Haeringer, M., Fournier, G. J. J., Meindl, M., and Polifke, W., 2020, "A Strategy to Tune Acoustic Terminations of Single-Can Test-Rigs to Mimic Thermoacoustic Behavior of a Full Engine," ASME J. Eng. Gas Turbines Power, ePub.

[49] Emmert, T., 2016, "State Space Modeling of Thermoacoustic Systems With Application to Intrinsic Feedback," Ph.D. thesis, TU München, München, Germany.

[50] Emmert, T., Meindl, M., Jaensch, S., and Polifke, W., 2016, "Linear State Space Interconnect Modeling of Acoustic Systems," Acta Acust. United Acust., **102**(5), pp. 824–833.

[51] Mensah, G. A., 2019, "Efficient Computation of Thermoacoustic Modes," Ph.D. thesis, Technische Universität Berlin.

Matthias Haeringer[1]
Department of Mechanical Engineering,
Technical University of Munich,
Garching D-85747, Germany
e-mail: haeringer@tfd.mw.tum.de

Guillaume J. J. Fournier
Department of Mechanical Engineering,
Technical University of Munich,
Garching D-85747, Germany
e-mail: fournier@tfd.mw.tum.de

Max Meindl
Department of Mechanical Engineering,
Technical University of Munich,
Garching D-85747, Germany
e-mail: meindl@tfd.mw.tum.de

Wolfgang Polifke
Department of Mechanical Engineering,
Technical University of Munich,
Garching D-85747, Germany
e-mail: polifke@tum.de

A Strategy to Tune Acoustic Terminations of Single-Can Test-Rigs to Mimic Thermoacoustic Behavior of a Full Engine

Thermoacoustic properties of can-annular combustors are commonly investigated by means of single-can test-rigs. To obtain representative results, it is crucial to mimic can–can coupling present in the full engine. However, current approaches either lack a solid theoretical foundation or are not practicable for high-pressure rigs. In this study, we employ Bloch-wave theory to derive reflection coefficients that correctly represent can–can coupling. We propose a strategy to impose such reflection coefficients at the acoustic terminations of a single-can test-rig by installing passive acoustic elements, namely straight ducts or Helmholtz resonators. In an iterative process, these elements are adapted to match the reflection coefficients for the dominant frequencies of the full engine. The strategy is demonstrated with a network model of a generic can-annular combustor and a three-dimensional (3D) model of a realistic can-annular combustor configuration. For the latter, we show that can–can coupling via the compressor exit plenum is negligible for frequencies sufficiently far away from plenum eigenfrequencies. Without utilizing previous knowledge of relevant frequencies or flame dynamics, the test-rig models are adapted within a few iterations and match the full engine with good accuracy. Using Helmholtz resonators for test-rig adaption turns out to be more viable than using straight ducts. [DOI: 10.1115/1.4048642]

Introduction

Thermoacoustic combustion instabilities are a major concern in the development of new low emission gas turbine combustors. Arising from constructive feedback between unsteady heat release and acoustics, these instabilities may result in large-amplitude oscillations of acoustic quantities, which can cause increased emission levels or even structural damage [1].

Latest generation land-based gas turbines are often equipped with a can-annular combustion system. In this combustor type, a number of cans are arranged equidistantly around the circumference of the engine. The individual cans are coupled acoustically by a large upstream plenum that is fed by the gas turbine compressor and thus called compressor exit plenum. On the downstream side, the cans are coupled via a small annular gap in front of the first turbine stator [2].

From a thermoacoustic point of view, this coupling is of particular interest although it is weak. It gives rise to azimuthal modes, which involve multiple cans and extend over the entire circumference of the engine. Several studies have characterized this coupling [2–4] and its importance regarding thermoacoustics of the entire engine [5–9]. Generally, due to the coupling of the individual cans, the thermoacoustic properties of an entire can-annular combustor cannot be directly represented by a single-can system.

However, full-scale numerical or experimental investigations of the thermoacoustic properties of an entire can-annular combustion system are extremely expensive and thus not feasible in the design phase of a new combustor. Typically in the late design phase, the thermoacoustic properties of the full engine are explored by means of single-can or single-sector test-rigs [5,6,10]. A variety of approaches are used to mimic can–can coupling in such single-can test-rigs. A commonly applied method is to extend the up- and downstream termination of the test-rig by straight ducts [6,10,11]. This, however, should be seen as an ad hoc approach without solid theoretical foundation. Another possibility to at least account for some modes resulting from can–can coupling is to employ two-can test-rigs [12], which obviously implies high effort.

More elaborate numerical approaches take into account the equivalent reflection coefficients that a single can is exposed to in the full can-annular system [13]. If these reflection coefficients can be imposed at the up- and downstream end of a single-can test-rig, it mimics the thermoacoustics of the entire engine. In numerical simulations, this has already been exploited to simulate an entire can-annular combustor by resolving only one single can [14].

In experimental test-rigs, active control methods could in principle be used to impose the appropriate reflection coefficients [15–17]. However, in high-pressure single-can test-rigs of applied can-annular combustors this approach seems difficult to implement, because of generally limited access and the hot gas environment.

This study instead focuses on test-rig adaption by passive acoustic elements. We critically assess the common practice of accounting for can–can coupling by extending the up- and downstream termination of test-rigs by straight ducts. In order to refine the current approach we propose and scrutinize an iterative adaption strategy to match the theoretically derived equivalent reflection coefficients with passive acoustic elements. We finally discuss two acoustic element types—straight ducts and Helmholtz resonators—that might be employed within the proposed strategy and apply them to adapt thermoacoustic models of single-can test-rigs. This study reveals that test-rig adaption using duct extensions is not practical.

---

[1] Corresponding author.

Manuscript received September 3, 2020; final manuscript received September 14, 2020; published online March 31, 2021. Editor: Jerzy T. Sawicki.

The paper is structured as follows: In the section Equivalent Reflection Coefficients Computed From Bloch-Wave Theory, we recall the application of Bloch-wave theory in the context of thermoacoustics. We employ it to derive the equivalent reflection coefficients for a single can at a given azimuthal mode order. In the section Passive Acoustic Elements to Approximate Equivalent Reflection Coefficient, we discuss appropriate passive acoustic elements to mimic the equivalent reflection coefficients and propose an iterative adaption strategy. In the sections Application to Network Model of a Generic Can-Annular Combustor and Validation With a Configuration of Applied Relevance, the proposed strategy is applied to a network model of a generic can-annular combustor adapted using straight ducts and a three-dimensional (3D) model of a realistic can-annular combustor adapted using Helmholtz resonators. After a discussion of the expected importance of effects that are neglected in the present thermoacoustic models, a conclusion is drawn in the section Conclusion.

Equivalent Reflection Coefficients Computed From Bloch-Wave Theory

Within this section, we present the reflection coefficients up- and downstream of a single can in a can-annular combustor for a given azimuthal mode order m. These reflection coefficients lump the acoustic response of all remaining cans of the engine. The situation is sketched in Fig. 1 for a generic multican combustor. The considered single can is marked by the inner (red) dashed box, the equivalent reflection coefficients $\mathcal{R}_{m,\mathrm{u}}$ and $\mathcal{R}_{m,\mathrm{d}}$ are defined at its up- and downstream termination. Provided plane acoustic waves, the reflection coefficients are defined as the ratio of the down- and upstream traveling acoustic Riemann invariants $f = \hat{p}/\rho c + \hat{u}$ and $g = \hat{p}/\rho c - \hat{u}$ and are related to the acoustic impedance Z at the respective positions by

$$\mathcal{R}_{m,\mathrm{u}} = \frac{f_\mathrm{u}}{g_\mathrm{u}} = \frac{Z_\mathrm{u}+1}{Z_\mathrm{u}-1}, \quad \mathcal{R}_{m,\mathrm{d}} = \frac{g_\mathrm{d}}{f_\mathrm{d}} = \frac{Z_\mathrm{d}-1}{Z_\mathrm{d}+1} \tag{1}$$

In general, $\mathcal{R}_{m,\mathrm{x}}$ (with $\mathrm{x}\,\hat{=}\,\mathrm{u}/\mathrm{d}$) in Fig. 1 depend on the thermoacoustic properties of the remaining cans. Therefore, in the most general case, the acoustic properties and especially flame dynamics of all individual cans have to be known in order to compute $\mathcal{R}_{m,\mathrm{x}}$.

However, typical can-annular combustors feature a discrete rotational symmetry, where the whole combustor consists of a number of N identical sectors arranged equidistantly around the circumference of the engine. These sectors—marked with the black dashed box in Fig. 1 and in the following denoted as “unit cells”—comprise one single can and the corresponding sector of the compressor exit plenum and the annular gap in front of the first turbine stage. For such a rotationally symmetric configuration, the equivalent reflection coefficients for a given azimuthal mode order m can be computed by utilizing Bloch-wave theory [18,19]. As shown in the following, in this case $\mathcal{R}_{m,\mathrm{x}}$ are only dependent on the elements coupling the individual cans and the degree of symmetry N and are independent of the thermoacoustics of the individual cans.

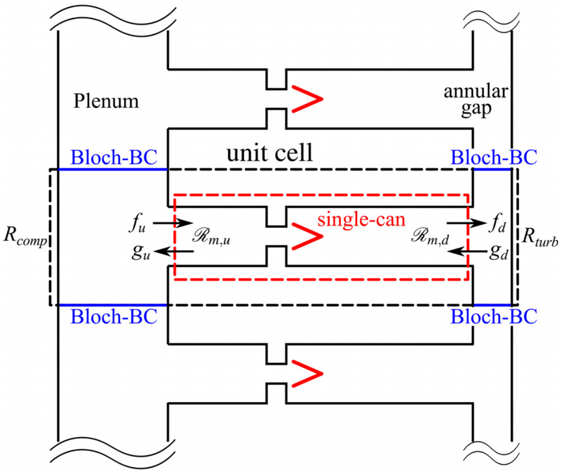

Fig. 1 Generic can-annular combustor. Cans are coupled at up- and downstream side via compressor exit plenum and annular gap. R_turb and R_comp denote reflection coefficients of turbine inlet and compressor exit.

Mensah et al. [19] showed that the (thermo-)acoustic eigenmodes of discrete rotationally symmetric systems can be computed efficiently by utilizing Bloch-wave theory [18]. The eigenmodes $\hat{p}$ of a can-annular combustor can thus be written as

$$\hat{p}(\mathbf{x}) = \Psi(\mathbf{x}) e^{im\phi}, \text{ with}$$
$$m = -(N/2-1), \ldots, -1, 0, 1, \ldots, N/2-1, N/2 \tag{2}$$

Here, $\mathbf{x} = (r, \phi, z)$ is the position vector comprised of the radial, circumferential, and axial coordinate, Ψ is a function that—for a given eigenmode—is identical in all N unit cells, and m is called the Bloch-wave number. For low frequencies relevant in the present context, the absolute value $|m|$ of the Bloch-wave number is equivalent to the azimuthal mode order [19] and both terms are used synonymously in the following.

The (thermo-)acoustic eigenmodes expressed by Eq. (2) can be classified into three types: azimuthally spinning modes with Bloch-wave numbers of $m = \pm 1, \ldots, \pm(N/2-1)$, purely axial modes with $m = 0$, and so-called “push–pull” modes with $m = N/2$. The latter only exist for combustors with an even number of cans and are characterized by an acoustic pressure and velocity field of alternating signs in adjacent cans [13,14]. Except for axial modes with $m = 0$, which feature identical pressure fields in all sectors, all other mode types result from coupling of the individual unit cells. Thus, a single-can test-rig, where this coupling is not accounted for will only show modes of azimuthal order $m = 0$.

For applied can-annular combustors, the mean flow in azimuthal direction is negligible. Provided discrete rotational symmetry, such a system features also reflection symmetry. In this case, the azimuthally spinning modes appear as degenerate pairs, where modes with Bloch-wave numbers of opposite sign merely differ by their direction of rotation. For the following derivations, we can therefore limit our considerations to non-negative m [14,19].

Without loss of generality, we consider a unit cell centered at $\phi = 0$ and extended over an azimuthal angle $\phi = [-\pi/N, \pi/N]$. By definition, $\Psi(\mathbf{x})$ is identical in each unit cell. As the pressure is continuous across the interfaces connecting two unit cells (marked blue in Fig. 1), $\Psi(\mathbf{x})$ at the left and right boundary of the unit cell has to be equal [13]

$$\Psi\left(r, \phi = -\frac{\pi}{N}, z\right) = \Psi\left(r, \phi = \frac{\pi}{N}, z\right) \tag{3}$$

Combining Eq. (3) with Eq. (2) leads to a quasi-periodic boundary condition—called Bloch boundary condition (BBC)—for the acoustic pressure [19]

$$\hat{p}\left(r, \phi = \frac{\pi}{N}, z\right) = \hat{p}\left(r, \phi = -\frac{\pi}{N}, z\right) e^{im\frac{2\pi}{N}} \tag{4}$$

Assuming that discrete rotational symmetry holds, a given azimuthal mode order m of the full can-annular combustor is completely represented by a single unit cell with BBC at the coupling interfaces, as sketched in Fig. 2. The equivalent reflection coefficients $\mathcal{R}_{m,\mathrm{x}}$ defined at the in-/outlet of a single can are in this case independent of the remaining cans. They only depend on the

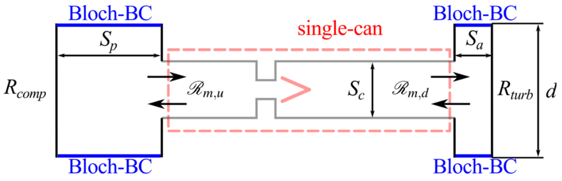

Fig. 2 Definition of $\mathcal{R}_{m,x}$ at the in-/outlet of a single can. $\mathcal{R}_{m,x}$ are dependent on the azimuthal distance d of two cans and the cross sections of can S_c, annular gap S_a and compressor exit plenum S_p.

acoustics of the coupling parts, i.e., the annular gap and the compressor exit plenum, the acoustic termination toward turbine R_{turb} and compressor R_{comp}, and the azimuthal mode order m and the number of cans N. $\mathcal{R}_{m,\text{x}}$ can thus be computed from an acoustic model that comprises these coupling parts and BBC. This strategy has already been applied by Ghirardo et al. [13] to compute the equivalent reflection coefficient of a generic can outlet section.

The equivalent reflection coefficients defined in this way are valid for a given mode order m. They may be interpreted as the cumulative acoustic response of all remaining cans for a given azimuthal mode order, i.e., they represent the response of a certain synchronization pattern across all cans.

Equivalent Reflection Coefficients of a Generic Can-Annular Combustor. In order to discuss the general features of the equivalent reflection coefficients, Fig. 3 shows $\mathcal{R}_{m,\text{x}}$ of a generic can-annular system with $N = 16$ cans for all azimuthal mode orders m. The shown $\mathcal{R}_{m,\text{x}}$ was computed using an acoustic network model similar as shown in Fig. 4. For simplicity, the acoustic termination toward turbine and compressor is assumed to be ideal sound hard walls with $R_{\text{turb}} = R_{\text{comp}} = 1$. $\mathcal{R}_{m,\text{x}}$ crucially depend on the area ratio A of annular gap and can ($A = S_a/S_c$) or plenum and can ($A = S_p/S_c$), respectively. Figure 3 shows the phase of the reflection coefficients for $A = 20$ (top) and $A = 0.06$ (bottom). The former is representative of the plenum/can transition (corresponds to $\mathcal{R}_{m,\text{u}}$), and the latter is typical for the transition can/annular gap (corresponds to $\mathcal{R}_{m,\text{d}}$). Due to rotational and reflectional symmetry, no acoustic energy is exchanged between individual cans. Thus, the gain of $\mathcal{R}_{m,\text{x}}$ only depends on the gain of R_{turb} and R_{comp}. In the present case, the gain $|\mathcal{R}_{m,\text{x}}|$ is thus uniformly unity for all mode orders and therefore not shown.

The phase of $\mathcal{R}_m$ of all azimuthal mode orders m is plotted versus the Helmholtz number $\text{He} = \omega d/c$, where ω is the angular frequency, c is the speed of sound, and d is the azimuthal distance of the individual cans. In the zero-frequency limit, the equivalent reflection coefficient behaves like a wall $\mathcal{R}_{m=0} = 1$ for $m = 0$ and like an ideal open end $\mathcal{R}_{m\neq 0} = -1$ for all other mode orders [13]. For $\text{He} = 2\pi \frac{m}{N}$, which correspond to purely azimuthal modes of order m that are only active in the plenum or the annular gap, the corresponding equivalent reflection coefficient equals $\mathcal{R}_m = 1$. For $\text{He} = \pi$, at which the distance d of two cans equals half a wavelength, Bloch-symmetry necessitates pressure nodes at the can centers for $m \neq N/2$, corresponding to an equivalent reflection coefficient $\mathcal{R}_{m\neq N/2} = -1$ [20]. In typical can-annular systems, $\text{He} = \pi$ is the cut-on frequency of transversal modes inside the cans. The validity of the 1D model employed here is thus questionable for $\text{He} > \pi$. However, the frequency range of interest in the present context is $\text{He} < \pi/4$.

For large area ratios A (top plot of Fig. 3), typical for the transition compressor-plenum/can, the equivalent reflection coefficient essentially represents an ideal open end with $\mathcal{R}_m \approx -1$ for a wide frequency range. Only in the vicinity of pure plenum modes of the respective azimuthal order $\mathcal{R}_m$ deviates from the ideal open end. This indicates that for typical area ratios and for frequencies sufficiently far away from pure plenum modes, the compressor exit plenum is essentially decoupled from the individual cans. $\mathcal{R}_m$ of higher azimuthal mode orders may thus be approximated with $\mathcal{R}_{m=0}$.

For small area ratios A (bottom plot of Fig. 3), typical for the transition can/annular gap, the general behavior of the equivalent reflection coefficients is similar. However, especially for frequencies $\text{He} < \pi/4$, the individual $\mathcal{R}_m$ are more distinct from each other, compared to $\mathcal{R}_m$ for large A. This indicates that for this frequency range, the coupling of individual cans via the annular gap with small A is more important than the coupling via the compressor exit plenum with large A. This preliminary result will be confirmed later by considering a realistic 3D configuration.

Overall, the phase of the equivalent reflection coefficients of individual mode orders m is closely spaced for both large and small A. This is a consequence of the weak coupling of individual cans for extreme values of A characteristic of can-annular combustors. It leads to clustering of eigenmodes with different m, because the reflection coefficient at the can entry and exit are similar for all m [8,13]. For intermediate values of $A \sim 1$, $\angle\mathcal{R}_m$ of individual mode orders would be more distinct, resulting from stronger coupling.

The objective of this work is to provide a strategy to investigate the thermoacoustics of a can-annular combustor by means of a single-can test-rig. If the equivalent reflection coefficients $\mathcal{R}_{m,\text{x}}$ can be imposed at the up- and downstream termination of the single-can test-rig, it will represent a given mode order m of the full engine and will have identical thermoacoustic properties. In the Passive Acoustic Elements to Approximate Equivalent Reflection Coefficient section, we discuss two types of passive acoustic elements that might be used to approximate $\mathcal{R}_{m,\text{x}}$.

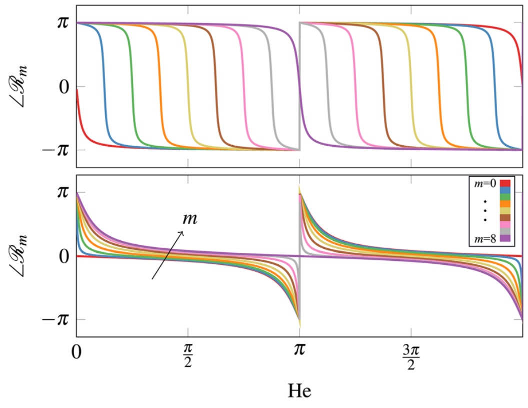

Fig. 3 $\angle\mathcal{R}_m$ of generic 16-can combustor with two different area ratios $A = 20$ (top) and $A = 0.06$ (bottom) plotted versus Helmholtz-number He

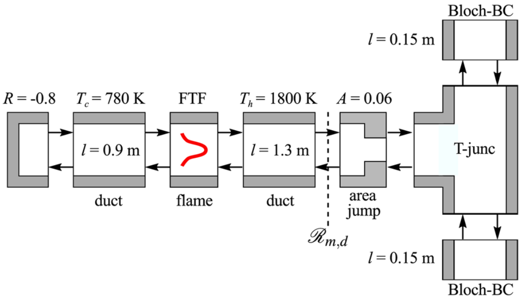

Fig. 4 Network model of considered generic can-annular combustor

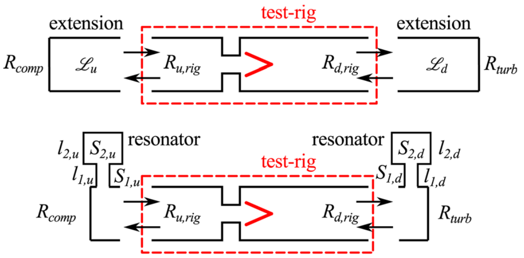

Fig. 5 Matching $\mathcal{R}_{m,x}$ of the full engine by extending the single-can test-rig with straight ducts (top) and by installing Helmholtz-resonators at the in-/outlet (bottom)

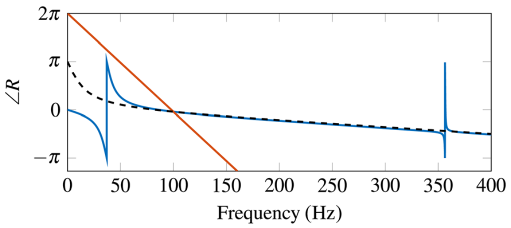

Fig. 6 $\angle\mathcal{R}_{m=1,d}$ from Fig. 7 (dashed black) compared to $\angle R_{d,rig}$ adapted by straight duct extension (red) and Helmholtz resonator (blue). Both elements are designed for $\nu_d = 100$ Hz.

Passive Acoustic Elements to Approximate Equivalent Reflection Coefficient

As shown in Fig. 3, the ensemble of cans reflects acoustic waves with a certain phase shift, which depends on frequency ω and azimuthal mode order m. The general idea of this work is to approximate this phase shift for a given azimuthal mode order m with passive acoustic elements. A common practice to account for can–can coupling in single-can test-rigs is to extend the (up- and) downstream termination of the test-rig by straight ducts. In order to critically assess—and improve—this current practice, we investigate how a straight duct extension can be used to approximate the equivalent reflection coefficients. The second element we consider is a Helmholtz-type resonator.

Figure 5 shows schematically how the two considered elements should be installed in a test-rig. The passive acoustic elements have to be adapted such that the phase of test-rig and equivalent reflection coefficient

$$\angle R_{\mathrm{x,rig}}(\omega_\mathrm{d}) \overset{!}{=} \angle\mathcal{R}_{m,\mathrm{x}}(\omega_\mathrm{d}) \tag{5}$$

match for the design frequency ω_d. As mentioned in the Equivalent Reflection Coefficients of a Generic Can-Annular Combustor section, the gain $|\mathcal{R}_{m,\mathrm{x}}|$ depends on the gain $|R_{\mathrm{comp/turb}}|$ and is identical for all mode orders m. It is thus crucial that the considered elements do not affect the gain of the test-rig reflection coefficient $R_{\mathrm{x,rig}}$. As the gain of R_{turb} is determined by the mean flow through the first turbine stator vanes [21], the duct extension used to shift the outlet termination $R_{\mathrm{comp,turb}}$ must have a constant cross section. The Helmholtz resonator in turn must be designed for a minimum damping rate, i.e., it should be operated sufficiently far away from its eigenfrequency [22].

The only design parameter of the straight duct extensions with constant cross section is their length $\mathcal{L}_\mathrm{x}$. Neglecting the effect of mean flow,[2] the phase shift induced by shifting the in-/outlet termination by the distance $\mathcal{L}_\mathrm{x}$ depends linearly on the frequency ω

$$\angle R_{\mathrm{x,rig}} = -\frac{2\omega\mathcal{L}_\mathrm{x}}{c} \tag{6}$$

In order to shape the frequency response of the Helmholtz resonator, four main design parameters are available: lengths l_1 and l_2 and cross sections S_1 and S_2 of the resonator neck and volume, respectively. Additional design parameters that are not considered here could be the purge mass flow rate and temperature.

Computing the exact frequency response of Helmholtz resonators depending on the mentioned design parameters requires sophisticated numerical or experimental methods [22]. However, in practice the same type of acoustic model will be used to obtain $\angle R_{\mathrm{x,rig}}$ and $\angle\mathcal{R}_{m,\mathrm{x}}$. In case the employed acoustic model does not include certain effects that might be relevant in practice, they are neglected in both computed $\angle R_{\mathrm{x,rig}}$ and $\angle\mathcal{R}_{m,\mathrm{x}}$. Thus, for the present purpose, comparably crude modeling approaches such as the Helmholtz equation employed in this study might be sufficient to compute $\mathcal{R}_{m,\mathrm{x}}$ and to design the passive acoustic elements. In the section Influence of Effects Neglected in Combustor Model, we discuss how effects neglected in the employed acoustic models may compromise the proposed strategy.

Figure 6 exemplarily shows $\angle R_{\mathrm{d,rig}}$ adapted by duct extension (blue line) and Helmholtz resonator (red line) to match $\angle\mathcal{R}_{m=1,\mathrm{d}}$ taken from Fig. 7 at a design frequency of $\nu_\mathrm{d} = \omega_\mathrm{d}/2\pi = 100$ Hz. From Fig. 6, it becomes apparent that the Helmholtz resonator is more appropriate to match the equivalent reflection coefficient shown. Due to its four degrees-of-freedom, it can be designed to well approximate $\mathcal{R}_m$ in a quite large frequency range around ν_d. In contrast, the straight duct extension matches $\mathcal{R}_m$ only directly at ν_d.

In order to use a single-can test-rig to study the thermoacoustic stability properties and possibly the limit cycle (LC) of mode order m of a full can-annular combustor, $R_{\mathrm{x,rig}}$ has to be designed to match $\mathcal{R}_{m,\mathrm{x}}$ at the dominant (respectively, most unstable) frequencies of the full engine. However, these design frequencies are normally not known a priori. Even if the pure acoustic eigenfrequencies might be known from an acoustic model, the (generally unknown) flame dynamics may alter these frequencies. Furthermore, intrinsic thermoacoustic (ITA) modes may play an important role [23–25]. Their frequencies are not predictable without knowledge of the flame dynamics. Therefore, the passive acoustic elements in general have to be adapted in an iterative procedure, which ensures that the dominant frequency observed in the single-can test-rig converges to the dominant frequency of the full engine of a given azimuthal mode order m. A strategy is presented in the Iterative Adaption of Passive Elements section.

If the initial design of the Helmholtz resonator is good enough to approximate the relevant frequency range sufficiently well, as shown in Fig. 6, iterative adaption may not be necessary. However, the large number of degrees-of-freedom complicates the search for an optimal design, while this is straightforward for the duct extension. In the present case, the parameters of the resonator were chosen such that the design frequency is well above the Helmholtz mode and below the first axial mode, which coincide with the abrupt phase transitions at 40 Hz and 355 Hz, respectively. Sufficiently far away from the resonator eigenfrequencies, its damping rates are expected to be comparably small [22]. While the design works properly for the present case, a general design guideline is not immediately obvious and the set of parameters has to be optimized from case to case. In the following, we therefore investigate the capabilities of both element types based on numerical models of single-can test-rig and full can-annular combustor.

Iterative Adaption of Passive Elements. As discussed previously, the frequency ν_d for which the Helmholtz resonator or the straight duct extension is initially designed to fulfill Eq. (5) does in general not coincide with the dominant frequencies of the full

---

[2] Axial mean flow can be accounted for by changing the propagation speed of f to $\bar{u} + c$ and g to $\bar{u} - c$.

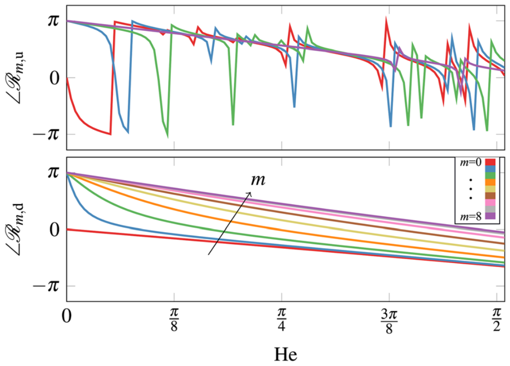

Fig. 7 Equivalent reflection coefficient of 3D configuration. $\angle\mathcal{R}_{m,\mathrm{u}}$ **for** $m=0,1,2,8$ **(top) and** $\angle\mathcal{R}_{m,\mathrm{d}}$ **(bottom) versus Helmholtz-number He.**

engine. We therefore propose a fixed point iteration strategy with the objective that the dominant frequency observed in the single-can test-rig approaches the dominant frequency of the full engine for a given mode order m.

At this point, the terminology *dominant frequency* has to be defined more clearly. In case of an unstable system, the dominant frequency is clearly visible as a narrow peak in the measured pressure spectrum (corresponds to LC frequency). For a stable system, the peaks in the pressure spectrum are broadened. However, the eigenmodes of the stable system still show up as maxima in the measured pressure spectrum. The peaks result from resonances of broad-band combustion noise emitted by the turbulent flame with stable eigenmodes of the system [26]. Thus, we define dominant frequency generally as the position of maxima in the sound pressure spectrum, no matter whether they appear as narrow or broad peaks.

Step zero of the proposed strategy is to compute the equivalent reflection coefficients $\mathcal{R}_{m,\mathrm{x}}$ of the full can-annular combustor as defined in the Equivalent Reflection Coefficients of a Generic Can-Annular Combustor section. If Helmholtz resonators are employed for the test-rig adaption, the initial parameters for a given m are selected to optimally approximate $\mathcal{R}_{m,\mathrm{x}}$ in the relevant frequency range. The passive acoustic elements installed at the test-rig are designed to fulfill Eq. (5) at an initial guess ν^0 of the dominant frequency of the full engine. For both computing $\mathcal{R}_{m,\mathrm{x}}$ and designing the elements, an acoustic solver based on the Helmholtz equation is employed.

The following steps of the proposed approach are:

(1) Run the adapted test-rig and measure the dominant frequency ν^n.
(2) Adapt the installed passive acoustic elements to fulfill Eq. (5) at the measured frequency ν^n.
(3) Iterate until the dominant frequency ν^n measured in the test-rig stays constant. Repeat with different m.

Unconditional convergence of the proposed iterative algorithm cannot be proven, as in practice a comprehensive mathematical description of all subsystems is not available. However, for all setups investigated in this study, the algorithm converged even for initial frequencies ν^0 far away from the final value. This suggests that the algorithm will converge for practically relevant cases.

In order to minimize the number of iterations necessary to adapt the passive elements, the initial frequency guess ν^0 should be as close to the dominant frequency for mode order m of the full system as possible. Due to the clustering of eigenmodes in typical can-annular combustors (see Fig. 8), the dominant frequencies of the individual azimuthal mode orders are generally close to each other [13]. Thus, the dominant frequency obtained for a certain m may serve as ν^0 for the next higher m. In case the single-can test-rig comprises an entire sector of the considered can-annular combustor (including the corresponding part of the compressor plenum and the annular gap), it represents mode order $m=0$ of the full engine and can be used to obtain the dominant frequency for $m=0$. Alternatively, if known from an acoustic model, the pure acoustic eigenfrequency of the considered m can be used as initial guess ν^0. In many cases, flame dynamics do not affect the acoustic eigenmode drastically and it can thus be considered as good approximation of the thermoacoustic eigenmode. This however is not the case if the dominant mode is of ITA origin [24].

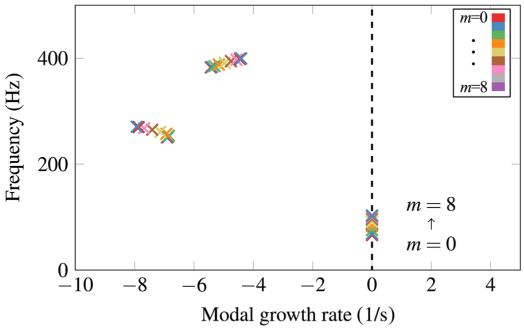

Fig. 8 Eigenfrequencies for all azimuthal mode orders m **of full can-annular combustor at** a_{LC}**. The corresponding amplitude levels are in the range** $a_{LC}=0.59-0.65$**.**

The relative change of dominant frequency $\Delta\nu^n$ between iteration $n-1$ and n may be used to define a convergence criterion

$$\Delta\nu^n=\frac{|\nu^n-\nu^{n-1}|}{\nu^n}<\epsilon \tag{7}$$

If $\Delta\nu^n$ is smaller than a predefined threshold ϵ, the iterations are stopped. An additional criterion based on the relative change of design parameters of the adapted elements may be used to distinguish slow progress from actual convergence of the algorithm. Although we cannot strictly prove that meeting these criteria is always sufficient for convergence of the algorithm, in all cases investigated in this study criterion (7) correctly indicated convergence.

If the test-rig is adapted by means of straight duct extensions, only the lengths $\mathcal{L}_{\mathrm{x}}$ are available to fulfill Eq. (5) at the observed dominant frequency. If Helmholtz resonators are used, at least the four geometrical parameters illustrated in Fig. 4 are available for the adaption process. In this work, we only modify one single parameter during the iteration process. In general, more sophisticated adaption strategies that modify multiple parameters at once in order to optimally approximate $\angle\mathcal{R}_{m,\mathrm{x}}$ around ν^n are conceivable. Deriving such strategies could be part of a follow-up study.

Application to Network Model of a Generic Can-Annular Combustor

Within this section, we demonstrate test-rig adaption for a generic can-annular combustor using straight duct extensions. Both full configuration and adapted test-rig are modeled by a quasi-1D thermo-acoustic network model. The results of the full configuration serve as a benchmark for the adapted test-rig. For the adaption using Helmholtz resonators, 3D effects might play a role. Consequently, this strategy is discussed in the section Validation With a Configuration of Applied Relevance, where a full 3D configuration is considered.

Setup. Figure 4 shows the network model of one unit cell of the generic can-annular combustor considered in the present section. The network model contains only 1D elements. The extension of the combustor in azimuthal direction is taken into account by a T-junction at the outlet. For simplicity we focus on matching only the downstream reflection coefficient $\mathcal{R}_{m,\mathrm{d}}$, but the approach could equally be applied to adapt both up- and downstream termination simultaneously. The upstream reflection coefficient of the individual cans is set to $R_{\mathrm{u}} = -0.8$ in order to take into account acoustic losses present in realistic systems. The dimensions and physical conditions of the system (cf. Fig. 4) are set in accordance with typical can-annular combustors. Fluid properties of air are used. The transition toward the turbine, which is often a choked nozzle in actuality, is represented by $R_{\mathrm{turb}} = 1$ [21].

Flame dynamics are modeled by a flame transfer function (FTF) of a swirl burner test-rig taken from [27]. The dimensions of the flame and the mean flow speed in this test-rig are comparable to realistic can-annular combustors, although the employed FTF was measured at atmospheric conditions. Full engine and adapted test-rig model are compared based on their LC frequency and amplitude, because these are the most relevant quantities in practice. The iterative algorithm to adapt the test-rig model is also based on LC frequencies, as these correspond to the dominant frequencies measured experimentally. In order to capture the formation of LC oscillations, we introduce a generic saturation factor s that models the amplitude dependence of the flame response F [28]

$$F(\omega, a) = \frac{\hat{\dot{Q}}(\omega, a)}{\hat{u}} = s(a)\mathrm{FTF}(\omega), \qquad s(a) = \frac{1}{1 + e^{16(a-0.5)}} \tag{8}$$

Here, $\hat{\dot{Q}}$ and $\hat{u}$ denote the Fourier transform of the heat release rate and acoustic velocity at the reference position of the FTF and a is a measure of the amplitude level. The network models of the full can-annular combustor and the adapted single-can system are built and solved using the tool *taX*[3] [29]. The LC amplitude level a_{LC}, which corresponds to a growth rate $\sigma = 0$ of the most unstable system eigenmode, is calculated using a gradient-based root search algorithm. The corresponding LC frequency is obtained by computing the eigenfrequencies of the network model with a saturation factor of $s(a_{LC})$.

Results of the Full Configuration. Figure 8 shows the eigenfrequencies of the full can-annular combustor with saturation factor $s(a_{\mathrm{LC}})$ for all azimuthal mode orders m. The clustering of eigenmodes of different m is clearly visible [13]. Among the clusters shown, one can identify an axial quarter-wave, three-quarter-wave, and five-quarter-wave mode. All modes in the quarter-wave cluster are unstable. The LC amplitude level a_{LC} and frequency is determined separately for each mode order m.

As a_{LC} is calculated separately for each m, any nonlinear interaction of individual mode orders m is neglected. Furthermore, the proposed approach of identifying equivalent reflection coefficients for the individual azimuthal mode orders assumes that those can be studied separately. In reality, at finite amplitude levels different azimuthal mode orders can interact, which may result in one dominant mode with LC frequency and amplitude level different from the values computed here. Additionally, the computed a_{LC} relies on Bloch-symmetry, which assumes that discrete rotational symmetry is retained even for finite amplitude levels [28]. This is not necessarily the case in practice. However, for the proposed approach, it is not crucial to exactly predict the LC amplitude and frequency that results from the interaction of multiple unstable modes and that is potentially influenced by a symmetry break. In case the proposed approach indicates a thermoacoustic instability at only *one single* azimuthal mode order, the combustor has to be redesigned anyway. Thus, it is not necessary to correctly represent the case of multiple unstable mode orders and accurately predict the exact amplitude level a_{LC}.

---

[3] Code available at https://gitlab.lrz.de/tfd/tax

The equivalent reflection coefficient $\mathcal{R}_{m,\mathrm{d}}$ of the considered can-annular combustor is defined at the location indicated in Fig. 4 and shown in the bottom plot of Fig. 3.

Iterative Adaption of the Test-Rig Model. In the following, we illustrate the adaption procedure for the “push–pull” mode $m = 8$. For all other mode orders, the procedure is exactly equivalent and we just show the final results. We use the LC frequency $\nu_1^0 = 66\,\mathrm{Hz}$ of $m = 0$ as initial frequency guess. This is the dominant frequency that would be measured in the single-can test-rig without any extensions. In order to demonstrate the robustness of the proposed approach, we repeat the procedure with an initial frequency of $\nu_2^0 = 300\,\mathrm{Hz}$ which is quite far away from the dominant frequency for $m = 8$. According to Eq. (6), the corresponding initial extension lengths are $\mathcal{L}^0_{d,1} = 4.33\,\mathrm{m}$ for ν_1^0 and $\mathcal{L}^0_{d,2} = 1.26\,\mathrm{m}$ for ν_2^0.

Figure 9 shows $\angle\mathcal{R}_{m,\mathrm{d}}$ for the considered azimuthal mode order $m = 8$ together with the phase of the outlet reflection coefficient of the test-rig $\angle R_{\mathrm{d,rig}}$ for the individual iterations. Starting the iterations at $\nu_1^0 = 66\,\mathrm{Hz}$, the process takes five steps until a prescribed $\Delta\nu < 0.5\,\%$ is reached. This is a very strict criterion that could probably be weakened in practice. However, here we want to demonstrate the accuracy that can be achieved by the proposed approach.

Figure 10 shows the corresponding LC frequencies ν^n observed in the test-rig model for the individual iterations. Within five iterations, the LC frequency $\nu^5 = 103.0\,\mathrm{Hz}$ matches the LC frequency of $m = 8$ of the full engine with a relative error below 0.2%. The obtained LC amplitude level after convergence is $a_{\mathrm{LC}} = 0.594$, which is the same value as for the full can-annular combustor. The final extension length is $\mathcal{L}^5_{\mathrm{d}} = 3.06\,\mathrm{m}$.

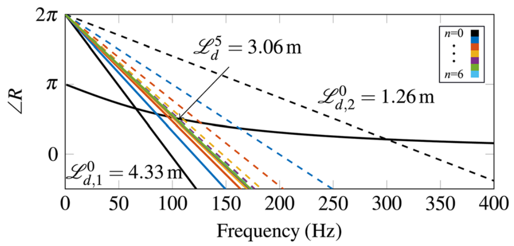

Fig. 9 $\angle\mathcal{R}_{m=8,\mathrm{d}}$ **(black curve) together with** $\angle R_{\mathrm{d,rig}}$ **for the individual iterations. Phase for initial lengths shown in black, solid lines indicate iterations for** $\nu^0 = 66\,\mathrm{Hz}$ **dashed lines for** $\nu^0 = 300\,\mathrm{Hz}$**.**

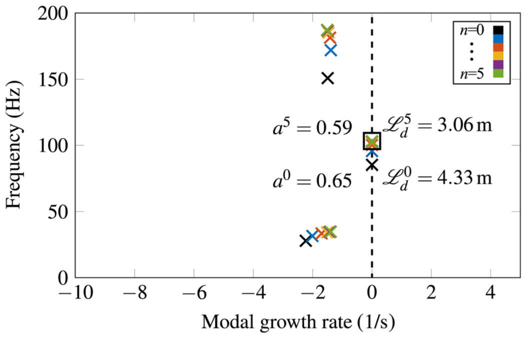

Fig. 10 LC frequencies of the test-rig for individual iterations with $\nu^0 = 66\,\mathrm{Hz}$ **(colored crosses), LC frequency for initial extension length marked with black crosses. Black square indicates LC frequency of the full engine for** $m = 8$**.**

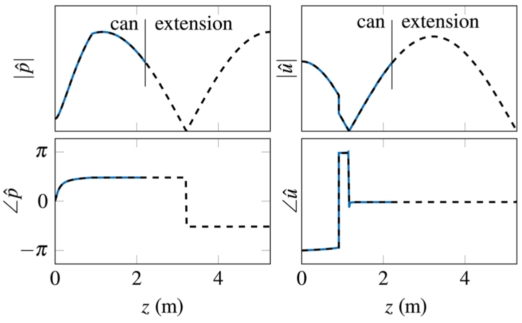

Fig. 11 Normalized absolute value and phase of acoustic pressure and axial velocity in test-rig can with extension (dashed black) and in can of full engine (solid blue) for $m=8$ plotted over the axial coordinate z

Table 1 Extension lengths for individual azimuthal mode orders m

m	1	2	3	4	5	6	7	8
$\mathcal{L}_\mathrm{d}$ (m)	6.12	5.31	4.51	3.89	3.49	3.24	3.10	3.06

Note that if the criterion in Eq. (7) is weakened to $\Delta\nu < 5\,\%$, which is more a realistic value due to limited measurement accuracy, the approach converges already after two iterations. In this case, the relative error of the test-rig LC frequency is below 3%, while the relative error in LC amplitude level is approx. 2%.

If $\nu_2^0 = 300\,\mathrm{Hz}$, which is far away from the actual LC frequency of the full engine, is used as initial frequency guess, the process converges after six iterations for $\Delta\nu < 0.5\,\%$ and after three iterations for $\Delta\nu < 5\,\%$, while the achieved accuracy is comparable to that of ν_1^0.

Figure 11 compares the mode shapes in one can predicted by the respective network model of the full engine and the adapted test-rig. Inside the can, the acoustic pressure and velocity of the full engine and the single-can test-rig agree well.

The procedure illustrated for $m=8$ is completely analogous for all other azimuthal mode orders. The dominant frequency $\nu = 66\,\mathrm{Hz}$ of $m=0$ is used as an initial guess for all mode orders. For each m, the approach converges within a maximum of five iterations, while the relative errors in LC frequency and amplitude levels are below 1%. If a weakened convergence criterion $\Delta\nu < 5\,\%$ is used, the approach converges within two iterations for each mode order m. Table 1 shows the resulting extension lengths for each mode order m.

Stability Properties of the Adapted Test-Rig. In the section Iterative Adaption of the Test-Rig Model, we pointed out that a single-can test-rig model can be adapted iteratively to show the same LC as the full configuration at a given azimuthal mode order.[4] So far, we have not discussed the stability properties of the adapted test-rig model. A LC is characterized by $\sigma=0$, while the (linear) stability of the system is determined by the sign of σ in the zero-amplitude limit $a=0$. The passive acoustic elements are designed such that Eq. (5) holds for *purely real-valued* design frequencies ω_d $(\sigma=0)$. For $\sigma \neq 0$, Eq. (5) does not hold in general. Thus, even if the LC frequencies of test-rig and full engine match, the eigenfrequencies in the zero-amplitude limit are generally not identical.

We can however argue that for a unique, stable LC to develop, the modal growth rate must be $\sigma > 0$ in the zero-amplitude limit. Provided that both systems develop an identical LC, both systems must be linearly unstable with $\sigma > 0$ in the zero-amplitude limit. To conclude, both adapted test-rig and full engine will have the same stability properties, although their eigenmodes do not necessarily have the same frequency and growth rate in the zero-amplitude limit.

Critical Assessment of the Adaption Strategy. The converged extension lengths for the individual mode orders shown in Table 1 are quite large compared to the length of the can. This will cause problems for the practical implementation of this strategy if the evaluated extension length cannot be realized in the high-pressure test-bench.

Figure 11 illustrates exemplarily for $m=8$, why the extension has to be that long. $\mathcal{R}_{m=8,\mathrm{d}}$ could be approximated by an acoustically soft termination at axial position $z = 3.2\,\mathrm{m}$ in Fig. 11 (pressure node). In this case, the mode in the full engine would be approximated by a half-wave mode in the test-rig. However, as $R_\mathrm{turb} = 1$ at the end of the extension is fixed, the full engine mode has to be approximated by a three-quarter-wave mode, which results in large $\mathcal{L}_\mathrm{d}$. It is apparent that in this case there exists also a lower frequency quarter-wave mode in the test-rig. This mode is observed in Fig. 10 at frequency $\nu = 34\,\mathrm{Hz}$. It has no counterpart in the full engine and can be seen as an artifact of the proposed method (in the following also called “spurious mode”).

This mode may become dominant in the test-rig, which causes ambiguity on which measured frequency the iterations should be based on. However, a general criterion can be formulated. We define the phase being wrapped in the interval $[-\pi, \pi]$: If $\angle\mathcal{R}_{m,\mathrm{d}} > 0$, the full engine mode is approximated by a three-quarter-wave mode, i.e., the iterations must be based on the second mode of the test-rig. If $\angle\mathcal{R}_{m,\mathrm{d}} \leq 0$, the full engine mode is approximated by a quarter-wave mode and the iterations must be based on the first mode of the test-rig. However, if for $\angle\mathcal{R}_{m,\mathrm{d}} > 0$ the spurious mode is unstable in the test-rig, it will be difficult or even impossible to identify the frequency of the second mode on which the iterations have to be based on. Additionally, if the spurious mode is unstable and dominates for the final extension length, the stability of the full engine mode cannot be assessed with the adapted test-rig.

The final extension lengths in Table 1 are not directly related to any characteristic length of the combustor. Thus, they cannot be deduced from geometrical consideration, as it is current practice. Instead, iterative adjustment according to the proposed strategy is necessary. This, however, would be very costly in high-pressure test-rigs. The high-pressure cell has to be opened for each iteration step and for each mode order. If instead of a single operating condition with a fixed dominant frequency, an entire operating window with variable dominant frequencies is investigated, the effort of implementing such an iterative strategy will be prohibitive.

In summary, the iterative test-rig adaption demonstrated within this section is most likely impractical, but when using straight duct extensions there is no obvious alternative to the proposed iterative strategy.

Validation With a Configuration of Applied Relevance

Within this section, we demonstrate test-rig adaption using Helmholtz resonators for a can-annular combustor with 16 cans modeled by the 3D inhomogeneous Helmholtz equation. The objective is to demonstrate the proposed test-rig adaption for a configuration that could similarly be found in practice (e.g., see Ref. [6]). Again, results from the adapted single-can system are compared to the full can-annular combustor model.

Setup. Figure 12 shows a slice through one sector of the considered setup along the axial direction. Flame dynamics are

---

[4] Provided that Bloch-symmetry holds and nonlinear interaction of individual mode orders is negligible.

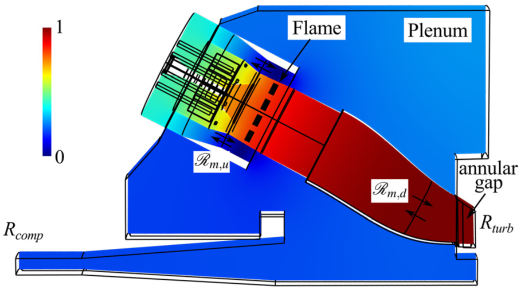

Fig. 12 3D model of realistic can-annular combustor. Individual cans are coupled via plenum and annular gap. Colors show normalized $|\hat{p}|$ for the dominant mode of azimuthal order $m = 1$.

represented by the flame model shown in Eq. (8) [27]. They are coupled to the acoustics by a source term that is active in the flame region indicated in Fig. 12. The flame divides the domain into a cold ($T_c = 780\,\mathrm{K}$) and hot ($T_h = 1800\,\mathrm{K}$) region. Fluid properties of air are used. BBCs are imposed at the cutting interface of plenum and annular gap. The acoustic terminations toward compressor and turbine are set to $R_{\mathrm{comp}} = R_{\mathrm{turb}} = 1$. To account for acoustic damping, which is not included in the Helmholtz equation, we assume that a LC is established at a positive modal growth rate of $\sigma = 2\,\mathrm{s}^{-1}$ [30]. The model is built and solved using the finite element software COMSOL MULTIPHYSICS [31].

Equivalent Reflection Coefficient. Due to nonplanar acoustic waves in the vicinity of the annular gap and the plenum-can transition, the equivalent reflection coefficients $\mathcal{R}_{m,\mathrm{x}}$ are defined in some axial distance to the azimuthal coupling interfaces (see Fig. 12). They are obtained by computing the forced response of the plenum and annular gap section at discrete frequencies for individual m.

Figure 7 shows $\angle\mathcal{R}_{m,\mathrm{u}}$ of the plenum (top) and $\angle\mathcal{R}_{m,\mathrm{d}}$ of the annular gap (bottom) versus $\mathrm{He} = \omega d/c$. For better visibility, only $m = 0, 1, 2, 8$ of $\angle\mathcal{R}_{m,\mathrm{u}}$ is shown. The characteristic length d is set to the can–can distance at the annular gap, i.e., 1/16th of the total annular gap perimeter. The relevant frequencies of the first axial mode order are in the range $\mathrm{He} \approx \pi/14 \ldots \pi/6$.

The equivalent reflection coefficient of the annular gap $\mathcal{R}_{m,\mathrm{d}}$ is in good agreement with that obtained from the network model shown in Fig. 3. Compared to the network model case, the individual values of $\angle\mathcal{R}_{m,\mathrm{d}}$ are more distinct from each other (due to a larger A in the present configuration), which indicates that the cluster of first axial mode order is not as closely spaced as in Fig. 8. The overall linear decrease of $\angle\mathcal{R}_{m,\mathrm{d}}$ with frequency reflects the axial distance of $\mathcal{R}_{m,\mathrm{d}}$ to the annular gap.

At first glance, $\angle\mathcal{R}_{m,\mathrm{u}}$ looks notably different from that in Fig. 3 and its behavior seems quite chaotic. The abrupt phase changes observed in Fig. 7 are related to eigenfrequencies of the plenum. As explained for Fig. 3, at these eigenfrequencies, the equivalent reflection coefficient equals $\mathcal{R}_{m,\mathrm{u}} = 1$. In case of the quasi-1D network model, the plenum eigenfrequencies are regularly spaced, resulting in a regular behavior of $\angle\mathcal{R}_{m,\mathrm{u}}$ as shown in Fig. 3. In the present configuration, the plenum is a large volume of complex shape, which features irregularly spaced eigenfrequencies with complex 3D mode shapes. In particular for higher frequencies ($\mathrm{He} > 3\pi/8$) the eigenfrequencies are closely spaced. However, except for the immediate vicinity of these plenum eigenfrequencies, $\angle\mathcal{R}_{m,\mathrm{u}}$ for all m closely follow a common trend, which linearly decreases from π. This linear decrease results from the axial distance of $\mathcal{R}_{m,\mathrm{u}}$ to the can-plenum transition. Thus, except for very low frequencies $\mathrm{He} < \pi/16$ and the immediate vicinity of plenum eigenfrequencies, all mode orders impose an almost ideal open end at the can inlet.

Importance of Upstream Coupling. Except for the immediate vicinity of plenum eigenfrequencies, the individual $\angle\mathcal{R}_{m,\mathrm{u}}$ are closely spaced in the frequency range $\mathrm{He} \approx \pi/16 \ldots 3\pi/8$ that is relevant to the first axial mode order. In particular, $\angle\mathcal{R}_{m,\mathrm{u}}$ are much closer together than the individual $\angle\mathcal{R}_{m,\mathrm{d}}$ in the same frequency range. The phase $\angle\mathcal{R}_{m=0,\mathrm{u}}$ of the uncoupled $m = 0$ configuration is thus a good approximation for all other azimuthal mode orders, except near plenum eigenfrequencies. This indicates that for most of the relevant frequency range, the coupling via the annular gap is much more important than the coupling via the plenum.

To substantiate this argumentation, we compare LC amplitude levels and frequencies of the full system and a system coupled at the downstream side only ($m = 0$ set at the plenum interfaces) in Table 2. All frequencies are normalized by the LC frequency of the $m = 0$ system. The azimuthal mode order $m = 5$ is stable, thus a_{LC} is undefined there. As observed in Table 2, the relative difference of the two configurations in terms of LC amplitude level and frequency is below 5% for all mode orders, except for ν of $m = 2$ and a_{LC} of $m = 6$. The LC frequency of azimuthal mode order $m = 2$ is close to a plenum eigenfrequency visible in Fig. 7 at $\mathrm{He} \approx \pi/10$. This explains the differences between fully coupled and downstream-only coupled systems for this mode order m. To conclude, for the present configuration can–can coupling via the plenum is negligible for frequencies that are not in the immediate vicinity of plenum eigenfrequencies. In the following, we will therefore only consider adaption of the downstream termination. The error of representing the upstream termination by the uncoupled plenum ($m = 0$) is considered to be small compared to other possible error sources.

However, this finding cannot be generalized for all practical relevant systems. The investigated setup does not have cross-fire tubes, which would directly connect the cans upstream of the flame. These could drastically increase the upstream coupling of the individual cans, which would have to be accounted for in the same manner as shown for the downstream termination.

Matching Downstream Termination. The initial design of the Helmholtz resonator with the considered four degrees-of-freedom (cf. Fig. 5) is nontrivial. However, the four parameters allow approximating $\angle\mathcal{R}_{m,\mathrm{d}}$ well for a wide frequency range. Due to the high computational effort when searching a four-dimensional parameter space for an optimal design, we only consider $m = 1$ and $m = 8$. However, the strategy can be applied accordingly to all other mode orders.

As indicated in Fig. 6 and discussed below, for a good match with $\angle\mathcal{R}_{m,\mathrm{d}}$ the Helmholtz mode of the resonator should be well below the relevant frequency range, while the first axial mode should be well above. To shift the Helmholtz mode to low frequencies, the resonator volume should be as large as the limitations of the high-pressure cell allow. However, the length of the volume l_2 is bounded by the lower frequency limit of the axial mode. The above guidelines are common for all mode orders m. The two remaining design parameters l_1 and S_1 are used to optimally approximate $\angle\mathcal{R}_{m,\mathrm{d}}$ for the given m.

Figure 13 shows $\angle R_{\mathrm{rig,d}}$ adapted with Helmholtz resonators designed for $m = 8$ (top) and $m = 1$ (bottom) compared to $\angle\mathcal{R}_{m,\mathrm{d}}$ of the respective mode orders. The resonators are mounted at the

Table 2 Normalized LC frequencies ν and amplitudes a_{LC} of individual m for fully coupled "u/d" and downstream-only coupled "d" configuration

m	1	2	3	4	5	6	7	8
ν, u/d	1.14	1.17	1.40	1.49	1.74	1.81	1.85	1.86
ν, d	1.09	1.28	1.44	1.49	1.76	1.82	1.85	1.86
a_{LC}, u/d	0.66	0.63	0.56	0.42	—	0.47	0.50	0.51
a_{LC}, d	0.68	0.64	0.56	0.44	—	0.36	0.49	0.50

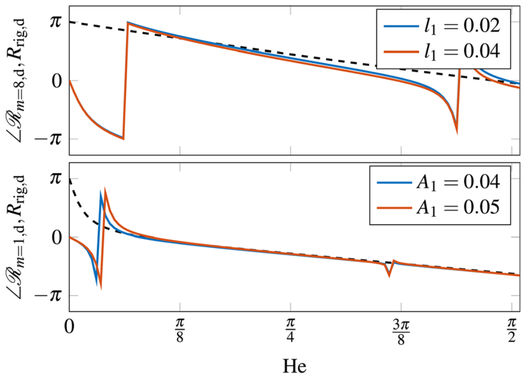

Fig. 13 $\angle R_{\mathrm{rig,d}}$ **adapted with Helmholtz resonator for** $m=8$ **(top) and** $m=1$ **(bottom) together with** $\angle\mathcal{R}_{m,\mathrm{d}}$ **of respective** m **(black dashed)**

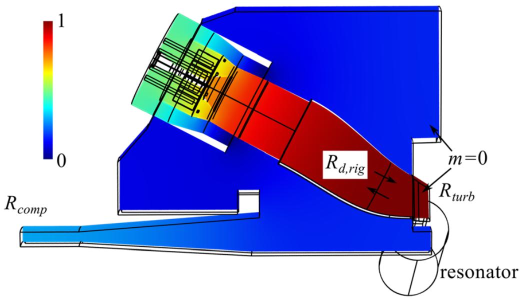

Fig. 14 Normalized $|\hat{p}|$ **of dominant mode in single-can test-rig model adapted with Helmholtz resonator for** $m=1$

azimuthal interfaces of the annular gap. The parameters chosen for $m=1$ and $m=8$ are summarized in Table 3. The parameters l_1 and A_1 (respectively, for $m=8$ and $m=1$), for which a range is specified, are employed for the iterative adaption. For $m=1$ $\angle\mathcal{R}_{m,\mathrm{d}}$ can be approximated very well for a wide frequency range. To achieve comparable accuracy for $m=8$, the necessary resonator volume would have to be even larger than the present one, which is not considered to be realistic. In general, the achievable accuracy crucially depends on the set of parameters that is realizable in the available test-bench.

The resonators are initially designed to exactly represent $\angle\mathcal{R}_{m,\mathrm{d}}$ at the LC frequency of the respective lower mode order. This results in initial parameters $A_1 = 0.04$ for $m=1$ and $l_1 = 0.03\,\mathrm{m}$ for $m=8$. With a convergence criterion $\Delta\nu < 0.5\,\%$ the adaption algorithm immediately converges with the initial resonator design for $m=8$. For $m=1$ convergence is reached after the first iteration with an updated $A_1 = 0.045$. The normalized LC frequencies and amplitude levels obtained with the adapted test-rig models are $\nu = 1.09$ and $a_{\mathrm{LC}} = 0.67$ for $m=1$ and $\nu = 1.86$ and $a_{\mathrm{LC}} = 0.48$ for $m=8$. Thus, the relative error compared to the downstream only coupled system is below 1% regarding LC frequency and below 5% regarding amplitude level. The relative error in LC frequency compared to the fully coupled configuration is below 5% (cf. Table 2). The normalized LC $|\hat{p}|$ obtained from the test-rig model adapted for $m=1$ is shown in Fig. 14 and agrees well with $|\hat{p}|$ of $m=1$ of the full configuration shown in Fig. 12. The outline of the adapted resonator is also visible in Fig. 14.

Critical Assessment of Adaption Strategy. Test-rig adaption by means of Helmholtz resonators seems much more practicable than using duct extensions. Due to the good initial agreement of $\angle R_{\mathrm{rig,d}}$ and $\angle\mathcal{R}_{m,\mathrm{d}}$ over a wide frequency range, the number of iterations necessary to adapt the resonator is very small, iterations might even be avoided altogether. At the same time, it is possible to investigate entire operating windows with variable dominant frequencies without having to redesign the up-/downstream terminations for each operating condition.

The design parameters of the considered resonator appear to be much easier accessible than the length of duct extensions. It should be possible to change the neck length and cross section remotely, without opening the high-pressure cell. Other design parameters not considered here, like the purge flow temperature, should be easily accessible, too.

Table 3 Parameters of Helmholtz resonators fitted for $m=1$ **and** $m=8$

	S_2/S_1	l_2 (m)	$A_1 = S_1/S_c$	l_1 (m)
$m=1$	20	1.2	0.04 – 0.05	0.43
$m=8$	20	1	0.4	0.02 – 0.04

The Helmholtz resonators will also introduce “spurious” modes that are not present in the full combustor. However, as their eigenfrequencies are related to the Helmholtz-mode of the resonator, they will be strongly damped and are expected to play a minor role.

A main drawback of this element type is that there is no generalized design guideline yet. The initial design and the iteration strategy have to be adjusted from case to case. Part of future work might be to develop an optimal iteration strategy that changes multiple parameters at once. Another drawback is the large size of the adapted resonators. In case the optimized initial resonator design does not fit in the high-pressure cell, the test-rig adaption will again rely more on the iterative algorithm. Furthermore, it is not yet clear how strong the damping of the resonator (which is designed to be small in the relevant frequency range) will affect the thermoacoustic properties of the test-rig.

Influence of Effects Neglected in Combustor Model

The strategy proposed in this work is only demonstrated with thermoacoustic models. The models used do not account for nonacoustic effects like heat transfer, entropy waves, and mean flow (in the Helmholtz solver). Furthermore, acoustic damping is only modeled in a simplistic way, i.e., by means of nonideal boundary conditions in the network model and by assuming uniformly distributed damping in the 3D configuration (which is equivalent to setting the LC growth-rate to $\sigma > 0$ [30]). Acoustic boundary conditions toward turbine and compressor are idealized.

These effects neglected in the present models will generally affect the thermoacoustic properties of the considered systems. However, it is important to note that in this study these effects are neglected in both the test-rig model and the model of the full configuration. In reality, those effects will in turn be present in both configurations. We do not aim to accurately model a real combustor configuration. Instead, we demonstrate the correspondence between adapted test-rig and full configuration.

To assess the importance of effects neglected in the thermoacoustic models of this study, we thus have to focus on the parts where test-rig and full configuration differ, i.e., the up-/downstream terminations of the can. In particular at the downstream termination, neglected effects related to entropy fluctuations, mean flow, and localized acoustic damping might have different influences on the thermoacoustic properties of test-rig and full engine.

In case duct extensions are used for test-rig adaption, the convective time delay relevant to entropy waves is drastically increased. Also, the Helmholtz resonator might be affected by entropy waves. However, due to the generally large convective time delays in realistic combustor configurations, effects caused by entropy waves typically occur at very low frequencies and are thus well separable from purely acoustic effects considered in this study.

The elements installed upstream the first turbine stator vanes may change the nonacoustic flow properties, which in turn affects R_{turb}. For example, the cooling of the duct extension or the purge flow through the Helmholtz resonator may change mean flow temperature and velocity. However, the expected changes of the mean flow are very small and so is the influence on R_{turb}.

Acoustic damping localized at the annular gap in the full engine and at the Helmholtz resonator in the adapted test-rig is only taken into account in the simplistic way mentioned above. With the methods employed in this study, we cannot quantify the influence of this localized acoustic damping on the thermoacoustics of test-rig and full engine. This has to be addressed by more sophisticated numerical models and/or by experimental validation of the proposed strategy.

Conclusion

This study discusses the strategies to adapt single-can combustion test-rigs to reproduce the thermoacoustic properties of a full can-annular combustor. The coupling of the individual cans inside the can-annular combustor can be lumped into equivalent reflection coefficients $\mathcal{R}_{m,\mathrm{x}}$ (with $\hat{x}u/d$) up- and downstream of a single can. If correct values of $\mathcal{R}_{m,\mathrm{x}}$ can be imposed at the up-/downstream terminations of a single-can test-rig, the rig mimics the thermoacoustic properties of the full engine.

We exploit the discrete rotational symmetry of typical can-annular combustors and employ Bloch-wave theory to obtain $\mathcal{R}_{m,\mathrm{x}}$. These reflection coefficients induce a frequency dependent phase shift, which generally depends on the coupling interfaces, the azimuthal mode order m and the number of cans, but not on the thermoacoustic properties of the individual cans.

Two types of passive acoustic elements, namely duct extensions of constant cross section and Helmholtz resonators, are employed to match the phase shift induced by $\mathcal{R}_{m,\mathrm{x}}$ for given design frequencies. For both computing $\mathcal{R}_{m,\mathrm{x}}$ and designing the passive elements, an acoustic solver based on the Helmholtz equation is employed. We propose an iterative strategy, which ensures that the design frequency converges to the dominant frequency of the given mode order of the full system. Following that approach, the single-can test-rig can be used to investigate each azimuthal mode order m of the full can-annular combustor in terms of stability, limit cycle frequencies, and amplitude levels without a priori knowledge of relevant frequencies of the full engine.

The proposed strategy is applied to a network model of a generic can-annular combustor and to a 3D applied configuration modeled by the Helmholtz equation. For the latter, we show that the coupling via the compressor exit plenum is negligible for frequencies that are not in the immediate vicinity of plenum eigenfrequencies. The test-rig models adapted following the proposed strategy mimic the full engine with comparably good accuracy for both considered element types. However, using Helmholtz resonators seems much more practical. Their design parameters are easier to access remotely and the geometrical dimensions of the adapted resonators are more reasonable than those of the duct extension. Most importantly, the up-/downstream reflection coefficient tuned by a Helmholtz resonator matches $\mathcal{R}_{m,\mathrm{x}}$ for a wide frequency range. Thus, fewer or no iterations are necessary to adapt the resonator and one single resonator design may be employed to investigate an entire operating window.

The proposed strategy has been demonstrated only with numerical models and has yet to be validated experimentally.

Acknowledgment

The authors gratefully acknowledge the Research Association for Combustion Engines (Forschungsvereinigung Verbrennungskraftmaschinen e.V. FVV) for the financial support to Matthias Haeringer. This project has received funding from the European Union's Horizon 2020 research and innovation program *Annular Instabilities and Transient Phenomena in Gas Turbine Combustors* (ANNULIGhT).

Funding Data

- Forschungsvereinigung Verbrennungskraftmaschinen (Project No. 6012700; Funder ID: 10.13039/501100003162).
- Horizon 2020 (Grant Agreement No. 765998; Funder ID: 10.13039/100010661).

Nomenclature

a = amplitude level
A = cross section area ratio
BBC = Bloch boundary condition
c = speed of sound
d = characteristic length
f, g = acoustic Riemann invariants
F = flame response
FTF = flame transfer function
He = Helmholtz number
ITA = intrinsic thermoacoustic
l = length
$\mathcal{L}$ = extension length
LC = limit cycle
m = Bloch-wave number/azimuthal mode order
n = iteration number
N = number of cans
p = acoustic pressure
$\dot{Q}$ = heat release rate
r, ϕ, z = radial, azimuthal, and axial coordinate
R = reflection coefficient
$\mathcal{R}$ = equivalent reflection coefficient
s = saturation factor
S = cross section area
u = acoustic velocity
x = position vector
Z = acoustic impedance
Δ = relative difference
ν = frequency
ρ = density
σ = modal growth rate
Ω = angular frequency

References

[1] Poinsot, T., 2017, "Prediction and Control of Combustion Instabilities in Real Engines," Proc. Combust. Inst., **36**(1), pp. 1–28.
[2] Farisco, F., Panek, L., and Kok, J. B., 2017, "Thermo-Acoustic Cross-Talk Between Cans in a Can-Annular Combustor," Int. J. Spray Combust. Dyn., **9**(4), pp. 452–469.
[3] Farisco, F., Panek, L., Kok, J. B. W., Pent, J., and Rajaram, R., 2015, "Thermo-Acoustic Coupling in Can-Annular Combustors—A Numerical Investigation," International Congress of Sound and Vibration (ICSV22), Florence, Italy, July 12–16, Vol. 23, p. 9.
[4] Panek, L., Farisco, F., and Huth, M., 2017, "Thermo-Acoustic Characterization of Can-Can Interaction of a Can-Annular Combustion System Based on Unsteady CFD LES Simulation," Proceedings of the First Global Power and Propulsion Forum, Zurich, Switzerland, Paper No. GPPF-2017-81.
[5] Bethke, S., Krebs, W., Flohr, P., and Prade, B., 2002, "Thermoacoustic Properties of Can Annular Combustors," AIAA Paper No. 2002-2570.
[6] Kaufmann, P., Krebs, W., Valdes, R., and Wever, U., 2008, "3D Thermoacoustic Properties of Single Can and Multi Can Combustor Configurations," ASME Paper No. GT2008-50755.
[7] Moon, K., Jegal, H., Gu, J., and Kim, K. T., 2019, "Combustion-Acoustic Interactions Through Cross-Talk Area Between Adjacent Model Gas Turbine Combustors," Combust. Flame, **202**, pp. 405–416.
[8] Ghirardo, G., Moeck, J. P., and Bothien, M. R., 2020, "Effect of Noise and Nonlinearities on Thermoacoustics of Can-Annular Combustors," ASME J. Eng. Gas Turbines Power, **142**(4), p. 041005.

[9] Jegal, H., Moon, K., Gu, J., Li, L. K., and Kim, K. T., 2019, "Mutual Synchronization of Two Lean-Premixed Gas Turbine Combustors: Phase Locking and Amplitude Death," Combust. Flame, **206**, pp. 424–437.

[10] Gruschka, U., Janus, B., Meisl, J., Huth, M., and Wasif, S., 2008, "ULN System for the New SGT5-8000H Gas Turbine: Design and High Pressure Rig Test Results," ASME Paper No. GT2008-51208.

[11] Mongia, H. C., Held, T. J., Hsiao, G. C., and Pandalai, R. P., 2003, "Challenges and Progress in Controlling Dynamics in Gas Turbine Combustors," J. Propul. Power, **19**(5), pp. 822–829.

[12] Venkatesan, K., Cross, A., Yoon, C., Han, F., and Bethke, S., 2019, "Heavy Duty Gas Turbine Combustion Dynamics Study Using a Two-Can Combustion System," ASME Paper No. GT2019-90327..

[13] Ghirardo, G., Di Giovine, C., Moeck, J. P., and Bothien, M. R., 2018, "Thermoacoustics of Can-Annular Combustors," ASME J. Eng. Gas Turbines Power, **141**(1), p. 011007.

[14] Haeringer, M., and Polifke, W., 2019, "Time Domain Bloch Boundary Conditions for Efficient Simulation of Thermoacoustic Limit-Cycles in (Can-)Annular Combustors," ASME J. Eng. Gas Turbines Power, **141**(12), p. 121005.

[15] Bothien, M. R., Moeck, J. P., and Oliver Paschereit, C., 2008, "Active Control of the Acoustic Boundary Conditions of Combustion Test Rigs," J. Sound Vib., **318**(4–5), pp. 678–701.

[16] Bothien, M. R., and Paschereit, C. O., 2010, "Tuning of the Acoustic Boundary Conditions of Combustion Test Rigs With Active Control: Extension to Actuators With Nonlinear Response," ASME J. Eng. Gas Turbines Power, **132**(9), p. 091503.

[17] Niether, S., 2018, "Modification of a High Pressure Test Rig for Thermoacoustic Measurements," Empirical dissertation, TU Berlin, Berlin.

[18] Bloch, F., 1929, "Über Die Quantenmechanik Der Elektronen in Kristallgittern," Z. Phys., **52**(7–8), pp. 555–600.

[19] Mensah, G. A., Campa, G., and Moeck, J. P., 2016, "Efficient Computation of Thermoacoustic Modes in Industrial Annular Combustion Chambers Based on Bloch-Wave Theory," ASME J. Eng. Gas Turbines Power, **138**(8), p. 081502.

[20] Fournier, G. J. J., Haeringer, M., Silva, C. F., and Polifke, W., 2020, "Low-Order Modeling to Investigate Clusters of Intrinsic Thermoacoustic Modes in Annular Combustors," ASME J. Eng. Gas Turbines Power, Epub.

[21] Marble, F. E., and Candel, S. M., 1977, "Acoustic Disturbance From Gas Non-Uniformities Convected Through a Nozzle," J. Sound Vib., **55**(2), pp. 225–243.

[22] Förner, K., and Polifke, W., 2017, "Nonlinear Aeroacoustic Identification of Helmholtz Resonators Based on a Local-Linear Neuro-Fuzzy Network Model," J. Sound Vib., **407**, pp. 170–190.

[23] Hoeijmakers, M., Kornilov, V., Lopez Arteaga, I., de Goey, P., and Nijmeijer, H., 2014, "Intrinsic Instability of Flame-Acoustic Coupling," Combust. Flame, **161**(11), pp. 2860–2867.

[24] Bomberg, S., Emmert, T., and Polifke, W., 2015, "Thermal Versus Acoustic Response of Velocity Sensitive Premixed Flames," Proc. Combust. Inst., **35**(3), pp. 3185–3192.

[25] Albayrak, A., Steinbacher, T., Komarek, T., and Polifke, W., 2017, "Convective Scaling of Intrinsic Thermo-Acoustic Eigenfrequencies of a Premixed Swirl Combustor," ASME J. Eng. Gas Turbines Power, **140**(4), p. 041510.

[26] Merk, M., Gaudron, R., Silva, C., Gatti, M., Mirat, C., Schuller, T., and Polifke, W., 2019, "Prediction of Combustion Noise of an Enclosed Flame by Simultaneous Identification of Noise Source and Flame Dynamics," Proc. Combust. Inst., **37**(4), pp. 5263–5270.

[27] Tay-Wo-Chong, L., Bomberg, S., Ulhaq, A., Komarek, T., and Polifke, W., 2012, "Comparative Validation Study on Identification of Premixed Flame Transfer Function," ASME J. Eng. Gas Turbines Power, **134**(2), p. 021502.

[28] Mensah, G. A., and Moeck, J. P., 2017, "Limit Cycles of Spinning Thermoacoustic Modes in Annular Combustors: A Bloch-Wave and Adjoint-Perturbation Approach," ASME Paper No. GT2017-64817.

[29] Emmert, T., Meindl, M., Jaensch, S., and Polifke, W., 2016, "Linear State Space Interconnect Modeling of Acoustic Systems," Acta Acust. Acust., **102**(5), pp. 824–833.

[30] Silva, C. F., Nicoud, F., Schuller, T., Durox, D., and Candel, S., 2013, "Combining a Helmholtz Solver With the Flame Describing Function to Assess Combustion Instability in a Premixed Swirled Combustor," Combust. Flame, **160**(9), pp. 1743–1754.

[31] COMSOL, Inc., 2014, "COMSOL Multiphysics Reference Manual, Version 4.4," COMSOL, Burlington, MA.

Guillaume J. J. Fournier[1]
Department of Mechanical Engineering,
Technical University of Munich,
Garching 85748, Germany
e-mail: fournier@tfd.mw.tum.de

Max Meindl
Department of Mechanical Engineering,
Technical University of Munich,
Garching 85748, Germany
e-mail: meindl@tfd.mw.tum.de

Camilo F. Silva
Department of Mechanical Engineering,
Technical University of Munich,
Garching 85748, Germany
e-mail: silva@tfd.mw.tum.de

Giulio Ghirardo
Ansaldo Energia Switzerland,
Haselstrasse 18,
Baden 5400, Switzerland
e-mail: giulio.ghirardo@gmail.com

Mirko R. Bothien
Institute of Energy Systems and
Fluid Engineering,
Zurich University of Applied Sciences,
Winterthur 8400, Switzerland
e-mail: mirko.bothien@zhaw.ch

Wolfgang Polifke
Department of Mechanical Engineering,
Technical University of Munich,
Garching 85748, Germany
e-mail: polifke@tum.de

Low-Order Modeling of Can-Annular Combustors

Heavy-duty land-based gas turbines are often designed with can-annular combustors, which consist of a set of identical cans, acoustically connected on the upstream side via the compressor plenum, and, downstream, with a small annular gap located at the transition with the first turbine stage. The modeling of this cross-talk area is crucial to predict the thermo-acoustic modes of the system. Thanks to the discrete rotational symmetry, Bloch wave theory can be exploited to reduce the system to a longitudinal combustor with a complex-valued equivalent outlet reflection coefficient, which models the annular gap. The present study reviews existing low-order models based purely on geometrical parameters and compares them to two-dimensional Helmholtz simulations. We demonstrate that the modeling of the gap as a thin annulus is not suited for can-annular combustors and that the Rayleigh conductivity model only gives qualitative agreement. We then propose an extension for the equivalent reflection coefficient that accounts not only for geometrical but also flow parameters, by means of a characteristic length. The proposed model is in excellent agreement with two-dimensional simulations and is able to correctly capture the eigenfrequencies of the system. We then perform a Design of Experiments study that allows us to explore various configurations and build correlations for the characteristic length. Finally, we discuss the validity limits of the proposed low-order modeling approach. [DOI: 10.1115/1.4051954]

1 Introduction

Can-annular combustors are commonly found in heavy-duty land-based gas turbines. In this application, N identical combustor cans are aligned along an annulus, hence the name. On the upstream side, the cans are acoustically connected to the compressor plenum. Downstream, a transition duct, as the name indicates, allows the cross-sectional area of the can to transform from a circular to an annular shape, in order to properly feed the turbine. Single can burners have often been considered to be a good approximation of the full system, since the combustion takes place in individual cans. However, a small annular gap is present just in front of the turbine inlet guide vanes, and this cross-talk area allows acoustic communication between neighboring cans. Recent studies showed that the can-to-can communication cannot be neglected when investigating thermoacoustic stability.

While annular combustors have been extensively studied in the last decades, can-annular configurations have received less attention. Bethke et al. [1] and Kaufmann et al. [2] were the first to numerically study can-annular configurations. They showed that accounting for the cross-talk area in a full system gives rise to new eigenmodes that were not observed in single can configurations. Panek et al. [3], based on experimental evidence and by means of a modal analysis, arrived at the same conclusion. Modes with mode shapes that involve multiple cans were observed for the full configuration but could not exist in a single can approximation. Farisco et al. [4] numerically investigated the effect of the geometry of the gap on the acoustic interaction between neighboring cans and showed that the cross-talk effect cannot be neglected. Ghirardo et al. [5] demonstrated numerically, by means of two-dimensional (2D) Helmholtz simulations, and gave experimental evidence that modes of various azimuthal order arise due to the weak coupling between cans. It was shown that these modes come in “clusters”, i.e. collections of several distinct modes with very close frequencies, but different growth rates.

Jegal et al. [6] and Moon et al. [7] experimentally investigated two adjacent burners connected with a cross-talk duct normal to the flow direction. They showed that the coupled system can exhibit strong oscillations, even if each single burner is stable when isolated. The oscillation patterns (axial and push-pull mode) have been observed to be strongly dependent on the equivalence ratio and on the geometrical location of the coupling duct. The work was extended to a configuration with four cans [8]. Because eigenmodes are closely-spaced and form clusters, the system can feature a mixed state with several distinct types of interaction patterns. The same test rig was used in Ref. [9] to analyze the effect of broken symmetry. It was shown that rotational asymmetry can lead to a variety of dynamic states (spinning azimuthal instabilities, mode localization, etc.) that are absent for the perfectly symmetric case, as discussed also by Ref. [5].

Recent studies tackled the problem at a more fundamental level by means of low-order network models. Using Bloch theory [10], the study of a can-annular system reduces to a single unit-cell. The behavior of the full system is preserved by accounting for all

---

[1] Corresponding author.

Manuscript received July 9, 2021; final manuscript received July 14, 2021; published online October 4, 2021. Editor: Jerzy T. Sawicki.

possible azimuthal orders. Von Saldern et al. [11] modeled the cross-talk communication between cans with the Rayleigh conductivity K_R. Using a simple constant K_R [12], they obtained an analytical model with only geometrical parameters, which was then used in a one-dimensional (1D) network configuration to investigate the influence of the coupling strength on the clusters of thermoacoustic modes. In parallel, Fournier et al. [13] suggested that the modeling of annular combustors could be applied to can-annular configurations, where the gap is described by a thin annulus. The model was applied by Haeringer et al. [14] to propose a strategy to tune experimental single-can test-rigs to mimic the thermoacoustic behavior of a full engine. Yoon [15] extended the model to account for mean flow and proposed a unified framework for both annular and can-annular combustors using a multi-input multi-output transfer function matrix.

In the present study, we want to investigate the validity of 1D models for can-annular combustors at a quantitative level by comparison of predictions with those of higher order models. We consider a 2D can-annular combustor, reduced to a single unit-cell with Bloch theory. We focus on the acoustic modeling of the cross-talk area. The paper is structured as follows: we first describe the dimensionless equivalent longitudinal network model. Then both the Rayleigh conductivity (RC) and the thin annulus (TA) models, which are based only on geometrical parameters, are compared to 2D Helmholtz reference simulations. We then propose an extension that accounts also for flow parameters, with a characteristic length, and demonstrate that such model can properly capture the eigenfrequencies. Finally, we perform a Design of Experiments study and propose correlations for the characteristic length. The limits of validity of the low-order model are discussed.

2 Network Model of a Can-Annular Geometry With Bloch Boundary Conditions

2.1 Case and Flow Description. A generic can-annular combustor consists of N identical cans, placed in an annular arrangement. Ghirardo et al. showed that a complex three-dimensional geometry such as Fig. 1 in Ref. [5] can be well approximated by a 2D model. Following this approach, we consider here 2D cans of length L and of width H, as depicted in Fig. 1. Upstream, we neglect any possible influence of the plenum: the cans are decoupled and the reflection coefficient R_{in} is set to unity, following prior studies [5,11]. On the downstream side, a high pressure turbine stage is placed to extract energy from the fluid. The acoustic response of such a turbine stage can be modeled by a reflection coefficient with a fixed gain lower than unity and a zero phase response [16]. In this study, we do not consider any loss mechanism and the outlet reflection coefficient is set to $R_{\text{out}} = 1$. Little quantitative change is expected when accounting for the losses [17]. The individual cans are acoustically coupled to each other through a small annular gap, of size L_g, located just upstream of the turbine.

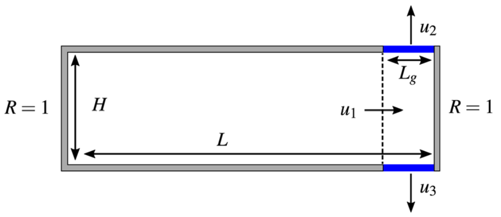

Fig. 1 Unit-cell of a generic can-annular combustor. The three-dimensional geometry, as shown in Fig. 1 in Ref. [5], is approximated by a 2D can, of length *L* and width *H*, closed at the inlet and the outlet. Acoustic communication with the neighboring cans is possible through the cross-talk area of length L_g.

In this study, we focus on the modeling of the acoustics of the set of transition pieces, where the Mach number is low, typically below 0.2 [3,5]. Consequently, and similarly to axial combustors, the low Mach number assumption can be invoked by assuming zero mean flow when modeling the thermoacoustic behavior of cans, in particular wave propagation along the cans. Combustion is not taken into account because it occurs upstream of the considered domain. Accounting for it would lead to sections, inside the cans, with different temperatures and therefore different speed of sound, not to mention the influence of flame dynamics on the thermoacoustic modes. Since the combustion takes place significantly upstream of the turbine, the mean temperature can be assumed to be uniform in the region of the gap and the modeling approach remains valid. Therefore, the model proposed here can be used in future studies to investigate a more complete configuration. We also assume that mean quantities are constant and uniform over the entire domain. Finally, entropy waves are assumed to have a negligible effect and are not taken into account [5,18].

2.2 Bloch-Wave Theory. The cans are geometrically identical, thus the system exhibits rotational symmetry. Bloch theory [10], which has been introduced in thermoacoustics by Mensah et al. [19] and is now well established [5,13,14,20,21], can then be applied. In the frequency domain, the acoustic pressure field can be written in the form:

$$\hat{p}(\boldsymbol{x}) = \psi(\boldsymbol{x}) e^{im\theta}, \quad m = \begin{cases} -\dfrac{N}{2}+1, \ldots, \dfrac{N}{2} & N \text{ even} \\ -\dfrac{N-1}{2}, \ldots, \dfrac{N-1}{2} & N \text{ odd} \end{cases} \tag{1}$$

where θ is the azimuthal coordinate around the axis of discrete rotational symmetry, $\psi(\boldsymbol{x})$ is a function identical in all unit-cell and periodic in θ with a period $2\pi/N$, m is the Bloch wave number and we neglect to express the explicit dependence of $\hat{p}$ on frequency. Note that $\psi(\boldsymbol{x})$ is not limited to a specific functional form, but can be any function that satisfies the aforementioned decomposition. The absolute value of m is identical to the azimuthal mode order [5].

The eigenmodes can be classified in three groups: axial ($m = 0$), push-pull ($m = N/2$), and degenerate pairs of spinning modes (all other values of m), which differ only by their spinning direction. From the study of a single unit-cell, the behavior of the full system can be assessed by considering all azimuthal mode orders m. In other words, we reduce our complete can-annular system to a single can where we apply Bloch boundaries in the region of the cross-talk, as depicted in Fig. 1.

2.3 Equivalent Longitudinal Network Model and Eigenvalue Problem. Low-order network models are well established for single can combustors [22–25] where, below the cut-on frequency of transverse modes, only acoustic plane waves propagate. The spatial extension of the gap is considered negligible compared to the wavelengths of interest meaning that the annular gap is acoustically compact. Therefore, the unit-cell can be modeled by an acoustic network as shown in Fig. 2. The can is replaced by a simple duct of length L, closed at the upstream side $R_{\text{in}} = 1$. On the downstream end, the behavior of the can-to-can communication through the annular gap is modeled by the equivalent reflection coefficient $\mathcal{R}_m(\omega)$, which is, in general, frequency dependent. This longitudinal network model is equivalent to the full system as we can recover all the eigenmodes by varying the azimuthal mode order m hidden in the outlet boundary condition.

The governing equations describing this longitudinal network model involve the following parameters: the frequency ω, the speed of sound c, the length of the can L, the width of the can H, the length of the cross-talk area L_g. These five parameters admit a basis of two fundamental dimensions, time and distance. Following the Buckingham Π theorem [26], the system is fully described

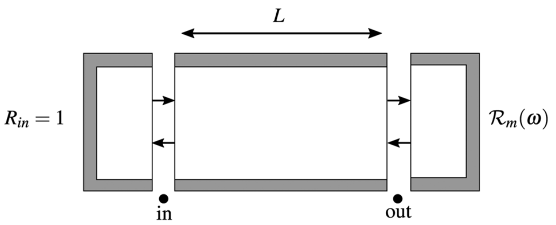

Fig. 2 Equivalent longitudinal network model of the unit-cell. The annular gap is modeled by the complex-valued reflection coefficient $\mathcal{R}_m(\omega)$, which depends on the frequency ω and the azimuthal order *m*.

by only three dimensionless parameters. For consistency with prior studies, we choose the same as those introduced by Ghirardo et al. [5]. The first dimensionless parameter is the Helmholtz number $\mathrm{He} = kL$, where $k = \omega/c$ is the wave number, which represents a dimensionless frequency. Small values of He correspond to acoustic waves whose wavelength is acoustically compact compared to the can length L. The second is the coupling strength $L_g^* = L_g/H$. The third number $L^* = L/H$ is interpreted as the aspect ratio of the can.

In the context of network modeling, it is convenient to use Riemann invariants. We recall the definition of characteristic waves amplitudes

$$f \equiv \frac{1}{2}\left(\frac{p'}{\bar{\rho} c} + u'\right), \quad g \equiv \frac{1}{2}\left(\frac{p'}{\bar{\rho} c} - u'\right) \tag{2}$$

In the duct, only plane waves propagate. The f and g waves at the cross-section "in" and "out" of Fig. 2 are related as follows:

$$\begin{bmatrix} f_{\mathrm{out}} \\ g_{\mathrm{out}} \end{bmatrix} = \begin{bmatrix} e^{-i\omega\tau} & 0 \\ 0 & e^{i\omega\tau} \end{bmatrix} \begin{bmatrix} f_{\mathrm{in}} \\ g_{\mathrm{in}} \end{bmatrix} \tag{3}$$

The term $e^{-i\omega\tau}$ models the acoustic propagation of a plane wave, where $\tau = L/c$ is the time that takes an acoustic wave to cover the length L. The boundary conditions are given by

$$\begin{cases} g_{\mathrm{out}} = \mathcal{R}_m(\omega) f_{\mathrm{out}} \\ f_{\mathrm{in}} = g_{\mathrm{in}} \end{cases} \tag{4}$$

Inserting Eq. (4) into Eq. (3) and rewriting in terms of dimensionless parameters leads to the eigenvalue problem

$$\mathcal{R}_m(\mathrm{He}) e^{-2i\mathrm{He}} = 1 \tag{5}$$

Equation (5) is complex-valued and thus gives conditions on the absolute value and the phase of the equivalent reflection coefficient $\mathcal{R}_m$. The first consequence is that $|\mathcal{R}_m(\mathrm{He})| = 1$. We considered a system with neither acoustic losses nor sources. It is therefore crucial to verify that the modeling approach does not introduce artificial losses or sources in the equivalent reflection coefficient $\mathcal{R}_m(\mathrm{He})$, i.e. its gain must be unity. The other consequence is that the eigenvalue problem reduces to a condition on the phase

$$2\mathrm{He} - \angle\mathcal{R}_m(\mathrm{He}) \equiv 0 \mod 2\pi \tag{6}$$

where $\angle\mathcal{R}_m(\mathrm{He})$ denotes the argument of the equivalent reflection coefficient $\mathcal{R}_m(\mathrm{He})$. Note that, in general, Eq. (6) is nonlinear in the Helmholtz number He and cannot be solved analytically.

3 Two-Dimensional Reference Case

In this section, we present the 2D Helmholtz case that serves as a reference for comparison with 1D low-order models. We choose the same parameters as in Ref. [5]: $N = 12$, $L^* = 2$, $L_g^* = 0.2$.

3.1 Numerical Setup. The reference simulations for obtaining the reflection coefficient from the 2D Helmholtz equation are carried out with the commercial finite element solver COMSOL MULTIPHYSICS. The parametrical setup of the geometry shown in Fig. 1 employs quadratic basis functions on a triangular mesh with cell sizes smaller than 10 mm to ensure grid independence. Boundary conditions for the sound hard walls, the non-reflecting inlet, as well as the superposed acoustic forcing at the inlet are imposed weakly via the flux. The Bloch boundaries are enforced via Lagrange multiplier constraints. The Helmholtz equation for this case is then solved in the frequency domain in 10 Hz steps, up to the maximum frequency corresponding to $\mathrm{He} = \pi$.

Figure 3 presents the forced response of the can at the frequency $\mathrm{He} = \pi/2$, for the azimuthal order $m = 1$. From the inlet, only plane waves propagate but, as they approach the gap region, distortion is observed. In the cross-talk area, the waves are not plane anymore and strong 2D effects are observed. These effects are not strictly confined in the vicinity of the gap but can also extend upstream, especially for higher azimuthal order. The results, in particular the reflection coefficients, are validated against those of Ghirardo et al. [5], which were obtained with an expansion on Chebyshev series of the 2D equations.

3.2 Two-Dimensional Equivalent Reflection Coefficients. The reflection coefficients $\mathcal{R}_{m,2D}(\mathrm{He})$ for an equivalent 1D geometry are obtained from 2D numerical simulations by computing the forced response of the set of cans at discrete frequencies and for each azimuthal order m. However, as seen in Sec. 3.1, strong 2D effects are present in the region of the gap, making any 1D post-processing at this location difficult. To overcome this limitation and to ensure reliable results, numerical measurements are performed at the inlet, upstream of the can, where the acoustics is closest to plane waves. In practice, for each azimuthal order m and for several discrete frequencies, we force the inlet with a wave f_{in} and measure the reflected wave g_{in}. From a 1D perspective, the measured ratio g_{in}/f_{in} is modeled as:

$$\frac{g_{in}}{f_{in}} = e^{-2i\mathrm{He}} \mathcal{R}_{m,2D}(\mathrm{He}) \tag{7}$$

The first term, $e^{-2i\mathrm{He}}$, represents the wave propagation in the duct from the inlet to the gap, and then again from the gap to the inlet, hence the factor of 2. $\mathcal{R}_{m,2D}(\mathrm{He})$ models the contribution of the annular gap.

From the 2D simulations, we computed the absolute value $|g_{in}/f_{in}|$ and verified that it is indeed unity. This result is expected: the waves can neither be amplified nor damped since no acoustic losses are taken into account and no energy is added to the system. On the other hand, the phase response is not trivial, and will

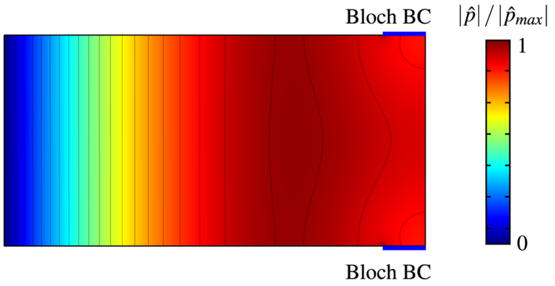

Fig. 3 Forced response of the system for the azimuthal order $m = 1$. The can is forced from the inlet with a wave f_{in} at the frequency $\mathrm{He} = \pi/2$. Color indicates the normalized absolute pressure and black lines indicate isolines of pressure. Upstream of the can, plane waves propagate. Downstream, the gap introduces strong 2D effects that are not confined in the vicinity of the gap region but also extend upstream.

especially depend on the azimuthal order of the mode, as reported in Ref. [5]. Although the equivalent reflection coefficient $\mathcal{R}_{m,2D}(\text{He})$ cannot be directly assessed in the gap region, Eq. (7) can be rewritten:

$$\angle \mathcal{R}_{m,2D}(\text{He}) = \angle\left(\frac{g_{in}}{f_{in}}\right) + 2\text{He} \tag{8}$$

This post-processing is useful because it allows us to keep only the behavior of the gap and remove the overemphasis of the contribution of the can (the phase shift due to the propagation in the can is much larger than the phase shift due to the gap, see Fig. 5 in Ref. [5]). Figure 4 shows the phase response of the equivalent reflection coefficient modeling the gap $\mathcal{R}_{m,2D}(\text{He})$ as a function of the dimensionless frequency He, for all azimuthal mode orders m. For the axial mode $m=0$, the phase is constant and equal to zero, meaning that $\mathcal{R}_{0,2D}=1$. The gap has no influence on the axial mode and the can is simply exposed to the acoustic boundary induced by the turbine. For all other azimuthal order, the characteristics of the phase are not trivial and depend on the frequency. Starting from π in the low-frequency limit, it converges toward zero but the slope depends on the azimuthal order (low azimuthal orders go faster toward zero).

Another interesting feature of this representation is the possibility to directly read off the eigenvalues of the full system. Equation (6) can be rewritten:

$$\angle \mathcal{R}_{m}(\text{He}) \equiv 2\text{He} \mod 2\pi \tag{9}$$

Equation (9) indicates that the first set of eigenfrequencies is located at the intersection between the phase response and the straight line of equation 2He (black dotted line on Fig. 4). The second cluster, which consists of the harmonics of the modes of the first cluster, is located at the intersection with the line of equation $2\text{He} - 2\pi$ (outside of the frequency range of Fig. 4) and so on for clusters of higher harmonics. Figure 4 shows that the eigenfrequencies of modes $m=4$, $m=5$, and $m=6$ are really close, hence the denomination "cluster".

4 Low-Order Models of the Annular Gap Based on Geometrical Parameters

In this section, we review the existing models proposed by von Saldern et al. [11] and Fournier et al. [13]. Both models are based on purely geometrical parameters and will be compared to the 2D Helmholtz simulations introduced in Sec. 3.

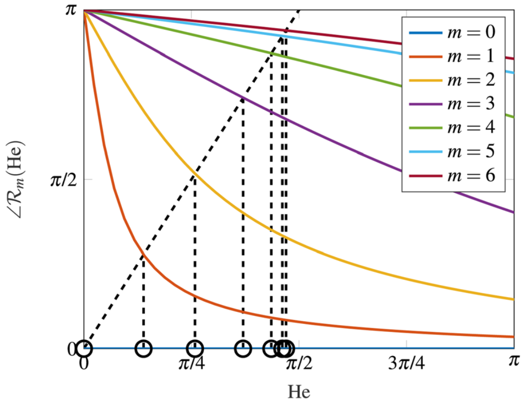

Fig. 4 Phase of the reflection coefficient $\mathcal{R}_{m,2D}$(He) of a set of $N=12$ cans as a function of the dimensionless frequency He and the azimuthal order m of the forcing pattern. Circles, located at the intersection between the phase response and the line of equation 2He (black dashed line), indicate the eigenfrequencies of the whole set of cans. Eigenmodes of azimuthal orders $m=4$, $m=5$ and $m=6$ have close frequencies, hence the denomination cluster.

4.1 Rayleigh Conductivity Model.

The Rayleigh conductivity K_R of an aperture, defined as $K_R = i\omega\rho Q/\Delta p$, relates the volume flux Q through the aperture to the pressure difference Δp between the two sides [12]. It is the analogue of Ohm's law for 1D lumped acoustic systems. Von Saldern et al. [11] derived a 1D model of the gap where the Rayleigh conductivity K_R is used to relate the acoustic velocities inside the gap to the pressure gradient between cans, because $Q = A_{\text{gap}}u'$. The can was assumed to be circular, of radius r_{can}. In order to obtain a simple analytical expression, the gap was treated as a circular aperture. With this hypothesis, the Rayleigh conductivity is constant and relates to the gap radius as $K_R = 2r_{\text{gap}}$. Writing Eq. (10) from Ref. [11] with dimensionless parameters leads to

$$\mathcal{R}_{m,RC}(\text{He}) = 1 - \frac{16\sin^2\left(\frac{\pi m}{N}\right)}{i\text{He}\,\frac{\pi}{2L^*\sqrt{L_g^*}} + 8\sin^2\left(\frac{\pi m}{N}\right)} \tag{10}$$

In the rest of the paper we refer to it as the RC model, where RC stands for *Rayleigh conductivity*.

4.2 Thin Annulus Model.

Fournier et al. [13] proposed an alternative modeling strategy, where can-annular combustors are seen as limit cases of annular geometries: the cans are burner tubes of significant dimensions and the annular gap is an annular chamber where the axial spatial extension is negligible and the total azimuthal length corresponds to N times the width of a can. The annular gap is modeled as a thin annulus, i.e. a compact T-junction and ducts of lengths $H/2$ representing the width of the can. Following the results of Fournier et al., Eq. (14) in Ref. [13] can be written with dimensionless parameters:

$$\mathcal{R}_{m,TA}(\text{He}) = 1 - \frac{4\cos\left(\frac{\text{He}}{L^*}\right) - 4\cos\left(\frac{2\pi m}{N}\right)}{\frac{i}{L_g^*}\sin\left(\frac{\text{He}}{L^*}\right) + 2\cos\left(\frac{\text{He}}{L^*}\right) - 2\cos\left(\frac{2\pi m}{N}\right)} \tag{11}$$

In the following, we refer to it as the TA model, where TA stands for *thin annulus*.

4.3 Analysis of the Low-Order Models.

For a real-valued Helmholtz number He (marginally stable mode), it is straightforward to mathematically prove that $|\mathcal{R}_{m,RC}(\text{He})| = |\mathcal{R}_{m,TA}(\text{He})| = 1$. It follows that both models are satisfactory in the sense that they do not introduce spurious damping or amplification.

As reported in Refs. [5], [11], and [13] and seen in Sec. 3.2, the phase response is nontrivial. Figure 5 shows the phase response for both 1D models compared to the 2D Helmholtz reference case. For the sake of clarity, only the axial mode and modes of azimuthal order $m = 1, 2, 5, 6$ are represented. The first observation is that both models do not accurately reproduce the results of the 2D reference case: they do not provide quantitatively accurate results. For example, the TA model underpredicts the eigenfrequency of the first azimuthal order, whereas the RC model overpredicts it. The errors on the eigenfrequency are 29.3% and 20.7%, respectively. Similar behaviors are observed for the other azimuthal orders, and the error on the eigenvalue prediction varies from 11% to 35%. Akin results were observed by Yoon where the theoretical model, which can be seen as an extension of the TA model, always underpredicts the eigenfrequencies compared to FEM (Fig. 9 in Ref. [15]). Both RC and TA model underpredict

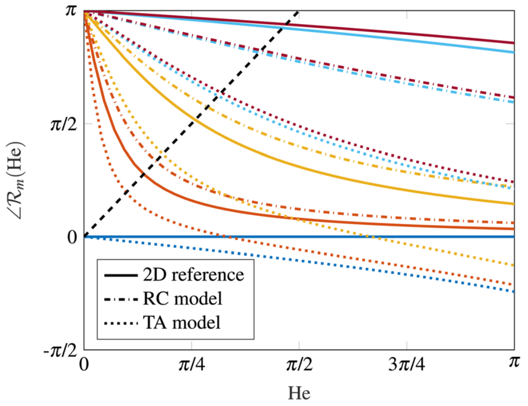

Fig. 5 Phase response of the annular gap as predicted by the Rayleigh conductivity model (dashed–dotted line) and thin annulus model (dotted line) compared to the 2D Helmholtz reference (full line). Colors indicate the azimuthal order as defined in Fig. 4. For each azimuthal order, the intersection of the phase response with the black dashed line gives the eigenfrequency. Both models are qualitatively correct in the low frequency limit. Nevertheless, they do not predict accurately the eigenfrequencies.

the frequency at which the modes tend to cluster by 12.3% and 32.1%, respectively.

Although being quantitatively inaccurate, the RC model exhibits a satisfactory qualitative behavior for the entire frequency range investigated. Starting from π, the phase decreases and converges asymptotically toward the horizontal zero line without crossing it. The axial mode is also well captured: the phase is constant and trivially zero. In contrast, the thin annulus (TA) model is not entirely satisfactory. For low frequencies, the TA model exhibits the correct qualitative behavior. This is explained by the fact that a Taylor expansion of Eq. (11) gives

$$\mathcal{R}_{m,TA}(\mathrm{He}) \approx 1 - \frac{8\sin^2\left(\dfrac{\pi m}{N}\right)}{i\mathrm{He}\dfrac{1}{L^* L_g^*} + 4\sin^2\left(\dfrac{\pi m}{N}\right)} \tag{12}$$

which is essentially the same structure as of the RC model (see Eq. (10)). However, as the frequency increases, for each mode order, the phase does not converge asymptotically toward the zero line but does cross it. These intersection points are located at the frequencies $\mathrm{He} = 2L^* m\pi/N$ and correspond to the passive acoustic mode of the thin annulus [13]. Therefore, for higher frequencies $\mathrm{He} \geq 2L^* m\pi/N$, the qualitative behavior is not satisfactory. We conclude that the cross-talk area of can-annular combustors should not be modeled as a thin annulus when considering higher frequencies. For the axial mode, the two ducts of the thin annulus that model the width of the can inherently add a non-negligible length to the total length of the can, hence the phase shift observed in Fig. 5. Note that this effect could be compensated but would require an individual tuning of the model for the axial mode.

In conclusion, the thin annulus assumption to model the gap in can-annular configurations is qualitatively valid only for low frequencies ($\mathrm{He} \leq 2L^* m\pi/N$). Conversely, the Rayleigh conductivity model gives the correct qualitative behavior over a wide frequency range. Nevertheless, because based purely on geometrical parameters, both models do not capture the correct phase response of the annular gap (see the error with the 2D reference on Fig. 5), and, for all azimuthal orders, do not predict accurately the eigenfrequencies. These shortcomings motivate the need of an extension of the RC model to obtain quantitatively accurate results.

4.4 A Few Considerations on the Spectrum Structure and Clusters. Although not suited for quantitative prediction, these simple models give good insight into the underlying physics. We consider two interesting limit cases.

- Case 1: L_g is zero. The gap is completely closed, i.e. the coupling strength is $L_g^* = 0$. The equivalent reflection coefficient becomes trivially $\mathcal{R}_{m,RC}(\mathrm{He}) = \mathcal{R}_{m,TA}(\mathrm{He}) = 1$: it is independent of the mode order and of the frequency. The gap closes and the annular configuration reduces to a purely longitudinal configuration where the outlet boundary condition is the choked exit. The eigenvalue problem becomes:

$$e^{-2i\mathrm{He}} = 1 \quad \Rightarrow \quad \mathrm{He} = p\pi, \quad p \in \mathbb{N} \tag{13}$$

  which is the half-wave mode and its harmonics. In the limit case where the gap closes, all the modes of the first cluster collapse into one degenerate mode, the half-wave mode.
- Case 2: large aspect ratio. In the limit case where the length becomes much more significant than the width, i.e. $1/L^* \rightarrow 0$, the equivalent reflection coefficient is

$$\mathcal{R}_{m,RC}(\mathrm{He}) \approx \mathcal{R}_{m,TA}(\mathrm{He}) \approx \begin{cases} 1, & m = 0 \\ -1, & m \neq 0 \end{cases} \tag{14}$$

  The axial mode is unaffected by the annular gap and remains exposed to the choked outlet. The eigenmode associated is the half-wave mode $\mathrm{He} = 0$ and harmonics. On the other hand, all other azimuthal modes are now exposed to an open end ($R = -1$). The solutions of the eigenvalue problem are

$$e^{-2i\mathrm{He}} = -1 \quad \Rightarrow \quad \mathrm{He} = \frac{\pi}{2} + p\pi, \quad p \in \mathbb{N} \tag{15}$$

  All the modes converge to the quarter-wave mode and its harmonics. This is physically explained by the fact that, in this limit case of a long can, any phase shift introduced by the gap becomes negligible compared to the phase shift due to the propagation in the can itself. The effect of the azimuthal order on the outlet boundary becomes negligible, hence the outlet boundary is independent of the mode order and all modes converge to the same solution.

The phase of the equivalent reflection coefficient can be analytically determined

$$\angle\mathcal{R}_{m,RC}(\mathrm{He}) = \pi - 2\arctan\left(\frac{\pi\mathrm{He}}{16L^*\sqrt{L_g^*}\sin^2\left(\dfrac{\pi m}{N}\right)}\right) \tag{16}$$

This equation can be used to understand the spectrum structure. Recall that the eigenfrequency is located at the intersection with the straight line of equation 2He (Eq. (9)). When L^* increases, Eq. (16) shows that the phase response is less and less steep, the eigenfrequency is "pushed" to the right to higher frequencies, with the limit $\mathrm{He} = \pi/2$. Figure 6 presents the influence of the aspect ratio on the first two eigenfrequencies for all azimuthal orders. For a given azimuthal order m, when L^* increases, the eigenfrequency increases and converges toward the quarter-wave mode. Therefore, can-annular combustors with large aspect ratio L^* tend to have a more pronounced clustering effect. Similarly, for a given geometry (L^* and L_g^* fixed), when m increases, the phase response is less and less steep, the eigenmode is located at a higher frequency. That explains the spectrum structure: the higher the azimuthal order, the higher the eigenfrequency. Modes with higher azimuthal order will be the closest within a cluster. This sheds a new light when designing can-annular combustors: modes always come in clusters, outcome of a system that behaves as a collection of oscillators (cans) weakly coupled (gap). The spread of the modes within a cluster depends on the system geometry

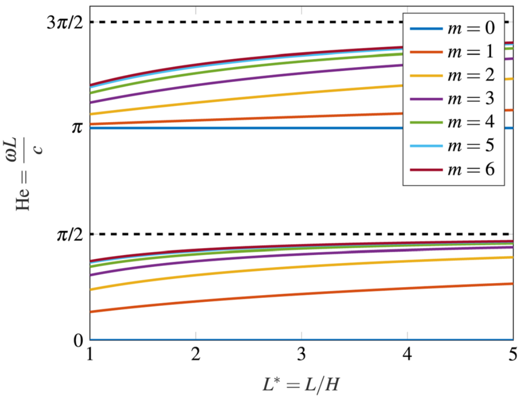

Fig. 6 Sensitivity of the first two eigenfrequencies as a function of the aspect ratio L^*. Small values of L^* correspond to a set of cans that are short compared to the circumference of the annular gap, that measures *NH*. Colors indicate the azimuthal order as defined in Fig. 4. When the length of the can becomes much larger than the other dimensions, the eigenmodes converge to the same solution, the quarter-wave mode and its harmonics. Modes with high azimuthal order converge faster and are closest within a cluster.

(length of the can, gap design, etc.). This needs to be taken into account at the design stage as clusters of modes cannot be avoided. A related question arises: how should the combustor be designed to guarantee that all thermoacoustic modes are stable? This crucial and interesting question is beyond the scope of this study and will be left for future research.

5 Low-Order Model Based on Characteristic Length

In this section, we derive an extension for the reflection coefficient model that accounts not only for geometrical but also flow parameters. The gap is assumed to be acoustically compact. The mass conservation equation integrated over the control volume depicted in Fig. 1 reduces to conservation of volumetric flow rate:

$$Hu'_1 - L_g u'_2 - L_g u'_3 = 0 \tag{17}$$

Equation (17) is rewritten with dimensionless parameters and Riemann invariants, which are more convenient to define a reflection coefficient.

$$\frac{1}{L_g^*}(f_1 - g_1) - (f_2 - g_2) - (f_3 - g_3) = 0 \tag{18}$$

Because of the rotational symmetry, we invoke Bloch theory to mutually connect location 2 and 3 with periodic Bloch boundaries [21].

$$\begin{cases} f_3 = g_2 e^{i\frac{2\pi m}{N}} \\ g_3 = f_2 e^{i\frac{2\pi m}{N}} \end{cases} \tag{19}$$

We define the equivalent reflection coefficient as $g_1 = \mathcal{R}_m f_1$. Using this definition and inserting Eq. (19) into Eq. (18) leads to

$$\frac{1}{L_g^*}(1 - \mathcal{R}_m)f_1 + \left(e^{i\frac{2\pi m}{N}} - 1\right)f_2 + \left(1 - e^{i\frac{2\pi m}{N}}\right)g_2 = 0 \tag{20}$$

Equation (20) has three unknowns, thus two more independent equations are required to close the problem. Note that for the axial mode $m = 0$, the equation directly reduces to $R_0(\mathrm{He}) = 1$: the equivalent reflection coefficient is constant and is not affected by the cross-talk area.

We use the unsteady Bernoulli equation for irrotational homentropic flow [27].

$$0 = \frac{\partial}{\partial x}\left(\frac{\partial \varphi}{\partial t} + \frac{u^2}{2} + \frac{\gamma}{\gamma - 1}\frac{p}{\rho}\right) \tag{21}$$

where φ is the velocity potential and γ is the ratio of specific heat capacities (ideal gas behavior is implied). The equation is integrated along two streamlines of the mean flow, from location 1 to location 2 and from location 1 to location 3, respectively. It is possible to find a standing wave with a nodal line that coincides with the symmetry axis of the can in the considered unit-cell. This symmetry allows us to treat locations 2 and 3 similarly. We consider the integral in space of the first term of Eq. (21), the velocity potential.

$$\int_1^2 \frac{\partial}{\partial x}\left(\frac{\partial \varphi}{\partial t}\right)dx = \int_1^2 \frac{\partial}{\partial t}\left(\frac{\partial \varphi}{\partial x}\right)dx = \frac{\partial}{\partial t}\int_1^2 u(x)dx \tag{22}$$

As depicted in Fig. 7, from a 1D perspective, we consider the flow through the compact annular gap to be similar to the flow in a converging compact nozzle, which is a well-established problem. Following prior studies for a compact element with a varying cross-section [27–31], we define the characteristic length $L_{\mathrm{char},\,m}$

$$L_{\mathrm{char},\,m} = \int_1^2 \frac{u(x)}{u_2}dx \approx \int_1^2 \frac{L_g}{h(x)}dx \tag{23}$$

where $h(x)$ is the cross-section of the flow along the stream-path of the acoustic flow, and not the geometric cross-section across the element. For that reason, the characteristic length depends on the azimuthal order m. Physically, the characteristic length accounts for the inertia of the volume of fluid between the two reference positions. Assuming harmonic time-dependence, Eq. (22) reduces to

$$\int_1^2 \frac{\partial}{\partial x_i}\left(\frac{\partial \varphi}{\partial t}\right)dx_i = i\omega L_{\mathrm{char},\,m}u_2 \tag{24}$$

The integral in space of the remaining two terms of Eq. (21) is simply evaluated at location 1 and 2. Linearization with Reynolds decomposition, assuming zero mean flow and neglecting higher order terms yields

$$ikL_{\mathrm{char},\,m}u'_2 + \frac{p'_2 - p'_1}{\bar{\rho}c} = 0 \tag{25}$$

where $k = \omega/c$ is the wavenumber. The integration from location 1 to 3 is done similarly. Switching to Riemann invariants, the problem can be cast into the homogeneous linear system of equations

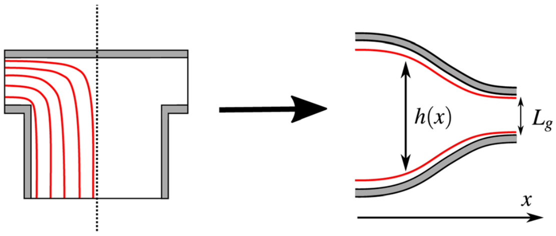

Fig. 7 Each half of the gap is treated as a 1D converging nozzle. *h*(*x*) is the cross-section of the flow along the stream-path of the acoustic flow. The inertia of the volume of fluid is expressed in terms of a characteristic length $L_{\mathrm{char},\,m}$.

$$\mathbf{M}(\mathrm{He}, m)\begin{bmatrix} f_1 \\ f_2 \\ g_2 \end{bmatrix} = \begin{bmatrix} 0 \\ 0 \\ 0 \end{bmatrix} \tag{26}$$

with the matrix $\mathbf{M}(\mathrm{He}, m)$ as

$$\underbrace{\begin{bmatrix} \dfrac{1-\mathcal{R}_m}{L_g^*} & e^{i\frac{2\pi m}{N}} - 1 & 1 - e^{i\frac{2\pi m}{N}} \\ -1-\mathcal{R}_m & 1 + ikL_{\mathrm{char},\,m} & 1 - ikL_{\mathrm{char},\,m} \\ -1-\mathcal{R}_m & e^{i\frac{2\pi m}{N}}(1 - ikL_{\mathrm{char},\,m}) & e^{i\frac{2\pi m}{N}}(1 + ikL_{\mathrm{char},\,m}) \end{bmatrix}}_{\mathbf{M}(\mathrm{He},m)} \tag{27}$$

The system shows nontrivial solution if the determinant of $\mathbf{M}(\mathrm{He}, m)$ is null, which gives a condition for the reflection coefficient:

$$\mathcal{R}_{m,CL}(\mathrm{He}) = 1 - \frac{4\sin^2\left(\dfrac{\pi m}{N}\right)}{i\mathrm{He}\dfrac{L^*_{\mathrm{char},\,m}}{L^* L_g^*} + 2\sin^2\left(\dfrac{\pi m}{N}\right)} \tag{28}$$

where $L^*_{\mathrm{char},\,m} = L_{\mathrm{char},\,m}/H$ is the dimensionless characteristic length.

As shown by Schuermans et al. [32], the concept of effective length is interchangeable to the Rayleigh conductivity. Equation (28) is similar to Eq. (10) and can be seen as an extension of the RC model. However, the proposed model accounts not only for geometrical parameters but also for flow parameters with the inertial length $L_{\mathrm{char},\,m}$. In particular, the dependence of $L_{\mathrm{char},\,m}$ on the azimuthal order m reflects the fact that the acoustic flow is influenced by the azimuthal mode, hence the denomination flow parameter. Note that this is a purely acoustic perspective and it is not connected to mean flow, turbulence or similar features. The use of a characteristic length is well established and applicable to all sorts of elements, e.g., a premixed burner [28], a sudden change in cross-sectional area [30], an orifice [31], a nozzle [29], a Helmholtz resonator [33], among others. Note that we did not take into account the losses due to the abrupt changes in geometry. This consideration of losses is a natural extension of the present model and will be covered in future work.

The characteristic length $L_{\mathrm{char},\,m}$ can be determined from the 2D simulations using Eqs. (22) or (23). However this post-processing can be tedious: it is not straight forward to determine an appropriate control volume, to extract a "characteristic" streamline representing the ensemble, to average the 2D quantities to compare with 1D, etc. Flohr et al. [31] proposed an alternative method to measure based on an analogy with the heat conduction equation but with a detrimental loss of accuracy. For the present case, we make use of the fact the reflection coefficient $\mathcal{R}_m$ numerically measured from the 2D simulations contains all the relevant information. In particular, $L_{\mathrm{char},\,m}$ is embedded in this measurement as it directly shapes the phase response of $\mathcal{R}_m$. As a result, $L_{\mathrm{char},\,m}$ becomes a physics-based parameter giving an additional degree of freedom. $L_{\mathrm{char},\,m}$ is assessed via an optimization problem by minimizing the normalized root-mean-squared error between the low-order model (LOM) and the numerical simulations, defined as

$$\mathrm{NRMSE} = \frac{\sqrt{\dfrac{1}{n}\displaystyle\sum_{j=1}^{n}\left(y_j - \hat{y}_j\right)^2}}{\sigma} \tag{29}$$

where y_j is the phase response of the gap, obtained from numerical simulations, at the discrete frequency j, $\hat{y}_j$ the predicted value from the 1D model, n the number of frequency samples, and σ the standard deviation. Note that $L_{\mathrm{char},\,m}$ only depends on the azimuthal order m and is independent of frequency. Figure 8 presents the phase response of the annular gap as predicted by the characteristic length model compared to 2D Helmholtz simulations. For every azimuthal order, the low-order model shows excellent agreement with the 2D reference. The normalized root-mean-square error (NRMSE) between the LOM and the reference remains lower than 2.2%.

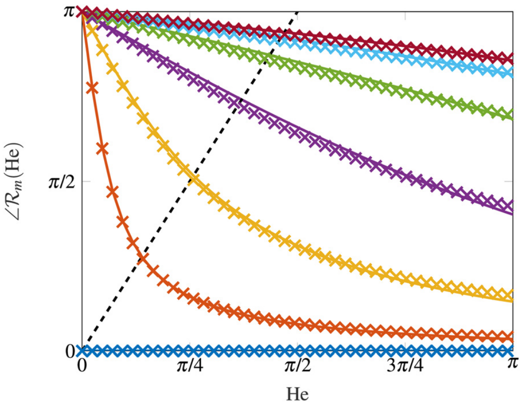

Fig. 8 Phase response of the annular gap as predicted by the characteristic length model (crosses) compared to the 2D Helmholtz reference (full line). Colors indicate the azimuthal order as defined in Fig. 4. For each azimuthal order, the intersection of the phase response with the black dashed line gives the eigenfrequency. The low-order model shows excellent agreement over the entire frequency range of interest compared to the 2D reference.

Table 1 Eigenfrequency prediction of the characteristic length model compared to the 2D Helmholtz reference for all azimuthal order

	f_{2D} (Hz)	f_{CL} (Hz)	Error (%)
$m = 1$	58.98	58.73	0.4
$m = 2$	109.80	108.24	1.42
$m = 3$	157.35	154.14	2.03
$m = 4$	185.31	182.70	1.41
$m = 5$	196.12	194.63	0.76
$m = 6$	199.80	198.48	0.65

Since the phase response is properly modeled over the entire frequency range, it implies a correct eigenfrequency prediction. Table 1 shows, for every azimuthal mode, the eigenfrequency predicted by the characteristic length model and the relative error with the 2D reference. The maximal error observed is 2%, which is considered acceptable regarding all the assumptions and simplifications of the low-order model.

A simple 1D model, based on geometrical and flow parameters, is able to accurately model the cross-talk area of a can-annular combustor, despite the strong 2D effects observed at this location. These 2D effects are lumped into the equivalent length correction, as it is common in the acoustics literature. It is highlighted that, although changing with the mode order, the characteristic length $L_{\mathrm{char},\,m}$ does not depend on frequency. For each mode order, it is obtained from numerical simulations and valid for that case only. However, such low-order method is computationally inexpensive and may prove to be useful in concept and pre-design studies, where geometrical parameters are rapidly changing. In order to use it for new designs and ensure reliable results, one needs to determine how $L_{\mathrm{char},\,m}$ can be generalized.

6 Generalization of the Model to Configuration With Different Geometrical Parameters

In this section, we investigate how the characteristic length $L_{\mathrm{char},m}$ can be generalized to other configurations. In particular, we analyze the influence of geometrical parameters.

6.1 Design of Experiments Study. We perform a design of experiments (DoE) study [34] where the two dimensionless input parameters L^* and L_g^* vary in the range $[1-5]$ and $[0.1-0.3]$, respectively. These values correspond to realistic parameters for a gas turbine combustor. Following Loeppky et al. [35], who suggest that the sample size should be at least ten times the number of input parameters, the parameter space is filled by 40 points following a Latin Hypercube method, as shown in Fig. 9. For each set of parameters, a 2D Helmholtz simulation is performed and post-processed following the method described for the reference case.

6.2 Correlations for $L_{\mathrm{char},m}$. For each case, and for every azimuthal order, the characteristic length $L_{\mathrm{char},m}$ is determined. We excluded four data points that exhibited NRMSEs between 2D and LOM greater than 5%, which was not considered acceptable. These larger errors, explained by the limits of validity of the LOM, are discussed later.

From a low-order network perspective, if we disregard the upstream can and consider only the gap itself, according to the Buckingham Π theorem [26], the latter can be modeled with only two parameters: a dimensionless frequency and the coupling strength L_g^*. But, as shown in Sec. 5, the characteristic length $L_{\mathrm{char},m}$ is independent of frequency. Therefore, from a 1D perspective, $L_{\mathrm{char},m}$ depends only on the coupling strength $L_g^* = L_g/H$. Figure 10 presents the normalized characteristic length $L^*_{\mathrm{char},m} = L_{\mathrm{char},m}/H$ as a function of the coupling strength L_g^*. For the sake of clarity, only mode order $m=1$, $m=3$, and $m=6$ are shown. The color of the data points indicates the aspect ratio L^*. We can see that, for a coupling strength L_g^* from 10% to 30%, the normalized characteristic length $L^*_{\mathrm{char},m}$ scales linearly in the explored range. The coefficients of determination R^2 of the proposed linear regressions are 0.86, 0.77 and 0.93, respectively.

From the numerical simulations, for a given azimuthal order m, we observe that, for large values of L^*, the characteristic length can be considered independent of the aspect ratio L^* and is determined only by the coupling strength L_g^*. Indeed, from Fig. 10, we see that data points associated with configurations with similar coupling strength L_g^* but different aspect ratio L^* tend to be close to each other and the proposed correlations. On the other hand, the scatter is more pronounced for configuration with small aspect ratios: these points have the largest errors with the proposed linear regressions. Note also that, for these configurations, the error between 2D simulations and LOM when determining the characteristic length $L_{char,m}$ also tend to increase (recall Fig. 9). This is due to the limits of validity of the LOM approach, discussed in Sec. 6.3. Considering the satisfactory linear regressions, it is reasonable to disregard the influence of the aspect ratio L^* and to consider the characteristic length $L_{\mathrm{char},m}$ primarily as a function of the azimuthal order m and the coupling strength $L_g^* = L_g/H$. In particular, for each mode order m, the linear regression gives:

$$L^*_{\mathrm{char},m} = a_{1,m}L_g^* + a_{0,m} \Rightarrow L_{\mathrm{char},m} = a_{1,m}L_g + a_{0,m}H \tag{30}$$

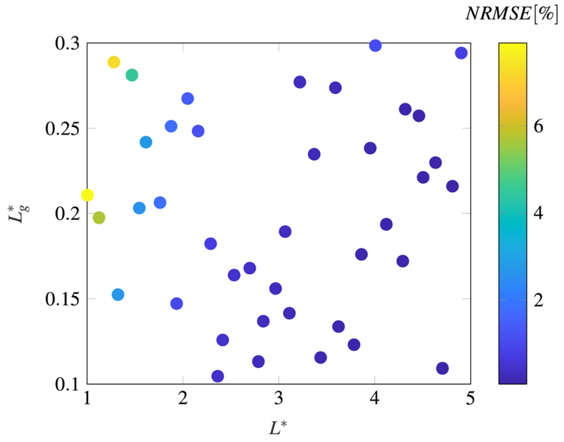

Fig. 9 Parameter space of the DoE filled by 40 points with a Latin Hypercube method. The color indicates the normalized root-mean-square error of the phase response between the low-order model and the 2D reference. For small aspect ratio L^* or for large coupling strength L_g^*, the error tends to increase.

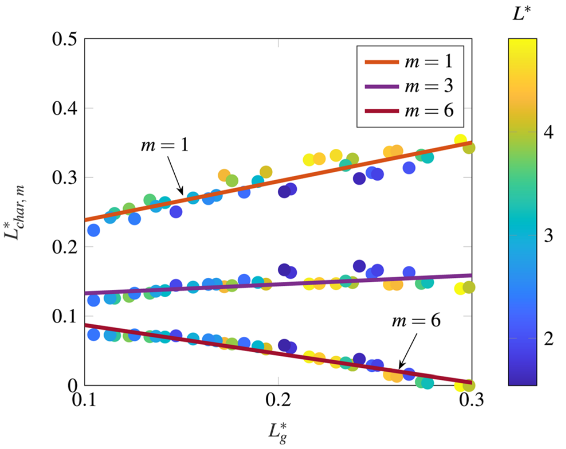

Fig. 10 Sensitivity of the normalized characteristic length $L^*_{\mathrm{char},m}$ as a function of the coupling strength L_g^* for azimuthal mode orders $m=1$, $m=3$ and $m=6$. The color of the points indicates the aspect ratio of the can L^*, showing that the dependence of $L^*_{\mathrm{char},m}$ on L^* is weak in the studied range. In the explored range, $L^*_{\mathrm{char},m}$ scales linearly with the coupling strength L_g^*.

It is highlighted that, as a first approximation, the characteristic length $L_{\mathrm{char},m}$ scales linearly with the gap size L_g and the width of the can H.

Depending on the coupling strength L_g^* and the azimuthal order m considered, the characteristic length can vary significantly. Physically, this is explained by the fact that an inertial length is strongly influenced by the contraction experienced by the flow. For example, it is common to observe a characteristic length much larger than the geometrical quantities of interest [27,33]. For a given geometry, the characteristic length decreases with the azimuthal mode order, which is consistent with the fact that modes with higher azimuthal order exhibit a higher eigenfrequency, as explained previously. Finally, when the coupling strength increases, the relative importance of $L^*_{\mathrm{char},m}$ compared to L_g^* decreases toward zero, leading, for high values, to $\mathcal{R}_m \approx -1$. Indeed, if the coupling strength is large, i.e. if the gap size L_g is significant, the system can be seen as a can terminating in a large vessel, i.e. the can is exposed to an open end.

6.3 Limits of Validity of the LOM Approach. In Secs. 5 and 6.2, we demonstrated that a low-order model based on a characteristic length can retrieve 2D results with a satisfying accuracy. In particular, the eigenfrequencies of the system are accurately predicted. However, such modeling approach has two limiting factors.

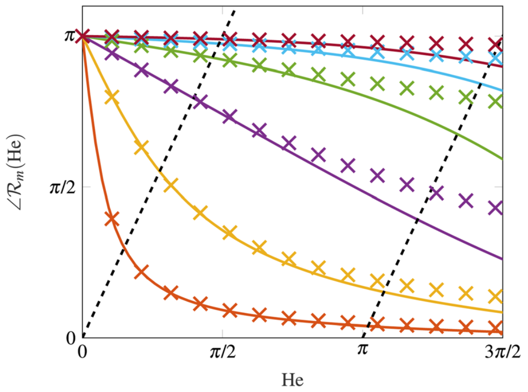

Fig. 11 Phase response of the gap as predicted by the characteristic length model (crosses) compared to the 2D Helmholtz reference (full line). Colors indicate the azimuthal order as defined in Fig. 4. Intersections with the black dashed lines give the eigenfrequencies. As the frequency increases, the gap becomes acoustically non-compact, the 1D modeling approach reaches its limits of validity and the model deviates from the reference case.

The first limitation comes from the assumption that, in the cans, only plane waves propagate and all other modes are said "cut-off." But as the frequency increases and reaches the cut-off frequency of a non-plane mode, that mode is no longer evanescent and can propagate: it is said cut-on. For example, for a circular can of radius $H/2$, the plane wave approximation remains valid up to the maximum frequency $\mathrm{He} < 2L^*\alpha_{11}$, where $\alpha_{11} \approx 1.84$ is the first zero of the Bessel function $J_1'(x)$ [36]. The maximum frequency is directly influenced by the aspect ratio of the can: for small aspect ratio L^*, the LOM will be able to accurately predict only the first cluster, whereas for large L^*, clusters at higher frequencies, which consist of the harmonics of the mode of the first cluster, will also be correctly captured.

The second limitation comes from the hypothesis of an acoustically compact gap $kL_g \ll 1$, i.e. $\mathrm{He} \ll L^*/L_g^*$ with dimensionless parameters. Figure 11 shows the phase response of the characteristic length model compared to 2D simulations for $L^* = 2.05$ and $L_g^* = 0.27$. In the low frequency region, the LOM has a perfect agreement with numerical simulations. The first cluster (intersection with the first black dashed line) is captured accurately for every azimuthal order. However, as the frequency increases, the gap becomes non-compact. The LOM deviates from the 2D reference and the second cluster is not captured at the correct frequencies. The error on the eigenfrequency prediction is around 6% for the second cluster, to put in perspective with an error of 1% or less for the first cluster. Although it might be considered still acceptable for the second cluster, note that it will be amplified for clusters at higher frequencies. It is therefore crucial, when considering clusters of higher harmonics, to verify that we remain within the domain of validity of our model.

7 Summary and Conclusion

In this paper, we investigated a generic can-annular combustor and focused on the acoustic modeling of the cross-talk area in front of the turbine that allows for can-to-can acoustic communication. We exploited the discrete rotational symmetry by using Bloch boundaries to reduce the combustor to a single unit-cell, while preserving the dynamics of the full system. We demonstrated that only three dimensionless parameters are required to model such configuration with a low-order network. The annular gap is replaced by a complex-valued equivalent reflection coefficient, which accounts for the azimuthal order of the mode.

We then reviewed two existing 1D models, based only on geometrical parameters, and compared them to a 2D Helmholtz reference. The first model describes the gap as a thin annulus. Although intuitive at first glance, this modeling approach is valid only in the low frequency limit and mainly suited for cans with large aspect ratios. The second model describes can-to-can communication with the Rayleigh conductivity. The qualitative behavior is satisfactory and valid for a wider frequency range. Both models can be used to understand the structure of the acoustic spectrum. However, they are based only on geometrical parameters and cannot predict, at a quantitative level, the correct eigenfrequencies of the system.

We then derived an extension that accounts not only for geometrical parameters but also flow parameters in terms of an inertial characteristic length $L_{\mathrm{char},m}$. This additional parameter models how the acoustic flow in the gap is influenced by the azimuthal order of the mode. We demonstrated that such a 1D model can accurately capture the physics and shows excellent agreement with the reference, despite the strong 2D effects observed in the region of the gap.

We performed a Design of Experiments study to apply this model to other geometrical configurations and built correlations for $L_{\mathrm{char},m}$. We demonstrated that the characteristic length depends primarily on the azimuthal order m and the coupling strength L_g^* and linear regressions were proposed with satisfactory results. Finally, we discussed the limits of validity of the model.

In this study, we considered a pure acoustic model. The impact of losses and mean flow on the characteristic length can be investigated in future work.

Acknowledgment

This project has received funding from the European Union's Horizon 2020 research and innovation programme under Grant Agreement No 765998 *Annular Instabilities and Transient Phenomena in Gas Turbine Combustors* (ANNULIGhT). Guillaume J. J. Fournier would like to thank Ansaldo Energia Switzerland for hosting him for this research. The authors would also like to thank Matthias Haeringer, Felix Schily, and Shuai Guo for valuable discussions.

Funding Data

- European Commission (Award No. 765998; 10.13039/501100000780).

Nomenclature

c = speed of sound (m s^{-1})
DoE = design of experiments
f, g = characteristic wave amplitudes (m s^{-1})
H = width of the can (m)
He = Helmholtz number, kL
k = wave number (rad m^{-1})
K_R = Rayleigh conductivity (m)
L = length of the can (m)
L^* = aspect ratio of the can, L/H
$L_{\mathrm{char},m}$ = characteristic length (m)
L_g = width of the annular gap (m)
$L^*_{\mathrm{char},m}$ = dimensionless characteristic length, $L_{\mathrm{char},m}/H$
L_g^* = coupling strength, L_g/H
LOM = low-order model
m = Bloch wave number
N = number of cans
NRMSE = normalized root-mean-square error
p' = acoustic pressure (Pa)
$\mathcal{R}_m$ = equivalent reflection coefficient
u' = acoustic velocity (m s^{-1})
γ = heat capacity ratio

ρ = density (kg m^{-3})
φ = velocity potential (m^2 s^{-1})
ω = complex frequency (rad s^{-1})

References

[1] Bethke, S., Krebs, W., Flohr, P., and Prade, B., 2002, "Thermoacoustic Properties of Can Annular Combustors," AIAA Paper No. 2002-2570.

[2] Kaufmann, P., Krebs, W., Valdes, R., and Wever, U., 2008, "3D Thermoacoustic Properties of Single Can and Multi Can Combustor Configurations," ASME Paper No. GT2008-50755.

[3] Panek, L., Farisco, F., and Huth, M., 2017, "Thermo-Acoustic Characterization of Can-Can Interaction of a Can-Annular Combustion System Based on Unsteady CFD LES Simulation," Proceedings of First Global Power and Propulsion Forum, GPPS, Zurich, Switzerland, Jan. 16–18, Paper No. GPPF-2017-81.

[4] Farisco, F., Panek, L., and Kok, J. B., 2017, "Thermo-Acoustic Cross-Talk Between Cans in a Can-Annular Combustor," Int. J. Spray Combust. Dyn., **9**(4), pp. 452–469.

[5] Ghirardo, G., Di Giovine, C., Moeck, J. P., and Bothien, M. R., 2019, "Thermoacoustics of Can-Annular Combustors," ASME J. Eng. Gas Turbines Power, **141**(1), p. 011007.

[6] Jegal, H., Moon, K., Gu, J., Li, L. K., and Kim, K. T., 2019, "Mutual Synchronization of Two Lean-Premixed Gas Turbine Combustors: Phase Locking and Amplitude Death," Combust. Flame, **206**, pp. 424–437.

[7] Moon, K., Jegal, H., Gu, J., 2019, "Combustion-Acoustic Interactions Through Cross-Talk Area Between Adjacent Model Gas Turbine Combustors," Combust. Flame, **202**, pp. 405–416.

[8] Moon, K., Jegal, H., Yoon, C., and Kim, K. T., 2020, "Cross-Talk-Interaction-Induced Combustion Instabilities in a Can-Annular Lean-Premixed Combustor Configuration," Combust. Flame, **220**, pp. 178–188.

[9] Moon, K., Yoon, C., and Kim, K. T., 2021, "Influence of Rotational Asymmetry on Thermoacoustic Instabilities in a Can-Annular Lean-Premixed Combustor," Combust. Flame, **223**, pp. 295–306.

[10] Bloch, F., 1929, "Über Die Quantenmechanik Der Elektronen in Kristallgittern," Z. Phys., **52**(7–8), pp. 555–600.

[11] von Saldern, J., Orchini, A., and Moeck, J., 2021, "Analysis of Thermoacoustic Modes in Can-Annular Combustors Using Effective Bloch-Type Boundary Conditions," ASME J. Eng. Gas Turbines Power, **143**(7), p. 071019.

[12] Howe, M. S., 1998, *Acoustics of Fluid-Structure Interactions*, 1st ed., Cambridge University Press, Cambridge, UK.

[13] Fournier, G. J. J., Haeringer, M., Silva, C. F., and Polifke, W., 2021, "Low-Order Modeling to Investigate Clusters of Intrinsic Thermoacoustic Modes in Annular Combustors," ASME J. Eng. Gas Turbines Power, **143**(4), p. 041025.

[14] Haeringer, M., Fournier, G. J. J., Meindl, M., and Polifke, W., 2021, "A Strategy to Tune Acoustic Terminations of Single-Can Test-Rigs to Mimic Thermoacoustic Behavior of a Full Engine," ASME J. Eng. Gas Turbines Power, **143**(7), p. 710029.

[15] Yoon, M., 2021, "Thermoacoustics and Combustion Instability Analysis for Multi-Burner Combustors," J. Sound Vib., **492**, p. 115774.

[16] Marble, F. E., and Candel, S. M., 1977, "Acoustic Disturbance From Gas Non-Uniformities Convected Through a Nozzle," J. Sound Vib., **55**(2), pp. 225–243.

[17] Bauerheim, M., Duran, I., Livebardon, T., Wang, G., Moreau, S., and Poinsot, T., 2016, "Transmission and Reflection of Acoustic and Entropy Waves Through a Stator–Rotor Stage," J. Sound Vib., **374**, pp. 260–278.

[18] Morgans, A. S., and Duran, I., 2016, "Entropy Noise: A Review of Theory, Progress and Challenges," Int. J. Spray Combust. Dyn., **8**(4), pp. 285–298.

[19] Mensah, G. A., Campa, G., and Moeck, J. P., 2016, "Efficient Computation of Thermoacoustic Modes in Industrial Annular Combustion Chambers Based on Bloch-Wave Theory," ASME J. Eng. Gas Turbines Power, **138**(8), p. 081502.

[20] Ghirardo, G., Moeck, J. P., and Bothien, M. R., 2020, "Effect of Noise and Nonlinearities on Thermoacoustics of Can-Annular Combustors," ASME ASME J. Eng. Gas Turbines Power, **142**(4), p. 041005.

[21] Haeringer, M., and Polifke, W., 2019, "Time Domain Bloch Boundary Conditions for Efficient Simulation of Thermoacoustic Limit-Cycles in (Can-)Annular Combustors," ASME J. Eng. Gas Turbines Power, **141**(12), p. 121005.

[22] Dowling, A. P., and Stow, S. R., 2003, "Acoustic Analysis of Gas Turbine Combustors," J. Propul. Power, **19**(5), pp. 751–764.

[23] Schuermans, B., Bellucci, V., and Paschereit, C. O., 2003, "Thermoacoustic Modeling and Control of Multi-Burner Combustion Systems," ASME Paper No. GT2003-38688.

[24] Bothien, M., Moeck, J., Lacarelle, A., and Paschereit, C. O., 2007, "Time Domain Modelling and Stability Analysis of Complex Thermoacoustic Systems," Proc. Inst. Mech. Eng., Part A: J. Power Energy, **221**(5), pp. 657–668.

[25] Emmert, T., Meindl, M., Jaensch, S., and Polifke, W., 2016, "Linear State Space Interconnect Modeling of Acoustic Systems," Acta Acust. United Acust., **102**(5), pp. 824–833.

[26] Barenblatt, G. I., 2003, *Scaling* (Cambridge Texts in Applied Mathematics) Cambridge University Press, Cambridge, UK.

[27] Polifke, W., 2004, "Combustion Instabilities," *Advances in Aeroacoustics and Applications*, eds. J. Anthoine and A. Hirschberg, Von Karman Institute, Rhode-St-Genèse, Belgium, Paper No. VKI LS 2004–05.

[28] Paschereit, C. O., and Polifke, W., 1998, "Investigation of the Thermo-Acoustic Characteristics of a Lean Premixed Gas Turbine Burner," ASME Paper No. 98-GT-582.

[29] Stow, S., Dowling, A., and Hynes, T., 2002, "Reflection of Circumferential Modes in a Choked Nozzle," J. Fluid Mech., **467**, pp. 215–239.

[30] Gentemann, A., Fischer, A., Evesque, S., and Polifke, W., 2003, "Acoustic Transfer Matrix Reconstruction and Analysis for Ducts With Sudden Change of Area," AIAA Paper No. 2003-3142.

[31] Flohr, P., Paschereit, C. O., and Bellucci, V., 2003, "Steady CFD Analysis for Gas Turbine Burner Transfer Functions," AIAA Paper No. 2003-1346.

[32] Schuermans, B., Bellucci, V., Guethe, F., Meili, F., Flohr, P., and Paschereit, O., 2004, "A Detailed Analysis of Thermoacoustic Interaction Mechanisms in a Turbulent Premixed Flame," ASME GT2004-53831.

[33] Bothien, M. R., and Wassmer, D., 2015, "Impact of Density Discontinuities on the Resonance Frequency of Helmholtz Resonators," AIAA J., **53**(4), pp. 877–887.

[34] McClarren, R., 2018, *Uncertainty Quantification and Predictive Computational Science: A Foundation for Physical Scientists and Engineers*, Springer International Publishing, New York.

[35] Loeppky, J. L., Sacks, J., and Welch, W. J., 2009, "Choosing the Sample Size of a Computer Experiment: A Practical Guide," Technometrics, **51**(4), pp. 366–376.

[36] Munjal, M. L., 2014, *Acoustics of Ducts and Mufflers*, 2nd ed., Wiley, Chichester, West Sussex, UK.

Guillaume J. J. Fournier[1]
TUM School of Engineering and Design,
Department of Engineering Physics and
Computation,
Technical University of Munich,
Boltzmannstr. 15,
Garching 85748, Germany
e-mail: fournier@tfd.mw.tum.de

Felicitas Schaefer
TUM School of Engineering and Design,
Department of Engineering Physics and
Computation,
Technical University of Munich,
Boltzmannstr. 15,
Garching 85748, Germany
e-mail: schaefer@tfd.mw.tum.de

Matthias Haeringer
TUM School of Engineering and Design,
Department of Engineering Physics and
Computation,
Technical University of Munich,
Boltzmannstr. 15,
Garching 85748, Germany
e-mail: haeringer@tfd.mw.tum.de

Camilo F. Silva
TUM School of Engineering and Design,
Department of Engineering Physics and
Computation,
Technical University of Munich,
Boltzmannstr. 15,
Garching 85748, Germany
e-mail: silva@tfd.mw.tum.de

Wolfgang Polifke
TUM School of Engineering and Design,
Department of Engineering Physics and
Computation,
Technical University of Munich,
Boltzmannstr. 15,
Garching 85748, Germany
e-mail: polifke@tum.de

Interplay of Clusters of Acoustic and Intrinsic Thermoacoustic Modes in Can-Annular Combustors

Thermoacoustic systems can exhibit self-excited instabilities of two nature, namely cavity modes or intrinsic thermoacoustic (ITA) modes. In heavy-duty land-based gas turbines with can-annular combustors, the cross-talk between cans causes the cavity modes of various azimuthal order to create clusters, i.e., ensembles of modes with close frequencies. Similarly, in systems exhibiting rotational symmetry, ITA modes also have the peculiar behavior of forming clusters. In the present study, we investigate how such clusters interplay when they are located in the same frequency range. We first consider a simple Rijke tube configuration and derive a general analytical low-order network model using only dimensionless numbers. We investigate the trajectories of the eigenmodes when changing the downstream length and the flame position. In particular, we show that ITA and acoustic modes can switch nature and their trajectories are strongly influenced by the presence of exceptional points. We then study a generic can-annular combustor. We show that such configuration can be approximated by an equivalent Rijke tube. We demonstrate that, in the absence of mean flow, the eigenvalues of the system necessarily lie on specific trajectories imposed by the upstream conditions. [DOI: 10.1115/1.4055381]

1 Introduction and Motivation

Lean premixed combustion systems have been developed in order to reduce emissions and address environmental issues. Unfortunately, such technology is also more prone to combustion instabilities [1,2]. The coupling between the unsteady heat release of the flame and the acoustics of the system may result in a positive feedback loop leading to self-excited instabilities with growing pressure fluctuations. It is crucial to understand and mitigate such phenomenon as repeated exposure to high level of pressure can lead to catastrophic engine failure [3].

Since the Apollo program and the development of modern rocket engines, thermoacoustic instabilities have been interpreted as acoustic eigenmodes of the system driven by unsteady heat release [4,5]. However, Hoeijmakers et al. [6,7], experimentally and with a simple analytical model, showed evidence of thermoacoustic instabilities in an anechoic environment. This situation was paradoxical and constituted a significant deviation from the established interpretation. These observations were later confirmed with high-fidelity numerical simulations [8,9]. Bomberg et al. [10] formally identified the so-called intrinsic thermoacoustic (ITA) feedback loop, a flame-flow-acoustic interaction intrinsic to the flame and its immediate surrounding and not involving the acoustics of the system, which allowed Emmert et al. [11] to justify the physical nature of the previous observations. Emmert et al. [12] then demonstrated that the ITA feedback loop gives rise to a new set of thermoacoustic modes of different nature also for reflecting boundaries and identified such an ITA mode as the most unstable mode in a longitudinal test-rig. Yong et al. [13] showed that for a marginally stable ITA mode, the velocity fluctuations and the gradient of pressure fluctuations change sign across the flame, thus providing a simple identification criterion.

This new paradigm fundamentally changed the understanding of thermoacoustic instabilities and shed a new light on inexplicable phenomena reported in earlier studies, such as “the new set of modes” described by Dowling and Stow [14], the “bulk mode” highlighted by Eckstein and Sattelmayer [15,16], or the “convective scaling” of thermoacoustic eigenfrequencies [17].

---

[1] Corresponding author.

Manuscript received July 11, 2022; final manuscript received July 27, 2022; published online October 14, 2022. Editor: Jerzy T. Sawicki.

Numerous studies then investigated the role of both types of thermoacoustic instabilities. Hosseini et al. investigated the interplay between modes of ITA and acoustic origin and showed that, when they are far away from one another, they do not influence each other [18]. Mensah et al. [19] highlighted the presence of exceptional points in the spectrum due to the coalescence of modes of ITA and acoustic origin. Silva et al. [20] and Orchini et al. [21] further investigated the role of exceptional points in the interplay between ITA and acoustic modes and highlighted characteristic trajectories. Buschmann et al. [22,23] observed the existence of ITA modes in an annular combustor and showed that they appear in clusters, i.e., a collection of eigenmodes with close oscillation frequencies but different growth rates. Fournier et al. [24] used a low-order model to explain why the ITA clusters align around a "pure ITA frequency," i.e., the frequency of an ITA mode in an anechoic environment.

Annular and can-annular combustors exhibit discrete rotational symmetry and the azimuthal dimension leads to interesting new properties. Numerical simulations [25,26] and experiments [27] revealed that the full can-annular configuration gives rise to new eigenmodes, with mode shapes involving multiple cans, that do not exist in a single can approximation. Farisco et al. [28] numerically investigated the effect of the gap, demonstrated that the cross-talk between cans cannot be ignored and estimated a transmission coefficient. Ghirardo et al. [29] gave further proof using two-dimensional Helmholtz simulations and experimental results. They highlighted that modes of various azimuthal orders emerge due to the weak coupling between cans and form clusters of acoustic modes. Jegal et al. [30] and Moon et al. [31,32] used a test-rig with two and four cans, respectively, to explore the effect of can coupling on the stability of the burners. Because the eigenmodes are closely spaced in clusters, mixed states, with several distinct types of interaction patterns, were observed.

Recent studies tackled the problem at a more fundamental level using low-order network models. Fournier et al. [24] proposed the modeling of the gap as a thin annulus and the method was applied by Haeringer et al. [33] in a strategy to tune single-can test-rigs to mimic full engines. Von Saldern et al. [34] proposed to model the cross-talk between cans with the Rayleigh conductivity, which relates the acoustic flux through the aperture to the pressure gradient between cans. Both modeling approaches were compared by Fournier et al. [35] and an extension was given, using a flow parameter in terms of a characteristic length, giving quantitatively accurate results. Von Saldern et al. [36] derived an effective impedance model for non-compact connections and analyzed the role of liners in damping azimuthal thermoacoustic modes. Orchini [37] and Pedergnana and Noiray [38] explored the effect of mean flow and derived effective impedance models that show explicit dependence on the grazing flow Mach number. Orchini et al. [39] then showed that such an effect gives rise to new sets of clusters of modes of aeroacoustic origin due to the coupling with the response of the shear layer in the apertures.

Both phenomena of ITA clusters in annular configuration and acoustic clusters in can-annular configurations are fairly well understood taken individually. In the present study, we want to investigate the interplay between clusters of acoustic and ITA modes in a can-annular combustor when they are located in the same frequency range. The motivation of our study is illustrated by Fig. 1, which shows the spectrum of two generic can-annular combustors obtained with FEM Helmholtz computations using COMSOL MULTIPHYSICS. The geometrical and thermodynamic parameters are given in Table 1 and both configurations are investigated more in-depth in Sec. 4. For Configuration A, the ITA and acoustic clusters are distinct and identifiable. In Configuration B, the flame position differs by only 15% but the total length of the combustor is kept constant. In this scenario, the clusters cannot be distinguished from one another and seem to be entangled. The paper aims at explaining such drastic change in the spectrum and giving more insight on the ITA and acoustic trajectories in can-annular combustors.

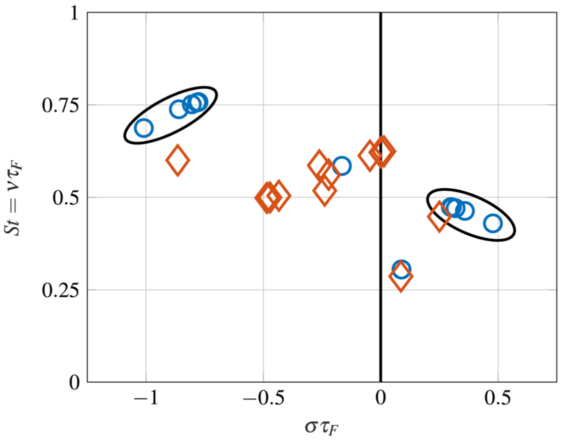

Fig. 1 Spectrum of two generic can-annular combustors obtained with FEM computations. Parameters are given in Table 1. For Configuration A (blue circles), the ITA and acoustic clusters are distinct and identifiable. Two modes are offset from their respective clusters, which is explained later in the paper. In Configuration B (orange diamonds), the flame position inside the combustor is changed but the total length is kept constant. The clusters become entangled and cannot be distinguished from one another.

Table 1 Geometrical and thermodynamic parameters of a generic can-annular combustor such as presented in Ref. [33]. The FTF parameters are adapted from Ref. [40].

	Configuration A	Configuration B
N	10	10
H (m)	0.15	0.15
L_g^*	0.25	0.25
n	1.2	1.2
τ_F (s)	3.5×10^{-3}	3.5×10^{-3}
L_u (m)	0.5	0.8
L_d (m)	1.5	1.2

Fournier et al. [24] and Haeringer et al. [33] showed that, under some assumptions discussed later in the paper, a can-annular combustor can be fairly well represented by an equivalent Rijke tube. The latter is one of the simplest thermoacoustic system and has been extensively studied for decades. This allows us to gain insight at a more fundamental level. Therefore, the paper structures as follows: in Sec. 2, we first consider a simple Rijke tube and analytically derive the dispersion relation. The problem remains generally applicable to configurations of arbitrary geometrical and thermodynamic parameters thanks to the use of Buckingham Π theorem and dimensionless numbers. In Sec. 3, we then investigate the influence of the length of the Rijke tube and the flame position inside it on both ITA and acoustic modes. In Sec. 4, the results are transposed to two generic can-annular combustors and allow us to explain the spectrum observed in Fig. 1. Finally, the modeling assumptions and the limits of validity are discussed.

2 Network Model of a Generic Rijke Tube Configuration

2.1 Case and Flow Description. The system considered is a generic Rijke tube, as depicted in Fig. 2. Ducts of length L_u and L_d are placed upstream and downstream of the flame, respectively. The acoustic boundaries are defined by the reflection coefficients R_i and R_o at the inlet and outlet, respectively. We assume zero mean flow when modeling the thermoacoustic behavior of the system, in particular wave propagation in the ducts. The model is based on a network approach. Recall the definition of the characteristic wave amplitudes

$$f \equiv \frac{1}{2}\left(\frac{p'}{\bar{\rho}c} + u'\right), \quad g \equiv \frac{1}{2}\left(\frac{p'}{\bar{\rho}c} - u'\right) \tag{1}$$

In the ducts, we assume that only one-dimensional (1D) planar acoustic waves propagate. The f and g waves in the system relate as follows:

$$\begin{bmatrix} f_u \\ g_u \end{bmatrix} = \begin{bmatrix} e^{-s\tau_u} & 0 \\ 0 & e^{s\tau_u} \end{bmatrix} \begin{bmatrix} f_i \\ g_i \end{bmatrix}, \quad \begin{bmatrix} f_o \\ g_o \end{bmatrix} = \begin{bmatrix} e^{-s\tau_d} & 0 \\ 0 & e^{s\tau_d} \end{bmatrix} \begin{bmatrix} f_d \\ g_d \end{bmatrix} \tag{2}$$

The term $e^{\pm s\tau}$ represents the phase change resulting from the acoustic propagation of the wave and τ is the time it takes to travel. $\tau_u = L_u/c_u$ and $\tau_d = L_d/c_d$ are the propagation times upstream and downstream the flame respectively, c_u and c_d are the speed of sound in the respective regions, and $s = \sigma + i\omega$ is the Laplace variable, with σ the growth rate and ω the angular frequency.

The acoustic boundary conditions of the system are defined using reflection coefficients. The latter write as follows:

$$R_i = \frac{f_i}{g_i}, \quad R_o = \frac{g_o}{f_o} \tag{3}$$

2.2 Flame and Unsteady Heat Release Model.

The acoustic flame model is derived using the linearized Rankine Hugoniot jump equations for a compact heat source at rest with unsteady heat release fluctuations [11,41]

$$\begin{cases} \dfrac{p'_d}{\bar{\rho}_d c_d} = \xi \dfrac{p'_u}{\bar{\rho}_u c_u} \\ u'_d = u'_u + \theta \dot{q}' \end{cases} \tag{4}$$

where $\xi = \bar{\rho}_u c_u / \bar{\rho}_d c_d$ is the ratio of specific impedances, $\theta \equiv (T_d - T_u)/T_u$ the normalized temperature ratio and $\dot{q}' = \dot{Q}' \bar{u}_u / \bar{\dot{Q}}$ the normalized global heat release fluctuations of the flame.

A flame transfer function (FTF) is used to relate the unsteady heat release fluctuations $\dot{q}'$ to the acoustic velocity fluctuations upstream the flame u'_u. For this study, the famous $n - \tau$ model from Crocco is used [42]

$$\frac{\dot{q}'}{u'_u} = \mathcal{F}(s) = n e^{-s\tau_F} \tag{5}$$

with n and τ_F the gain and time delay of the flame respectively. Such a simple model captures the essential aspects of a generic flame and is convenient to use in the context of low-order models as it allows to derive analytical solutions.

Writing Eq. (4) with the characteristic wave amplitudes f and g and inserting Eq. (5) leads to the flame transfer matrix:

$$\begin{bmatrix} f_d \\ g_d \end{bmatrix} = \begin{bmatrix} \mathcal{T}_a(s) & \mathcal{T}_b(s) \\ \mathcal{T}_b(s) & \mathcal{T}_a(s) \end{bmatrix} \begin{bmatrix} f_u \\ g_u \end{bmatrix} \tag{6}$$

The matrix is symmetric, with $\mathcal{T}_a(s) = \frac{1}{2}(\xi + 1 + n\theta e^{-s\tau_F})$ and $\mathcal{T}_b(s) = \frac{1}{2}(\xi - 1 - n\theta e^{-s\tau_F})$.

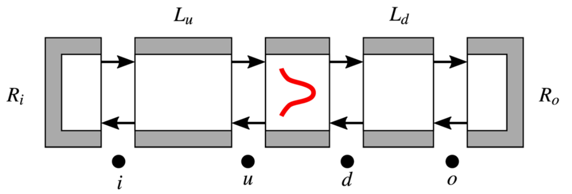

Fig. 2 Schematic of a generic Rijke tube of length L_u upstream the flame, L_d downstream the flame. The acoustic boundaries are defined by the reflection coefficients R_i and R_o at the inlet and outlet respectively.

2.3 Dimensionless Nonlinear Eigenvalue Problem.

Combining Eqs. (2), (3), and (6), the governing equations of the system can be cast in the matrix form:

$$\begin{bmatrix} 1 & -R_i & 0 & 0 \\ 0 & 0 & -R_o & 1 \\ \mathcal{T}_a(s)e^{-s(\tau_u+\tau_d)} & \mathcal{T}_b(s)e^{s(\tau_u-\tau_d)} & -1 & 0 \\ \mathcal{T}_b(s)e^{-s(\tau_u-\tau_d)} & \mathcal{T}_a(s)e^{s(\tau_u+\tau_d)} & 0 & -1 \end{bmatrix} \begin{bmatrix} f_i \\ g_i \\ f_o \\ g_o \end{bmatrix} = \begin{bmatrix} 0 \\ 0 \\ 0 \\ 0 \end{bmatrix} \tag{7}$$

The four governing equations describing the system involve the following parameters: the Laplace variable s, the propagation times τ_u and τ_d, the ratio of specific impedances ξ, the temperature ratio θ, the reflection coefficients R_i and R_o, the time delay of the flame τ_F and its gain n. Among these nine parameters, five are already dimensionless: n, ξ, θ, R_i and R_o. The remaining four parameters admit a basis of one fundamental dimension, time. Applying Buckingham Π theorem [43,44], we define the following dimensionless numbers:

$$s^* = s\tau_F, \quad \tau_u^* = \frac{\tau_u}{\tau_F}, \quad \tau_d^* = \frac{\tau_d}{\tau_F} \tag{8}$$

The system is therefore fully described using eight independent dimensionless numbers. The nondimensionalization of the problem allows us to generalize the results to configurations of arbitrary geometrical and thermodynamic parameters, and therefore allows us to draw general conclusions. This approach has successfully been applied in thermoacoustics [29,35,44].

Mathematically, Eq. (7) has nontrivial solutions if the determinant of the matrix is null. Solving for the determinant and using the dimensionless numbers defined in Eq. (8) leads to the dispersion relation:

$$\begin{aligned} \mathcal{D}(s^*) = {} & \left(\xi + 1 + n\theta e^{-s^*}\right)\left(1 - R_i R_o e^{-2s^*\left(\tau_u^* + \tau_d^*\right)}\right) \\ & + \left(\xi - 1 - n\theta e^{-s^*}\right)\left(R_i e^{-2s^*\tau_u^*} - R_o e^{-2s^*\tau_d^*}\right) = 0 \end{aligned} \tag{9}$$

Equation (9) is nonlinear in s^* and can generally not be solved analytically. Instead, we solve it numerically using taX,[2] the open-source MATLAB package developed by the TFD group to build and solve low-order thermoacoustic network models [45]. taX transforms Eq. (9) into a linear eigenvalue problem, thus facilitating the use of direct solvers to easily find all eigenmodes, in particular ITA modes, which remain difficult to find with iterative methods due to their small basin of attraction [22,46].

2.4 Interesting Special Cases.

Although Eq. (9) is nonlinear in s^*, in some cases, it can be solved analytically. We discuss here three interesting limit cases. In the following, we assume the reflection coefficients R_i and R_o to be real-valued and independent of frequency.

- For the case of a very weak flame (i.e., $n \approx 0$), the dispersion relation reduces to $1 - R_i R_o e^{-2s^*\left(\tau_u^* + \tau_d^*\right)} = 0$ and we recover the classical solution for an acoustic mode in a duct [7,47]:

---

[2] https://gitlab.lrz.de/tfd/tax

$$\begin{cases} \mathrm{St} = \nu\tau_F = \dfrac{j}{4(\tau_u^* + \tau_d^*)} \\ \sigma\tau_F = \dfrac{1}{2(\tau_u^* + \tau_d^*)}\ln\left(R_i R_o (-1)^j\right) \end{cases}, \quad j \in \mathbb{N} \tag{10}$$

where the Strouhal number St is the dimensionless frequency.

- In the case of anechoic boundaries $R_i = R_o = 0$, Eq. (9) becomes $\xi + 1 + n\theta e^{-s^*} = 0$. The acoustic modes disappear and only the pure ITA modes remain, i.e., ITA modes in an anechoic environment. This was extensively discussed in previous studies [7,11] and the eigenfrequencies are given by:

$$\begin{cases} \mathrm{St} = \nu\tau_F = \dfrac{(2j+1)}{2} \\ \sigma\tau_F = \ln\left(\dfrac{n\theta}{1+\xi}\right) \end{cases}, \quad j \in \mathbb{N} \tag{11}$$

- A third remarkable case arises when the boundaries are identical $R_i = R_o$, and when the flame is placed in the Rijke tube specifically such as the propagation times in the upstream and downstream ducts are identical $\tau_u^* = \tau_d^*$. In this configuration, the dispersion relation becomes:

$$\left(\xi + 1 + n\theta e^{-s^*}\right)\left(1 - R_i R_o e^{-2s^*\left(\tau_u^* + \tau_d^*\right)}\right) = 0 \tag{12}$$

The dispersion relation is factored in two terms. The first term corresponds to the dispersion relation in an anechoic environment, leading to pure ITA modes, and the second term is the dispersion relation for a pure acoustic system. Although a flame is present and the acoustic boundaries are not anechoic, the eigenvalues of the thermoacoustic system correspond exactly to the pure ITA and acoustic modes defined by Eqs. (10) and (11). Such a result can be explained using phasor analysis, which has already been used in thermoacoustics [13,16,17,24,48–50]. For example, if we consider the case of fully reflecting boundaries $R_i = R_o = \pm 1$, the acoustic mode is marginally stable, thus simplifying the phasor analysis with arrows of fixed length. At the inlet and the outlet, to satisfy the boundary conditions, the phasor f and g have opposite directions (case Open–Open) or the same direction (case Closed–Closed) respectively. Traveling from the boundaries to the flame, from both upstream and downstream sides, the phasors rotate by an identical angle $\omega\tau_u = \omega\tau_d = \pi/2$. The flame is located at a velocity node or a pressure node, respectively. The eigenmodes are simply the half-wave modes for a simple acoustic system with a temperature jump.

3 Interplay of Intrinsic Thermoacoustic and Acoustic Eigenmodes

In this section, we investigate the impact on the eigenmodes of the length of the Rijke tube and the position of the flame inside it. We consider here only the case Open–Open $R_i = R_o = -1$. The FTF parameters n and τ_F are kept constant, as well as the flame thermodynamic parameters θ, ξ.

3.1 Short Upstream Length. In this case, we consider a short upstream length, the dimensionless upstream propagation time is small $\tau_u^* = 0.1$. We change the downstream length, i.e., we vary the downstream dimensionless propagation time τ_d^* from 0 to 2, all other parameters being held constant. We consider only the fundamental acoustic and ITA thermoacoustic modes and disregard all the higher-order modes.

Figure 3 depicts the trajectories in the complex plane of both eigenmodes. When increasing the downstream length, the frequency of the acoustic mode decreases, as expected. For the ITA mode, when τ_d^* is small, the acoustic mode is far away and the two modes do not interplay. Therefore, its growth rate changes but the frequency remains constant and equal to the pure ITA frequency $\mathrm{St} = \nu\tau_F = 1/2$ [20,21,51]. When increasing τ_d^*, the ITA mode eventually converges to a special point, indicated by the cross in Fig. 3. The point can clearly be identified: the system behaves exactly as if, just after the flame, the duct L_d and the outlet boundary are replaced by a non-reflecting boundary, i.e., $R = 0$, while the upstream condition remains unchanged ($R_i = -1$). The flame is placed in an effective semi-anechoic environment. This can be explained by the fact that $R_d = g_d/f_d = R_o e^{-2s^*\tau_d^*}$, and for positive growth rate, when τ_d^* increases, $\lim_{\tau_d \to \infty} |R_d| = |R_o| e^{-\sigma\tau_d} \approx 0$. In other words, the longer the downstream duct, the weaker the effective reflection coefficient for an unstable mode. The system downstream of the flame is equivalent to a non-reflecting boundary.

The red circles mark the setup where $\tau_d^* = \tau_u^*$. For this specific scenario, the two modes are decoupled as shown by Eq. (12). Here, the acoustic mode is outside of the frequency range of interest and therefore not shown in Fig. 3. However, the ITA mode is indeed present and verifies the analytical expression Eq. (11).

Figure 4 shows similar results for a different upstream configuration. In this case, the upstream length is such that $\tau_u^* = 0.2$, and all other parameters are kept constant and identical to the previous case. We vary the downstream length, i.e., τ_d^* increases from 0 to 2. Similarly to the previous case, when τ_d^* remains small, the ITA and acoustic modes are far away from each other and do not interplay: the ITA mode has a constant pure ITA frequency $\mathrm{St} = 1/2$, and its growth rate changes. However, for larger downstream lengths, the ITA mode does not converge to the semi-anechoic mode, but passes around it and keeps decreasing in frequency: it turns into the acoustic mode. Conversely, the mode initially classified as acoustic, when τ_d^* is small, first decreases in frequency but then converges to the semi-anechoic eigenmode. It is highlighted that the two modes can switch nature, as previously reported [18,34,47]. However, we will not discuss how the eigenmodes can be classified as ITA and acoustic and when precisely the modes switch nature as this question is out of the scope of this study and already discussed by Yong et al. [50].

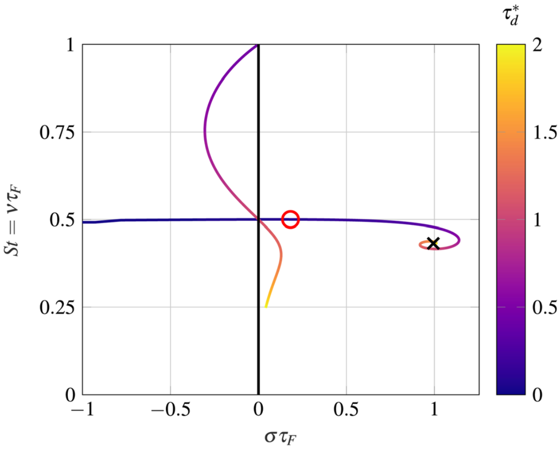

Fig. 3 Trajectories of the eigenmodes in the complex plane for a short upstream, $\tau_u^* = 0.1$ fixed. When increasing τ_d^*, i.e., increasing the downstream length, as expected, the frequency of the acoustic mode decreases. On the other hand, the ITA is around its pure ITA frequency St = 1/2 but its growth rate changes. Eventually, the ITA mode converges to the semi-anechoic configuration identified by the cross. The circle indicates when $\tau_d^* = \tau_u^*$, i.e., when the modes are fully decoupled according to Eq. (12). However, note that the acoustic mode is outside of the frequency range of interest and therefore not visible.

3.2 Long Upstream Length: The Impact of an Exceptional Point on the Acoustic and Intrinsic Thermoacoustic Trajectories. We now investigate the trajectories when the dimensionless upstream propagation time is large $\tau_u^* = 0.45$. All other parameters are kept constant and equal to the case described in Sec. 3.1. The downstream length is again varied such that τ_d^* increases from 0 to 2. Figure 5 shows the trajectories of the eigenmodes in the complex plane. When increasing τ_d^*, the two eigenmodes first converge toward each other before changing directions, which suggests the presence of an exceptional point (XP) in the vicinity of the parameter space. The circles indicate when the propagation times are identical $\tau_d^* = \tau_u^*$: the eigenmodes satisfy the pure ITA and acoustic modes defined by Eqs. (10) and (11).

Exceptional points are found in various disciplines, including thermoacoustics [19,20]. At an exceptional point, at least two eigenvalues and their respective eigenfunctions coalesce, and the eigenvalue sensitivity with respect to changes in parameters becomes infinite. Recall that the eigenvalues are the solution of the dispersion relation:

$$\mathcal{D}(s^*; \tau_d^*, n) = 0 \tag{13}$$

Eigenvalues can be classified according to their algebraic and geometric multiplicity, *am* and *gm* respectively. The algebraic multiplicity quantifies the multiplicity of the eigenvalue as a root of the dispersion relation Eq. (13). The geometric multiplicity is the dimension of the associated eigenspace, i.e., the number of linearly independent eigenvectors. Eigenvalues can be simple ($am = gm = 1$), semi-simple ($am = gm > 1$) or defective ($am > gm$). Defective eigenvalues that are branch-point singularities are called exceptional points (XPs). In the context of thermoacoustics, XPs are primarily attributed to the interplay between intrinsic thermoacoustic modes (ITA) and acoustic modes, i.e., thermoacoustic modes of different natures [19]. Previous studies have investigated XPs associated with the parameters (n, τ_F) [19,44], or (τ_c, R_o), where τ_c is the time-delay of a realistic flame impulse response [52]. Indeed, for the modes to coalesce, they need to have the same frequency, mainly driven by τ_F or τ_c for an ITA mode, and the same growth rate, mainly driven by the gain (strength of the flame n) or losses ($R_o \neq \pm 1$).

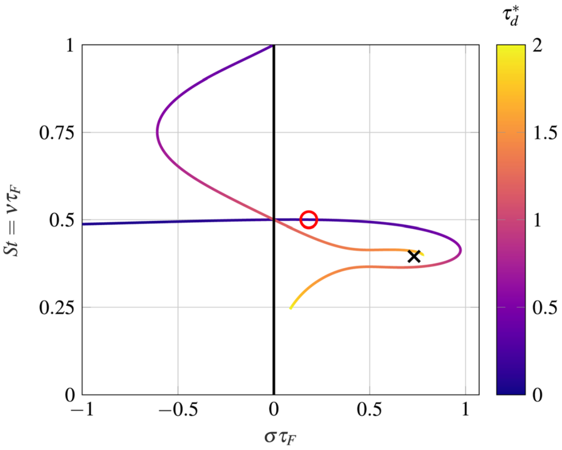

Fig. 4 Trajectories of the eigenmodes in the complex plane for a longer upstream length $\tau_u^* = 0.2$ fixed. For small values of τ_d^*, the ITA mode has once more its frequency near the pure ITA frequency St = 1/2, and its growth rate increases with τ_d^*. However, the ITA mode does not converge to the semi-anechoic point, identified by the cross, but passes around it while its frequency keeps decreasing. Conversely, the acoustic mode first decreases in frequency but then converges to the semi-anechoic eigenmode. The two eigenmodes switch nature. The circle indicates when $\tau_d^* = \tau_u^*$ and the ITA mode is a solution of Eq. (11).

In the present study, the approach is different because the time-delay of the flame τ_F is fixed, which in turn settles the value of the pure ITA frequency (solution of Eq. (11)). By changing τ_d^*, we allow the acoustic mode to move in the complex plane and be in the same frequency range as the ITA mode. For the modes to coalesce, their growth rates must also be equal, which is obtained by changing the strength of the flame n. According to Mensah et al. [19], for an ITA and acoustic mode to coalesce, the following relations need to be satisfied:

$$\begin{cases} \dfrac{\partial \mathcal{D}(s^*; \tau_d^*, n)}{\partial s^*} = 0 & (14) \\[2ex] \dfrac{\partial^2 \mathcal{D}(s^*; \tau_d^*, n)}{\partial s^{*2}} \neq 0 & (15) \end{cases}$$

The solution of the complex-valued Eqs. (13) and (14) is the set of parameters ($\tau_{d,XP}^*$, n_{XP}) and the defective eigenvalue s_{XP}^*. We highlight here one special configuration where an easy analytical solution is found. For the special case where $\tau_d^* = \tau_u^* = 1/2$, following Eqs. (10) and (11), the ITA and the acoustic mode share the same frequency St = 1/2. For the modes to coalesce, they need also to have the same growth rate. The acoustic mode is marginally stable. For the ITA mode to also be marginally stable, the gain of the flame response must be $n_{XP} = (1 + \xi)/\theta$. It is straight forward to demonstrate that the eigenvalue $s_{XP}^* = i\pi$ and the set of parameters ($\tau_{d,XP}^* = 1/2$, n_{XP}) satisfy Eqs. (13) and (14).

However, in general, the *XP* cannot be found analytically, and even finding it numerically remains challenging. For the configuration $\tau_u^* = 0.45$ depicted in Fig. 5, the method introduced by Schaefer et al. [52] is applied to identify the exceptional point. Results are shown in Fig. 6. Colors indicate isolines of flame strength n, along which the downstream propagation time τ_d^* varies. We observe strong mode veering, a manifestation of avoided crossing of two eigenvalues [20,21,44,53]. The presence of the XP induces the eigenvalues to strongly veer, resulting in the characteristic trajectories observed in Fig. 5. This also explains why modes can switch nature, i.e., the mode of acoustic nature when τ_d^* is small becomes ITA for large values of τ_d^*, and vice versa.

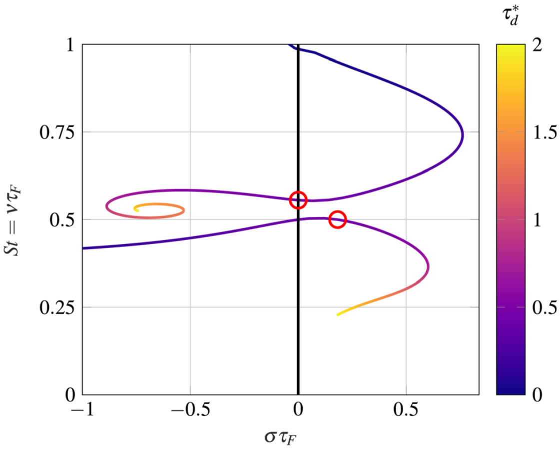

Fig. 5 Trajectories of the eigenmodes for the upstream configuration $\tau_u^* = 0.45$. When increasing τ_d^*, the modes first converge toward each other before changing direction, suggesting the presence of an exceptional point. The circles indicate when $\tau_d^* = \tau_u^*$, the acoustic and ITA modes are effectively decoupled and are solutions of Eqs. (10) and (11). Similarly to the results shown in Fig. 4, the eigenmodes also switch nature.

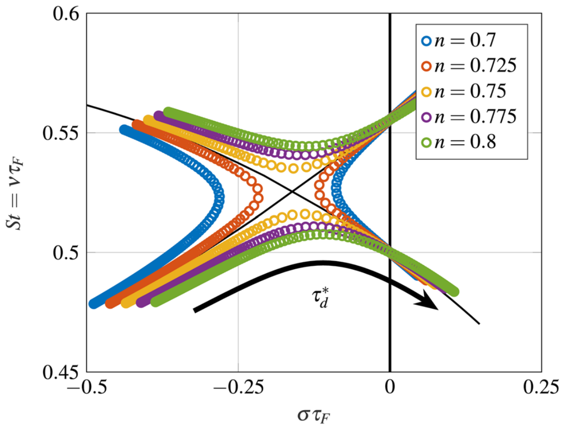

Fig. 6 Identification of an exceptional point for the upstream case $\tau_u^* = 0.45$. Colors indicate isolines of flame strength *n*. When varying the dimensionless downstream propagation time τ_d^* from 0.42 to 0.48, the *XP* causes the eigenmodes to strongly veer, leading to the characteristic trajectories observed in Fig. 5.

4 Application to Can-Annular Combustors

In this section, we want to extend the model to can-annular configurations. We first describe a typical can-annular combustor. We then show how such a system can be reduced to a simple Rijke tube, thus allowing us to transpose the methods and results of Secs. 2 and 3. Finally, we discuss the assumptions and limitations of our modeling approach.

4.1 Case Description and Low-Order Modeling. The generic combustor consists of N identical cans placed in an annular arrangement. Upstream the cans, we neglect the impact of the plenum, as it often shows little influence [33]. The cans are acoustically decoupled and the inlet reflection coefficient is set to $R_i = -1$. At the outlet of the cans, a turbine is placed to extract energy from the fluid. The acoustic response of the turbine stage is modeled by a reflection coefficient with a fixed gain and a zero phase response [54], we choose $R_o = 1$ as losses have little quantitative impact [55]. The Mach number is low, typically below 0.2 [27,29]. Consequently, we assume zero mean flow when modeling the thermoacoustic behavior of the cans. Finally, entropy waves are assumed to have a negligible effect and are not taken into account [29,56].

Figure 7 depicts a unit-cell of the investigated can-annular combustor. Following previous studies [29,35], we consider cans of width H and a gap of size L_g, leading to the coupling strength between cans $L_g^* = L_g/H$. The flame is placed inside the can at a distance L_u and L_d from the inlet and outlet, respectively. Two cases are investigated: Configuration A has a shorter upstream duct than Configuration B, however, the total length of the combustor $L_u + L_d$ is kept constant. The modeling of the flame is identical to Sec. 2.2. For the sake of simplicity, we consider a simple $n - \tau$ model adapted from Ref. [40], but results could be easily extended to realistic flames, since distributed time delay models are nothing more but a collection of individual $n - \tau$ models [48]. The geometrical and thermodynamic parameters, inspired from a realistic combustor such as presented in Ref. [33], are given in Table 1.

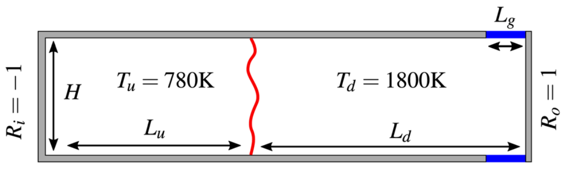

Fig. 7 Unit-cell of a generic can-annular combustor. The flame is placed at a distance L_u and L_d from the inlet and the outlet, respectively. The can is decoupled from the plenum at the inlet and closed at the outlet. However, acoustic communication with the neighboring cans is possible through the gap L_g. Parameters are given in Table 1.

4.2 Bloch Theory. As the cans are geometrically identical, the system exhibits discrete rotational symmetry. Applying Bloch theory [57], which is now well established in thermoacoustics [24,29,33–35,58,59], the acoustic pressure in the frequency domain can be written as

$$\hat{p}(\boldsymbol{x}) = \psi(\boldsymbol{x})e^{im\varphi},\ m = \begin{cases} -\dfrac{N}{2}+1, \ldots, \dfrac{N}{2} & N\,\text{even} \\ -\dfrac{N-1}{2}, \ldots, \dfrac{N-1}{2} & N\,\text{odd} \end{cases} \tag{16}$$

where φ is the azimuthal coordinate around the axis of rotational symmetry, m is the Bloch wave number, identical to the azimuthal order [29] and $\psi(\boldsymbol{x})$ a function identical in all unit-cells and $2\pi/N$ periodic in φ.

The eigenmodes are classified into three groups: axial or push-push ($m = 0$), push-pull ($m = N/2$), and azimuthal modes (all other values of m). We additionally assume reflection symmetry along the planes $\varphi = \text{const.}$ that pass through the center of the cell (no mean flow in the azimuthal direction): the azimuthal modes come in degenerate pairs which differ only by their spinning direction. From the study of a single unit-cell, the behavior of the full system is preserved by considering all azimuthal mode orders m. We reduce the can-annular system to a single unit-cell and apply Bloch boundaries in the gap region.

4.3 Equivalent Rijke Tube Model. Previous studies [24,33–35] showed the possibility of transforming a can-annular configuration into an equivalent longitudinal combustor, where all the two-dimensional effects of can-to-can communication in the cross-talk area are lumped into an equivalent outlet reflection coefficient $\mathcal{R}_m$. Using the characteristic length model introduced by Fournier et al. [35], the equivalent reflection coefficient writes

$$\mathcal{R}_m = 1 - \frac{2\sin^2\left(\dfrac{\pi m}{N}\right)}{iSt\dfrac{\pi L^*_{char,m}\tau^*_c}{L^*_g} + \sin^2\left(\dfrac{\pi m}{N}\right)} \tag{17}$$

with $L_g^* = L_g/H$ the coupling strength between the cans due to the size of the gap, $L^*_{\text{char},m} = L_{\text{char},m}/H$ the dimensionless characteristic length that models the inertia of the volume of fluid, and $\tau_c^* = H/(c_d\tau_F)$ the dimensionless propagation time in the azimuthal direction. The axial mode is a special case because the equivalent reflection coefficient is simply $\mathcal{R}_{m=0} = 1$: the push-push mode is not affected by the acoustic communication with neighboring cans, i.e., the eigenmode is exactly the same as in the single can system. For all the other azimuthal mode orders, the gain of the equivalent reflection coefficient $\mathcal{R}_m$ is unity, however, its phase response is not trivial, as shown in Fig. 8. Starting from π, the phase monotonically decreases and converges toward zero as the frequency increases. The characteristic length model shows perfect agreement with the FEM Helmholtz reference obtained with COMSOL MULTIPHYSICS. For low frequencies $\text{St} < 1$, the phase response of the gap can be approximated by the tangent at the origin, indicated by the dashed lines in Fig. 8. Since the phase depends linearly on the frequency St, following the approach of Fournier et al. [24], the equivalent reflection coefficient $\mathcal{R}_m$ can therefore be replaced by a duct of length $\mathcal{L}_m$ terminated by a fully

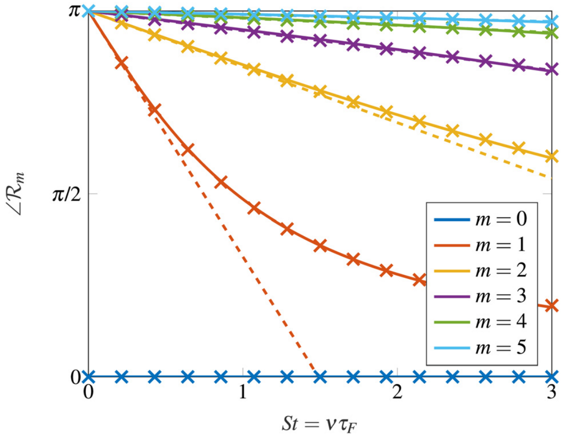

Fig. 8 For the considered generic can-annular configuration, the phase response of the gap obtained with FEM Helmholtz computations (full lines) is shown as a function of the dimensionless frequency St. The 1D model based on a characteristic length (crosses) shows perfect agreement with the reference. The phase response of the gap for the axial mode is trivially null. For all other azimuthal orders, starting from π, the phase monotonically decreases toward zero. For low frequencies St < 1, the phase response of the gap can be approximated by the tangent at the origin (dashed line). The higher the azimuthal order m, the wider the frequency range over which this approximation holds.

reflecting open end as shown in Fig. 9. This equivalent duct of length $\mathcal{L}_m$ induces an additional propagation time $\tau^*_m = \mathcal{L}_m/(c_d\tau_F)$ downstream of the cans that writes:

$$\mathcal{L}_m = \frac{L^*_{\text{char},m} H}{2L^*_g \sin^2\left(\frac{\pi m}{N}\right)}, \qquad \tau^*_m = \frac{L^*_{\text{char},m}\tau^*_c}{2L^*_g \sin^2\left(\frac{\pi m}{N}\right)} \tag{18}$$

For a given geometry, the higher the azimuthal order, the shorter the equivalent duct. The full configuration is, therefore, reduced to a simple Rijke tube, whose downstream length varies with the azimuthal order m, representing the fact that the acoustic response of the gap is mode order dependent. In consequence, the methodology and analysis introduced in Secs. 2 and 3 can be used to understand the spectrum of the can-annular configurations. Note however that this does not apply to the axial mode, which is simply obtained by solving the single can combustor.

4.4 Clusters of Eigenmodes and Their Trajectories.

Figures 10 and 11 show the spectrum of the can-annular combustor of Configurations A and B, respectively. Following the methodology introduced in Sec. 3, since the upstream condition is, in both cases, fixed, the trajectories when varying the downstream length are obtained. The circles indicate the eigenvalues computed with the reference FEM Helmholtz simulations, while the crosses are the results from the equivalent Rijke tube model described in Sec. 4.3. The latter shows excellent agreement with the reference. A small discrepancy is observed for the first azimuthal order $m = 1$. This is explained by the fact that the approximation of a linear phase response of the gap is valid only for low frequencies, as shown in Fig. 8, and the low azimuthal orders are the first to deviate from this approximation.

For Configuration A, $\tau^*_u = 0.251$ and the trajectories obtained resemble those shown in Fig. 4. For Configuration B, $\tau^*_u = 0.402$ and the trajectories are similar to Fig. 5. In particular, an

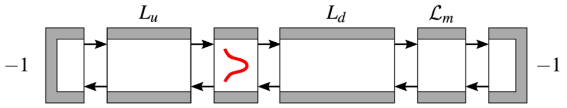

Fig. 9 Equivalent Rijke tube with fully reflecting boundaries. The equivalent length $\mathcal{L}_m$ varies with the azimuthal order of the mode considered and models the behavior of the acoustic communication through the gap. The larger the azimuthal order, the shorter $\mathcal{L}_m$.

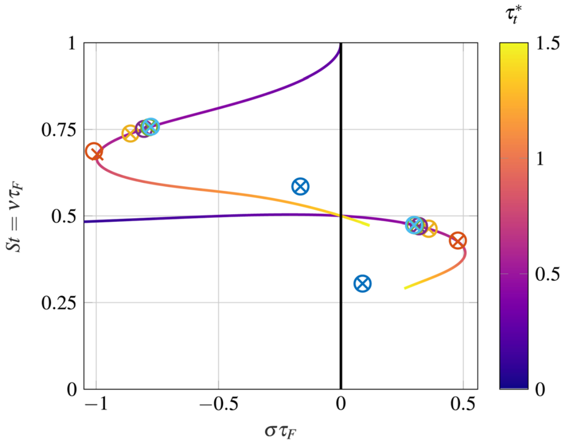

Fig. 10 Eigenvalues of the can-annular Configuration A as predicted by FEM Helmholtz simulations (circles) compared to the equivalent Rijke tube model (crosses). The latter shows excellent agreement with the reference. Colors indicate the azimuthal order as defined in Fig. 8. Except for the axial mode, all the eigenvalues are located on the trajectories obtained when varying τ^*_d. Their position on the trajectory depends on the mode order through the additional equivalent length $\mathcal{L}_m$. Note that modes $m = 4$ and $m = 5$ almost coincide. The ITA and acoustic clusters are distinct.

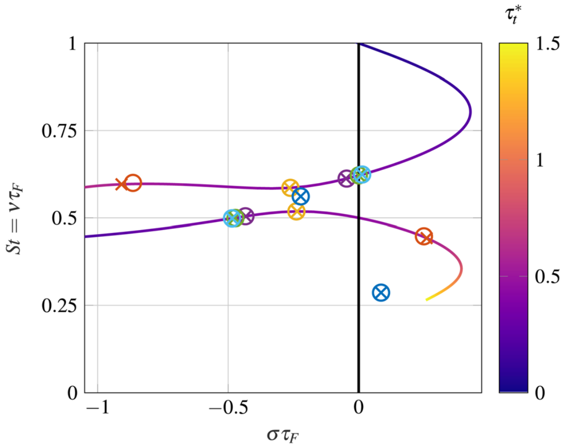

Fig. 11 Eigenvalues of the can-annular Configuration B as predicted by FEM Helmholtz simulations (circles) compared to the equivalent Rijke tube model (crosses). The latter shows excellent agreement with the reference. Colors indicate the azimuthal order as defined in Fig. 8. All azimuthal eigenmodes are located on the trajectories obtained when varying τ^*_d and their exact position on it depends on the mode order through the additional equivalent length $\mathcal{L}_m$. Note that modes $m = 4$ and $m = 5$ almost coincide. For this configuration, the presence of an XP makes the eigenmodes strongly veer.

exceptional point forces the trajectories to veer in order to avoid crossing. It is highlighted that, for both configurations, all the other eigenvalues are located on the trajectories (except for the special case of the axial mode $m=0$, which behaves differently from the rest of the cluster due to its different boundary conditions). Indeed, for all the azimuthal orders, the Rijke tube models are identical, in particular, they share the same flame response and upstream conditions. However, they differ by their total downstream propagation times, which is $\tau_t^* = \tau_d^* + \tau_m^*$, where τ_d^* is here a constant fixed by the can length L_d, whereas τ_m^*, due to the effective length $\mathcal{L}_m$ added to model the behavior of the gap, shows an explicit dependence on the azimuthal mode order. This fully explains the presence of all the eigenmodes on these trajectories. Their exact position is, however, determined by the total downstream propagation time τ_t^*. Following Eq. (18), low azimuthal order modes are associated to large values of τ_m^*, leading to a larger total downstream propagation time τ_t^* as observed in Figs. 10 and 11. In summary, the upstream conditions impose the eigenmodes to follow specific trajectories, while their exact position is fixed by the downstream conditions. This helps us to better understand the spectrum observed initially in Fig. 1. For Configuration A, the clusters are well separated, they do not interplay and can easily be identified. For Configuration B, the presence of an exceptional point plays a decisive role in shaping the trajectories (with a characteristic veer where the modes seem to repel each other), and, consequently, the spectrum of the considered system. Although the clusters seem entangled, we can now easily understand the trajectories the eigenmodes will follow when changing parameters.

This new insight could be exploited for early stage designs of new can-annular engines. Assuming that the design of the burners is fixed and that the flame response is known for a given amount of operating conditions, it may be possible to investigate the role of the upstream and downstream geometry on the thermoacoustic spectrum. The choice of the upstream can length L_u will impose the trajectories in the complex plane on which the eigenmodes are necessarily located. Finally, choosing the downstream length and the gap parameters will then govern their exact position on these trajectories. Note that changing the downstream parameters affects the system and the modes location in different ways. For example, changing the downstream length L_d induces a change in the total downstream length that is identical for all mode orders: all the modes are translated along the trajectories. Conversely, the impact of a modification in the geometry of the cross-talk area (width of the can or coupling strength) is different for each azimuthal order, since τ_m^* shows an explicit dependence to the mode order as shown in Eq. (18). Note also that changing the size of the gap or the width of the can have antagonist effects. Indeed, the larger the gap, ceteris paribus, the smaller the equivalent length, and the closer the eigenvalues along the trajectories. Modes of higher azimuthal order are closest within a cluster. Conversely, increasing the width of the can increases the effective length $\mathcal{L}_m$, leading to a wider spread of the clusters.

This could be used to develop strategies to stabilize an engine. Note that when we refer here to variations of L_u and L_d, we do not necessarily mean a drastic change of geometry, which is out of the question for later stages in the design. Instead, we refer to L_u and L_d as parameters indicating the effect of acoustic transport times upstream and downstream of the flame, which may be emulated by tuning the flow circuits belonging to the combustion chamber. For example, in the Configuration A shown in Fig. 10, the modes of azimuthal order $m = 1$, 2, 3, 4, and 5 on the lower branch are unstable. Changing the cross-talk area, by either changing the can width or gap size, will have a marginal effect on stabilizing the cluster: $\mathcal{L}_m$ is already very short for the highest azimuthal order and, no matter the cross-talk design, τ_t^* cannot be smaller than $\tau_t^* = \tau_d^* = 0.49$, which would still be unstable. However, reducing the downstream length of the can L_d would translate all eigenmodes along the trajectory (in the direction of smaller τ_t^*) and have a stabilizing effect on the entire cluster. Note, however, that a change in L_d will also have an impact on the axial modes $m=0$ and their trajectories should also be considered for a robust design. Similarly, for Configuration B, as shown in Fig. 11, the eigenmodes associated to the azimuthal order $m=1$ on the lower branch and $m=4$ and $m=5$ on the upper branch are unstable. Increasing the can length L_d would translate all the eigenvalues along the trajectories in the direction of higher τ_t^*, thus stabilizing the two unstable modes of the upper branch. However, it will further destabilize the azimuthal mode $m=1$ and will impact the stability of the axial modes $m=0$ as well. Conversely, reducing the coupling strength of the gap L_g^* would tend to increase τ_m^*, which would also have a stabilizing effect on the two unstable modes of the upper branch (τ_m^* small for high azimuthal order). Note, however, that the axial modes $m=0$ would remain unaffected since the cross-talk area with the neighboring cans has no impact on them. The above analysis is an example of what the present work offers, which could be of help to develop new strategies for designing stable can-annular combustors during early stage studies. For a complete robust design, clusters of harmonics should also be considered as they may be the most unstable modes.

4.5 Modeling Assumptions and Limits of Validity. In this section, we want to put our results in perspective and briefly discuss the main modeling assumptions and the limits of validity of our models. In Sec. 4.3, we showed the possibility to replace the complex-valued reflection coefficient $\mathcal{R}_m$ by an effective duct length $\mathcal{L}_m$. The main advantage of this approach is to model a complex system—a cross-talk area in can-annular combustor—with a very simple element, i.e., a duct, which gives good insight and helps the fundamental understanding of the underlying physics. As shown in Fig. 8, for higher azimuthal order m, this modeling assumption is valid over a large frequency range, even for frequencies $\mathrm{St} > 3$. On the other hand, for lower azimuthal order, in particular for $m=1$, the range of validity is much narrower, up to $\mathrm{St} < 1$ in our case. However, since we assumed a purely reactive coupling, the error made only affects the phase response of the gap. Consequently, as shown in Figs. 10 and 11, the eigenmodes obtained with the equivalent Rijke tube models are indeed located on the trajectories, but their exact positions are mispredicted. In conclusion, for understanding or when considering only the clusters associated with the fundamental modes, the equivalent Rijke tube model can be used. However, when considering clusters of harmonics or to ensure quantitatively accurate results, the characteristic length model of Fournier et al. [35] should be preferred.

In Sec. 4.4, we showed that all the eigenmodes (except the special case $m=0$) necessarily lie on the same trajectory. This result comes from two main assumptions. First of all, the plenum was considered perfectly decoupled. However, if the plenum is taken into account and modeled as a thin annulus [24,60], it will also introduce an equivalent length $\mathcal{L}_m$ at the inlet that changes with the azimuthal order. Consequently, for each azimuthal order, the upstream condition will be different and each eigenmode will follow its own trajectory. The second reason is the fact that the cross-talk area, modeled with a characteristic length model, is purely reactive. For each azimuthal order, the gap introduces a different phase shift, but there is no amplification or damping. However, recent studies by Pedergnana and Noiray [38] and Orchini et al. [39] showed that, when accounting for mean flow effects, the effective coupling impedance exhibit resistive effects. In particular, as shown in Fig. 5 in [39], the magnitude of the equivalent reflection coefficient is mode order dependent, i.e., depending on the azimuthal order considered, the gap will introduce different amplification or damping. This effect causes the mode to follow distinct trajectories. Finally, and more generally, the 1D low-order modeling approach is inherently limited by two factors: the gap needs to be acoustically compact (or its finite extension modeled as in Ref. [36]) and only plane waves propagate in the cans, all other modes being cut-off. These two factors were already discussed by Fournier et al. [35] and will also limit the number of clusters that can be properly captured with a 1D approach.

5 Summary and Conclusion

Starting from the observation that two similar can-annular configurations can lead to drastically different spectra, we investigated the interplay of acoustic and ITA clusters when they are in the same frequency range. To simplify the problem, we first considered a Rijke tube, which is one of the simplest thermoacoustic system and a fair approximation of can-annular combustors [24,33], and we derived an analytical low-order network model. Buckingham Π theorem allowed us to define dimensionless numbers so that the problem remains generally applicable to configuration of arbitrary parameters. We then investigated the interplay between the acoustic and ITA modes. In particular, for a given flame response, the impact on the eigenmodes of the downstream duct length and the flame position inside the system was analyzed.

For short upstream configurations, when increasing the downstream length, the frequency of the acoustic mode decreases whereas the ITA mode converges to a point identified as the eigenvalue of the semi-anechoic system. Conversely, for longer upstream configurations, the eigenmodes follow more peculiar trajectories and can, for example, switch nature, which confirmed previous observations [18,34,47]. In particular, the role of exceptional points in the complex plane was highlighted since it causes the eigenvalues to strongly veer, leading to characteristic trajectories.

We then considered two generic can-annular configurations. Using Bloch theory, we exploited the discrete rotational symmetry to reduce the study to a single unit-cell while preserving the dynamics of the full system. We confirmed the possibility to approximate the systems by a simple Rijke tube where the behavior of the gap was simply lumped into an additional effective length. Such modeling allowed us to explain the spectra of both systems. In particular, we showed that, in the absence of mean flow, the eigenmodes necessarily follow specific trajectories, imposed by the upstream conditions, and their exact position along the latter is determined by the gap and downstream parameters. We highlighted that, when ITA and acoustic clusters do not interplay, they are well distinct and identifiable, as exemplified in Configuration A (see Fig. 10). However, the presence of an exceptional point in the complex plane strongly influences the trajectories, as already reported by Silva et al. [44] and Mensah et al. [19]. ITA and acoustic clusters can also be entangled, as illustrated in Fig. 11 with Configuration B. New insight is gained when considering the trajectories the modes follow. In that sense, we confirmed the conclusion of Orchini et al. [21] who showed that the interaction between acoustic modes, ITA modes and exceptional points is essential to predict the stability in (can-)annular combustors.

The proposed framework may be of great utility for the design of can-annular combustors. This is exemplified by the two cases under investigation at the end of Sec. 4.4. The assumptions made by the proposed modeling strategy, as well as the limits of validity, are explicitly discussed in Sec. 4.5.

In this study, we considered a perfectly symmetric can-annular configuration. Symmetry breaking, due to, for example, geometrical imperfections, flow asymmetry, or nonlinear response of the flames, plays a major role in annular cavities because the degenerate pairs of azimuthal eigenmodes split into two distinct modes [61]. In can-annular configurations, it would double the number of modes in the acoustic and ITA clusters and could potentially affect their trajectories or lead to peculiar behaviors such as mode localization. This effect should be investigated in future studies.

Acknowledgment

This project has received funding from the European Union's Horizon 2020 research and innovation programme under Grant Agreement No 765998 *Annular Instabilities and Transient Phenomena in Gas Turbine Combustors* (ANNULIGhT) and from the Research Association for Combustion Engines (Forschungsvereinigung Verbrennungskraftmaschinen e.V. FVV, project number 6012700). The authors would also like to thank Max Meindl for valuable discussions and his help with FEM COMSOL MULTIPHYSICS simulations.

Funding Data

- European Commission (Grant No. 765998; Funder ID: 10.13039/501100000780).
- Forschungsvereinigung Verbrennungskraftmaschinen (Grant No. 6012700; Funder ID: 10.13039/501100003162).

Nomenclature

Roman

c_u, c_d = speed of sound upstream/downstream (m s^{-1})
$\mathcal{F}$ = flame transfer function
f, g = characteristic wave amplitudes (m s^{-1})
H = width of a can (m)
L_g = size of the gap (m)
$\mathcal{L}_m$ = equivalent length (m)
L_u, L_d = length of the upstream/downstream duct (m)
L_g^* = coupling strength, $L_g^* = L_g/H$
m = Bloch wave number
n = interaction index of the flame
N = number of cans
p' = acoustic pressure (Pa)
$\dot{q}'$ = normalized heat release fluctuations
R_i, R_o = reflection coefficient at the inlet/outlet
$\mathcal{R}_m$ = equivalent reflection coefficient
s = Laplace variable, $s = \sigma + i\omega$ (rad s^1)
s^* = dimensionless Laplace variable, $s^* = s\tau_F$
St = Strouhal number, St $= \nu\tau_F$
T_u, T_d = upstream/downstream temperature (K)
u' = acoustic velocity (m s^{-1})

Greek Symbols

θ = normalized temperature ratio, $\theta = T_d/T_u - 1$
ν = frequency (Hz)
ξ = ratio of specific impedances, $\xi = \bar{\rho}_u c_u/\bar{\rho}_d c_d$
$\bar{\rho}_u$, $\bar{\rho}_d$ = upstream/downstream mean density (kg m^{-3})
σ = growth rate (s^{-1})
τ_F = time delay of the flame (s)
τ_u, τ_d = upstream/downstream propagation time, $\tau_i = L_i/c_i$ (s)
τ_m^* = dimensionless equivalent propagation time
τ_t^* = total dimensionless propagation time, $\tau_t^* = \tau_d^* + \tau_m^*$
τ_u^*, τ_d^* = dimensionless upstream/downstream propagation time, $\tau_i^* = \tau_i/\tau_F$
ω = angular frequency, $\omega = 2\pi\nu$ (rad s^{-1})

Abbreviations

FTF = flame transfer function
XP = exceptional point

References

[1] Lieuwen, T., and McManus, K., 2003, "Combustion Dynamics in Lean-Premixed Prevaporized (LPP) Gas Turbines," J. Propul. Power, **19**(5), pp. 721–721.

[2] Poinsot, T., 2017, "Prediction and Control of Combustion Instabilities in Real Engines," Proc. Combust. Inst., **36**(1), pp. 1–28.

[3] Lieuwen, T., and Yang, V., eds., 2005, "Combustion Instabilities in Gas Turbine Engines: Operational Experience, Fundamental Mechanisms and Modeling," AIAA Paper No. v. 210.

[4] Culick, F., 1988, "Combustion Instabilities in Liquid-Fuelled Propulsion Systems - An Overview," *Combustion Instabilities in Liquid-Fuelled Propulsion Systems*, Vol. 450, Agard/NATO, Neuilly-sur-Seine, France.

[5] Lieuwen, T. C., 2012, *Unsteady Combustor Physics*, Cambridge University Press, New York.

[6] Hoeijmakers, M., Lopez Arteaga, I., Kornilov, V., Nijmeijer, H., and de Goey, P., 2013, "Experimental Investigation of Intrinsic Flame Stability," European Combustion Meeting, ECM2013, Scandinavian-Nordic Section of the Combustion Institute, Lund, Sweden, June 25–28.

[7] Hoeijmakers, M., Kornilov, V., Lopez Arteaga, I., de Goey, P., and Nijmeijer, H., 2014, "Intrinsic Instability of Flame-Acoustic Coupling," Combust. Flame, **161**(11), pp. 2860–2867.

[8] Silva, C. F., Emmert, T., Jaensch, S., and Polifke, W., 2015, "Numerical Study on Intrinsic Thermoacoustic Instability of a Laminar Premixed Flame," Combust. Flame, **162**(9), pp. 3370–3378.

[9] Courtine, E., Selle, L., and Poinsot, T., 2015, "DNS of Intrinsic Thermoacoustic Modes in Laminar Premixed Flames," Combust. Flame, **162**(11), pp. 4331–4341.

[10] Bomberg, S., Emmert, T., and Polifke, W., 2015, "Thermal Versus Acoustic Response of Velocity Sensitive Premixed Flames," Proc. Combust. Inst., **35**(3), pp. 3185–3192.

[11] Emmert, T., Bomberg, S., and Polifke, W., 2015, "Intrinsic Thermoacoustic Instability of Premixed Flames," Combust. Flame, **162**(1), pp. 75–85.

[12] Emmert, T., Bomberg, S., Jaensch, S., and Polifke, W., 2017, "Acoustic and Intrinsic Thermoacoustic Modes of a Premixed Combustor," Proc. Combust. Inst., **36**(3), pp. 3835–3842.

[13] Yong, K. J., Silva, C. F., and Polifke, W., 2021, "A Categorization of Marginally Stable Thermoacoustic Modes Based on Phasor Diagrams," Combust. Flame, **228**, pp. 236–249.

[14] Dowling, A. P., and Stow, S. R., 2003, "Acoustic Analysis of Gas Turbine Combustors," J. Propul. Power, **19**(5), pp. 751–764.

[15] Eckstein, J., and Sattelmayer, T., 2006, "Low-Order Modeling of Low-Frequency Combustion Instabilities in Aeroengines," J. Propul. Power, **22**(2), pp. 425–432.

[16] Ghani, A., Steinbacher, T., Albayrak, A., and Polifke, W., 2019, "Intrinsic Thermoacoustic Feedback Loop in Turbulent Spray Flames," Combust. Flame, **205**(7), pp. 22–32.

[17] Albayrak, A., Steinbacher, T., Komarek, T., and Polifke, W., 2018, "Convective Scaling of Intrinsic Thermo-Acoustic Eigenfrequencies of a Premixed Swirl Combustor," ASME J. Eng. Gas Turbines Power, **140**(4), p. 041510.

[18] Hosseini, N., Kornilov, V., Lopez Arteaga, I., Polifke, W., Teerling, O., and de Goey, L., 2018, "Intrinsic Thermoacoustic Modes and Their Interplay With Acoustic Modes in a Rijke Burner," Int. J. Spray Combust. Dyn., **10**(4), pp. 315–325.

[19] Mensah, G. A., Magri, L., Silva, C. F., Buschmann, P. E., and Moeck, J. P., 2018, "Exceptional Points in the Thermoacoustic Spectrum," J. Sound Vib., **433**, pp. 124–128.

[20] Silva, C., Yong, K. J., and Magri, L., 2019, "Thermoacoustic Modes of Quasi-One-Dimensional Combustors in the Region of Marginal Stability," ASME J. Eng. Gas Turbines Power, **141**(2), p. 021022.

[21] Orchini, A., Silva, C. F., Mensah, G. A., and Moeck, J. P., 2020, "Thermoacoustic Modes of Intrinsic and Acoustic Origin and Their Interplay With Exceptional Points," Combust. Flame, **211**, pp. 83–95.

[22] Buschmann, P. E., Mensah, G. A., Nicoud, F., and Moeck, J. P., 2020, "Solution of Thermoacoustic Eigenvalue Problems With a Noniterative Method," ASME J. Eng. Gas Turbines Power, **142**(3), p. 031022.

[23] Buschmann, P. E., Mensah, G. A., and Moeck, J. P., 2020, "Intrinsic Thermoacoustic Modes in an Annular Combustion Chamber," Combust. Flame, **214**, pp. 251–262.

[24] Fournier, G. J. J., Haeringer, M., Silva, C. F., and Polifke, W., 2021, "Low-Order Modeling to Investigate Clusters of Intrinsic Thermoacoustic Modes in Annular Combustors," ASME J. Eng. Gas Turbines Power, **143**(4), p. 041025.

[25] Bethke, S., Krebs, W., Flohr, P., and Prade, B., 2002, "Thermoacoustic Properties of Can Annular Combustors," AIAA Paper No. 2002-2570.

[26] Kaufmann, P., Krebs, W., Valdes, R., and Wever, U., 2008, "3D Thermoacoustic Properties of Single Can and Multi Can Combustor Configurations," ASME Paper No. GT2008-50755.

[27] Panek, L., Farisco, F., and Huth, M., 2017, "Thermo-Acoustic Characterization of Can-Can Interaction of a Can-Annular Combustion System Based on Unsteady CFD LES Simulation," Proceedings of First Global Power and Propulsion Forum, GPPS, Zurich, Switzerland, Jan. 16–18, Paper No. GPPF-2017-81.

[28] Farisco, F., Panek, L., and Kok, J. B., 2017, "Thermo-Acoustic Cross-Talk Between Cans in a Can-Annular Combustor," Int. J. Spray Combust. Dyn., **9**(4), pp. 452–469.

[29] Ghirardo, G., Di Giovine, C., Moeck, J. P., and Bothien, M. R., 2019, "Thermoacoustics of Can-Annular Combustors," ASME J. Eng. Gas Turbines Power, **141**(1), p. 011007.

[30] Jegal, H., Moon, K., Gu, J., Li, L. K., and Kim, K. T., 2019, "Mutual Synchronization of Two Lean-Premixed Gas Turbine Combustors: Phase Locking and Amplitude Death," Combust. Flame, **206**, pp. 424–437.

[31] Moon, K., Jegal, H., Gu, J., and Kim, K. T., 2019, "Combustion-Acoustic Interactions Through Cross-Talk Area Between Adjacent Model Gas Turbine Combustors," Combust. Flame, **202**, pp. 405–416.

[32] Moon, K., Jegal, H., Yoon, C., and Kim, K. T., 2020, "Cross-Talk-Interaction-Induced Combustion Instabilities in a Can-Annular Lean-Premixed Combustor Configuration," Combust. Flame, **220**, pp. 178–188.

[33] Haeringer, M., Fournier, G. J. J., Meindl, M., and Polifke, W., 2021, "A Strategy to Tune Acoustic Terminations of Single-Can Test-Rigs to Mimic Thermoacoustic Behavior of a Full Engine," ASME J. Eng. Gas Turbines Power, **143**(7), p. 071029.

[34] von Saldern, J., Orchini, A., and Moeck, J., 2021, "Analysis of Thermoacoustic Modes in Can-Annular Combustors Using Effective Bloch-Type Boundary Conditions," ASME J. Eng. Gas Turbines Power, **143**(7), p. 071019.

[35] Fournier, G. J. J., Meindl, M., Silva, C. F., Ghirardo, G., Bothien, M. R., and Polifke, W., 2021, "Low-Order Modeling of Can-Annular Combustors," ASME J. Eng. Gas Turbines Power, **143**(12), p. 121004.

[36] von Saldern, J. G. R., Orchini, A., and Moeck, J. P., 2021, "A Non-Compact Effective Impedance Model for Can-to-Can Acoustic Communication: Analysis and Optimization of Damping Mechanisms," ASME J. Eng. Gas Turbines Power, **143**(12), p. 121024.

[37] Orchini, A., 2022, "An Effective Impedance for Modelling the Aeroacoustic Coupling of Ducts Connected Via Apertures," J. Sound Vib., **520**, p. 116622.

[38] Pedergnana, T., and Noiray, N., 2022, "Coupling-Induced Instability in a Ring of Thermoacoustic Oscillators," Proc. R. Soc. A Math., Phys. Eng. Sci., **478**(2259), p. 20210851.

[39] Orchini, A., Pedergnana, T., Buschmann, P. E., Moeck, J. P., and Noiray, N., 2022, "Reduced-Order Modelling of Thermoacoustic Instabilities in Can-Annular Combustors," J. Sound Vib., **526**, p. 116808.

[40] Tay-Wo-Chong, L., Bomberg, S., Ulhaq, A., Komarek, T., and Polifke, W., 2012, "Comparative Validation Study on Identification of Premixed Flame Transfer Function," ASME J. Eng. Gas Turbines Power, **134**(2), p. 021502.

[41] Chu, B.-T., 1953, "On the Generation of Pressure Waves at a Plane Flame Front," Symp. (Int.) Combust., **4**(1), pp. 603–612.

[42] Crocco, L., 1951, "Aspects of Combustion Stability in Liquid Propellant Rocket Motors Part1: Fundamentals. Low Frequency Instability With Monopropellants," J. Am. Rocket Soc., **21**(6), pp. 163–178.

[43] Barenblatt, G. I., 2003, *Scaling. Cambridge Texts in Applied Mathematics*, Cambridge University Press, Cambridge, UK.

[44] Silva, C. F., and Polifke, W., 2019, "Non-Dimensional Groups for Similarity Analysis of Thermoacoustic Instabilities," Proc. Combust. Inst., **37**(4), pp. 5289–5297.

[45] Emmert, T., Meindl, M., Jaensch, S., and Polifke, W., 2016, "Linear State Space Interconnect Modeling of Acoustic Systems," Acta Acust. United Acust., **102**(5), pp. 824–833.

[46] Mensah, G. A., 2019, "Efficient Computation of Thermoacoustic Modes," Ph.D. thesis, TU Berlin, Fak. V, Verkehrs- und Maschinensysteme, Berlin, Germany.

[47] Sogaro, F. M., Schmid, P. J., and Morgans, A. S., 2019, "Thermoacoustic Interplay Between Intrinsic Thermoacoustic and Acoustic Modes: Non-Normality and High Sensitivities," J. Fluid Mech., **878**, pp. 190–220.

[48] Polifke, W., 2020, "Modeling and Analysis of premixed flame Dynamics by Means of Distributed Time Delays," Prog. Energy Combust. Sci., **79**, p. 100845.

[49] Æsøy, E., Nygård, H. T., Worth, N. A., and Dawson, J. R., 2022, "Tailoring the Gain and Phase of the Flame Transfer Function Through Targeted Convective-Acoustic Interference," Combust. Flame, **236**, p. 111813.

[50] Yong, K. J., Silva, C. F., Fournier, G. J. J., and Polifke, W., 2021, "Categorization of Thermoacoustic Modes in an Ideal Resonator With Phasor Diagrams," Combust. Flame, epub.

[51] Mukherjee, N. K., and Shrira, V., 2017, "Intrinsic Flame Instabilities in Combustors: Analytic Description of a 1-D Resonator Model," Combust. Flame, **185**, pp. 188–209.

[52] Schaefer, F., Guo, S., and Polifke, W., 2021, "The Impact of Exceptional Points on the Reliability of Thermoacoustic Stability Analysis," ASME J. Eng. Gas Turbines Power, **143**(2), p. 021010.

[53] Sogaro, F., Schmid, P., and Morgans, A. S., 2017, "Sensitivity Analysis of Thermoacoustic Instabilities," 24th International Congress on Sound and Vibration (ICSV 24), IIAV, London, UK, July 23–27.

[54] Marble, F. E., and Candel, S. M., 1977, "Acoustic Disturbance From Gas Non-Uniformities Convected Through a Nozzle," J. Sound Vib., **55**(2), pp. 225–243.

[55] Bauerheim, M., Duran, I., Livebardon, T., Wang, G., Moreau, S., and Poinsot, T., 2016, "Transmission and Reflection of Acoustic and Entropy Waves Through a Stator–Rotor Stage," J. Sound Vib., **374**, pp. 260–278.

[56] Morgans, A. S., and Duran, I., 2016, "Entropy Noise: A Review of Theory, Progress and Challenges," Int. J. Spray Combust. Dyn., **8**(4), pp. 285–298.

[57] Bloch, F., 1929, "Über Die Quantenmechanik Der Elektronen in Kristallgittern," Z. Phys., **52**(7–8), pp. 555–600.

[58] Mensah, G. A., Campa, G., and Moeck, J. P., 2016, "Efficient Computation of Thermoacoustic Modes in Industrial Annular Combustion Chambers Based on Bloch-Wave Theory," ASME J. Eng. Gas Turbines Power, **138**(8), p. 081502.

[59] Ghirardo, G., Moeck, J. P., and Bothien, M. R., 2020, "Effect of Noise and Nonlinearities on Thermoacoustics of Can-Annular Combustors," ASME J. Eng. Gas Turbines Power, **142**(4), p. 041005.

[60] Bauerheim, M., Parmentier, J.-F., Salas, P., Nicoud, F., and Poinsot, T., 2014, "An Analytical Model for Azimuthal Thermoacoustic Modes in an Annular Chamber Fed by an Annular Plenum," Combust. Flame, **161**(5), pp. 1374–1389.

[61] Bauerheim, M., Salas, P., Nicoud, F., and Poinsot, T., 2014, "Symmetry Breaking of Azimuthal Thermo-Acoustic Modes in Annular Cavities: A Theoretical Study," J. Fluid Mech., **760**, pp. 431–465.